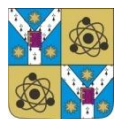


---

*Joint PhD Thesis*



Alexandru Ioan Cuza University of Iasi  
Faculty of Physics  
Iasi Plasma Advanced Research Center  
(IPARC)

Université Lille1  
Institut d'Electronique, de  
Microélectronique et de Nanotechnologie

---

# Synthesis and characterization of complex nano-structures at the interface with biological medium

**Roxana IJIE**

**Supervisor:**

Dr. Nicoleta DUMITRAȘCU  
Romania

**Co-supervisor:**

Dr. Rabah BOUKHERROUB  
France

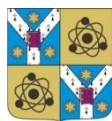
---

**Iasi – October 27, 2016**

---

---

**These de Doctorat**  
**EN COTUTELLE**



Université Alexandru Ioan Cuza de Iasi  
Faculté de Physique  
Iasi Plasma Advanced Research Center  
(IPARC)

Université Lille1  
Institut d'Electronique, de  
Microélectronique et de Nanotechnologie

---

# **Préparation et caractérisation de nanostructures complexes à l'interface avec le milieu biologique**

**Roxana ILJIE**

**Directrice de thèse :**

Dr. Nicoleta DUMITRAȘCU  
Roumanie

**Co-directeur de thèse :**

Dr. Rabah BOUKHERROUB  
France

---

**Iasi - 27 Octobre 2016**

---

TO MY PARENTS

# ABSTRACT

The increase of infections by multi-drug resistant pathogens has become an important worldwide healthcare issue that requires the development of new strategies to prevent biofilm formation and to kill bacteria.

In this context, the aim of this thesis was the design of complex nano-structures to control cells adhesion to surfaces and to inactivate pathogenic bacteria. To this end, we propose different strategies relying on the use of i) micro-structured plasma polymerized styrene (pPS) films, ii) particle-based photodynamic therapy combined with a pulsed laser in the near infrared (NIR) region and iii) ampicillin-functionalized, fluorescent carbon dots (CDs) as possible solutions for bacterial killing.

Firstly, we performed a detail characterization of pPS films used as substrates to study the behavior of biological systems. A special attention was devoted to pPS films stability in biological media. The pPS films topography has changed during the immersion, the surfaces became microporous, resembling a honeycomb pattern. Our results proved the complexity of the processes occurring at the interface biological media/plasma film and particularly the role of topography which mediates cell response, preventing *Escherichia coli* (*E.coli*) colonization and biofilm formation.

Secondly, we demonstrated that gold nanorods surrounded by an indocyanine green-embedded silica shell (Au NRs@SiO<sub>2</sub>-ICG) display an enhanced capacity to kill pathogenic bacteria under 810 nm pulsed-mode laser irradiation. We achieved a 6 log<sub>10</sub> reduction in *E. coli* LF82 viability by using composite gold nanorods displaying a plasmonic band at 900 nm, without any photothermal effects. The results revealed that the amount of generated singlet oxygen (<sup>1</sup>O<sub>2</sub>) is highly sensitive to the indocyanine green (ICG) concentration loaded to the silica shell and fine tuning of the plasmonic structures seems to enhance the photodynamic therapy efficiency.

Thirdly, we examined the bactericidal activity of amino functionalized carbon dots, covalently functionalized with ampicillin. The results showed that the ampicillin conjugated fluorescent carbon dots (CDs@Amp) exhibit enhanced antibacterial activity against Gram negative bacteria strains. The minimal inhibitory concentration of CDs@Amp conjugate was significantly reduced when compared to free ampicillin. The bioimaging properties of carbon dots (CDs) and the antibacterial function of ampicillin were integrated into a single system.

**Keywords:** Micro-structured polystyrene, antibiofouling, pathogens, photodynamic therapy, enhanced antibacterial activity

# RÉSUMÉ

L'augmentation des infections causées par des pathogènes résistants aux médicaments est devenue un problème de santé majeur dans le monde entier qui impose le développement de nouvelles stratégies destinées à empêcher la formation de biofilms et à éliminer les bactéries.

Dans ce contexte, l'objectif de cette thèse a été la préparation de nanostructures complexes pour contrôler l'adhérence des cellules à des surfaces et inactiver les bactéries pathogènes. Ainsi, nous proposons différentes approches qui consistent en l'utilisation de : i) une couche micro-structurée de polystyrène polymérisé à l'aide d'un plasma (pPS), ii) la thérapie photodynamique à base de nanoparticules hybrides activées par un rayon laser dans le proche infrarouge (NIR) et iii) des nanoparticules de carbone fonctionnalisées par l'ampicilline, comme solutions possibles pour éliminer les bactéries.

D'abord, nous avons réalisé une caractérisation détaillée de couches de polystyrène polymérisé par plasma, utilisées comme substrats pour étudier les comportements des systèmes biologiques. Une attention particulière a été dédiée à la stabilité des films de polystyrène dans des milieux biologiques. Au cours de l'immersion, la topographie des films de polystyrène est modifiée, les surfaces deviennent microporeuses. Nos résultats montrent la complexité des processus qui se produisent à l'interface milieu biologique/polymère, notamment l'importance de la topographie de surface sur la réponse des cellules et la colonisation bactérienne.

Ensuite, nous avons démontré que des nano-bâtonnets d'or recouverts d'une couche mince de silice chargée en vert d'indocyanine (Au NRs@SiO<sub>2</sub>-ICG) ont une capacité accrue pour éliminer les micro-organismes pathogènes par irradiation au moyen d'un laser pulsé ayant une longueur d'onde de 810 nm. Nous avons obtenu une réduction de 6 log<sub>10</sub> de la concentration de *Escherichia coli* (*E. coli*) sans effet photo-thermique. Les résultats ont montré que la quantité d'oxygène singulet produite est directement liée à la quantité de vert d'indocyanine incorporé dans la couche de silice et le choix de la longueur d'onde d'irradiation semble augmenter encore l'efficacité de la thérapie photodynamique.

Enfin, nous avons évalué les propriétés antibactériennes de nanoparticules de carbone fonctionnalisées avec l'ampicilline. Les résultats ont démontré que l'ampicilline conjuguée aux nanoparticules de carbone (CDs@Amp) présente une activité antibactérienne élevée comparée à l'ampicilline libre. La concentration minimale inhibitrice (CMI) de CDs@Amp a été considérablement réduite. La combinaison des propriétés de fluorescence des nanoparticules de carbone et les propriétés antibactérienne de l'ampicilline dans un même système permet de synthétiser un système multifonctionnel.

**Mots clés:** Polystyrène micro-structuré, antibiofouling, pathogènes, thérapie photodynamique, activité antibactérienne accrue

## ACKNOWLEDGMENTS

Preparing my PhD thesis has been a wonderful and often overwhelming experience. During my PhD, I have the opportunity to explore new research directions, to gain experience, knowledge and to meet remarkable people. I learned a lot from them about life, research, how to tackle and solve the problems.

First of all, I would like to express my deepest thanks to my supervisors, Prof. Dr. Nicoleta Dumitrascu and Dr. Rabah Boukherroub, for their support, guidance, kindness and discussions over these three years.

I would like to express my thanks to Dr. Sabine Szunerits, Dr. Alexandre Barras, and Dr. Julie Bouckaert for their patience, consistent support, and guiding me to explore new areas that I was not familiar with.

I would like to extend my thanks to supervisory committee members Prof. Dr. Dumitru Luca, Conf. Dr. Gabriela Borcia and lect. Dr. Ionut Topala for their suggestions, critics and honest evaluations of my research studies.

I would like to thank my thesis committee members Prof. Dr. Gheorghe Dinescu, Dr. Jean-Olivier Durand and Dr. Mariana Pinteala for accepting to review my PhD thesis.

I would like to thank all the IPARC and NanoBioInterfaces group (IEMN) members: Dr. Vasile Tiron, Dr. Valentin Pohoata, Dr. Marius Dobromir, Dr. Cătălin Agheorghiesei, Dr. Alina Silvia Chiper, Dr. Claudiu Costin, Dr. Ilarion Mihaila, Toma Mihai, Dr. Teodora Teslaru, Alexandra Demeter, Florentina Samoila, Alexandra Besleaga, Tetiana Shkandina, Yannick Coffinier, Kostiantyn Turcheniuk, Amer Al Nafiey, Ioana Hosu, Florina Teodorescu, Corina Marinescu, Diana Zb, Ning Cao, Pawan Kumar, Santosh Singh, Yuanyuan Cheng, Patrik Aspermair, Yavuz Oz, Abderrahmen Hamdi, Sonia Amdouni, Chekin Fereshteh, Mehdi Hammadi, Houcem Elmaaoui, Qian Wang, Li Chengnan, Fei Wang, Hakim Belkhalifa, Faouzia Khili, Vladimir Turcheniuk, Monaam Benali for providing a stimulating research environment and for their friendship, support and accompany during the thesis.

I am grateful for the financial support provided by the French Institute of Romania and France Government represented by Campus France, but also to give me the opportunity to pursue my doctoral studies in a joint PhD program.

I am thankful to:

❖ Project *Synthesis of transient complex molecular systems in laboratory plasmas as with relevance for molecular astrophysics of hot cores* (2013-2016), Funding agency: Romanian Space Agency, under the programme Space Technology and Advanced Research, grant no. 96/11.12.2013, director dr. Ionut Topala.

❖ Project *Development, diagnostic and modelling of cold plasma jets at atmospheric pressure for direct treatment of living tissues* (2011-2013), Funding agency: UEFISCDI, Romania-Cyprus Bilateral cooperation, director dr. Ionut Topala.

❖ Dr. Marius Dobromir, IPARC, Faculty of Physics, Alexandru Ioan Cuza University of Iasi, Blvd. Carol I, No. 11, Iasi, 700506, Romania for helping with XPS measurements.

❖ Dr. V. Antoci and dr. C. I. Ciobanu – Research Department, Faculty of Chemistry, Alexandru Ioan Cuza University of Iasi, Blvd. Carol I, No. 11, Iasi, 700506, Romania for helping with  $^1\text{H-NMR}$  measurements.

❖ Dr. Corentin Spriet – responsable Plateforme d' Imagerie Cellulaire - Sciences et Technologies *biophotonique et microscopie électronique* - (Leica AF6000 LX system ;

❖ Dr. Yannick Coffinier, IEMN, Université Lille 1, Avenue Poincaré, BP 60069, 59652 Villeneuve d'Ascq, France for helping *with SEM analysis*;

❖ Dr. Nicolas Barrois, Centre for infection and immunity of Lille for helping with *SEM analysis*.

❖ Dr. Tetiana Shkandina and Dr. Olivier Vidal, Unité de Glycobiologie Structurale et Fonctionnelle, Université Lille 1, Cité Scientifique, 59000 Lille, France.

Finally, I owe my deepest gratitude to my parents Olga and Ioan Jijie for their unconditional love and invaluable support all over these years.

Thank you for your support and encouragement,

Roxana JIJIE

September 2016




# CONTENTS

## ABSTRACT/ RESUMÉ

### PART I: Antibiofouling properties of plasma polymerized styrene film

Introduction	2
<b>CHAPTER 1. Non-thermal plasma technology for synthesis of antibiofouling surfaces</b>	
1.1 Fundamental and applied aspects of plasma polymerization	3
1.1.1 Basic concepts of plasma	3
1.1.2 Atmospheric pressure plasma – status and challenges for film deposition	3
1.2 Living organism–material interaction	8
1.2.1 Biofouling	8
A. Eukaryotic cell-surface interactions	8
B. Bacteria-surface interactions	9
1.2.2 Antibiofouling surfaces synthesized by plasma techniques	10
A. Surfaces processed by plasma for controlling cell attachment	10
B. Grafting and deposition of antibacterial films assisted by plasma	12
 <b>CHAPTER 2. Styrene atmospheric pressure plasma polymerization</b>	
2.1 Plasma polymerized styrene films – state of the art	15
2.2 Experimental details	18
2.2.1 Atmospheric pressure plasma reactor	18
2.2.2 Plasma and films characterization techniques	19
2.3 Plasma diagnostics	20
2.3.1 Electrical measurements	20
2.3.2 Optical Emission Spectroscopy	21
2.4 Physico-chemical properties of plasma polymerized styrene films	21
 <b>CONCLUSIONS</b>	24
 <b>CHAPTER 3. Behavior of plasma polymerized styrene films in biological media</b>	
3.1 Introduction	25
3.2 Experimental details	26
3.3 Stability of plasma polymerized styrene films in air	27
3.4 Stability of plasma polymerized styrene films in aqueous media	28
 <b>CONCLUSIONS</b>	34
<b>CHAPTER 4. Response of eukaryotic and prokaryotic cells to plasma polymerized styrene surface properties</b>	
4.1 Introduction	35
4.2 Experimental details	36



4.2.1 Chemicals	36
4.2.2 Film cytotoxicity	36
4.2.3 Film antibacterial properties	37
4.3 Antibiofouling properties of plasma polymerized styrene film	38
4.3.1 Influence of surface properties on cell adhesion and viability	38
4.3.2 Antibacterial activity of plasma polymerized styrene films	41
<b>CONCLUSIONS</b>	42
Appendix	43
 Bibliography	45
 <b>PART II: Nanoparticles-based platforms for light-triggered anticancer or antibacterial activity and for drug delivery</b>	
Introduction	53
<b>CHAPTER 1. Antimicrobial photodynamic and/or photothermal therapy</b>	
1.1 Fundamental and applied aspects of photodynamic therapy	55
1.2 Particle-based Photodynamic and/or Photothermal treatment of bacterial suspensions	59
 Bibliography	61
 <b>CHAPTER 2. Photodynamic inactivation of <i>Escherichia coli</i> using plasmonic nanostructures loaded with indocyanine green</b>	
2.1 Gold nano-particles: properties and applications	64
2.2 Experimental details	65
2.2.1 Chemicals	65
2.2.2 Synthesis of gold nanorods (Au NRs)	66
2.2.3 Synthesis of Au NRs@SiO <sub>2</sub> particles	66
2.2.4 Loading of Au NRs@SiO <sub>2</sub> particles with indocyanine green (Au NRs@SiO <sub>2</sub> -ICG)	66
2.2.5 Characterization techniques of Au NRs@SiO <sub>2</sub> and Au NRs@SiO <sub>2</sub> -ICG particles	66
2.2.6 Singlet oxygen ( <sup>1</sup> O <sub>2</sub> ) detection	67
2.2.7 The <i>in vitro</i> cytotoxicity study	67
2.2.8 Photodynamic ablation of bacteria solutions	67
2.2.9 Measurements of the photothermal effect	68
2.3 Results and discussion	
2.3.1 Chemical and structural characterization of Au nanorods coated by an indocyanine green-embedded silica shell	68
2.3.2 Antimicrobial photodynamic therapy	74
<b>CONCLUSIONS</b>	75
 Bibliography	76

## CHAPTER 3. Therapeutic and bio-imaging platforms based on carbon dots

3.1 Carbon dots: synthesis, properties and applications	79
3.1.1 Introduction	79
3.1.2 Nitrogen-doped carbon dots	80
3.1.3 Biological applications of carbon dots	81
3.2 Experimental details	87
3.2.1 Chemicals	87
3.2.2 Synthesis of carbon dots (CDs)	87
3.2.3 Synthesis of ampicillin conjugated carbon dots (CDs@Amp)	87
3.2.4 Characterization techniques of CDs and CDs@Amp conjugate	87
3.2.5 The <i>in vitro</i> cytotoxicity study and cellular uptake	88
3.2.6 Evaluation of the photodynamic properties	89
3.2.7 Antibacterial activity of Amp@CDs conjugate	90
3.3 Results and discussion	
3.3.1 Chemical and structural characterization of fluorescent carbon dots	91
3.3.2 Carbon dots for visible light-triggered photodynamic therapy	95
3.3.3 Enhanced antibacterial activity of ampicillin conjugated fluorescent carbon dots	98

## CONCLUSIONS 105

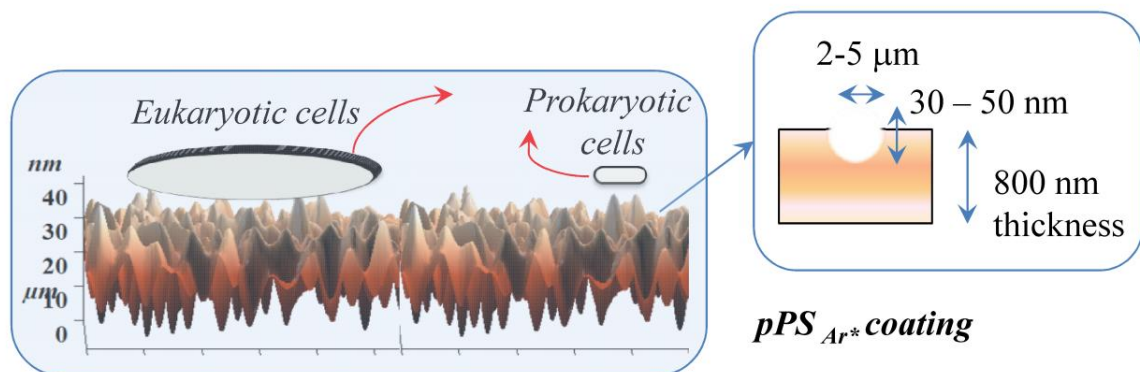
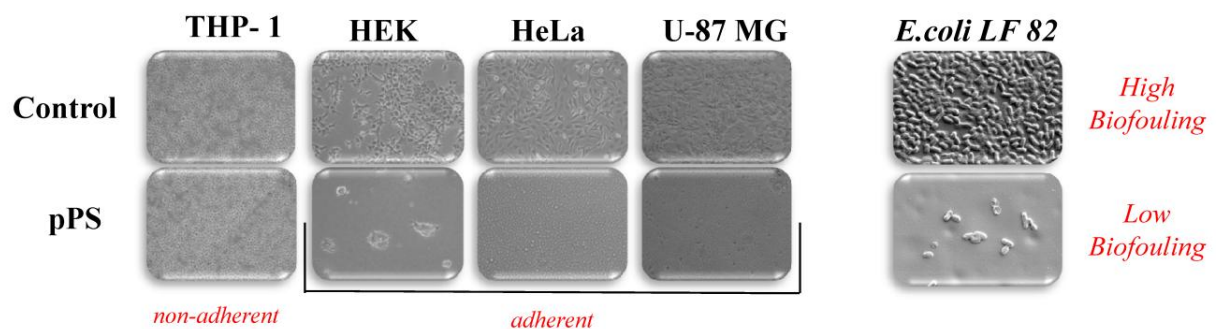
## Bibliography 106

## List of abbreviations and acronyms 111

## Scientific activity 113

## PART I

### *Antibiofouling properties of plasma polymerized styrene film*



## INTRODUCTION

*Biofouling* is a serious problem in domains such as bio-medicine (e.g. biosensors, biomedical devices), food processing, marine industry or for water filtration and purification systems. For this reason, there is a growing interest for the design and processing of new *antibacterial surfaces* or to improve the performance of existing surfaces.

The antibacterial surfaces can be classified in *antibiofouling* and *bactericidal* surfaces, according to their action mode. The *antibiofouling surfaces* prevent the attachment and accumulation of unwanted biomolecules and living organisms, while *biocidal surfaces* are those that kill cells. [1-3]

Plasma polymerization, surface treatment and material etching have become particularly attractive for the design of antibacterial coatings because they have the advantage to modify the surface chemistry without affecting the material bulk properties. Moreover, the material surface properties, like chemical composition, roughness or wettability can be tailored by tuning the plasma parameters, the gas composition or the reactor geometry. Plasma etching can be employed to obtain various kinds of nano- and micro-structured surfaces [4], while plasma polymerization allows to deposit films with different domains, from cell-repulsive to cell-adhesive area [5] hydrophilic alternating with hydrophobic regions [6] or antibacterial coatings [2, 7]. Particularly, plasma modified surfaces were used to attach or to incorporate biocidal or bacteriostatic molecules, including natural compounds [8-11] or silver ions and others nanoparticles [12-14].

Plasma polymerization is a versatile technique used to synthesize organic, inorganic and hybrid coatings on complex shaped substrates, under dry conditions. Plasma polymers present a more random structure and a higher degree of cross-linking and branching, in contrast with their counterparts polymerized by conventional methods. Currently, there is a growing interest in the synthesis of hybrid films using the *non-thermal atmospheric pressure plasma* because it does not require expensive and time consuming vacuum systems.

In this thesis, we performed a detailed characterization of plasma polymerized styrene (pPS) films used as substrate to study the behavior of eukaryotic and prokaryotic (bacteria) cells. The films were synthesized in a dielectric barrier discharge reactor, working in argon/styrene and helium/styrene gas mixture at atmospheric pressure. A special attention was devoted to pPS films stability in air and in aqueous environments. A comparative characterization of plasma gas phase and of coatings was carried out in order to establish a correlation between plasma gas phase and films properties. The deposition parameters were optimized according to the film stability in aqueous media. The low biofouling behavior of plasma polymerized styrene films have been tested towards three adherent cells line, including HeLa, U-87 MG and HEK-293 cells. In addition, the capacity of the coatings to prevent the bacteria adhesion and biofilm formation was determined using *Escherichia coli* strain LF82.

Our results prove the complexity of the process occurring at the interface cell/material and particularly the role of topography which mediates cell response.

It has to be highlighted that few studies have investigated the stability of plasma polymerized films in aqueous media and have followed bacteria attachment and biofilm formation onto their surface.

# CHAPTER 1. NON-THERMAL PLASMA TECHNOLOGY FOR SYNTHESIS OF ANTIBIOFOULING SURFACES

---

## 1.1 FUNDAMENTAL AND APPLIED ASPECTS OF PLASMA POLYMERIZATION

### 1.1.1 Basic concepts of plasma

*Plasma*, a macroscopically electrically quasi-neutral medium, is known as the 4<sup>th</sup> state of matter together with solids, liquids and gases. In 1928, Irving Langmuir (1881-1957) introduced the term “plasma”, a Greek word, to describe the behavior of ionized species. The term was borrowed from the bio-medical field, in correlation with the complex composition of blood plasma. *Plasma in biology* describes an assemblage of different molecules, like small molecules, proteins and nucleic acids, either inside a nucleus (the karyoplasma), a cell (the cytoplasm) or in the blood stream (the blood plasma). *In physics*, *plasma* is a mixture of positive and negative ions, electrons, photons, neutral and excited species (e.g. atoms and molecules), whose properties (density, energy etc.) can be set by tuning the gas composition, the plasma reactor geometry and the processing parameters, such as the gas pressure and flow rate, the input power or reactor geometry.

Plasma is found in various forms in nature and also can be generated artificially. There are two main categories of plasma, equilibrium and non-equilibrium plasmas. The equilibrium or ‘thermal’ discharges occur when the electron and gas temperatures in the plasma are approximately equal. Non-equilibrium or ‘cold’ plasmas occur when the electron temperature is much higher than that of other particles, allowing electron initiated physical and chemical reactions. Depending on required applications, there are different methods of generating plasmas in the laboratory. Depending on the method, plasma have a high or low density, high or low temperature, it is steady or transient, stable or unstable, and so on. For example, the plasma can be classified according to the pressure at which it is initiated (low pressure, medium or atmospheric pressure) or according to the energy source used to energize the gas (e.g. DC, RF and MW discharges). [15-19]

### 1.1.2 Atmospheric pressure plasma-status and challenges for film deposition

In the early 1990s, the non-thermal atmospheric pressure glow plasma technology was developed [20]. Atmospheric pressure plasma (APP) is an effective source of radicals, metastable species, ions and photons, used in different areas of applications, such as *biomedicine* (inactivation of micro-organisms [21, 22], blood coagulation, acceleration of wound healing [23], tooth bleaching, action against cancer cells). Moreover, the APPJ systems are used also in textile industry (anti-igniters and antistatic treatment, improved dyeing qualities, water-repellent properties) [24], optics (antireflecting, contact lenses), chemical technology (ozone production) [25], decomposition of volatile organic compounds [26], astrochemistry (for simulation of astrochemical environments) [27-29] and in a variety of materials processes, including deposition, surface modification and material etching (**Figure 1**) [19].

In the last years, the APPs have received increasing attention to synthesize thin coatings, because they do not require expensive and time consuming vacuum systems. On the other hand, low pressure plasmas have a low deposition rate and the surface size that can be treated is limited by the dimension of the vacuum chamber. Low pressure plasmas have the advantage of requiring only low amounts of process gas. Moreover, the films synthesized at low pressure are crystalline and denser compared with the organic coatings obtained at atmospheric pressure [30].

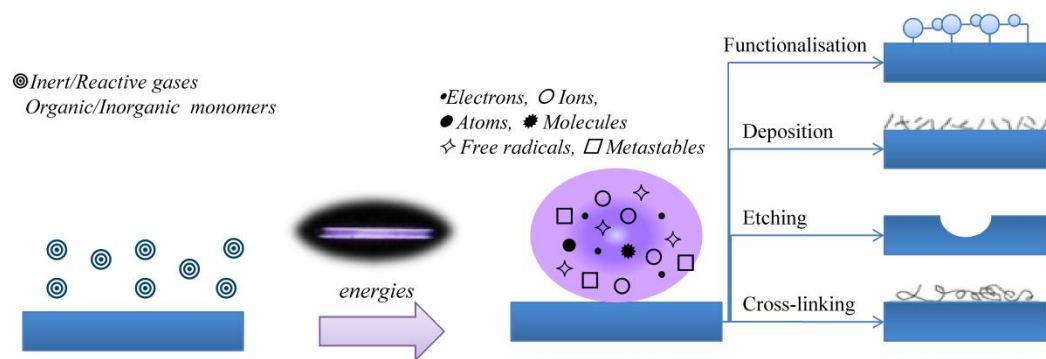


**Figure 1.** Surface modification induced by plasma techniques [31].

**Plasma polymerization** can be defined as “*formation of polymeric materials under the influence of plasma*” (Yasuda, 1985).

Plasma polymerization is a versatile technique that exhibits many advantages, such as:

- + it is a one step process,
- + allows the synthesis of thin films using various monomers, also precursors that cannot be polymerized using conventional wet chemistry, with controllable thickness,
- + can be performed on various shaped substrates (like textiles, metal, polymers, glass),
- + it is environmentally friendly process, with low consumption of chemicals and absence of solvents,
- + the substrate can be selectively modified without altering the bulk properties and it is maintaining close to ambient temperature, so that thermally sensitive substrates are not damaged.

Therefore, *the conventional thermo-chemical polymerization techniques* in contrast with plasma polymerization technique are multi-steps, time consuming and environmentally unfriendly due to a high consumption of reactants and solvents. [18, 31-34]

*Plasma polymer* is an individual class of polymers that is created as a result of a passage of monomers gas or vapors through the glow discharge. Plasma polymers are highly branched and cross-linked, different from their counterparts polymerized by conventional methods and can be deposited as uniform films with thicknesses ranging from 10 nm to several microns.

#### → Structure of plasma polymers

Although a considerable number of investigations have been carried out on growth kinetics and properties of plasma films, the mechanism of their formation is still not fully understood. Due to the multitude of chemical reactive species, generated during polymerization, it is difficult to control and anticipate the final compounds chemical structure. Additional new units are likely created and intercalated in the organic coating structure.

The parameters that control the material properties can be grouped into two classes, *one associated with the substrate* (temperature, presence of catalyst, material chemical composition) and the other one *associated with the plasma* parameters [35].

Various studies are dedicated to preserve the structure and the functional groups of the monomers during deposition and also to synthesize stable films with a high retention of functional groups using a plasma reactor operating at medium [36] or atmospheric pressure. For example, carboxyl (-COOH) and amine (-NH<sub>2</sub>) rich films are of high interest for the biomedical applications, including drug delivery and tissue engineering thanks to their high reactivity allowing the formation of covalent linkages between biomolecules and surface [37].



*Copolymerization reactions* provide an alternative way to control the films solubility, polarity or hydrophilic/hydrophobic balance by introducing simultaneously two compatible gaseous vapors from a monomer solution. Atmospheric plasmas can be used easily to deposit hybrid coatings by introducing organic-inorganic monomers or organic-organic monomers. [38, 39]

*Mechanism of atmospheric plasma polymerization.* Plasma polymerization can take place in vapor phase and/or at the surface, the monomer being fragmented in reactive species that recombine and are deposited onto the substrate surface. In cold APPs the high density of reactive species results from dissociation and recombination processes, as well as photons emitted from de-exciting atoms.

Methods to synthesize polymers are generally classified in two categories *step-growth polymerization and chain growth polymerization*. In contrast with the conventional thermo-chemical polymerization techniques, plasma polymerization is an atomic process, is not necessary specific chemical structures. For example, nearly all organic and organometallic compounds polymerize in plasma. Glow discharge polymerization of organic compound seems to proceed by the free radical mechanism.

The mechanism of polymerization consists of three major steps: *initiation* – formation of free radicals or atoms of monomers under the influence of plasma, *polymerization propagation step* – addition of radical atoms to other radicals or molecules leaving a growing radical chain and *termination* – similar to propagation, but ends in the final product or a closed polymer chain [40]. Yasuda *et al.* introduced a composite parameter, W/FM (energy per mass of monomer: W is the discharge power, F is the monomer flow rate and M is the molecular weight of monomer) and identified the domain of plasma polymerization (such as energy-deficient region, competitive region and energy-sufficient region). The discharge power per unit of molecule is considered to be proportional to the concentration of activated species in plasma.

*Plasma chemistry.* Chemical reactions that occur under plasma conditions are very complex and non-specific. In general, plasma-chemical processes in a reactor can be classified into two basic categories, *homogeneous and heterogeneous gas-phase reactions*.

*The gas phase homogeneous reactions* result from inelastic collisions between electrons and heavy species and between heavy species themselves. Some examples of the homogeneous reactions are given below:

- ❖ excitation -  $e^- + A \longrightarrow e^- + A^*$
- ❖ dissociative attachment -  $e^- + AB \longrightarrow A + B^-$
- ❖ dissociative ionization -  $e^- + AB \longrightarrow A^+ + B^- + e^-$
- ❖ dissociation -  $e^- + AB \longrightarrow A + B + e^-$
- ❖ ionization -  $e^- + A_2 \longrightarrow A_2^+ + 2e^-$
- ❖ recombination -  $e^- + A^+ \longrightarrow A + h\nu$
- ❖ charge transfer -  $A + B^+ \longrightarrow A^+ + B$
- ❖ associative detachment -  $A^- + BC \longrightarrow ABC + e^-$
- ❖ penning ionization -  $A + B^* \longrightarrow A^+ + B + e^-$
- ❖ attachment of atoms -  $A + BC + M \longrightarrow ABC + M$

*The gas phase heterogeneous reactions* occur at surface in contact with the plasma or plasma species which may be atoms (A or B), monomer (M), radicals (R) or polymer formed in the plasma phase. Typical heterogeneous reactions are adsorption, recombination, sputtering and polymerization. [41, 42]

**Deposition plasma process parameters.** The plasma polymers properties like thickness, chemical composition, morphology and stability can be tailored by controlling *plasma deposition parameters* (e.g. pulsed or CW plasma conditions, duty cycle in pulsed plasma, plasma power, monomer flow rate, working gas pressure and substrate position in the plasma reactor) and *the reactor geometry* as well. [32, 43-45] Retzko *et al.* [46] reported that cyclic, alicyclic and aromatic monomers yield higher deposition rates than aliphatic monomers.

Depending on the location of the substrate on which plasma polymerized films is deposited, there are two main categories of deposition '*in discharge*' and '*post-discharge*' *atmospheric pressure plasma deposition*. One of the major drawbacks of APP is the dependence of the applied voltage with the pressure and the distance between electrodes. This is expressed by the Paschen law:

$$V_{breakdown} = \frac{B \times p \times d}{C + \ln(p \times d)}$$

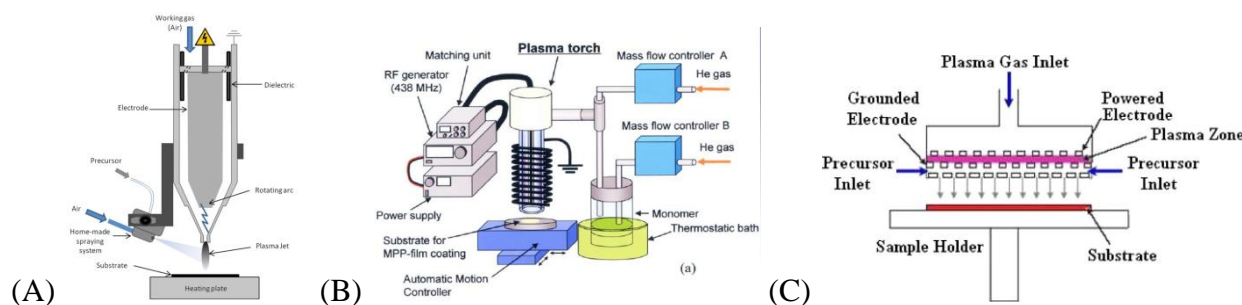
with d – is the inter-electrode spacing, o – the pressure, B and C – constants depending on the gas nature and the electrode materials. The breakdown voltage depends on the plasma gas nature and on the inter-electrode spacing (gap). Typically, the distance between electrodes is small, in the range of a few mm, to avoid elevated breakdown voltage. These limitations have contributed to the development of *post-discharge deposition processes* [43].

→ **Dilution gas.** Various studies related to plasma polymerization have been performed by employing argon (Ar) or helium (He) as carrier gas, or an inert/reactive gas mixture.

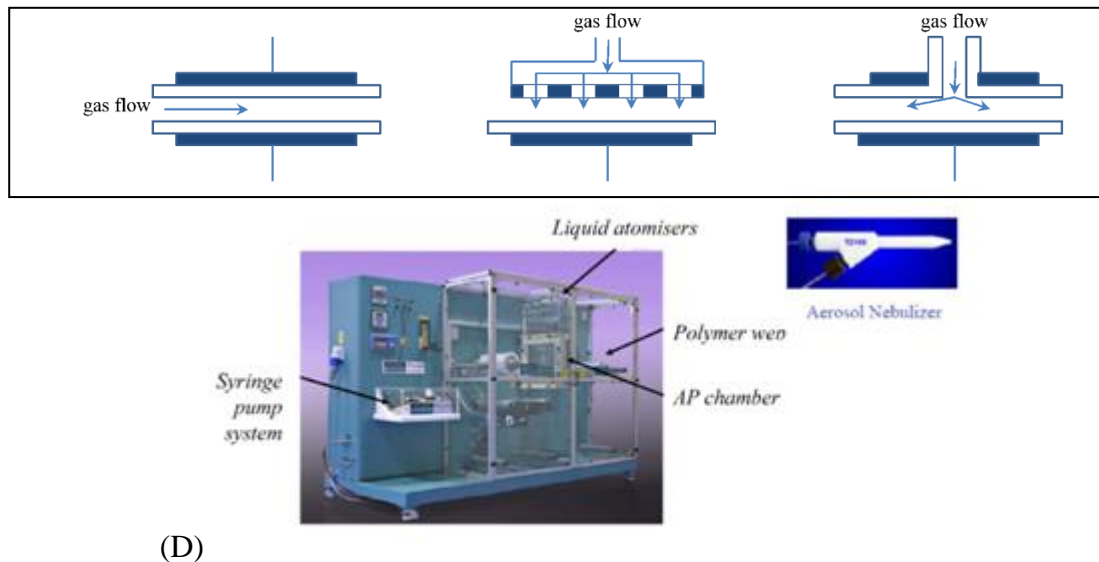
→ **Monomers.** The monomers gas or vapors could be injected into the plasma reactor using a classic bubbler system. In the case of aerosol-assisted plasma deposition, known as atmospheric plasma liquid deposition technique, the liquid monomers are transported in the discharge as a finely dispersed aerosol [30].

→ **Plasma reactors.** A variety of atmospheric pressure plasma reactors are being investigated for thin films deposition, including DBD, plasma torch or plasma jet (**Figure 2**). In addition, plasma polymerization is highly system-dependent, the final products depending on operational conditions and reactor geometry [47].

**Dielectric barrier discharges (DBDs).** DBDs (called *silent discharges*) are typically generated between two electrodes (parallel plates, pin-to-plane, coaxial cylinders, etc.) separated by a gap and at least one of the electrodes is covered with a dielectric material, such as glass, quartz, ceramics or polymer, materials with low dielectric loss and high breakdown strength, to help to stabilize the discharge. Depending on the applied voltage and working gas, the gap varies from 0.1 mm to several centimeters. The charges accumulated on the dielectric layer help to sustain the discharge at lower voltage with amplitude between 10 kV and 100 kV and a frequency of a few Hz to MHz. The current is from a few mA up to several tens of mA. DBDs are operated in different gases, in noble gases such as helium or argon or gas mixtures such as He-air, He-O<sub>2</sub>, He – water mixtures. Two basic configurations of DBDs can be distinguished: the *volume discharges* (VD) and the *surface discharges* (SD). Volume DBDs have been shown to operate in at least two distinct modes: *diffuse* and *filamentary*.







(D)  
**Figure 2.** Different experimental setups used for films deposition, including (A) APPJ [48], (B) microplasma polymerization torch [49, 50], (C) RF APP torch [51] and the different ways to introduce the working gas or (D) LabLine™ atmospheric pressure plasma system (<http://miics.net/>). [52]

**Applications.** The various plasma processed surfaces are employed in many applications, including the production of thin-film capacitors, reverse osmosis membranes, optical waveguides, antireflection coatings, protective coatings, selective permeation membranes and functional layers for biomaterials and medical applications. [5, 53-55] In **Figure 3** are briefly presented the main bio-medical applications of plasma processed surfaces.

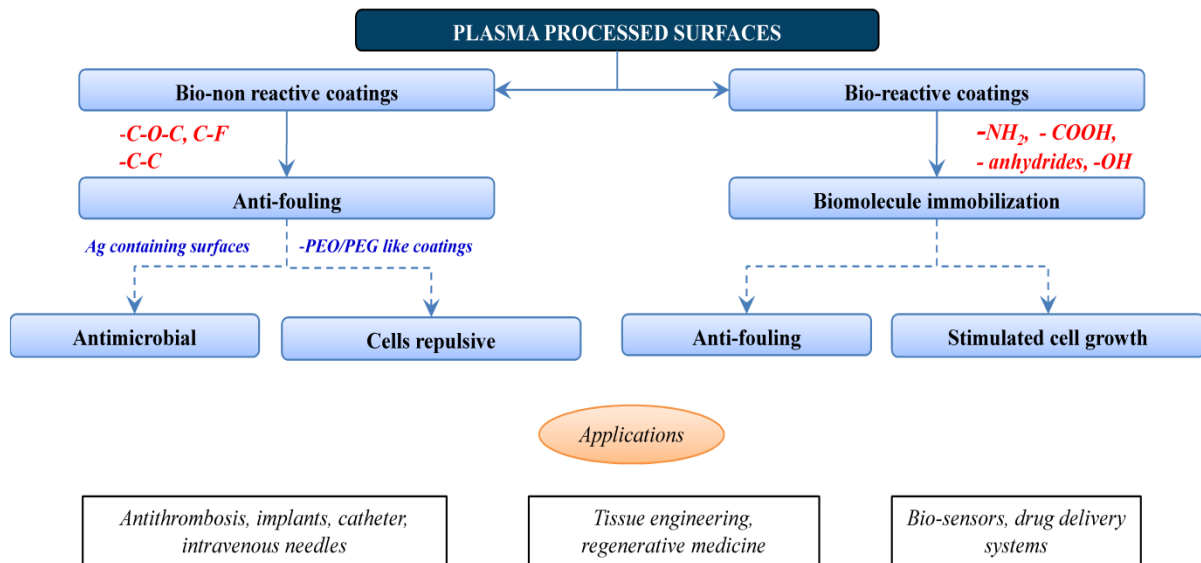


**Figure 3.** Applications of plasma processed surfaces [55].

Various methods could be employed for the analysis of *atmospheric pressure plasma*, including voltage-current probes, optical emission spectroscopy (OES) to get gas temperature from emission profiles and electron density from Stark broadening, laser absorption spectroscopy (LAS), two-photon absorption laser induced fluorescence (TALIF) techniques to determine the density of atoms, and recently molecular beam mass spectrometry to determine the ionic composition from atmospheric pressure plasma.

The polymerized films were investigated by Fourier transform infrared spectroscopy (FT-IR), X-ray photoelectron spectroscopy (XPS), gel permeation chromatography (GPC), proton nuclear magnetic resonance ( $^1\text{H}$  NMR), UV-Vis spectroscopy, water contact angle measurements (WCA), dielectric relaxation spectroscopy (DRS) and thermogravimetry (TG).

## 1.2 LIVING ORGANISM - MATERIAL INTERACTION

### 1.2.1 BIOFOULING

Biofouling defined as the attachment and accumulation of unwanted biomolecules, bacteria, cells, organisms on material surfaces, is a serious problem in bio-medicine, food processing or marine industry.

Cells may be classified in two types, *eukaryotic and prokaryotic (bacteria) cells*, depending on the presence of nuclei inside the cells (**Figure 4**). All cells share 4 common components: a *plasma membrane* (that separates the interior of all cells from the outside environment), *cytoplasm* (comprises the cytosol and the organelles), *DNA* (deoxyribonucleic acid, the cell genetic material) and *ribosomes* (particles that synthesize proteins). If the bacteria range in diameter from 0.1 – 5  $\mu\text{m}$ , the eukaryotic cells tend to be 10 to 100 times the size of prokaryotic cells.

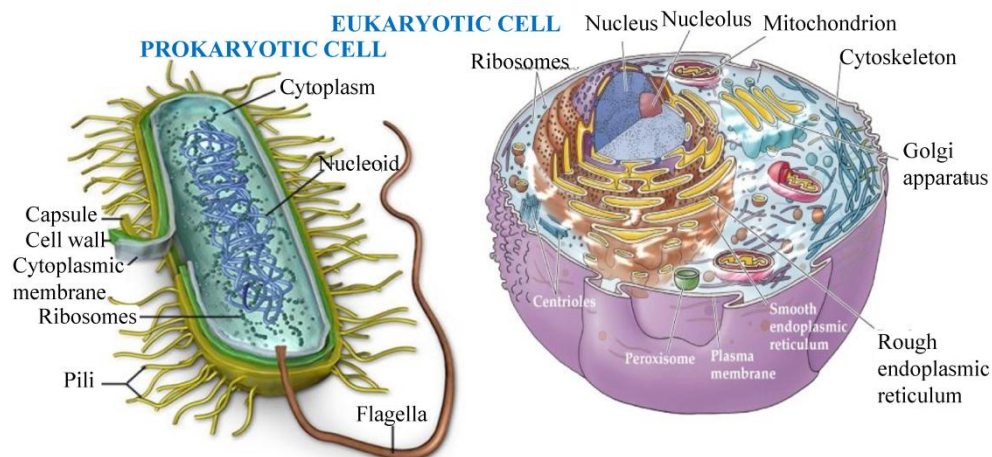


**Figure 4.** Comparison between prokaryotic and eukaryotic cells (2001, Sinauer Associates, Inc.).

#### A. *Eukaryotic cells-surface interactions*

Most cells derived from solid tissues are adherent, requiring a substrate upon which they can attach, grow and divide [56]. The cell adhesion to a surface proceeds in a number of steps, including:

- ✚ the *protein adsorption*, the first event that takes place after the material surface comes into contact with biological fluids,
- ✚ the *attachment* which occurs rapidly and involves short-term events
- ✚ and the *adhesion phase* which occurs over longer periods and involves various biological molecules (extracellular proteins, cellular membrane and cytoskeleton proteins), which interact together to induce the subsequent response in terms of migration and differentiation (**Figure 5**). Fibronectin and vitronectin are two adhesive proteins that may influence cell attachment. However, less information exists about the effects of material surface characteristics on the protein adsorption and cellular activity. Recent studies showed that cells behave differently on smooth and rough surfaces. [52, 57-59]

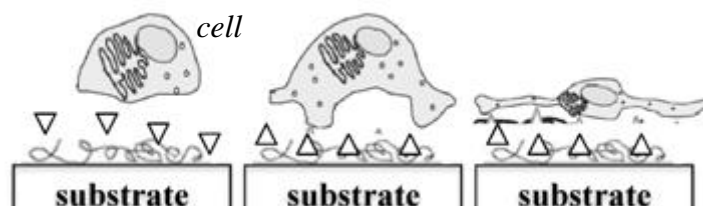


**Figure 5.** Schematic of the processes occurring when a cell attaches to a surface [55].

The surface of materials can be tailored to control cell adhesion, proliferation and differentiation. Moreover, the cell attachment is affected by the presence and the density of surface functional groups (such as hydroxyl (-OH), primary amino (-NH<sub>2</sub>) or carboxylic (-COOH). For example, the methyl group (-CH<sub>3</sub>) is inert in terms of protein and cell adsorption, whereas charged groups such as -COOH and -NH<sub>2</sub> enhance cell and protein attachment. [57, 60, 61]

### B. Bacteria-surface interactions

There are numerous types of bacteria, most of them being useful. For example, bacteria play an important role in the digestive processes; lactobacillus is used in the preparation of fermented foods such as cheese, pickles, soy sauce, wine and yoghurt. The ability of bacteria to degrade a variety of organic compounds is remarkable and for this reason it is used in waste processing. On the other hand, the contamination of food, water or medical equipment by pathogenic bacteria can cause serious health problems. For example, in the medical field, bacterial infection of implants and prosthetic devices constitutes more than half of hospital acquired infections which are expensive and complex to treat.

Bacteria may be found in two distinct states as *planktonic* (free bacteria in suspension) and *sessile* cells (biofilm). *Sessile bacteria* provide resistance to the inhibitory effects of antibacterial agents (e.g. antibiotics, chlorine and heavy metals) and the immune system. In addition, they are a major cause of morbidity and mortality [62-67]. For example, important approaches for killing or inactivating bacteria include the design of photoactive surfaces, materials that release antibacterial agents, or surfaces functionalized with antimicrobial peptides or coatings that contain enzymes [68].

A **biofilm** is defined as "a structured community of bacterial cells enclosed in a self-produced polymeric matrix (containing polysaccharide, protein and DNA) and adherent to an inert or living surface" [69, 70].

The extracellular polymeric substances (EPS) play a significant role in mediating the bacterial colonization of surfaces by facilitating cell adhesion and cohesion with each other [31]. Biofilm formation takes place in a sequence of steps and is very complicated (**Figure 6**). The first step of biofilm formation is bacteria adherence and attachment response. As is illustrated in **Figure 7**, bacterial attachment is dependent on the surface properties, characteristics of the aqueous medium and types of cell. The following stages involve the bacteria aggregation in micro-colonies and subsequent growth and maturation. Final stage is characterized by a return to transient motility where fragments of micro-colony detach; these are carried by the bulk fluid until they lodge in a new location and initiates a new sessile population. [31, 69, 71]

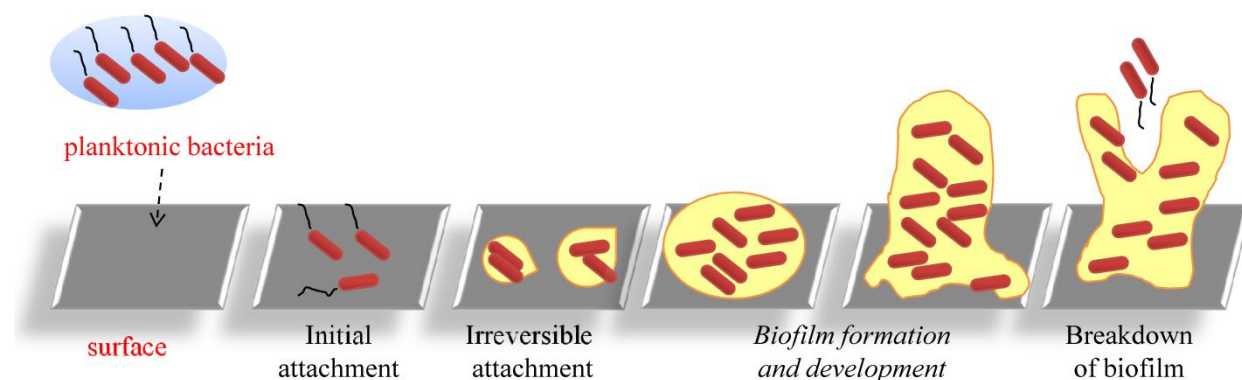


**Figure 6.** Model for biofilm formation and development [70, 72].

Various investigations proved that bacteria attachment occurs most readily on surfaces that are rougher and hydrophobic. For example, microorganisms attach more rapidly to non-polar surface (like Teflon) than to hydrophilic materials (like glass or metals).

Most pathogens are hydrophilic under physiological conditions; therefore, the material antibacterial properties can be improved by decreasing the material water contact angle (WCA). Previously studies showed that the number of gram-positive bacteria are higher on the surfaces containing carboxylic and methyl functional groups than those containing hydroxyl functionality [73].

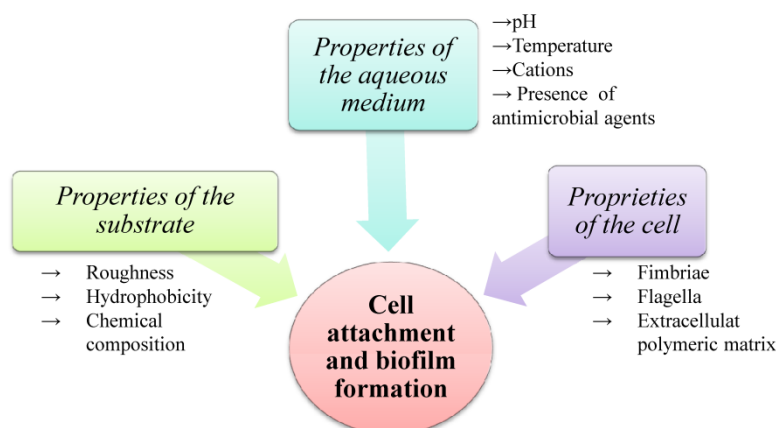


**Figure 7.** Variables involved in cell attachment and biofilm formation [74].

## 1.2.2 ANTIBIOFOULING SURFACES SYNTHESIZED BY PLASMA TECHNIQUES

### A. Surfaces processed by plasma for controlling cell attachment

In recent years, various studies proved that surfaces with various oxygen-containing functionalities, such as hydroxyl, carboxyl and ether groups affect cells adhesion and spreading on surfaces. For example, plasma-deposited acrylic acid films induce attachment and growth of keratinocytes, osteoblasts and fibroblasts, while plasma-deposited PEO-like films prevent protein and cell adhesion [4, 75, 76]. Many papers indicate a close relationship between the percentage of ether carbon content ( $R-O-R'$ ) of PEO-like films and their properties to prevent biomolecules adsorption and cell attachment. Sardella *et al.* [77] reported that by tuning the power delivered to the discharge, it is possible to switch the surface character of PEO-like films from cell-repellent to cell-adhesive (**Figure 8**) depositing films with high antibiofouling performance under *soft plasma conditions*.

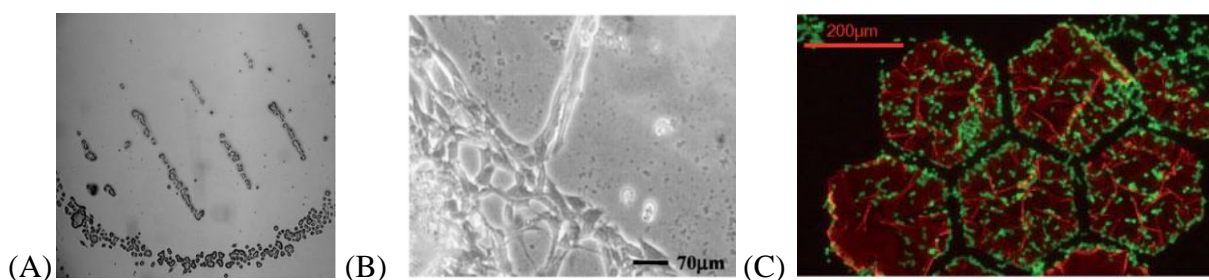


**Figure 8.** (A) NCTC 2544 keratinocytes on polystyrene surface decorated with poly ethylene glycol-like films after 4 days incubation. (B) The adhesion pattern of 3T3 murine fibroblast on a substrate of PEO10W patterned with PEO5W coating deposited through a G50p mask after 24 h of incubation. (C) Behavior of RINm5f cells on microstructures of AAC plasma deposited layers onto a previously  $CHF_3$  treated substrate (as mask was used a TEM grid) after 24 h of incubation. [5, 6, 77]



Studies performed on surfaces with different topography and similar chemistry showed that topography affects the adsorption of proteins, and default the cell adhesion processes. The cell behavior on flat surfaces is significantly different from that on structured surfaces, cells adhering better on rougher surfaces [4]. Moreover, the influence of the shape size, organization and distance between nano-features need to be considered (**Figure 9**) and the topography enhances cell adhesion only if the surface chemistry allows. [52, 78-80]

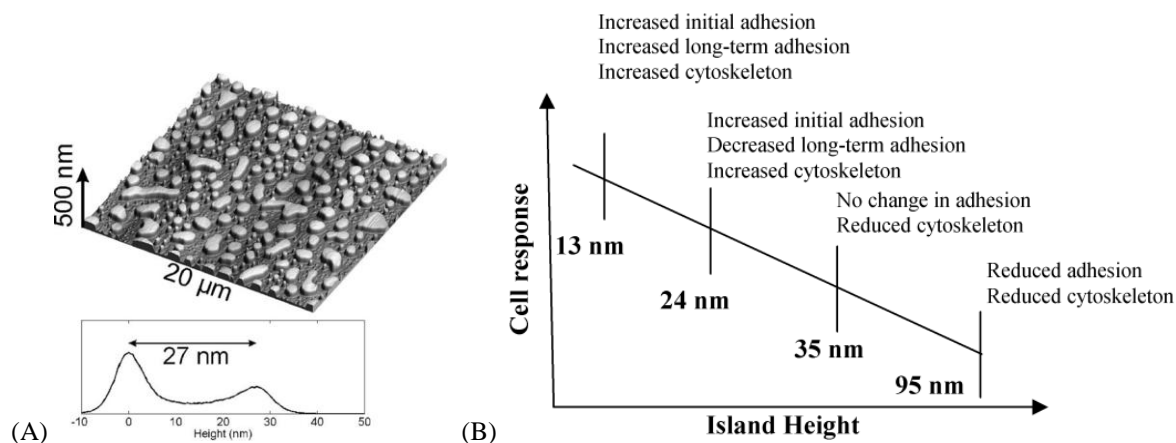


**Figure 9.** (A) Typical AFM image of 27 nm high PS/PBrS island. (B) The relationship between PS/PBrS island size and fibroblast response [81].

Surface wettability, which in part reflects the surface chemistry, has an important role in cell behavior and the better cell adhesion is achieved for *moderately hydrophilic* surfaces, respectively for WCAs in the range of 40 - 65°. Dowling *et al.* [52] observed the optimum adhesion of MG63 osteoblast cells onto plasma deposited siloxane films of a WCA of 64°, with a decrease of cell adhesion on more hydrophilic or hydrophobic coatings. Rebl *et al.* [82] found the ‘biocompatibility window’ of plasma polymerized allylamine (PPAAm) coatings on titanium surfaces between 40° and 55°. In addition, their study proved that the plasma chemical modification of a surface is dominant over its topography (**Figure 10**). The deposition of a PPAAm coating on Ti surface overcomes the limitation of surface topography and the cells spread in all direction (c), in contrast with (a,b,d) where the cells are elongated along the grooves and ridges features [82].

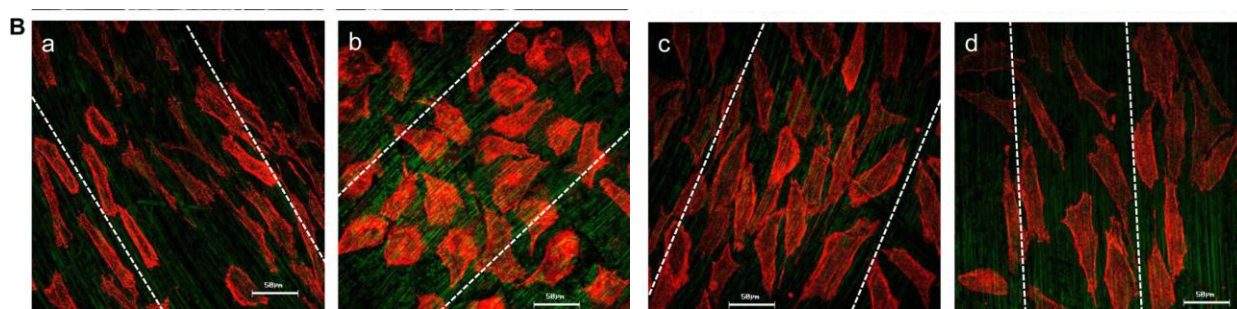


**Figure 10.** Alignment of MG-63 cells after 24 h on (a) untreated Ti-M, (b) Ti-M PPAAm, (c) Ti-M PEG DA-Col and (d) Ti-M GDA DA-Col. Actin is stained red and Ti surfaces is colored in green [82].

The recent studies have proved the importance of individual functional groups on cell adhesion and proliferation. [82] Cheng *et al.* [83] showed that PLLA microfibrillar scaffolds treated with Ar plasma was more effective in increasing the proliferation rate of both bovine aorta endothelial cells (BAECs) and bovine smooth muscle cells (BSMCs), while the Ar-NH<sub>3</sub>/H<sub>2</sub> plasma treatment was more effective in promoting cell spreading. Further, the *in vitro* and *in vivo* cell infiltration studies proved that plasma treatments enhanced cell migration into the

microfibrous scaffolds. The *in vivo* experiments involved the subcutaneous implantation of plasma-treated PLLA scaffolds under the skin of Spragues-Dawley rats.

Design of surfaces that stimulate or inhibit the adhesion of a specific cell type in a controlled way is of particular interest. In the last years, special efforts have been devoted to the synthesis of surfaces with different chemically structured domains. For example, non-fouling and cell adhesive areas have been created by depositing PEO and plasma polymerized polyallylamine coatings (pPAAc) on polystyrene (PS) surfaces. The selective adhesion and growth have been tested against NCTC 2544 keratinocytes and 3T3 murine fibroblasts (**Figure 8**). [5]

The hydrophilic alternating with hydrophobic region proved to be very useful to induce preferential cell adhesion or proliferation. Sciarratta *et al.* [6] investigated the selective adhesion and proliferation of lymphocyte- (KYM-1D4), fibroblast-(HEK293) and epithelia- like (RINm5f) cells on plasma polymerized acrylic acid films (hydrophilic) and CHF<sub>3</sub>-based plasma films (hydrophobic). The response of the three different cell lines to plasma-deposited layers is different; the HEK293, KYM-1D4 and RINm5f cells adhere on pp-AAc films, and the RINm5f cells do not adhere on the CHF<sub>3</sub>-based plasma films. Microstructures of AAC plasma deposited layers onto a previously CHF<sub>3</sub> treated substrate showed selectivity for RIN5f cells (**Figure 8**). Moreover, they demonstrated that Ca<sup>2+</sup> ions and albumin adsorption play a fundamental role in the cell-substrate adhesion.

### B. Grafting and deposition of antibacterial coatings assisted by plasma

There is a growing interest in the development of new strategies to prevent bacteria attachment and biofilm formation. Compared to planktonic bacteria, a biofilm shows increased resistance to antibacterial agents. For example, the minimal inhibitory concentration (MIC) may be up to 100-1000-fold higher [70].

It is known that the nano-structured materials influence the adhesion of microorganisms, inhibiting adhesion and biofilm formation. The naturally occurring anti-biofouling surfaces are rich sources of inspiration, like leaves, shark skin and the feet of geckos [84]. For example, Ivanova *et al.* [85] studied the behavior of *Pseudomonas aeruginosa* ATCC 9027 cells on cicada wing surfaces and they observed that the nanopillars began to penetrate the cells immediately upon cell attachment, killing most of them in 5 min (**Figure 11**).

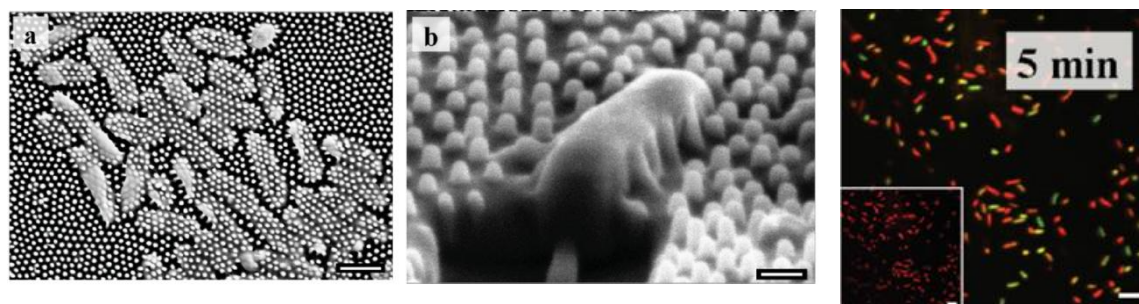


**Figure 11.** Bactericidal effect of cicada wing surface on *Pseudomonas aeruginosa* ATCC 9027 [85].

*Biocidal and non-biocidal surfaces* are used to prevent contamination by biological entities and involve one of the following mechanisms:

- ✚ prevention of the adhesion by grafting of antibacterial compounds and by designing of micro-/nanopatterns;
- ✚ degradation through the elution of antimicrobial agents from the materials.

Therefore, *biocidal films* are the coatings that kill bacteria and prevent them to adhere to the surface. These can be further divided into two subcategories based on their mechanism of action, as can be seen in **Figure 12**. *Contact killing surfaces* rely on direct interaction between immobilized antimicrobial molecules and micro-organism and *releasing of*

*biocides/antibacterial agents over time*, such as antibiotics, silver into the surrounding aqueous environment. One of the main drawbacks of these substrates is that they lose their antimicrobial properties when these substrates are depleted of antimicrobial agents, they cannot be regenerated.

*Non-biocidal* approaches also known as *biopassive approaches*, utilize surfaces that hinder the adhesion of proteins or cells. In the case of marine equipments like platforms, jetties and ship hulls, the *non-toxic antifouling surfaces* are useful to prevent biofouling by sea microorganisms and algae. [68, 86]

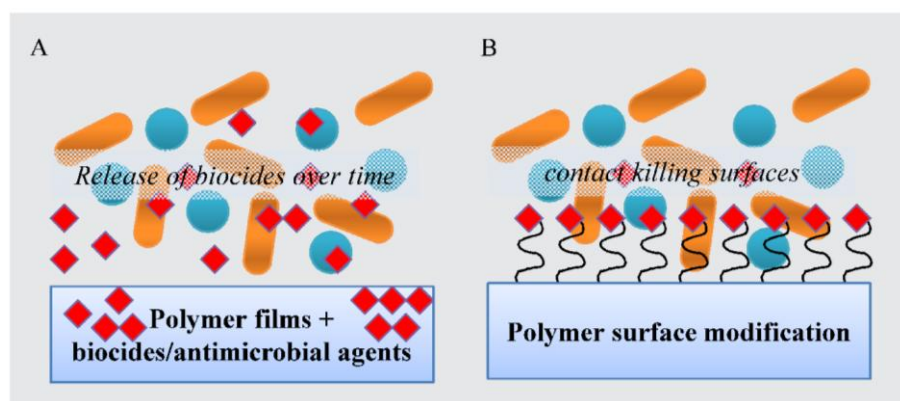


**Figure 12.** Schematic representation of the various strategies used in the design of antibacterial coatings [66].

Two main approaches have been reported to obtain antimicrobial hybrid materials based on a plasma method:

- (i) plasma-assisted surface grafting of antimicrobial agents and
- (ii) plasma deposition of antimicrobial coatings.

In the **Tables 1** and **2** are summarized the main results obtained until now related to the synthesis of antibacterial surfaces using plasma techniques.

In contrast to wet chemistry methods, the *plasma deposition of antimicrobial coatings and grafting* is independent on substrate properties, can be deposited on various substrates, including synthetic polymers, ceramics or wood surfaces. In addition, the surface characteristics such as roughness, microstructure, chemical composition or hydrophilicity can be tailored by using the appropriate plasma processing parameters. [86, 87]

According to Vasilev *et al.* [67] and Kenawy *et al.* [88], an antimicrobial polymer should possess the following characteristics:

- easy to synthesize and inexpensive,
- stable in long-term usage,
- non-toxic, biocompatible and easy to handle,
- can be regenerated upon loss of activity,
- active against a broad spectrum of pathogenic microorganisms upon brief contact.

For bio-medical applications, the toxicity of antibacterial coatings to mammalian cells is an important criterion.

**Table 1.** Plasma-assisted surface grafting of antimicrobial agents.

Nr. Crt.	Samples	Plasma pre-treatment	Cytotoxicity	Antibacterial activity	Ref
1	grafting of chitosan onto polyester fabrics	Ar/O <sub>2</sub> APP-DBD, 100-150 W, 3 kHz, 1-2 min	fibroblast cell line, L929 cells	<i>Bacillus subtilis</i> and <i>S. aureus</i>	[8]
2	grafting of chitosan onto poly(ethylene)	air DBD, 15 kV, 350 Hz, 10 - 20 s	-	<i>E. coli</i> and <i>S. aureus</i>	[10]

3	grafting of chitosan onto poly(ethylene terephthalate)	air APP-DBD, 12.5 kV, 325 Hz, 10 s	-	<i>E. coli</i> and <i>S. aureus</i>	[9]
4	grafting of nisin onto low density poly(ethylene)	RF, Ar/O <sub>2</sub> and N <sub>2</sub> plasmas, 30 mTorr	-	<i>L. innocua</i>	[11]
5	silver nanoparticles bounded on polyallylamine film	RF, 10 W, 10 min	primary human dermal fibroblasts HDF	<i>S. aureus</i> <i>S. epidermidis</i> <i>P. aeruginosa</i>	[12]
6	nisin peptides immobilized onto steel surfaces via a plasma polymerized amino-silica interlayer	N <sub>2</sub> DBD, APTMS precursor, 8 kV, 10 kHz sinusoidal signal	-	<i>Bacillus subtilis</i> 168	[13]
7	silver loaded cotton/polyester fabrics	air DBD	-	<i>S. aureus</i> <i>E. coli</i> <i>C. albicans</i>	[14]

**Table 2.** Plasma deposition of antibacterial coatings.

Nr. Crt.	Samples	Plasma deposition	Cytotoxicity	Antibacterial activity	Ref
1	plasma polymerized oxazoline films	RF, 10 -50 W, ~ 10 <sup>-1</sup> mbar, 1 – 5 min	primary human dermal fibroblasts (HDF)	<i>S. epidermidis</i>	[2, 89]
2	plasma polymerized carvone film	RF, 10 W, 0.25 mbar, 10 min	primary human endothelial cell (HUVEC)	<i>E. coli</i> and <i>S. aureus</i>	[90]
3	Plasma polymerized trichloroethane film	RF, 25 W, 0.26 mbar, 2 min	KG1a cells	<i>S. epidermidis</i>	[91]
<b>hybrid materials</b>					
4	wound dressing materials covered with silicon dioxide embedded silver nanoparticles	APPJ, 250 W, 10 mm nozzle-substrate distance, 3.5 mL/min HMDSO	human adult keratinocytes (HaCaT, 432)	<i>S. aureus</i> and <i>K. pneumoniae</i>	[92]
5	organosilicon films with silver nanoparticles	APPJ, N <sub>2</sub> with admixing of O <sub>2</sub> , TMDSO and AgNPs, 22.5 W	-	<i>E. coli</i> and <i>S. aureus</i>	[93, 94]
6	plasma poly(n-heptylamine) films loaded with silver nanoparticles	RF, 40 W, 0.2 Torr	osteoblastic cells	<i>S. epidermidis</i>	[54]
7	silver nanoparticles entrapped between two maleic anhydride plasma layers	DBD, 20 W, 816 Hz, 0.2 mbar, 10-30 min, 2-50% duty cycle,	-	<i>PHL628-based E. coli</i> SCC1 strain	[95]



## CHAPTER 2. STYRENE ATMOSPHERIC PRESSURE PLASMA POLYMERIZATION

We have focused on the polymerization and characterization of plasma polymerized styrene (pPS) films using an atmospheric pressure plasma dielectric barrier discharge reactor, working in helium or argon gas and styrene vapors. A comparative characterization of plasma gas phase and of coatings was performed. The plasma gas phase was investigated by means of electrical measurements and optical emission spectroscopy and the pPS coatings physico-chemical properties were examined by Fourier transform infrared spectroscopy (FTIR), X-ray photoelectron spectroscopy (XPS), Scanning electron microscopy (SEM), Atomic force microscopy (AFM) and water contact angle (WCA) measurements.

### 1.1 PLASMA POLYMERIZED STYRENE FILMS – state of the art

#### *Polystyrene (PS)*

PS is an aromatic polymer synthesized from styrene *via* free-radical polymerization. It was first prepared in 1839. PS is a non-toxic and transparent material in the visible range used in different fields, such as a material for making optical glasses or various consumer products, including food packaging, household goods and laboratory ware. [96] Due to its non-immunogenic properties and low cytotoxicity it is used in various bio-medical applications. For example, PS dishes have been used for cell culture since about 1965. It is known that the PS surfaces, as prepared are unsuitable for cell attachment and pre-treatments are required. (Sigma Aldrich) Both dry processes (plasma discharge, electrons and UV irradiation) and wet chemical methods (exposure to concentrated sulfuric acid or chloric acid) have been used successfully to modify the polymer surface. [56, 97] The PS surface, in general, is treated using a corona discharge under atmospheric conditions or low pressure plasma. These treatments generate oxygen radicals which oxidize the polystyrene network, therefore once a biological medium is added the surface becomes hydrophilic and negatively charged.

#### *Plasma polymerized styrene films*

Styrene preferentially polymerizes *via* radicals, which are stabilized by the aromatic system (Figure 13). This feature provides the possibility for a radical grafting mechanism. Fragmentation and random recombination, known as ‘polyrecombination’ or ‘atomic polymerization’ of the styrene monomer during the plasma pulse is less important. [46, 98] The reaction mechanism of aromatic compounds proposed by Asandulesa *et al.* [99] is based on *plasma induced radical chain-growth concept* and includes activation/fragmentation of chemical compounds, radical oxidation reactions and recombination of reaction products into random structures. The energy needed to dissociate the chemical bonds in the molecules is generally between 3-8 eV [45].

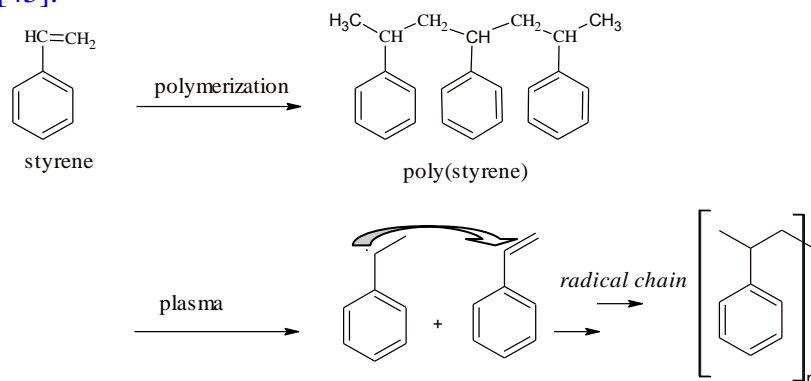


Figure 13. Free radical vinyl polymerization of styrene. (ChemSketch) [46].

As can be observed in the **Table 3**, there are a considerable number of studies done on plasma polymerization of styrene at low pressure with a variety of carrier gases, reactor design and plasma sources. The advantage of our plasma system is that it operates at atmospheric pressure, therefore it does not require expensive and time consuming vacuum systems.

**Table 3.** Literature review – plasma polymerized styrene films.

Nr. crt	Aim	Pasma parameters	Results	Ref.
<b>homopolymer</b>				
1	The objective of this study was to identify the potential intermediary reactions during plasma polymerization process.	DBD, low pressure, 50 kHz, 30 W, styrene, He, 15 – 45 min	The results indicate the presence of oxygen containing groups in the films chemical composition and during plasma polymerization the benzene ring is fragmented.	Asandulesa (2014) [40]
2	They investigated plasma polymerization reactions of aromatic compounds using a cold atmospheric pressure glow discharge working in helium.	DBD, atm pressure, He, 6 kV, 250 $\mu$ s, 2 kHz, 2.5 l/min He, 4 $\mu$ l/min styrene, 10 min, glass and NaCl substrates	The chemical polymerization mechanism of aromatic compounds under atmospheric pressure plasma conditions is based on plasma induced radical chain-growth concept and includes activation/fragmentation of chemical compounds, radical oxidation reactions and recombination of reaction products into random structures.	Asandulesa (2013) [99]
3	The specific aim of this work was to investigate the chemical modification induced by O <sub>2</sub> , Ar plasmas and (plasma) UV-irradiation on cPS films (spin coated). The modified PS samples were compared with plasma polymerized (PPS) and commercial polystyrene (cPS).	RF, 100 W, 50 %, 0.1 mbar, 10 g/h (75 °C), 1 KHz, glass and aluminum	The dielectric measurements show that the plasma deposited films are not thermally stable.	Fahmy (2012) [100]
4	They studied the influence of RF power and working pressure on the structure and properties of pPS deposited by RF-PECVD, using argon/styrene gas mixture.	RF, 13.56 MHz, 40-150 W, 7-16 $\times 10^{-2}$ mbar, one side of polished bell metal, 10 min	The deposition rate, the non uniformity, the degree of branching and cross-linking, the percentage of carbon content in plasma polystyrene films increased with increasing RF power. The results showed the possible application of polystyrene films as corrosion resistance coating on bell metal.	Choudhury (2010) [101]
5	The aim of the study was to synthesize hydrophobic coatings by means of plasma polymerization at atmospheric pressure using a mixture of helium gas and styrene vapors.	DBD, atm pressure, 50 kHz, 2-4 kV, styrene, He, 3 l/min total flow rate, 10 min	WCA ~ 130 ° The electrical plasma parameters, like the voltage waveforms and its rise time have a strong influence on the maximum discharge current.	Topala (2009) [102]
6	The goal of this paper was to prepare and characterize polystyrene films by plasma polymerization under atmospheric pressure or near atmospheric pressure by a DBD and into a post discharge of a RF plasma torch.	*DBD: He and Ar, 1 kV, 14 kHz, 2 $\times 10^4$ Pa, 4 mm, 1- 10 min *RF plasma Torch: 13.56 MHz, 30-80 W, Ar 30 L/min, 1- 15 min, 1 mm to 1 cm the distance plasma-head-substrate	The films obtained by the DBD plasma exhibit a wormlike pattern.	Merche (2009) [51]

	styrene monomer was kept at 40 °C in a thermostated bath Si wafer, glass, polymer and stainless steel		
7	This work is devoted to the relationship between external plasma parameters (such as RF input power, pressure or deposition duration), substrate topography and pPS coating morphology.	RF, 120 -200 W, 50 %, 0.13-0.66 mbar, 10 KHz, stainless steel, gold and glass, 1 -10 min	<p>The roughness (as well as the thickness) of the films increases as a function of the input power and gas pressure and no particular structure is observed for the film deposited with a low input power.</p> <p>The plasma deposited films are unsaturated, branched and/or cross-linked. These properties of the films are found to depend on fragmentation and re-arrangement of the monomer molecules in plasma, which could be controlled by external plasma parameters.</p> <p>When the plasma deposited films are exposed to air, extensive oxygen incorporation occurs</p>
8	The objective of this study was to synthesize polystyrene films using CO <sub>2</sub> as carrier gas and styrene vapor as monomer for biomedical applications.	CO <sub>2</sub> as carrier gas, RF 13.56 MHz, 85 W, 35 mm gap, glass, 15 min	<p>The composition and morphology of plasma polymerized films are controlled by the flow rate of CO<sub>2</sub>. The plasma polymerized films deposited on glass substrates exhibit a wave-like pattern and the contents of oxygen-containing groups increases with CO<sub>2</sub> flow rate.</p>
9	They investigated the potential effect of CH <sub>4</sub> containing reactive carrier gas on the plasma polymerized films and the possibility of such film for use in the preparation of sensors.	argon/CH <sub>4</sub> /styrene gas mixture, RF, 10 sccm, 35 W, 0.27 mbar	<p>Using Ar and CH<sub>4</sub> mixture gas caused increase of deposition rate and the films have the original characteristics of monomer.</p>
10	The aim of this work is the deposition and characterization of polymer coatings by FTIR spectroscopy, UV spectroscopy and contact angle measurements.	30 MHz RF source, 30 W input power, 0.13 – 0.66 mbar, Ge, glass, quartz, PAC	<p>At low pressures (0.13 mbar), a transparent thin film was deposited on substrate and at higher pressure (0.3 – 0.7 mbar) a white powder.</p>
copolymer			
1	The structure-property relationships of pulsed plasma deposition AA (acrylic acid)/S (styrene) copolymers dependence on the co-monomer ratio were studied.	RF, DC = 0.5, 1 kHz, 100 W, Al substrate	<p>The concentration of the COOH groups increases proportionally with increasing the fraction of AA in the precursor mixture</p>
2	The effect of power, pressure, deposition time and duty cycle of RF pulsed plasma on the polymerization of styrene and methyl methacrylate (MMA) were investigated.	inductively coupled planar RF discharge, 120 W, 50 % DC, 0.25 mbar, silicon substrate	<p>Films with different chemical composition can be deposited by controlling the monomer content in the gas phase.</p>

HaiDopoulos (2007) [32]

Luo (2007) [34]

Kim (2004) [103]

Kinzig (1981) [104]

Fahmy (2013) [105]

Li (2011) [106]

## 2.2. EXPERIMENTAL DETAILS

### 2.2.1 Atmospheric pressure plasma reactor

The plasma polymerized styrene coatings (pPS) were deposited using an atmospheric pressure dielectric barrier discharge, which operates in helium (He, Messer Romania Gas SRL) or argon (Ar, Messer Romania Gas SRL) as shown in **Figure 14**. The plasma reactor consists of a stainless steel chamber containing two circular parallel plate copper electrodes, deposited as thin films on glass dielectric. Positive high voltage (HV) pulses with 6 kV amplitude, 2 kHz frequency and 250  $\mu$ s width were applied on the HV electrode. The substrates were placed in the center of the bottom electrode and the gap between the two electrodes was kept constant at 5 mm. Glass substrates were cleaned first by Piranha solution (mixture of sulfuric acid –  $H_2SO_4$  and hydrogen peroxide –  $H_2O_2$ ).

The plasma reactor is equipped with two gas lines, one for process gas used to sustain the discharge and other line to transport styrene vapors into plasma volume. The styrene monomer was injected into the reactor using a classic bubbler system that is connected to a shower ring. The 6.5 cm diameter shower ring contains 12 holes which allow a uniform vapor distribution in the reactor chamber. Gas flow rates were constantly kept by electronic flow-meters (MKS type 1179 B) and a flow controller (MKS type 247). The deposition time for each film was 10 min. In order to clean and enhance adhesion between the layer and the substrate, same substrates were exposed 1 min to Ar plasma (pPS<sub>Ar\*</sub>) before deposition.

Samples used for cell culture and bacteria experiments were stored in clean tissue culture polystyrene dishes at ambient temperature.

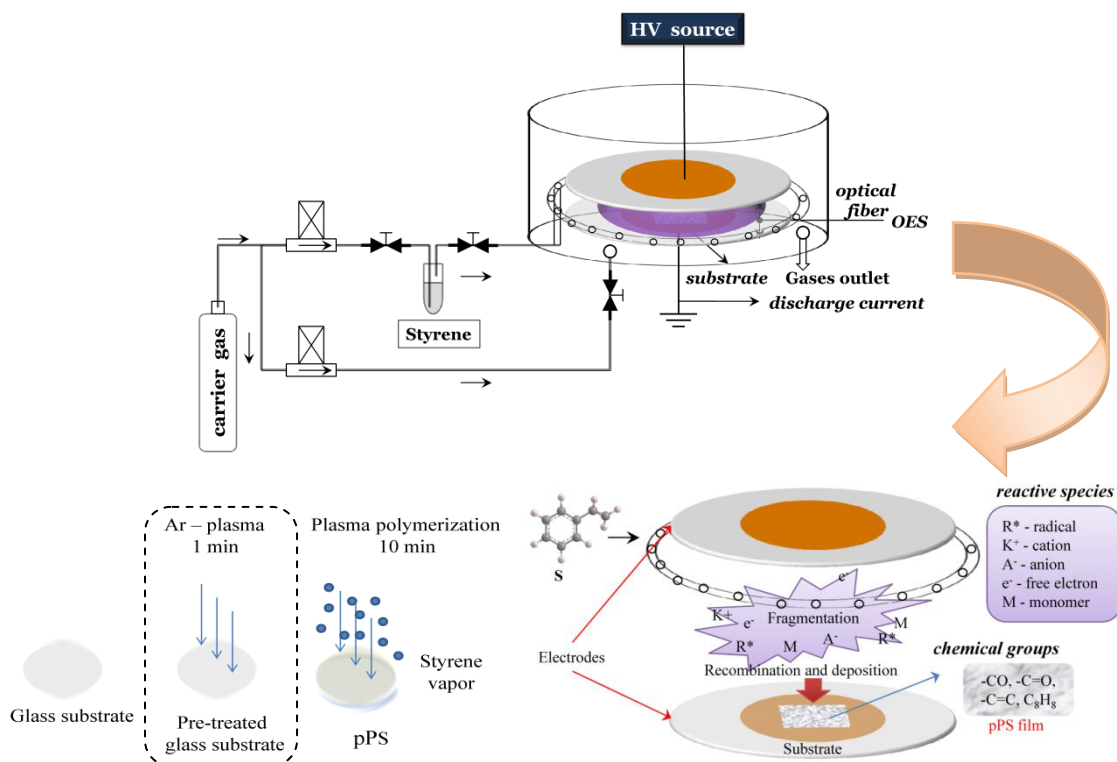


**Figure14.** Schematic representation of the plasma polymerization system, including the gas-inlet system and the discharge system. Formation mechanism and chemistry of plasma deposited styrene coatings [100, 107].

### 2.2.2 Plasma and films characterization methods

#### → *plasma gas phase*

The plasma gas phase was investigated by means of electrical measurements and optical emission spectroscopy (OES).

The applied voltage and discharge currents waveforms of plasmas were monitored and stored using a high voltage probe (P6015A, Tektronix) and a current probe (6485, Pearson) connected to a digital oscilloscope (TDS5034, Tektronix, 350 MHz, 5 GSa/s). The displacement current ( $I_d$ ), the current measured without gas flow, was removed from the total signal.

The optical diagnosis of plasmas (with and without monomers) was performed using a computer-controlled monochromator (Jobin Yvon Triax 550) with a CD detector (Symphony). The light emitted by the plasma was collected through quartz windows by an optical fiber (400  $\mu\text{m}$  diameter, 24° acceptance angle, 200 – 1100 nm range) guided to the entrance slit of the monochromator. The emission spectra were measured in the 200 – 900 nm range.

#### → *plasma polymerized styrene films*

*Fourier transform infrared spectra (FTIR)* of plasma polymerized styrene films were recorded using a BOMEM MB-Series 104 spectrometer. Each spectrum was collected by accumulating 5 scans at a resolution of 4  $\text{cm}^{-1}$ , in the range of 4000 – 500  $\text{cm}^{-1}$ . The FTIR spectra of pPS deposited on NaCl and ZnSe substrates were acquired in the transmission mode. The software GRAMs-AI was employed for measurements and for correction of the background.

*X-ray photoelectron spectroscopy (XPS)* spectra were recorded with a PHI 5000 VersaProbe (Physical Electronics) spectrometer, using a monochromatic Al  $K\alpha$  X-ray source ( $h\nu=1486.7$  eV), under a vacuum of about  $2 \times 10^{-6}$  Pa at a photoelectron take-off angle of 45°.

*Atomic force microscopy (AFM)* measurements (NT-MDT Solver Pro-M type apparatus) were carried out in ambient air, in the tapping (non-contact) mode, with commercial standard silicon-nitride tips with a radius of approximately 10-15 nm (NT-MDT, NSG03). The topography, magnitude and phase were recorded simultaneously for each sample on various scanned areas between 70  $\mu\text{m}$  x 70  $\mu\text{m}$  and 3  $\mu\text{m}$  x 3  $\mu\text{m}$ . Scans were repeated on different sites of the samples to check the surface uniformity, under the same conditions in ambient atmosphere. AFM technique was used to visualize and compare the topography of plasma polymer films before and after immersion in distilled water for 72 h. Maximum roughness parameter  $R_{\text{max}}$  is the vertical distance between the highest and lowest data points in the image.

*Scanning electron microscopy (SEM)* images were obtained using an electron microscope ULTRA 55 (Zeiss, France) equipped with a thermal field emission emitter and three different detectors (BSE detector with a filter grid, a high efficiency In-lens SE detector and an Everhart–Thornley secondary electron detector). The biological samples were fixed with 1 % glutaraldehyde solution (G6257, Sigma Aldrich) for 30 min in the dark at room temperature and coated with a conductive material.

*Thickness measurement.* The coatings thickness was quantified using an interferometric-based technique (Linik MII type).

*Wettability* was evaluated by measuring the contact angle between water drops (2  $\mu\text{L}$ ) and the plasma polymer surface using a horizontal optical microscope with a digital camera (OPTIKAM 4083.BS) connected to a computer and with a Digidrop instrument (GBX, France). All measurements were made under ambient conditions. WCA values reported are the mean of 6 individual measurements on 3 replicated samples. The corresponding standard deviations are reported in the graphs as error bars.



## 2.3 PLASMA DIAGNOSTICS

Understanding the correlation between mechanism of film growth and properties can help to design coatings for specific applications. Various studies related to plasma polymerization have been performed by employing argon (Ar) or helium (He) as carrier gas, or an inert/reactive gas mixture. Compared with He, Ar is cheaper and requires low ionization energies, but He plasmas operate in a diffuse glow regime which is a desirable plasma regime to deposit homogeneous films. The homogeneity of the He discharge is due to existence of its high energy metastables (He ( $2^3S_1$ ) at 19.82 eV and He ( $2^1S_0$ ) at 20.62 eV). The ionized air species are most likely created through Penning ionization of air molecules by helium metastables and helium dimer metastables. Contrary, argon requires low ionization energies (11.5 eV for  $^3P_2$  and 11.7 eV for  $^3P_0$ ) than helium, therefore its capability of causing Penning ionization is smaller, the discharge has to proceed *via* the streamer process to generate filamentous plasma between the electrodes. The  $Ar^+$  (15.78 eV) ions affect more the plasma polymerized structure than metastable species. [103, 108, 109]

The external plasma parameters, including pulse width, deposition time and applied voltage were optimized in order to improve the stability of pPS films in aqueous medium.

### 2.3.1 Electrical measurements

Analyzing the discharge current waveforms, two current pulses (positive and negative) appear which are related with two consecutive discharges (primary and secondary). The primary discharge current pulses appear during the rise cycle of the applied voltage, when the ground electrode acts as cathode and the power electrode as anode. Consequently, the second discharge current pulses are generated during the falling cycle of the applied voltage and the power electrode acts as cathode and the ground electrode as anode. Typical forms of the applied voltage and discharge current are shown in **Figure 15**. The discharge current shape and amplitude (several tens of milliamperes) observed during the primary and secondary discharges confirm the homogeneous regime of the atmospheric pressure discharge (APD) [110]. The results indicate that when in the plasma volumes are transported monomers vapor, the discharge current intensity decreases, because part of plasma energy is used to induce fragmentation, molecular excitation and plasma polymerization reactions. A significant decrease was measured for Ar/S gas mixture, therefore an energy supply per unit monomer higher, leading to more fragmentation of the styrene molecules.

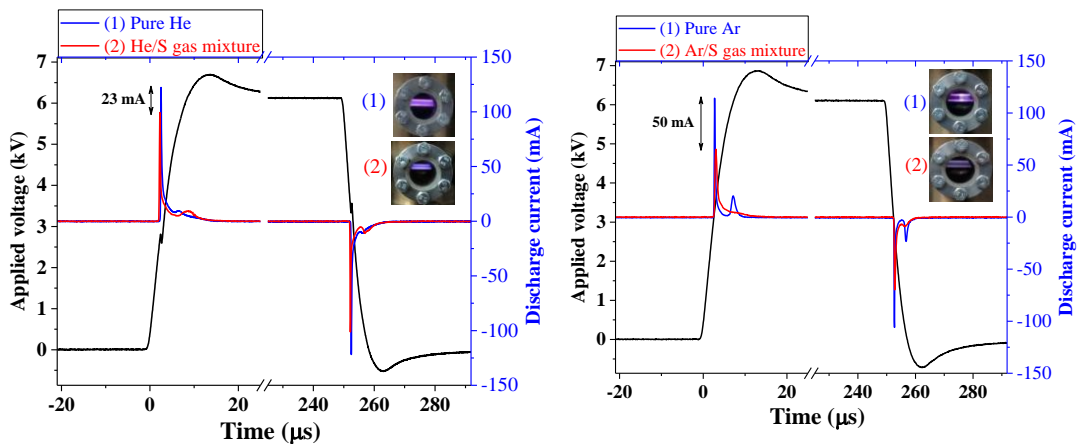


**Figure15.** Typical forms of the applied voltage and of the discharge current waveforms.

### 2.3.2 Optical emission spectroscopy

Optical emission spectroscopy (OES) was employed to analyze the plasma phase and to identify the active species. All emission spectra contain the helium/argon lines and atomic lines/molecular bands specific of air impurities (e.g. atomic oxygen (777.4 and 845.2 nm), molecular nitrogen (315.8, 336.4, 358.4 and 380.4 nm), molecular nitrogen ion (391.6, 427 nm and 470.6 nm) and hydroxyl radical (309.1 nm)). The OES spectra of the two discharges, He/S and Ar/S are quite similar in contrast to pure plasmas (**Figure 16**). Comparison of the emission spectra revealed that when in the discharge volume are injected monomers, the emission spectra intensity decreases. In the case of Ar/S plasma the spectrum is almost completely quenched. According to XPS and FTIR measurements, the residual N<sub>2</sub> bands present in the emission spectra did not participate in the polymer deposition, no nitrogen-containing groups were incorporated in the films bulk or at the surface.

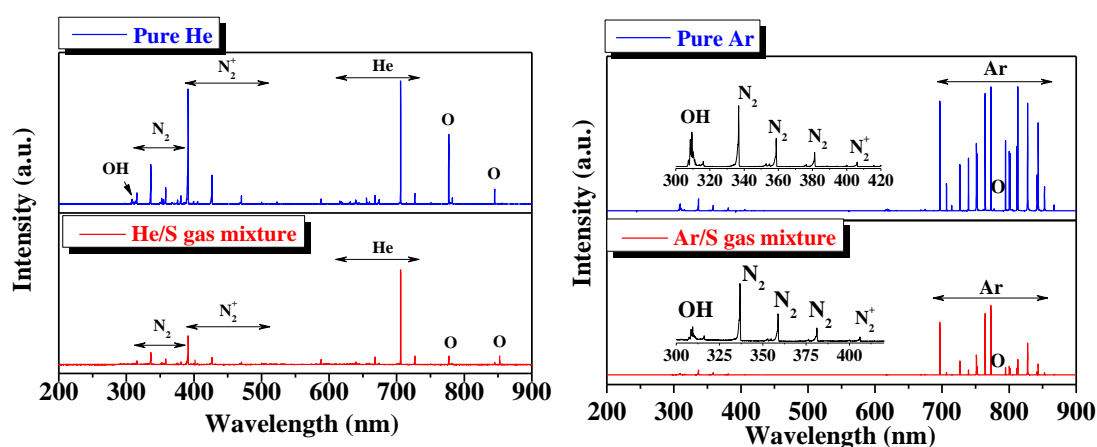


**Figure 16.** The optical emission spectra of the discharges. Spectroscopic parameters - exposure time: 5 s, accumulations: 1, slit: 0.1 nm, range 200 ÷ 900 nm.

## 2.4 PHYSICO-CHEMICAL PROPERTIES OF PLASMA POLYMERIZED STYRENE FILMS

In order to create and to optimize a surface for a particular application, a detailed characterization of the film is necessary. The chemical composition and morphology of plasma polymerized styrene (pPS) films were analyzed by means of Fourier Transform Infrared Spectroscopy (FTIR) and X-ray Photoelectron Spectroscopy (XPS), Atomic Force Microscopy (AFM) and Scanning Electron Microscopy (SEM). The wettability properties were evaluated by water contact angle (WCA) measurements.

As shown in **Figure 17**, the pPS<sub>He</sub> and pPS<sub>Ar</sub> spectra are similar. FTIR studies indicate a partial retention of the monomer characteristic groups in the polymer films. The styrene bands are well resolved compared to the broad spectra obtained for pPS coatings. In addition, for S monomer spectrum in the 1665-2000 cm<sup>-1</sup> region, the presence of the aromatic CH vibrations, named *the five aromatic fingers*, can be observed. For plasma polymerized coatings the intensity of these five peaks decreases, meaning that the phenyl rings are broken under plasma influence. The aromatic ring breakage is confirmed also by the disappearance of aromatic CH bands at 908 and 991 cm<sup>-1</sup> and the IR bands present in the aliphatic region. [99]

The two new peaks that appear in the spectra at 2964 and 2866 cm<sup>-1</sup> suggest that the films are branched. Merche *et al.* [51] reported that films deposited in the presence of He are less branched than those synthesized in the presence of Ar.

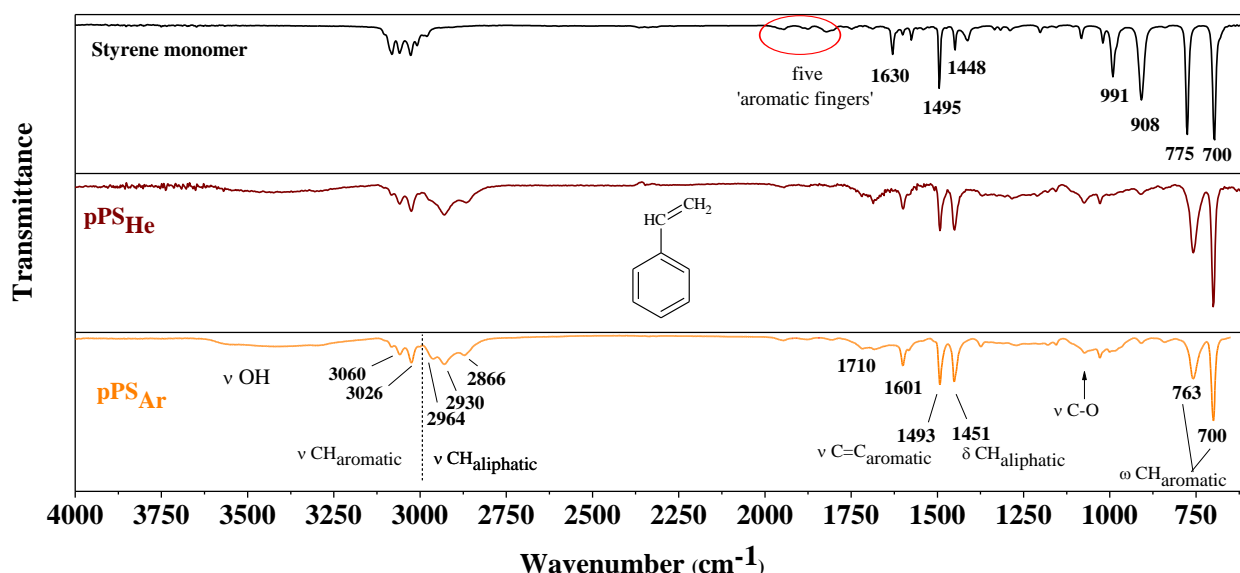


**Figure 17.** FTIR spectra of styrene and freshly deposited plasma polystyrene films onto NaCl substrates.

Identification of the spectral peaks and bands was made according to the literature, systematically presented in **Table 4**. The strong absorption band observed in the region  $3500 - 3100 \text{ cm}^{-1}$ , can be attributed to OH stretching vibration. The  $2930 \text{ cm}^{-1}$  and  $2866 \text{ cm}^{-1}$  peaks correspond to the stretching vibration of the aliphatic C-H groups ( $-\text{CH}_x$ ), while the  $1452 \text{ cm}^{-1}$  and  $1430 \text{ cm}^{-1}$  peaks are due to C-H bending in methylene ( $-\text{CH}_2-$ ) and vinyl groups ( $-\text{CH}=\text{CH}_2$ ). The bands positioned at  $3059 \text{ cm}^{-1}$  and  $3025 \text{ cm}^{-1}$  correspond to aromatic  $=\text{C}-\text{H}$  stretching, at  $1600 \text{ cm}^{-1}$  and  $1492 \text{ cm}^{-1}$  to aromatic C=C stretching, at  $1075 \text{ cm}^{-1}$  and  $1028 \text{ cm}^{-1}$  to C-H in-plane deformation bending of aromatic ring, at  $758$  and  $700 \text{ cm}^{-1}$  to aromatic C-H bending.

**Table 4.** Detailed assignments of relevant features in the plasma polystyrene IR spectra.

Wavenumber ( $\text{cm}^{-1}$ )	Type of vibration	Ref.
3450	hydroxyl O-H stretching	[34, 45, 51]
3082, 3060, 3026	aromatic C-H stretching	[34, 45, 46, 51, 101]
2964, 2864,	methyl ( $-\text{CH}_3$ ) C-H stretching	[34, 45, 46, 101, 111]
2930	methylene C-H stretching	[34, 45, 46, 101, 111]
2000-1665	five aromatic fingers	[46, 101]
2350 and 668	$\text{CO}_2$ bands	[51]
1710	carbonyl C=O stretching	[51, 101, 112, 113]
1601, 1493	aromatic C-H in plane and C=C aromatic	[34, 45, 51]
1451	methyl C-H bending, in plane phenyl ring-bending mode	[34, 45, 51]
1250	C-O	[34, 45, 51]
763, 700	out of plane phenyl ring bending mode	[34, 45, 46, 51, 101]



The presence of oxygen in the pPS network is confirmed by the peaks at 3400 and 1710  $\text{cm}^{-1}$  attributed to hydroxyl and carbonyl stretchings and also by XPS measurements. The oxygen incorporation may originate from two sources, the presence of oxygen and water vapors in the plasma reactor before and during plasma polymerization and from post-oxidation of the coatings exposed to air after plasma deposition. Also, the optical emission spectroscopy confirms the presence of atomic oxygen (77.4 nm and 845.2 nm) and hydroxyl radical (309.1 nm).

The XPS results are summarized in **Table 5** and show that both pPS<sub>He</sub> and pPS<sub>Ar</sub> films contain oxygen and carbon elements (**Figure 18**). The C<sub>1s</sub> peak was deconvoluted into four main components, assigned to C-C and/or C-H (at 284.6 eV), C-O-C and/or C-OH (at 286.3 eV), C=O and/or H-C=O (at 288 eV) groups and  $\pi$ - $\pi^*$  shake-up satellite (at 294.2 eV).

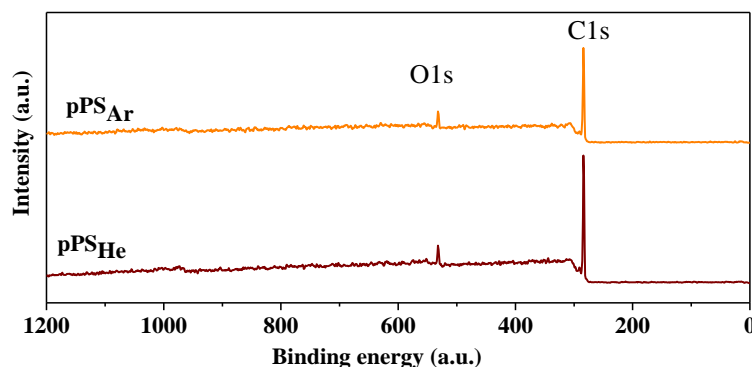


**Figure 18.** XPS survey spectra of plasma polystyrene synthesized using He/S and Ar/S gas mixture.

**Table 5.** Elemental composition, the functional groups content and WCA of commercial (C), thermal (T) and plasma (p) polymerized styrene films.

Samples	T-PS [34]	C-PS[114] amorphous	C-PS[114] cross-linked	DBD[114]		MPP-PS (Ar)[114]	pPS <sub>He</sub>	pPS <sub>Ar</sub>
				He	Ar			
C (%)	96.1	98	86	94	95	74	<b>92.3</b>	<b>92.7</b>
O (%)	3.9	2	14	6	5	26	<b>7.7</b>	<b>7.3</b>
C-C %	97.3	98	89	92.5	94.5	73	<b>85.9</b>	<b>86.4</b>
C-O %	-	2	10	7	5	17	<b>9.3</b>	<b>10.4</b>
C=O %	-	-	-	0.5	0.5	5	-	-
COOH	-	--	1	-	-	5	-	-
$\pi$ - $\pi^*$	2.7	6.7	0.5	4.4	4.76	-	<b>4.8</b>	<b>3.2</b>
WCA (°)		87	123	72	71	35	<b>83 ± 2</b>	<b>84 ± 2</b>

The characteristic  $\pi$ - $\pi^*$  shake-up satellite is due to resonance of the PS aromatic ring, emphasizing that the films retained the monomer chemicals structure. The ratio between the satellite shake-up (aromatic carbon) and the main peak (aliphatic carbon) can be used to evaluate *the aromaticity of the films*. In our case, the ratio of pPS<sub>He</sub> is 5 % and pPS<sub>Ar</sub> is 3.3 %. The results are in good agreement with those obtained by Haidopoulos *et al.* [115] They showed that the degree of aromaticity depends on the external plasma parameters and the pPS ratio ranging from 1% (high input power) to 6.5 % (lower input power). For example, the ratio of commercially PS is 7.5 %.

The presence of the intact aromatic ring in the pPS films is also confirmed by <sup>1</sup>H-NMR measurements (Bruker Avance III 500 spectrometer equipped with a 5 mm PABBO detection probe, 500.1 MHz, deuterated dimethylsulfoxide – DMSO-d<sub>6</sub>). The styrene <sup>1</sup>H-NMR spectrum contains strong signals at 7.47 – 7.25 ppm assigned to aromatic protons from benzene and three distinct signals corresponding to aliphatic protons from vinyl type group at 6.7, 5.8 and 5.2 ppm.

As can be seen in **Figure 19**, the vinyl protons present in  $^1\text{H}$ -NMR spectra of monomer have disappeared in the spectra of  $\text{pPS}_{\text{He}}$ . Asandulesa *et al.* [99], suggested that  $\text{C}=\text{C}$  is replaced by  $\text{C}-\text{C}$ . Three new peaks appear in the spectra at 4.3 ppm, which correspond to aliphatic  $\text{CH}$  type groups, at 1.2 and 0.8 ppm which are specific to methylene  $\text{CH}_2$  protons and methyl  $\text{CH}_3$  protons.

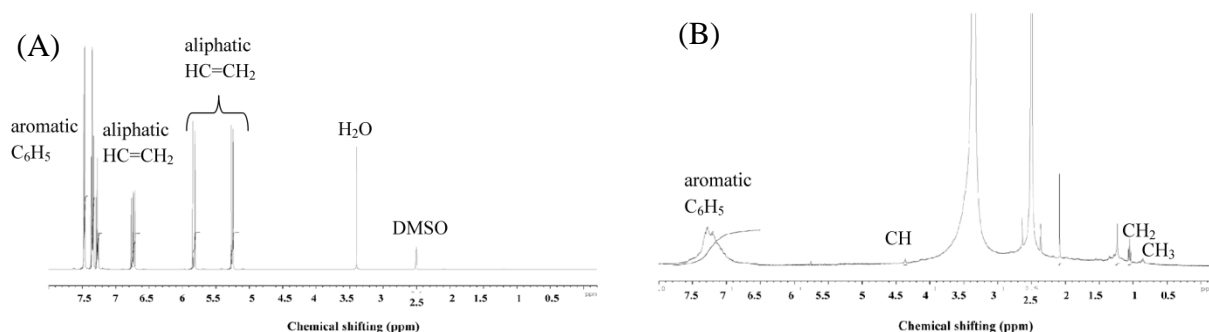


**Figure 19.**  $^1\text{H}$  NMR spectra of (A) styrene and (B)  $\text{pPS}_{\text{He}}$  in  $\text{DMSO}-d_6$ .

The AP-DBD allows the deposition of macroscopically smooth polystyrene films across the whole length of the glass substrate, with no specific structure (**Figure 20**). In addition, the employed carrier gas (He and Ar) or substrate plasma pre-treatment does not affect the topography or the wettability of plasma polymerized styrene film. The water contact angle of the  $\text{pPS}$  coating is around  $83^\circ$ , in agreement with the value reported for its counterpart (**Table 5**).

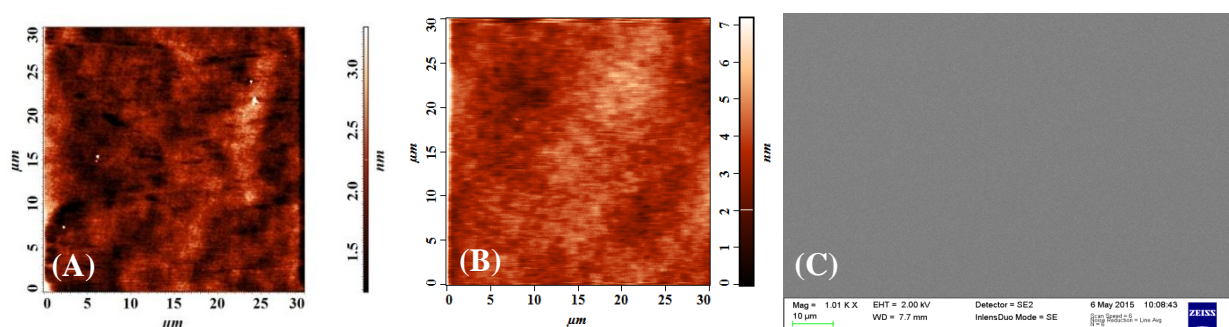


**Figure 20.** AFM topographic images scanned over  $30 \times 30 \mu\text{m}^2$  of (A)  $\text{pPS}_{\text{He}}$  and (B)  $\text{pPS}_{\text{Ar}}$  films. (C) SEM images of  $\text{pPS}_{\text{Ar}}$ .

Furthermore, the thickness of the films synthesized using a mixture of argon gas and styrene vapors are higher. For 10 min deposition time, the  $\text{pPS}_{\text{He}}$  thickness is around 550 nm and for  $\text{pPS}_{\text{Ar}}$  is around 950 nm.

## CONCLUSIONS

Plasma polymerized styrene films were successfully synthesized by means of atmospheric pressure plasma technique, using a mixture of helium or argon gas and styrene vapors.

The obtained results show that the  $\text{pPS}$  chemical composition, topography and wettability are similar for both coatings synthesized in the presence of helium or argon used as main and carrier gas. The  $\text{pPS}$  films are smooth and uniform across the whole length of the substrates, without any visible features with a WCA of around  $83^\circ$ . In particular, the film synthesized using  $\text{Ar/S}$  mixture has a higher deposition rate and is more cross-linked.

The XPS, FTIR and  $^1\text{H}$ -NMR measurements confirm the presence of oxygen-containing groups and of intact aromatic ring in the  $\text{pPS}$  coating chemical composition.

## CHAPTER 3. BEHAVIOR OF PLASMA POLYMERIZED STYRENE FILMS IN BIOLOGICAL MEDIA

*A special attention was devoted to the stability of the plasma polymerized styrene films in air and in aqueous environments. The plasma parameters and deposition conditions were optimized according to the film stability in aqueous media. Also, a detailed characterization of surface-composition and morphology was performed.*

### 3.1 INTRODUCTION

The stability of plasma polymers in aqueous environment is a key parameter which determines their successful application. In contrast with the material stability under ambient conditions, which already has certain limitation, the stability of plasma polymers in aqueous media is a more complex problem. Due to the random structure of the plasma polymers, it is impossible to predict the mechanism involved in their degradation. According to Mielczarski *et al.* [116] when a polymer is immersed in a solvent the following process can occur:

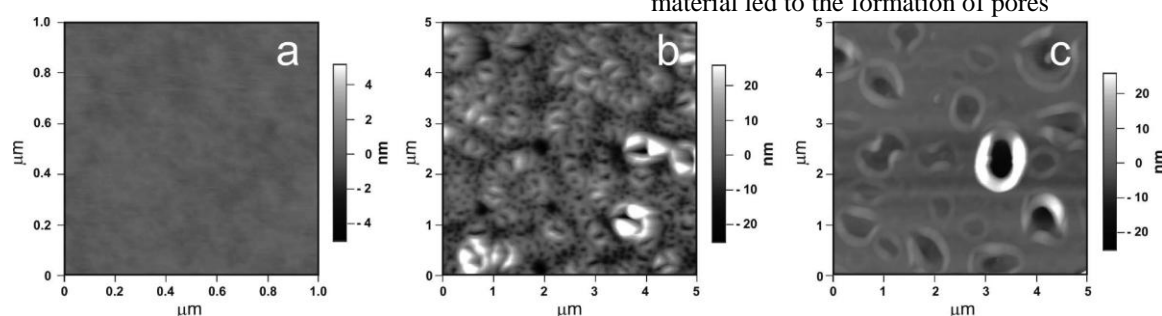
- ✚ swelling, a process which involves the diffusion of water into the polymer network, leading to an increase in the film thickness and volume;
- ✚ homogeneous degradation facilitated by chain cleavage;
- ✚ diffusion of the oligomers and the formation of a reaction-erosion front at the surface;
- ✚ complete delamination of the film from the substrate.

The behavior of plasma polymers in aqueous media is affected by several factors, including the polymer molecular weight, thickness, crosslinking degree, adhesion to substrate, nature of the solution and plasma deposition conditions. In general, films with high functional groups density, like carboxylic, hydroxyl or amino groups, can be unstable in liquids and the coatings deposited at high powers present a good stability. Abbas *et al.* [117] reported the dissolution process and the washing out of the uppermost polymer layer contribute to the material loss. It has to be highlighted that a very few studies are devoted to the physico-chemical modification induced in plasma polymers by the aqueous media (**Table 6**). Even though, the coatings intended for biologically related applications should be tested at least in water.

**Table 6.** Literature review – stability of plasma films in aqueous media.

Plasma films	Plasma technique	Conclusions	Ref.
allylamine (C <sub>3</sub> H <sub>7</sub> N) ethylenediamine (C <sub>2</sub> H <sub>8</sub> N <sub>2</sub> )	low –pressure RF discharge reactor	- the film stability depends on applied RF power and the chemistry of the monomer	Daunton (2015) [118]
acrylic acid (CH <sub>2</sub> =CHCO <sub>2</sub> H)/ methylene-bis-acrylamide (H <sub>2</sub> C=CHCONH) <sub>2</sub> CH <sub>2</sub> )	atmospheric pressure air plasma jet	- coating water-stability was significantly improved by optimizing the deposition parameters, heating the substrate during deposition and by adding a cross-linking to the precursor	Carton (2015) [48]
L-PPE:N	low –pressure RF discharge reactor	- a NH <sub>3</sub> or N <sub>2</sub> plasma pre-treatment of the substrate enhances the plasma film adhesion on PTFE substrate	Lerouge (2015) [119]
cyclopropylamine (C <sub>3</sub> H <sub>5</sub> NH <sub>2</sub> )	low-pressure capacitively coupled RF discharge in continuous and pulsed wave mode	- at optimized monomer flow rate, the PW film exhibited only 20 % thickness loss after 48 h immersion in water - 4 at% oxygen concentration increase after water immersion	Manakhov (2014) [120, 121]

saturated and unsaturated acids, glymes and hydrocarbons	low –pressure RF discharge reactor	- the film stability depends on applied RF power and the chemistry of the monomer	Micheltore (2013) [122]
acrylic acid (CH <sub>2</sub> =CHCO <sub>2</sub> H)	dielectric barrier discharge operating at medium pressure	- stable surfaces were obtained at high discharge power and close to the monomer inlet	Morent (2010) [36]
C-NH <sub>2</sub> (from N <sub>2</sub> , NH <sub>3</sub> and C <sub>2</sub> H <sub>4</sub> )	atmospheric pressure/ low-pressure systems/vacuum-ultraviolet photo-polymerization	- low-pressure plasma polymerization and UV photo-polymerization allow deposition of stable films, during long-term exposure to air or aqueous solvents	Ruiz (2010) [123]
allylamine (C <sub>3</sub> H <sub>7</sub> N)	low-pressure RF discharge in continuous wave mode	- was found a dependence between swelling and the loss of material as a function of RF input power; - films deposited at 125 W present no significant loss of material	Abbas (2009) [44]
allylamine (C <sub>3</sub> H <sub>7</sub> N) and acrylic acid (CH <sub>2</sub> =CHCO <sub>2</sub> H)	low-pressure downstream microwave plasma	- confirm the relationship between process parameters and dissolution stability	Finke (2009) [124]
n-heptylamine CH <sub>3</sub> (CH <sub>2</sub> ) <sub>6</sub> NH <sub>2</sub>	low-pressure RF discharge in pulsed wave mode	- the stability and the structure of films upon immersion in various solvents varies with deposition conditions and aging in air - the extraction of soluble polymeric material led to the formation of pores	Vasilev (2008) [125]



AFM topographic images of HA plasma polymer films before and after immersion in water for 24 h after deposition or after aging in air for 72 h.

### 3.2 EXPERIMENTAL DETAILS

*The ageing of pPS films* was investigated by means of FTIR spectroscopy, AFM and WCAs, after 30 days of storage in ambient conditions.

*The stability of pPS films in aqueous solution* was studied by immersing the samples in distilled water, deionized water, tris-buffer solution, DMEM or LB medium (volume of ~ 5 mL) for a set time in ambient atmosphere at room temperature or 37 °C. Then, the pPS coatings were dried at 50 °C for 1 - 2 h to evaporate the water. Reference samples were prepared by heating directly the films without water immersion.

The pPS films were analyzed before and/or after soaking in aqueous medium by XPS, FTIR, AFM, SEM, optical microscopy, Zeta sizer, UV-Vis spectroscopy and water contact angle measurements, detailed in Chapter 2.

*UV-vis absorption spectra* of films deposited on ZnSe substrates and solution collected after immersion of samples for various time intervals were recorded using a Thermo Scientific Evolution 300 UV-Vis spectrophotometer. The wavelength range was between 200 and 500 nm.

The size of soluble part released during pPS water immersion was measured at 20 °C with an equilibration of 2 min using a *Zetasizer ZS* (Malvern Instruments S.A., Worcestershire, U.K.) in 173° scattering geometry.

### 3.3 STABILITY OF PLASMA POLYMERIZED FILMS IN AIR

Ageing involves monitoring of plasma polymer surface composition over extended periods of time after deposition. The ageing process is also known as auto-oxidation. In long term applications, *ageing* is a limitation that plasma polymers may present. It is known that plasma films undergo certain reactions when exposed to ambient conditions. For example, the radicals from freshly deposited plasma polymers rapidly react with oxygen or water molecules during exposure to air. The ageing process consists in two steps:

- (i) *primary ageing oxidation*, molecular oxygen reacts with C-radical sites, resulting in the peroxy radicals (C-O-O\*) and
- (ii) *secondary reaction step*, decay of the peroxy radicals and formation of different oxygen functionalities like C=O and COOH. [95]

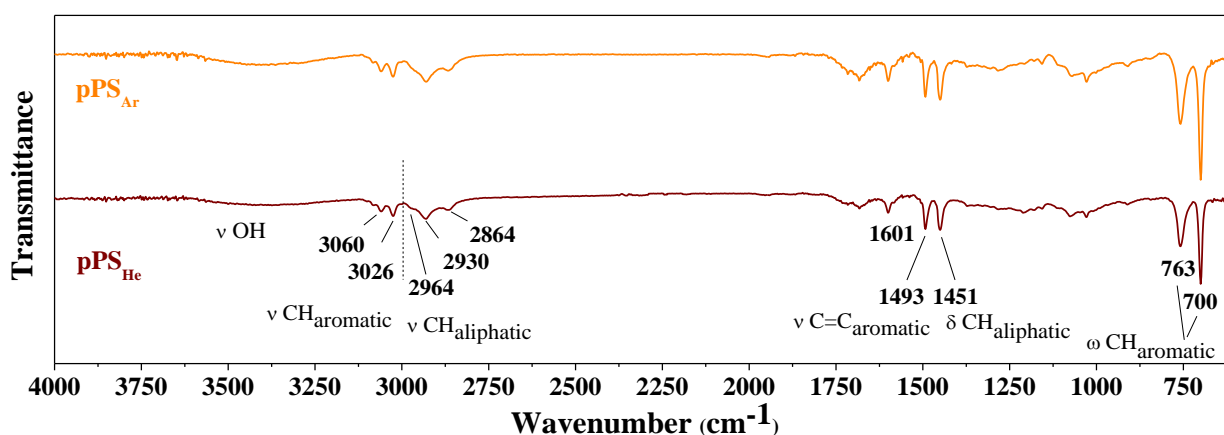


**Figure 21.** FTIR spectra of pPS<sub>He</sub> and pPS<sub>Ar</sub> after 30 days of storage in ambient air.

Ageing studies were performed to simulate the storage conditions before bacteria and cell studies. The FTIR, WCAs and AFM measurements confirm that pPS films did not experience detectable degradation, even after 30 days of storage in ambient conditions (**Figure 21-23**). It is known that when a plasma polymer is exposed to air, oxygen incorporation occurs. Oran *et al.* [98] observed a higher oxygen uptake at the beginning and for harder plasma conditions (lower monomer flow rate and higher plasma power). Increasing the discharge power leads to a higher energy per monomer molecule, a high degree of fragmentation and re-arrangement of monomer molecules, and consequently a higher concentration of surface radicals. The oxygen-free deposited plasma polystyrene sample is characterized by an oxygen uptake less than 5 % after 1-month storage time. [46]

The pPS film stability studies during aqueous media exposure shows that the amount of low molecular weight fragments removed from pPS matrix decreases significantly for air-aged film compared with as-deposited coating. Therefore, the post-deposition reactions make the coating more stable, inducing cross-linking between polymer segments.



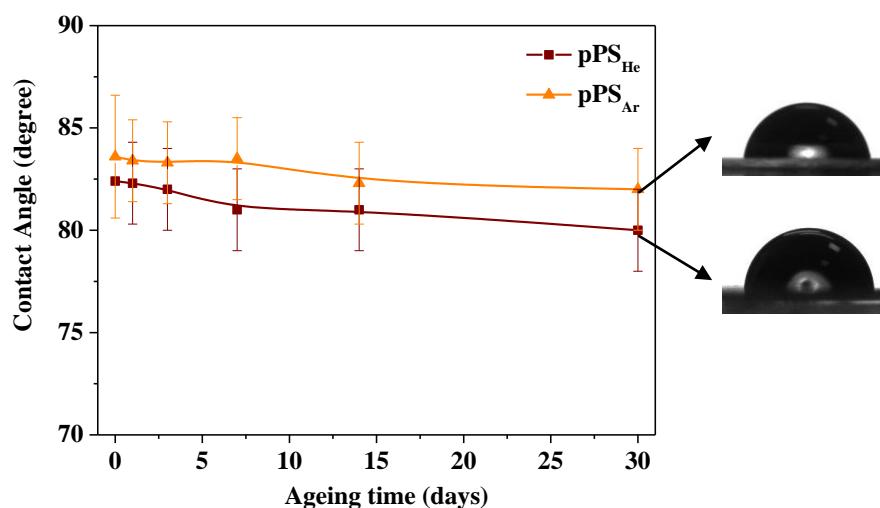


**Figure 22.** Water contact angle of (a) pPS<sub>He</sub> and (b) pPS<sub>Ar</sub> films as a function of storage time.

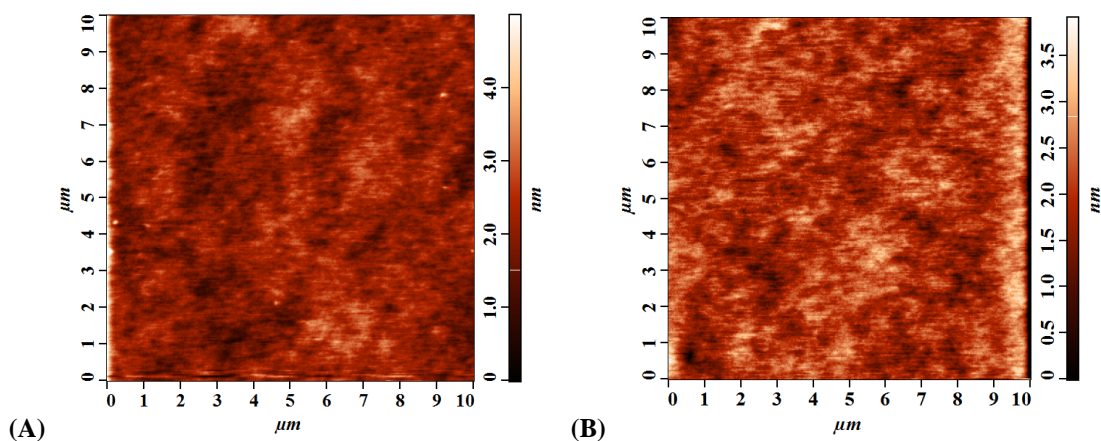


**Figure 23.** AFM topographic images scanned over 10 x 10 μm<sup>2</sup> of pPS<sub>Ar</sub> film (A) as-deposited and (B) after 30 days storage in ambient air.

### 3.4 Stability of plasma polymerized styrene films in aqueous media

To monitor the amount of material dissolved during the immersion in Milli-Q water, we acquired the absorbance spectra of the liquid in which the pPS films were soaked for different durations ranging from 1 h to 72 h (**Figure 24.A**). We cannot estimate the amount of low molecular weight fragments extracted from the plasma polymers because their thicknesses are different, around 550 nm for pPS<sub>He</sub> and 950 nm for pPS<sub>Ar</sub>. The higher amount of oligomers removed from the pPS films have been observed in the first two hours, and then no significant change in absorbance was measured. Similar results were reported by Manakhov and co-workers [121], according to their study the most significant loss appearing in the first hour of layer immersion. Initially we supposed that the absorbance increase is related to desorption of fragments which was physically deposited at the end of plasma polymerization process, after the discharge has been turned off. This assumption was not verified since there was no difference between samples kept 5 min in plasma reactor in continuous Ar flow and as-deposited ones. A slight decrease of pPS<sub>He</sub> thickness was measured, but it is difficult to quantify because the film thickness increases when is soaked in water, due to water diffusion in the polymer network (**Figure 24.B**).

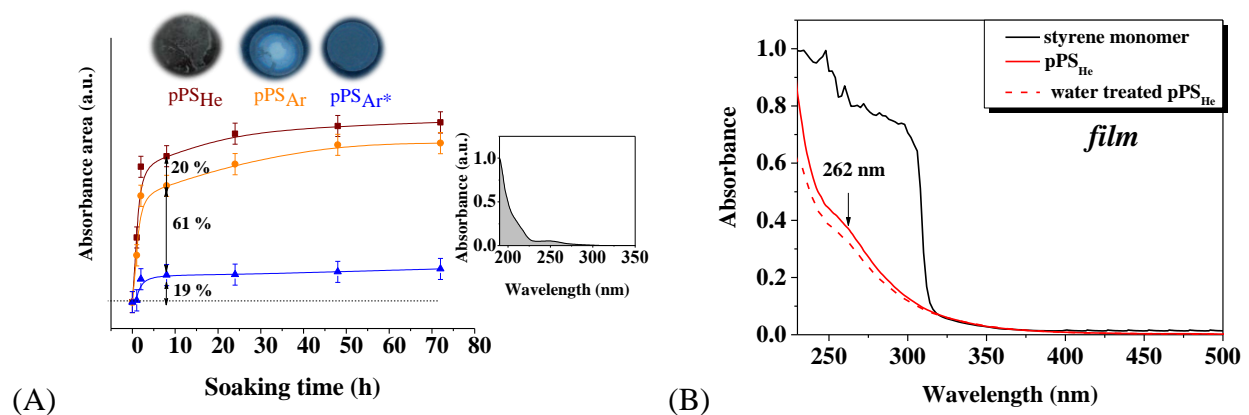


**Figure 24.** (A) The kinetics of the pPS films dissolution. Insert: UV spectrum of water in which the pPS<sub>He</sub> film was soaked for 72 h and the images associated to each film. (B) –UV-vis spectra of styrene and pPS film as deposited and after 72 h of immersion in distilled water (230-500 nm).

AFM imaging was carried out in order to understand the influence of aqueous elution on the pPS films topography. As can be shown in **Figure 25 A-B**, during immersion of plasma polymerized coatings in aqueous environment, the surfaces become *microporous*, resembling a *honeycomb pattern*. The  $\mu\text{m}$  voids are uniformly distributed on the entire film surface and have diverse depths and widths. We suppose that the main cause of voids formation is the hydrolysis of the oligomeric part non-covalently bonded to the film matrix, which is related to plasma polymer cross-linking density.

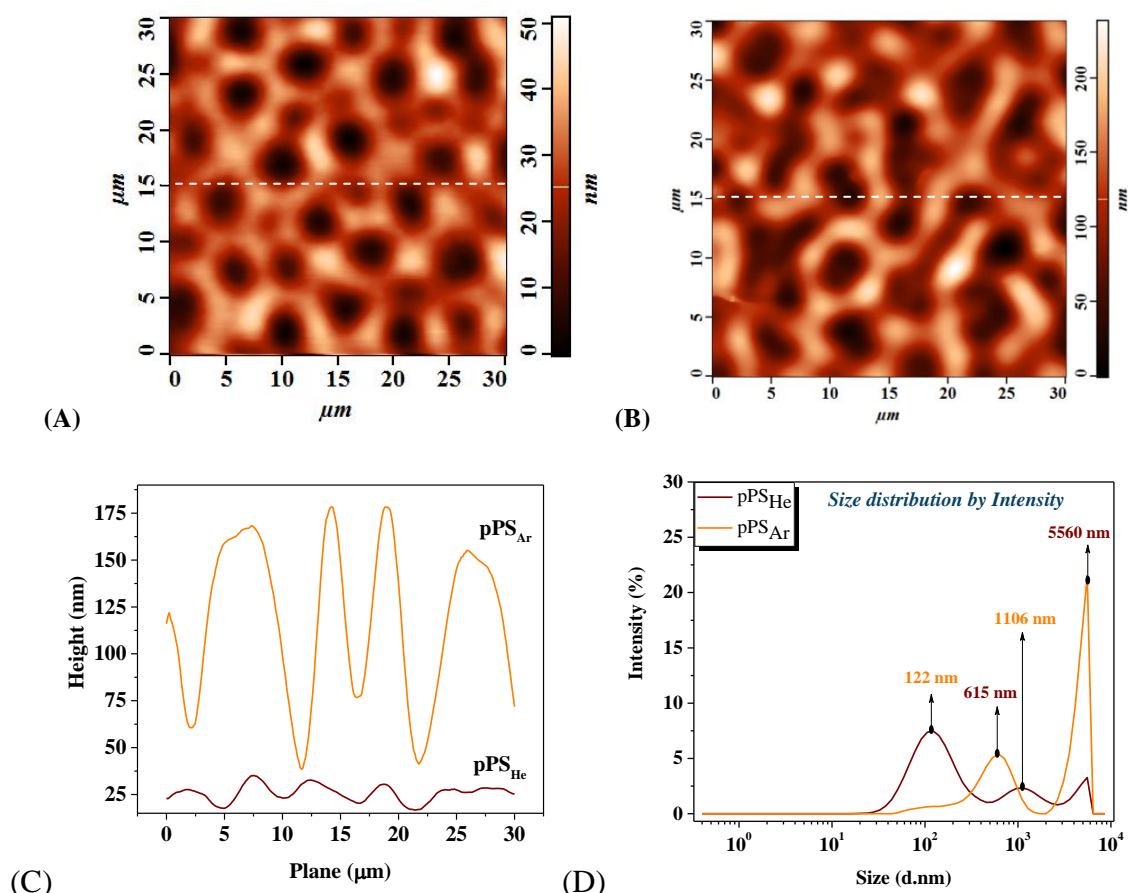


**Figure 25.** Representative AFM topographic images of (A) pPS<sub>He</sub> (stable part) and (B) pPS<sub>Ar</sub> after immersion in distilled water for 72 h, scanned over  $30 \times 30 \mu\text{m}^2$  and (C) their height profile. (D) Zeta size of low molecular weight constituents released from the pPS matrix.

A similar result was reported by Vasilev *et al.* [125], noting that the solvent induces formation of pore in n-heptylamine plasma polymers and by Carton *et al.* [48], reporting that the surface of plasma polymerized acrylic acid (-COOH) coating after water soaking is significantly modified by a lot of valleys.

Honeycomb structured porous interfaces were obtained by Hernandez *et al.* [126] from blends of polystyrene with a glycopolymer using the breath figures assay (**Figure 26**). They found that the composition of the blend, humidity and temperature have a strong influence on the pore size and distribution

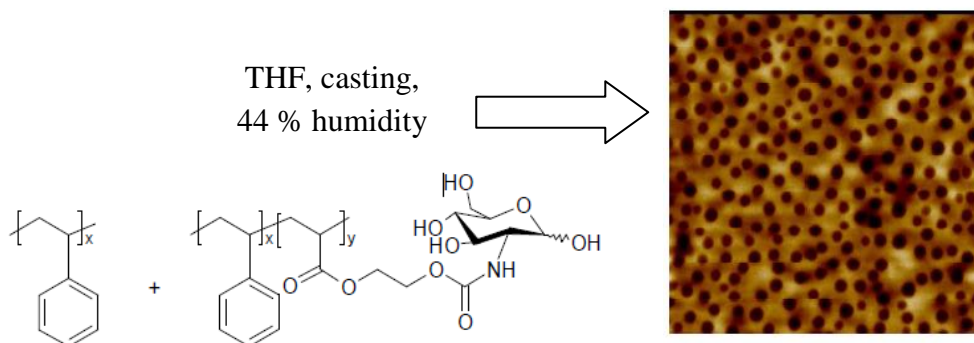


**Figure 26.** AFM images ( $10 \times 10 \mu\text{m}^2$ ) obtained by spin coating in a 44 % humid atmosphere with a blend composition of 20/80 [126].

Compared with untreated substrate, the pPS films deposited onto substrate pre-treated with Ar plasma for 1 min before deposition show better stability in aqueous media. As can be seen in **Figure 24**, the pPS<sub>Ar\*</sub> films exhibit less extraction of water soluble material. In addition, styrene polymerized using a mixture of helium gas and styrene vapors are sticky and easy to remove from the substrate. We observed a partial delamination of the coatings and floating sheets in solution, in contrast with films synthesized using a mixture of argon gas and styrene vapors. In addition, we performed a surface treatment with vinyltrimethoxysilane in order to enhance the adhesion between pPS film and glass substrate; however, no significant enhancement of the film stability was observed (experimental details are presented in Appendix I).

Lerouge *et al.* [119] have reported that plasma pre-treatment of the substrate enhances the film adhesion to substrate and Abbas *et al.* [44] have proved that UV light-Ozone treatment of the substrate surface prior to deposition improves the adhesion and the stability in aqueous media.

We found that the structures dimension and density depend on the plasma polymerization conditions and ageing effect. As can be observed in **Figure 25.C-D**, the voids diameter and depth depend on working gas (He/Ar), which is in good agreement with size distribution of fragments extracted from pPS films. The higher oligomer size measured for pPS<sub>Ar</sub> confirms that pPS synthesized using Ar exhibits a higher degree of cross-linking than pPS deposited with He as the main gas, in agreement with Merche *et al.* [51].

In addition, a complete film delamination and dissolution were identified for 2-min deposition time and for higher monomer flow rates. Thus, the deposition time and monomer flow rate are key parameters that affect the stability of pPS coatings during aqueous media exposure. After aging in air followed by immersion in aqueous environment for 72 h the pPS topography is different, the voids dimension and the amount of material dissolved decrease. These findings confirm that the post-deposition reactions induce cross-linking between polymer segments making more stable to extraction of low molecular weight fragments from pPS. Vasilev *et al.* [125] observed the same behavior, the amount of material extracted from plasma polymers is reduced significantly for air-aged films compared with freshly deposited plasma polymers films.



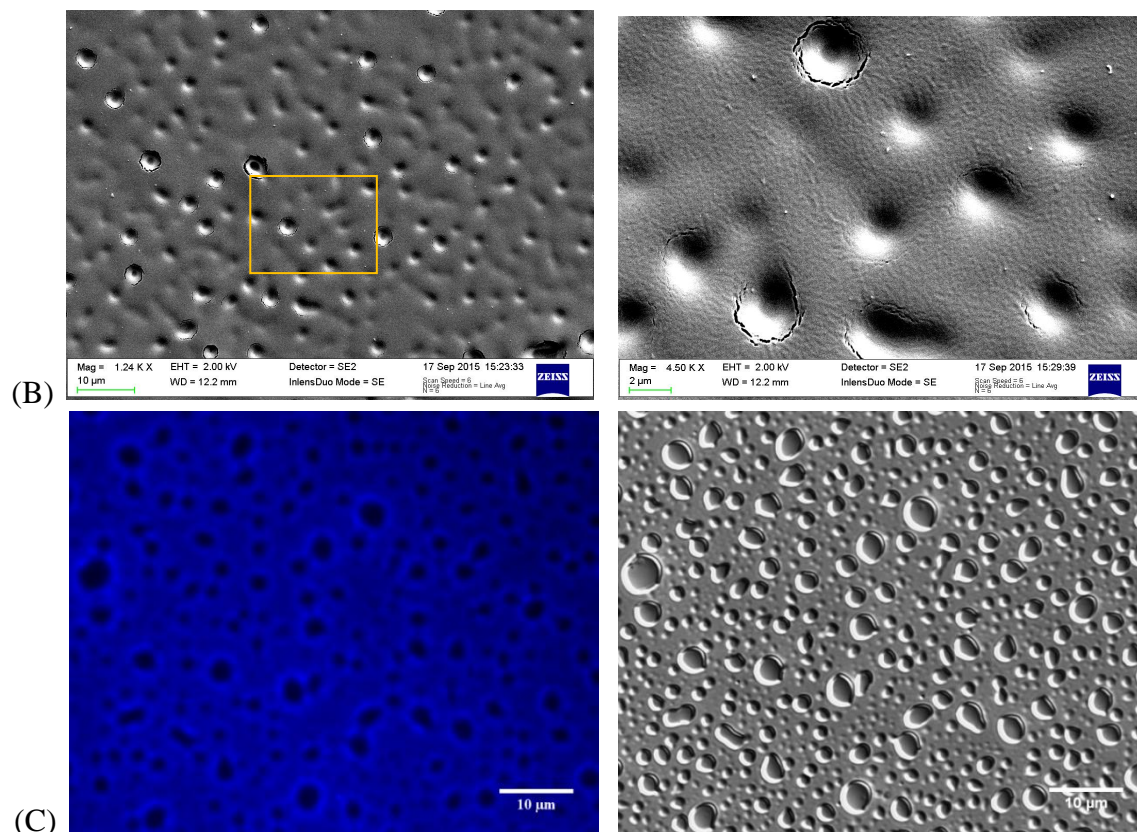
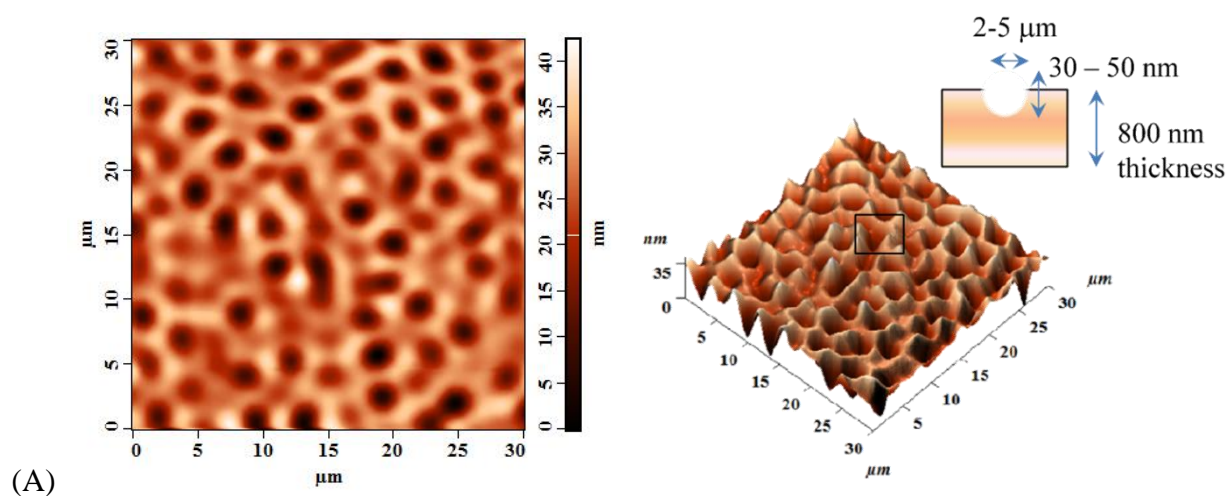


**Figure 27.** A) 2D and 3D AFM topographic images ( $30 \times 30 \mu\text{m}^2$ ), B) SEM ( $10 \mu\text{m}$  and  $2 \mu\text{m}$  bar) and C) top view images by using a fluorescence microscope (thioflavin S staining,  $71.64 \times 71.5 \mu\text{m}^2$ ) of pPS<sub>Ar</sub>\* film after 72 h of immersion in aqueous environments.

The stability of pPS films in aqueous media was also investigated by FTIR spectroscopy. As can be observed in **Figure 28**, there is no significant difference between the FTIR spectra of as-deposited films and those of samples immersed in aqueous medium for 72 h.

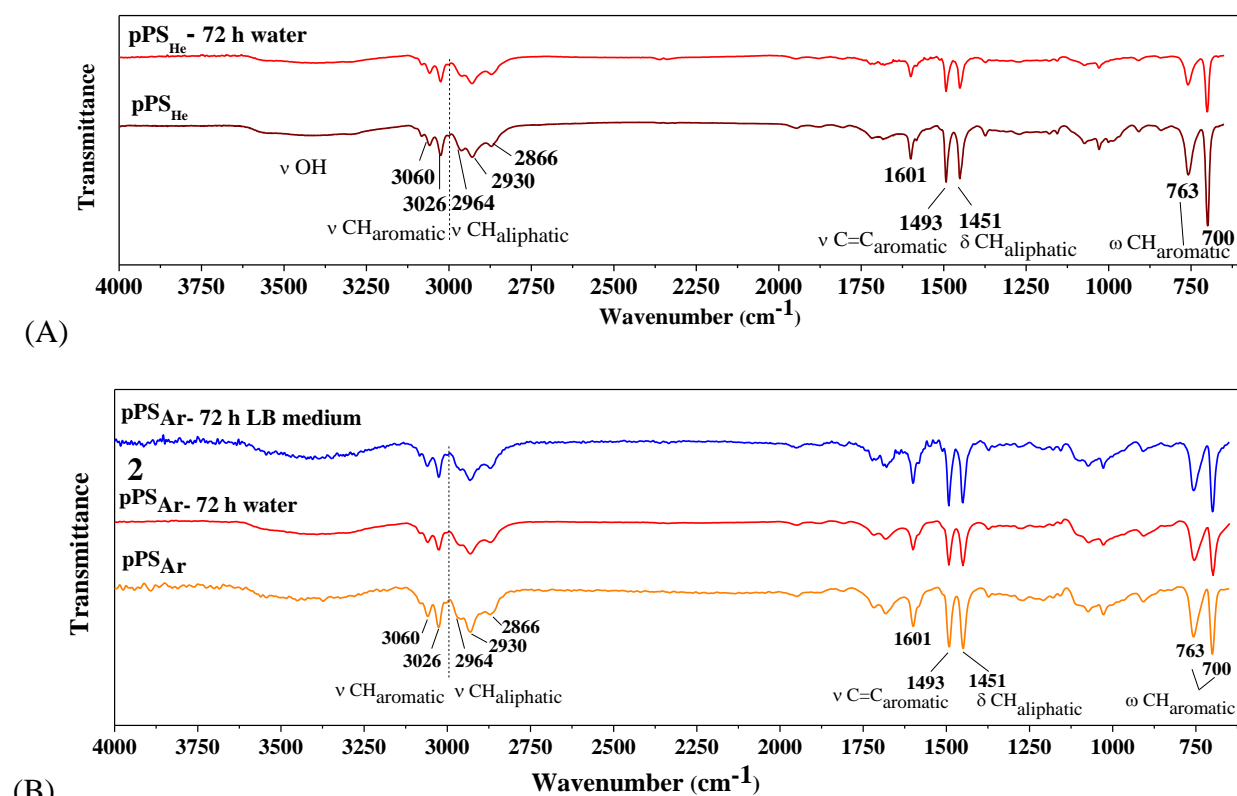


**Figure 28.** FTIR spectra of (A) pPS<sub>He</sub> and (B) pPS<sub>Ar</sub> films as-deposited and after immersion in MQ-water and/or LB medium for 72 h. The films were deposited on ZnSe substrate.

According to XPS results, presented in **Table 7** and **Figure 29**, the films chemical composition did not change so much after 72 h of immersion in Milli-Q water. The concentration of oxygen increased to 7.5 % for pPS<sub>He</sub> and 5 % for pPS<sub>Ar</sub>, in agreement with Manakhov *et al.* [121] results who measured an increase of 3-4 % after 48 h of immersion in water. Moreover, after water immersion, the ratio between the satellite shake-up (aromatic carbon) and the main peak (aliphatic carbon) decreases to 2 % for both films.

**Table 7.** Elemental composition of pPS<sub>He</sub> and pPS<sub>Ar</sub> films before and after immersion in water for 72 h.

pPS	pPS <sub>He</sub>		pPS <sub>Ar</sub> *	
	before	after	before	after
C (%)	92.3	84.8	92.7	87.7
O (%)	7.7	15.2	7.3	12.3
O/C	0.083	0.18	0.078	0.14

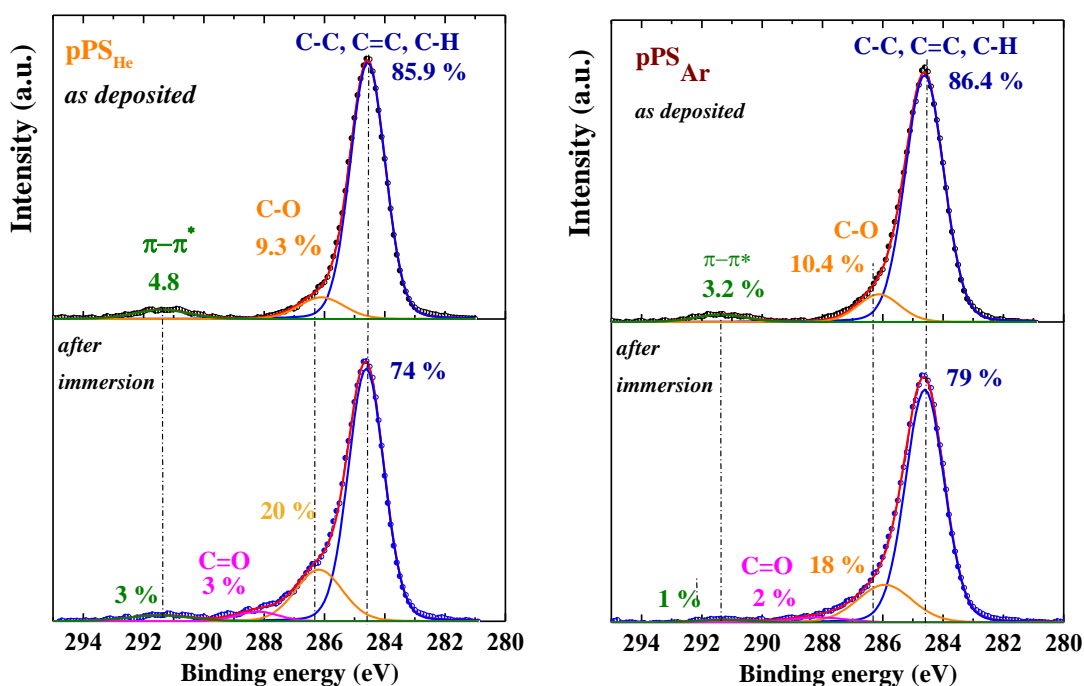


**Figure 29.** C<sub>1s</sub> high resolution XPS spectra of pPS<sub>He</sub> and pPS<sub>Ar\*</sub> as-deposited and after 72 h of immersion in distilled water. The line + symbol represent the experimental data and the lines represent the individual contributions.

The immersion of pPS films in water leads to an increase and to formation of polar groups such as C-O and C=O, in agreement with WCA measurements (**Figure 30.A**). The coatings after 72 h of immersion in distilled water became more hydrophilic.

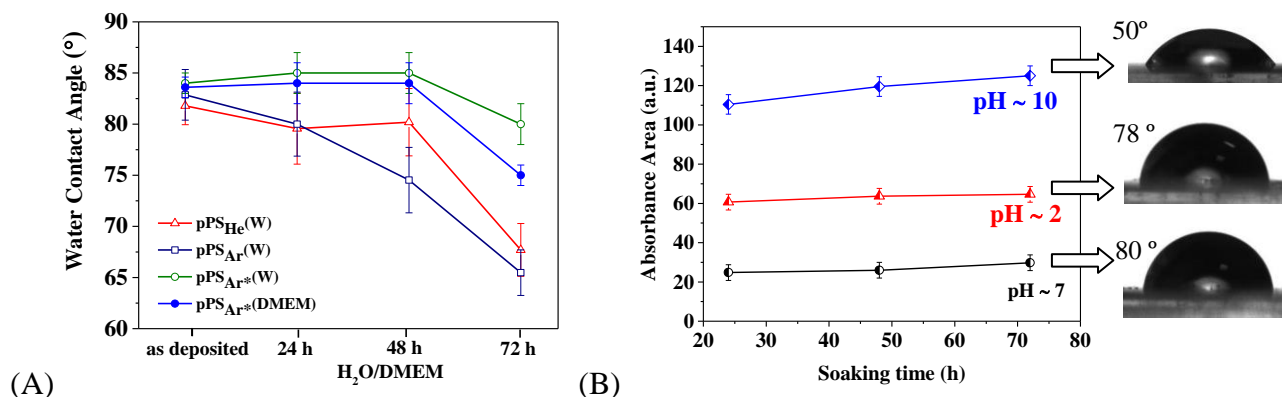


**Figure 30.** WCA measurements as a function of immersion time in Milli-Q water and DMEM. Error bar shows a standard deviation of 10 drops for one sample.

We identified that the stability of pPS<sub>Ar</sub> films is sensitive to pH changes of the solution in which they are immersed (**Figure 30.B**). The film in basic solution was completely removed and in acidic solution we found an increase of oligomeric components loss.

According to the published results, the annealing may be a proper method to improve the water solubility of plasma polymers. Further, the thermal annealing is used as sterilization procedure. Carton *et al.* [48] reported that by heating (200 °C) the substrate during the deposition, the coatings stability increases significantly and Mielczarski *et al.* [97] observed that annealing of PS films (average MW, 250 000, Acros Organics and Sigma Aldrich) at 75 °C and 85 °C for 2 h makes them more stable under PBS treatment.

In our case the thermal or plasma treatment and UV irradiation for a shorter period of time led to complete delamination or photo-degradation of the coatings.

## CONCLUSIONS

Plasma polymerized styrene films synthesized using a mixture of helium or argon gas and styrene vapors are stable at least 30 days in air.

One of the main challenges was to obtain films relatively stable in aqueous media. The optimum stability under biological media was achieved for aged plasma polystyrene films deposited using Ar/S mixture onto pre-treated glass coverslips for 1 min with Ar plasma. Therefore, the post-deposition reactions induce cross-linking between material segments and the pPS films synthesized using Ar exhibit a higher degree of cross-linking than pPS deposited with He due to the higher energy supplied per unit monomer.

Our results show clearly that the pPS surface changes when it is soaked in water-based liquids, resulting in a honeycomb pattern. We found that the amount of fragments extracted from pPS coating and the voids diameter and depth depend on the working gas (helium or argon), deposition time and monomer flow rate. The films deposited at low monomer flow rate are more stable compared to the films deposited at a high monomer vapor pressure and low deposition time. In addition, the modification occurs quickly, in two hours once the films are soaked in biological environments and the chemical compositions of films did not change significantly after immersion in aqueous media. We assume that a main cause of the solubility is the low degree of cross-linking and of pore formation is the extraction of the oligomeric parts non-covalently bonded to the film network.

## CHAPTER 4. RESPONSE OF EUKARYOTIC AND PROKARYOTIC CELLS TO PPS SURFACE PROPERTIES

---

*The low fouling behavior of plasma polymerized styrene films have been tested against HeLa (human cervical carcinoma), U-87 MG (human glioblastoma) and HEK-293 (human embryonic kidney) cell lines. In addition, the capacity of the coatings to prevent the bacteria adhesion and biofilm formation was determined using Escherichia coli (E. coli) strain LF82.*

### 4.1 INTRODUCTION

*Biofouling* represents a serious problem in domains such as bio-medicine (biosensors, biomedical devices), food processing, marine industry or water filtration and purification systems. For this reason, there is a growing interest on the design of new *antibacterial surfaces* or to improve the performance of existing surfaces. The antibacterial surfaces can be classified into *antibiofouling* and *bactericidal* surfaces, according to their action mode. The antibiofouling surfaces prevent the attachment and accumulation of unwanted biomolecules and micro-organisms, while biocidal surfaces are those that kill cells through chemical mechanism or agents. [1-3]

Plasma polymerization, surface treatment and material etching have become particularly attractive for the design of antibacterial coatings, because they have the advantage to modify the surface chemistry without affecting the material bulk properties. In addition, the material surface properties, like chemical composition, roughness or wettability can be tailored by tuning the gas composition, the plasma reactor geometry or the external plasma parameters. Plasma etching can be employed to obtain various kinds of nano- and micro-structured surfaces [4], and plasma polymerization to deposit films with different chemical domains, from cell-repulsive to cell-adhesive area [5], hydrophilic alternating with hydrophobic regions [6] or antibacterial coatings [2, 90]. Particularly, plasma modified surfaces were used to attach or to incorporate biocidal or bacteriostatic molecules, including natural compounds [8-11] or silver ions and other nanoparticles [12-14].

The cell/surface material interface is a complex topic, depending on the physico-chemical properties of the substrate, characteristics of biological medium and cells type. In recent years, various studies have shown that the surface topography is an important factor, that can influence the micro-organism/surface interaction. The results proved that the surface features size, shape, the distance between them and their organization have a strong impact on the cell behavior. Special attention has been devoted to micro-organism response to nanoscale surface features, then to microscale.

Moreover, only a few studies have investigated the material properties influence on bacteria biofilm. Compared with planktonic bacteria, sessile bacteria are much more difficult to remove and to kill, owing to extracellular polysaccharide matrix that provides more resistance to the inhibitory effects of antibacterial agents.

A major challenge remains the design of surfaces able to favor cell adhesion and inhibit bacteria colonization or the design of surfaces that can prevent bacterial attachment and release of antibacterial agents only when is needed.



## 4.2 EXPERIMENTAL DETAILS

### 4.2.1 Chemicals

Thioflavin S (230456), glutaraldehyde solution (G6257), dopamine hydrochloride (H85502), tris buffered saline (T6664), Hoechst 33342 (H3570), propidium iodide solution (P4864), Dulbecco's modified Eagle's medium (DMEM), fetal-calf serum and penicillin/streptomycin mix, Cell Counting Kit-8 were purchased from Sigma-Aldrich and used as received.

### 4.2.2 Film cytotoxicity

**Cell lines** (Appendix II):

- **THP-1** - human monocytic cell line derived from an acute monocytic leukemia patient.
- **HeLa** - human cervical cancer cell line.
- **U-87 MG** - human glioblastoma cell line.
- **HEK – 293** - human embryonic kidney cell line

**Cell culture.** Human **THP-1 cells** were grown in RPMI-1640 supplemented with 10 % fetal-calf serum (FCS) and 1 % penicillin/streptomycin mix and **HeLa, U-87 MG** and **HEK – 293 cells** were grown in Dulbecco's Modified Eagle's medium (DMEM, Gibco®) supplemented with 10 % fetal-calf serum (FCS, Gibco®) and 1 % penicillin/streptomycin mix (Gibco®). The cells were maintained at 37 °C and 5 % CO<sub>2</sub> in a humidified incubator. Cells were seeded on 1.2 cm round glass coverslips, plasma polymerized styrene films as deposited (pPS) and pre-treated in DMEM (pPS-72 h) (before experiment the samples were immersed in DMEM for 72 h). Each well was loaded with approximately  $1 \times 10^5$  THP-1 cells and  $5 \times 10^4$  HeLa, U-87 MG and HEK – 293 cells, in 500 µL of medium.

During the incubation, cell adhesion, spreading and growth were assessed using phase-contrast light microscopy. Images of cells were taken at 24 h intervals over a period of 3 days using a phase-contrast light microscope (Nikon Eclipse TS 100, Nikon – ELWD 0.3/OD75) and a mounted camera.

**Cytotoxicity assay.** The cell viability was evaluated using Cell Counting Kit-8 (CCK-8, Sigma Aldrich) assay. Briefly, after 72 h of incubation in a 5 % CO<sub>2</sub> atmosphere at 37 °C, the medium was aspirated, further to remove dead cells debris and remaining growth medium the cells were washed with 500 µl PBS. The incubated surfaces were transferred into a new 24-well cell culture plate. Cells were harvested by trypsination, 50 µl trypsin (0.05 %)/well was spread in a uniform layer and incubated for 5 - 10 min at 37 °C and 5 % CO<sub>2</sub> in the humidified incubator. Then the cell suspension was transferred to a 96-well plate (100 µl/well, 5 wells per sample) and incubated for 6 h at 37 °C and 5 % CO<sub>2</sub>. After 6 h in each well of the plate (+ 2 well with DMEM) was added 10 µl of the CCK-8 solution and then the plate was incubated for an additional 3 h in the incubator. The absorbance of each well at 450 nm was recorded using a microplate reader (PHERAstar FS, BMG LABTECH GmbH, Germany). The cytotoxicity was expressed as the percent cell viability to the viability of the control cells, the cells grown on the glass coverslips represented the 100 % viability value. Each condition was replicated for five times; data are presented as means  $\pm$  standard deviation.

In **Figure 31** is schematically illustrated the protocol followed to study the pPS<sub>Ar\*</sub> film cytotoxicity.



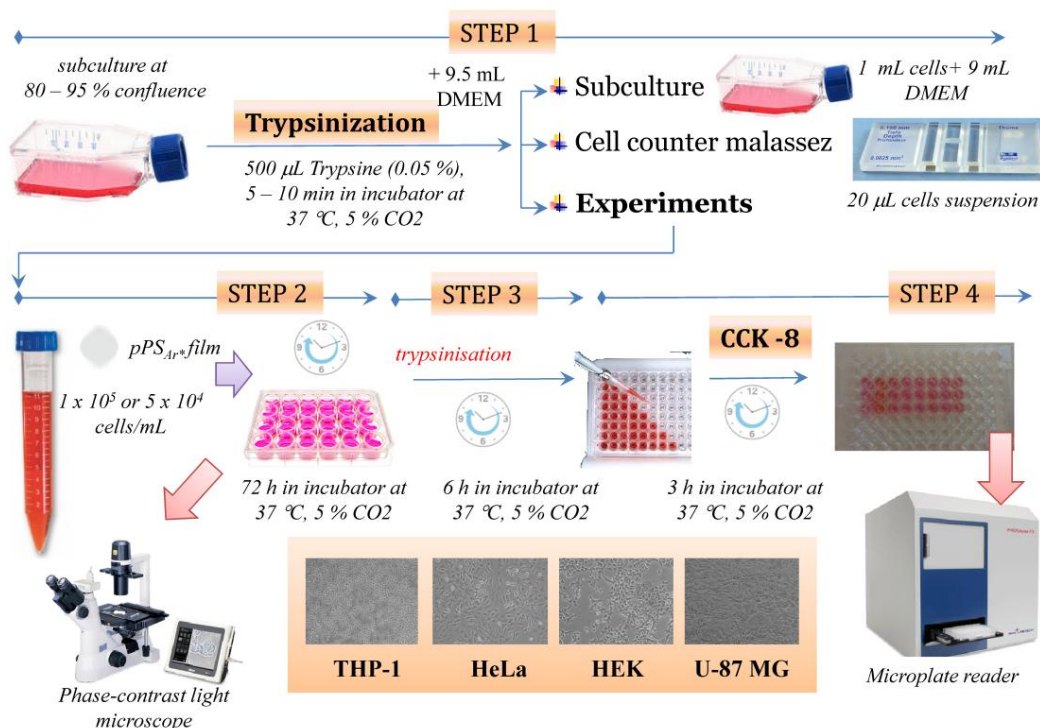


**Figure 31.** Schematic illustration of the experimental steps followed to study the pPS<sub>Ar</sub>\* cytotoxicity.

### 4.2.3 Film antibacterial properties

**Culture conditions and the spread plate method:** A single *E. coli* LF82 colony from LB agar plate was inoculated overnight in LB (Luria-Bertani) medium at 37 °C with moderate shaking. The pre-culture was diluted 50-fold and allowed to continue for another 3–4 h, until the OD<sub>600 nm</sub> had reached 0.6–1. The culture was then diluted to 10<sup>3</sup> CFU/mL and transferred to a 24-well plate. The 12 mm surfaces were placed in each well and incubated for 72 h at 37 °C with 1 mL bacteria (10<sup>3</sup> CFU/mL) to form biofilms. As control we used glass and polystyrene (PS) culture plate. After incubation all samples were washed twice with Milli-Q water.

**Viability test.** The loss of LF82 viability was evaluated by colony counting method in LB agar. This method is known as spread plate method and is frequently used for antibacterial assessment. Non-diluted samples and series of 10-fold cell dilutions (10 µL each) were spotted onto LB-agar plates and left to grow overnight at 37 °C. Colonies were counted and compared with those on control plates.

#### Proliferation test.

- **Static** – the samples were placed in 24-well plates and incubated for 24 h at 37 °C with 1 mL bacteria (10<sup>3</sup> CFU/mL). After the incubation, the optical density at 600 nm was measured.

- **Dynamic** – the samples were placed in 15 mL centrifuge tubes and incubated with 2 mL bacteria (10<sup>3</sup> CFU/mL) for 24 h at 37 °C in an incubator shaker. After the incubation, the optical density at 600 nm was measured.

**Biofilm observation and fluorescence staining.** Visualization of bacteria was performed by Leica AF6000 LX system after staining with Thioflavin S (Sigma Aldrich, 1326-12-1). The Thioflavin S stains the amyloid proteins that typify bacteria biofilm.

Briefly, the biofilm was stained by adding 1 mL in each well-plate of a 40 µg/mL TH-S solution for 10 min in the dark at room temperature. For microscopy measurements, the samples were placed on microscope slides and the edge glass coverslips were sealed with nail polish.

**Live/dead staining.** The cells were stained with DAPI/PI. The propidium iodide (PI, λ<sub>ex</sub> = 538 nm, λ<sub>em</sub> = 617 nm, red) penetrates only damaged cells in contrast to 4',6'-diamidino-2-phenylindole (DAPI, λ<sub>ex</sub> = 358 nm, λ<sub>em</sub> = 463 nm, blue) that labels all bacteria, live (green fluorescence) and dead (red fluorescence).

The bacteria were stained by adding 1 mL in each well-plate of a 2  $\mu\text{g}/\text{mL}$  DAPI and 0.4  $\mu\text{g}/\text{mL}$  PI solution for 10 min in the dark at room temperature. For microscopy measurements, the samples were placed on microscope slides and the edge glass coverslips were sealed with nail polish.

In **Figure 32** is schematically illustrated the protocol followed to assess the capacity of the pPS<sub>Ar</sub>\* film to prevent bacteria adhesion and biofilm formation.

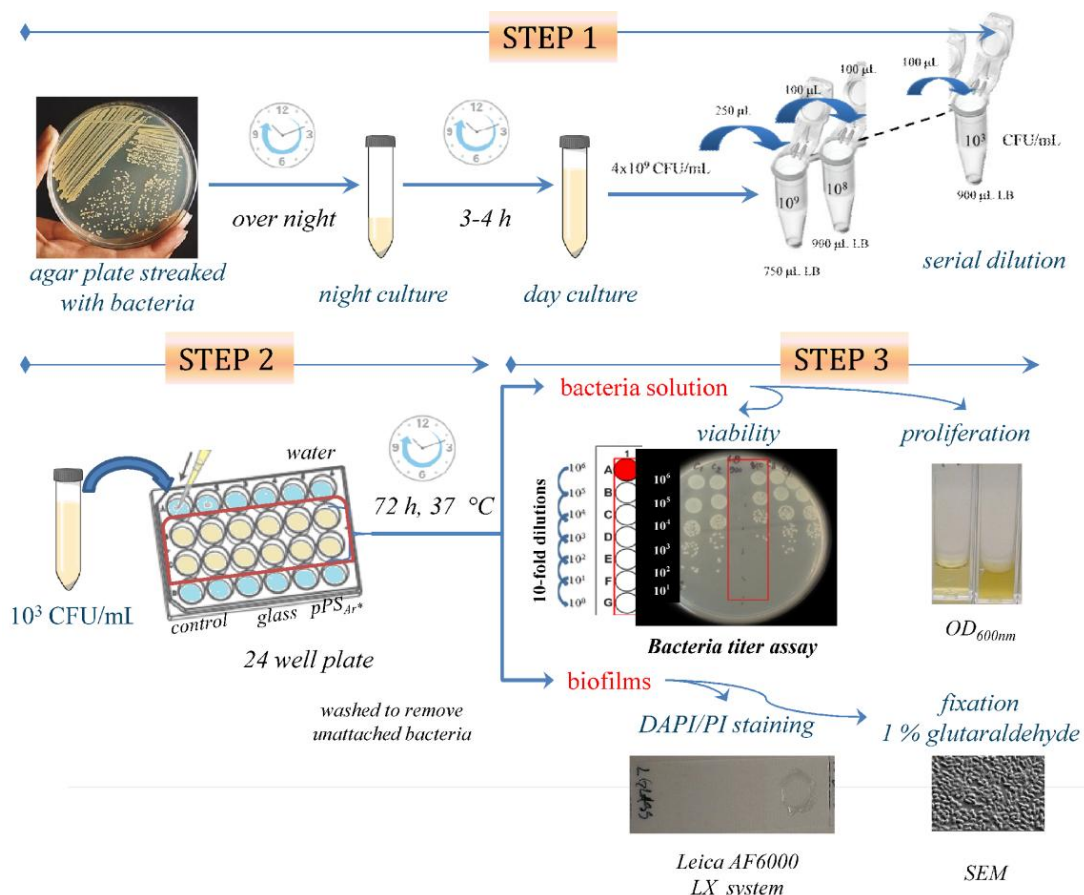


**Figure 32.** Schematic illustration of the experimental steps followed to assess the bactericidal effect of plasma polymerized styrene films.

## 4.3 ANTIBIOFOULING PROPERTIES OF PLASMA POLYMERIZED STYRENE FILM

### 4.3.2.1 Influence of surface properties on cell adhesion

#### A. Influence of surface properties on cell adhesion and viability

The *in vitro* cytotoxicity of pPS<sub>Ar</sub>\* coating with and without pre-incubation in DMEM demonstrated that the film is toxic for several types of eukaryotic cells, like HeLa (human cervical carcinoma), U-87 MG (human glioblastoma) and HEK-293 (human embryonic kidney) and non-toxic for HTP-1 (human monocyte type, non-adherent). As can be seen in **Figure 33**, in the case of adherent cells, after 72 h of incubation significant differences in the number of the adherent cells between glass and plasma coatings were observed. The low biocompatibility can be related to the coating solubility, topography and chemical composition.

It is known that the coating instability can affect protein adsorption and default cell adhesion. Initially, we supposed that the cells attached to the surface are removed with the oligomeric parts of the films in the cell medium, although the surface modification occurs quickly. In order to validate this hypothesis, we seeded cells on both as-deposited and 72 h DMEM pre-treated pPS<sub>Ar</sub>\* coatings. The results confirm that the adherent-cells are not able to attach and grow on both samples and the products leached from pPS matrix did not exhibit negative effects on non-adherent cell viability after 72 h of culture.

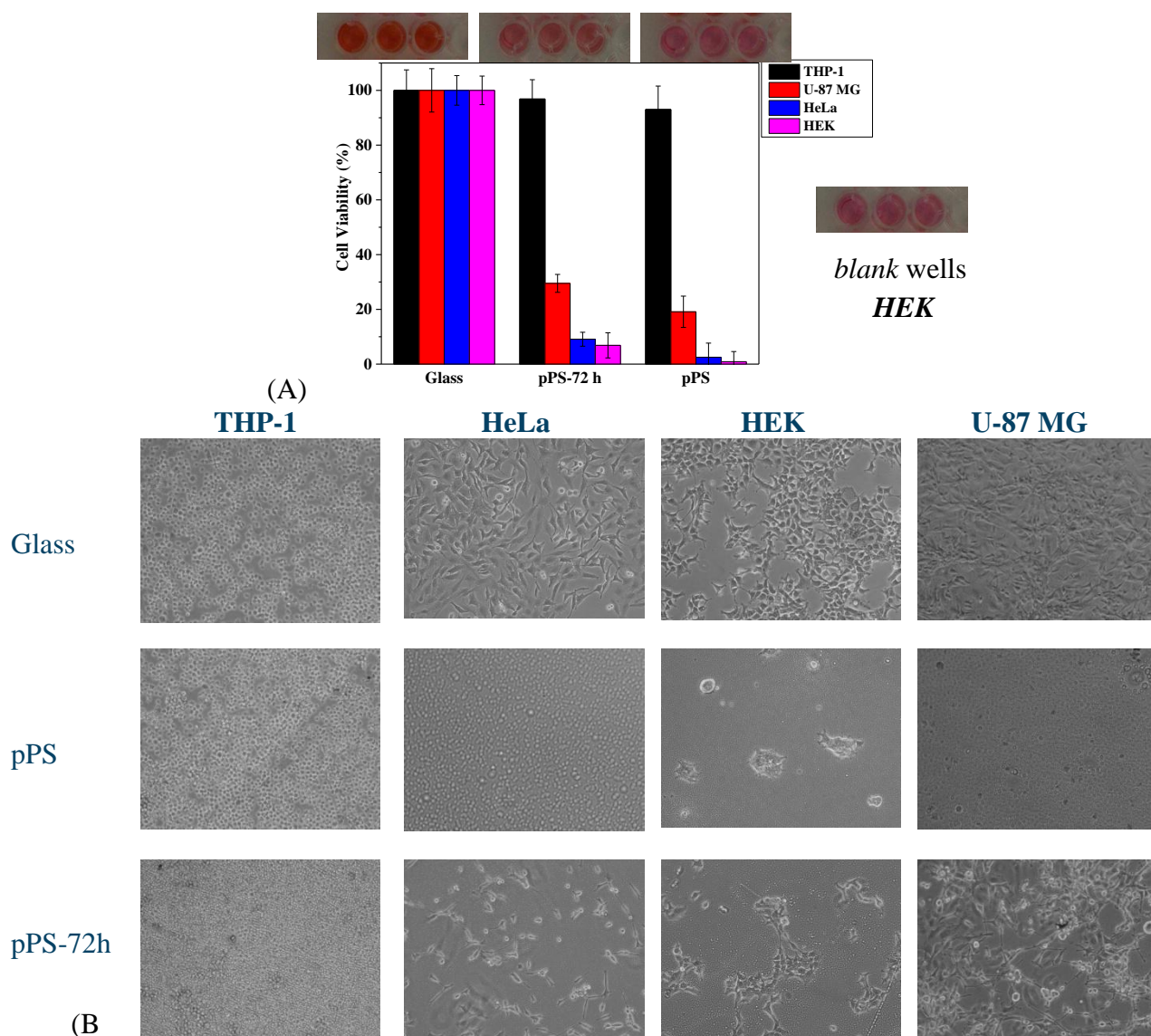


**Figure 33.** (A) Relative cell viability of THP-1 (non-adherent) and U-87 MG, HeLa and Caco-2 (adherent) cells, grown on glass, as deposited and DMEM pre-treated pPS<sub>Ar</sub>\* after 72 h of culture. (B) Phase contrast microscopy images (×10) of THP-1, HeLa, HEK and U-87 MG cells after seeding on glass, as deposited and DMEM pre-treated pPS<sub>Ar</sub>\* after 72 h of culture.

### B. Evaluation of cell adhesion on polydopamine-coated plasma polymerized styrene film

It is known that an alternative way to control the cell-material response and to reduce the surface cytotoxicity is the immobilization or grating of biomolecules, such as collagen, chitosan, gelatin or fibronectin or to deposit a biocompatible coating [127].

With the aim to understand if the cells' response is mediated by film chemical composition, we coated the pPS<sub>Ar</sub>\* surface with a polydopamine (PDA) layer. The biocompatibility of polydopamine layer is confirmed by various studies [128-130].

The PDA deposition was performed *via* self-polymerization of dopamine in alkaline pH. Briefly, the pPS films were immersed into a dopamine solution (2 mg/ml in 10 mM Tris-HCl buffer at pH 8.5) for 1 and 4 h at room temperature and then rinsed with distilled water to remove the unattached dopamine molecules (Figure 34). Lee *et al.* [131] reported that the PDA film thickness after 3 h of immersion is 10 nm and 50 nm after 24 h. The WCAs and FTIR measurements confirm the deposition of PDA layer (Figure 35).

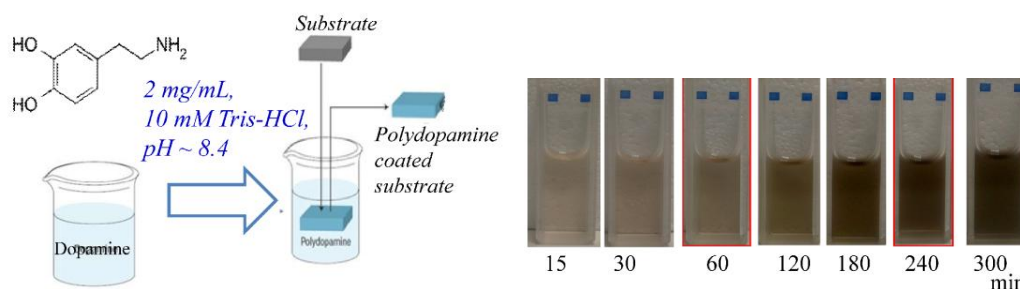


**Figure 34.** A schematic illustration of polydopamine thin film deposition and the color changes of solutions at different reaction times.

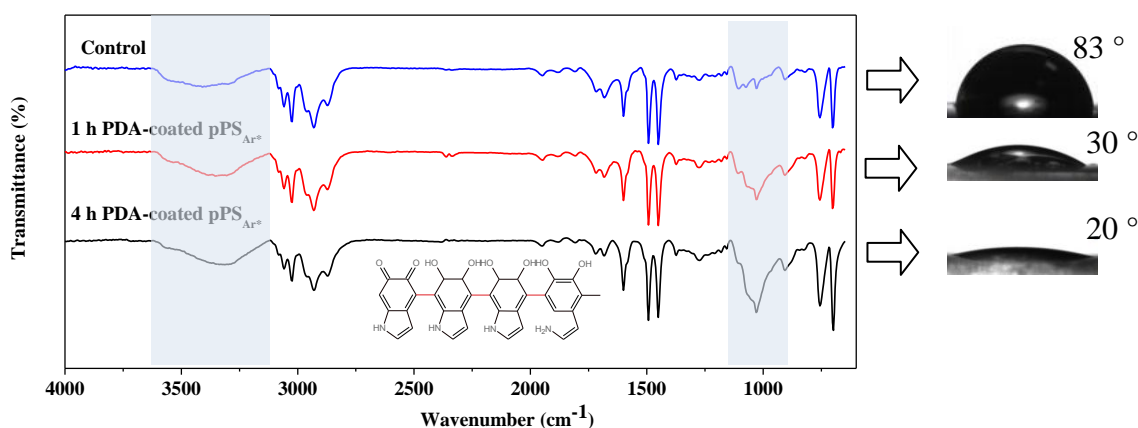


**Figure 35.** FTIR spectra of pPS<sub>Ar\*</sub> film before and after immersion in dopamine solution for 1 h and 4 h. The inset shows the theoretical polydopamine structure.

As seen in **Figure 36**, there is no significant difference in HEK cell viability between as-deposited and polydopamine-coated pPS<sub>Ar\*</sub> film. Consequently, the results confirm that the cell-repulsive properties of pPS<sub>Ar\*</sub> films are mediated mainly by surface topography. The presence of voids uniformly distributed on the entire pPS<sub>Ar\*</sub> surface with 2-5  $\mu\text{m}$  width and 30 - 50 nm depth prevents the attachment of mammalian cells.

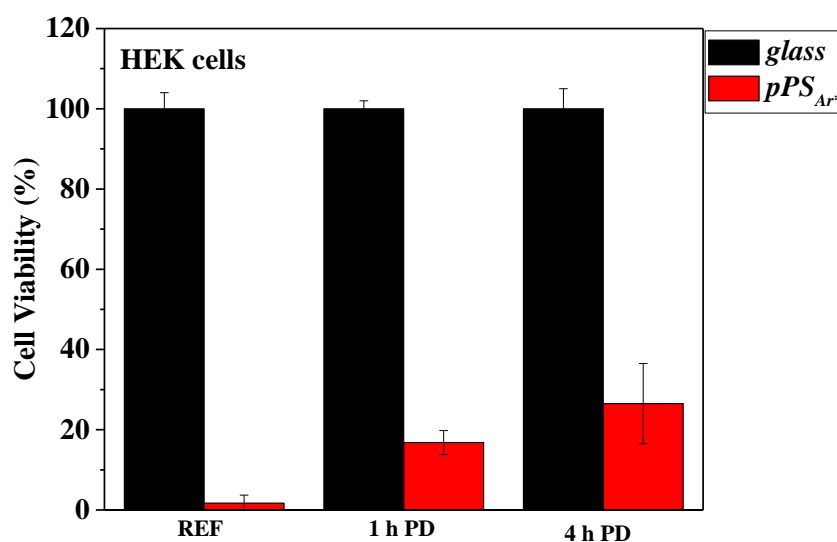


**Figure 36.** Relative cell viability of HEK cells, grown on glass, as-deposited and PDA-coated pPS<sub>Ar\*</sub> after 72 h of culture.



### 4.3.2 Antibacterial activity of plasma polymerized styrene films

*Escherichia coli* (*E. coli*) strain LF82 isolated from a patient with Crohn's disease (CD) was used to evaluate the antibiofouling properties of the pPS<sub>Ar\*</sub> films.

Crohn's disease is an inflammatory bowel disease characterized by a chronic transmural segmental and typically granulomatous inflammation of the intestine in humans. [132-134]

As seen in **Figure 37**, the adherent bacteria number on the plasma polymerized styrene film was significantly reduced compared to glass and polystyrene (commercial) surfaces. The *E. coli* cells seeded onto control surfaces are embedded in a thin film of extracellular polysaccharide matrix, which is stained in blue. By using Thioflavin S could be visualized the surrounding matrix of bacteria biofilm. Moreover, a large fraction of bacteria anchored on pPS<sub>Ar\*</sub> surfaces are dead (red).

We assume that the low fouling behavior of pPS<sub>Ar\*</sub> surface was determined by the presence of micro-topographical features of 2-5  $\mu\text{m}$  in width and 30 -50 nm in depth. A similar result was found by Ploux and co-workers [135], showing that bacteria are not able to attach on surfaces composed of a grooves succession with 1.6  $\mu\text{m}$  width and 40 nm depth. Also, Xu *et al.* [136] demonstrated that submicron surface textures, composed of ordered and uniform pillars with 400/400 nm and 500/500 nm pattern, inhibit *S. epidermidis* biofilm formation, due to the decrease in surface that bacteria can attach to.

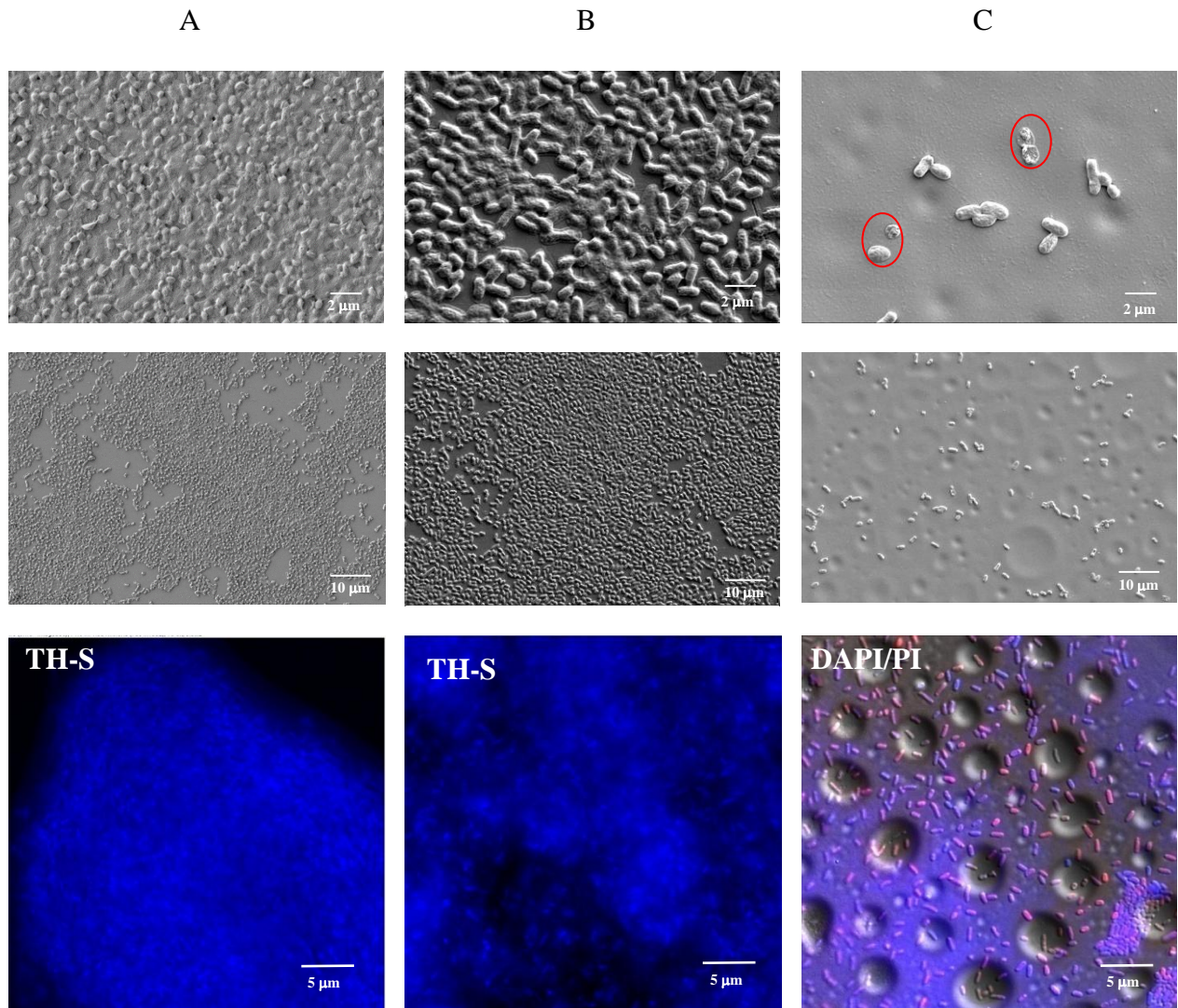


**Figure 37.** Scanning electron micrograph and epifluorescence microscopic images (bottom) of live(blue)/dead (red) *E. coli* species, stained with DAPI/PI and thioflavin S on (A) PS, (B) glass and (C) pPS<sub>Ar\*</sub> surfaces.

Furthermore, the activity of planktonic bacteria living in the near surrounding of the material is not affected, which correlated well with the result obtained for non-adherent cells (**Figure 38**).

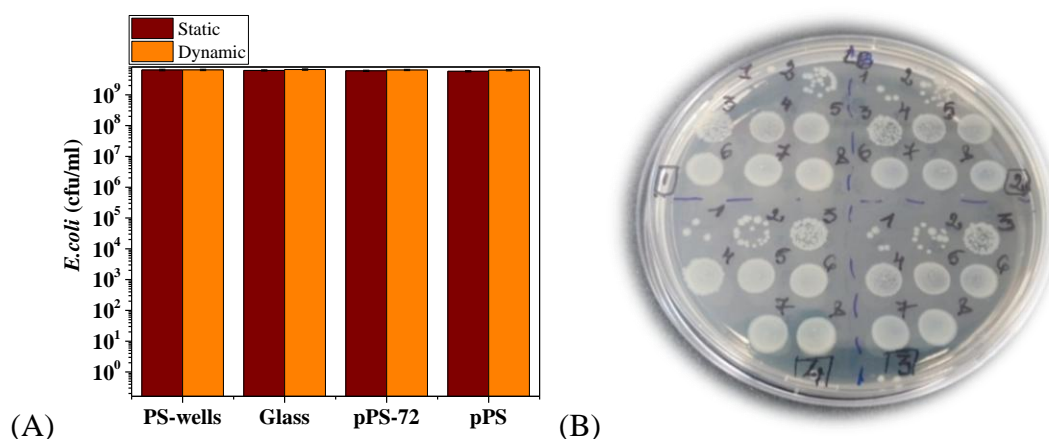


**Figure 38.** (A) Final concentration of *E. coli* in static and dynamic conditions for different samples. (B) Photographs of the *E. coli* colonies incubated on the solid medium with different treatments.

## CONCLUSIONS

Our results prove that the topography of plasma polymerized styrene film plays a significant role in mediating the attachment of eukaryotic and prokaryotic cells.

We assume that cell behavior onto pPS<sub>Ar\*</sub> surface is controlled by the interaction between surface and its surrounding environment, like DMEM or LB medium and then between cells and the micro-structured substrate.

The pPS micro-structured surface influences the adhesion and proliferation of mammalian cells and prevents *E. coli* bacteria adhesion and biofilm formation. In addition, the biological activity of non-adherent cells and planktonic bacteria living in the near surrounding of the coatings is not affected.

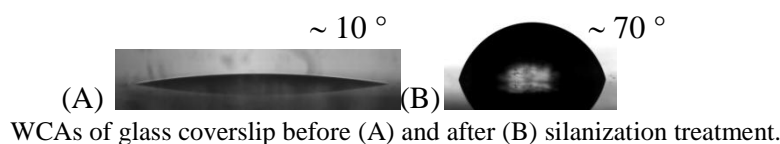
Therefore, the non-biocidal pPS coating can be useful in application where micro-organism colonization and biofilm formation is not desired, such as marine equipments or air filters.



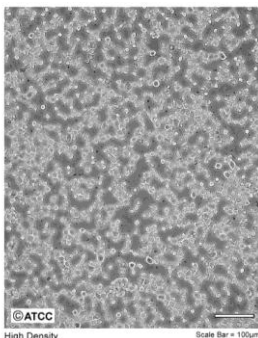
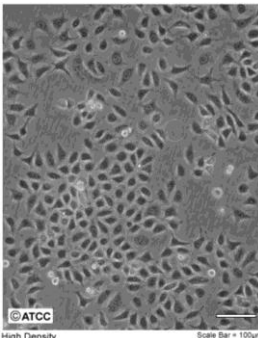
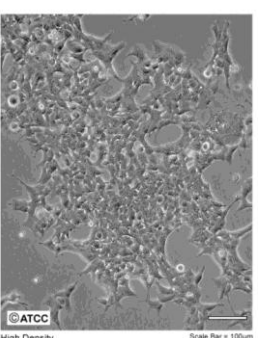
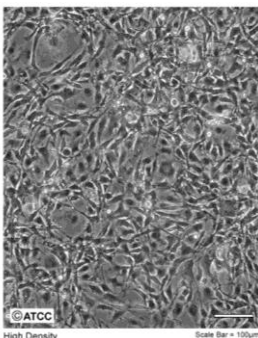
## Appendix

### I. Glass surface treatment with vinyltrimethoxysilane ( $C_2H_6Si$ )

The glass coverslips (12 mm) were rinsed with acetone, ethanol, Mili-Q water and dried in oven at 50 °C, followed by immersion in Piranha solution (mixture of sulfuric acid and hydrogen peroxide). Then the substrates were submerged into a 10 mM vinyltrimethoxysilane solution in toluene for 2 h at 85 °C. The excess of unreacted vinyltrimethoxysilane was removed by rinsing copiously with toluene.

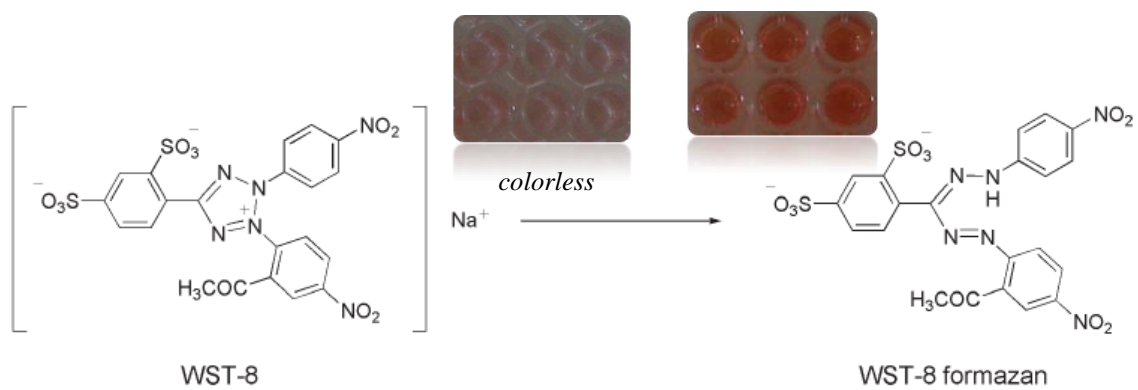


### II. Description of cell lines used in this study. ([lgcstandards-atcc.org](http://lgcstandards-atcc.org))

	THP-1	HeLa	HEK – 293	U-87 MG
				
Organism	Human	Human	Human	Human
Tissue	Peripheral blood	Cervix	Embryonic kidney	Brain
Cell type	Monocyte	Epithelial cell	Epithelial cell	Epithelial cell
Culture properties	Non-adherent	Adherent	Adherent	Adherent
Biosafety level	1	2	2	1
Disease	Acute monocytic leukemia	adenocarcinoma	-	Glioblastoma, astrocytoma
Age	1 year infant	31 years adult	Fetus	44 years
Gender	Male	Female	-	Male

### III. Cytotoxicity assay

**Cell Counting Kit-8** is sensitive colorimetric assay, used for the determination of the number of viable cells in cell proliferation and cytotoxicity assays. The WST-8 (2-(2-methoxy-4-nitrophenyl)-3-(4-nitrophenyl)-5-(2,4-disulphophenyl)-2H-tetrazolium, monosodium salt), highly water soluble tetrazolium salt, is reduced by dehydrogenases in cells to give an orange colored product (formazan), which is soluble in the culture medium. The number of the formazan dye generated by the activity of dehydrogenases in cells is directly proportional to the number of living cells. The absorbance at 450 nm is proportional to the viable cell number. The detection sensitivity of CCK-8 is higher than other tetrazolium salts such as MTT, XTT, MTS or WST-1. ([www.sigmaaldrich.com](http://www.sigmaaldrich.com))



Structure of WST-8 and WST-8 formazan.

## BIBLIOGRAPHY

1. Blaschek, H.P., et al., *Biofilms in the food environment*. 2015: John Wiley & Sons.
2. Cavallaro, A.A., et al., *Antibiofouling Properties of Plasma-Deposited Oxazoline-Based Thin Films*. ACS Applied Materials & Interfaces, 2016. **8**(10): p. 6354-6362.
3. Hasan, J., et al., *Antibacterial surfaces: the quest for a new generation of biomaterials*. Trends in Biotechnology, 2013. **31**(5): p. 295-304.
4. Sardella, E., et al., *Nano-Structured Cell-Adhesive and Cell-Repulsive Plasma-Deposited Coatings: Chemical and Topographical Effects on Keratinocyte Adhesion*. Plasma Processes and Polymers, 2008. **5**(6): p. 540-551.
5. Favia, P., et al., *Novel plasma processes for biomaterials: micro-scale patterning of biomedical polymers*. Surface and Coatings Technology, 2003. **169**: p. 707-711.
6. Sciarratta, V., et al., *Controlled Cell Attachment, Using Plasma Deposited Polymer Microstructures: A Novel Study of Cells-Substrate Interactions*. Plasma Processes and Polymers, 2006. **3**(6-7): p. 532-539.
7. Chan, Y.W., et al., *Plasma polymerized carvone as an antibacterial and biocompatible coating*. Materials Science and Engineering: C, 2016. **68**: p. 861-871.
8. Chang, Y.-B., et al., *A study on chitosan modification of polyester fabrics by atmospheric pressure plasma and its antibacterial effects*. Fibers and Polymers, 2008. **9**(3): p. 307-311.
9. Sophonvachiraporn, P., et al., *Surface characterization and antimicrobial activity of chitosan-deposited DBD plasma-modified woven PET surface*. Plasma Chemistry and Plasma Processing, 2011. **31**(1): p. 233-249.
10. Theapsak, S., et al., *Preparation of chitosan-coated polyethylene packaging films by DBD plasma treatment*. ACS Applied Materials & Interfaces, 2012. **4**(5): p. 2474-2482.
11. Karam, L., et al., *Study of nisin adsorption on plasma-treated polymer surfaces for setting up materials with antibacterial properties*. Reactive and Functional Polymers, 2013. **73**(11): p. 1473-1479.
12. Taheri, S., et al., *Antibacterial plasma polymer films conjugated with phospholipid encapsulated silver nanoparticles*. ACS Biomaterials Science & Engineering, 2015. **1**(12): p. 1278-1286.
13. Duday, D., et al., *Atmospheric pressure plasma modified surfaces for immobilization of antimicrobial nisin peptides*. Surface and Coatings Technology, 2013. **218**: p. 152-161.
14. Kostić, M., et al., *Silver-Loaded Cotton/Polyester Fabric Modified by Dielectric Barrier Discharge Treatment*. Plasma Processes and Polymers, 2009. **6**(1): p. 58-67.
15. Bittencourt, J.A., *Fundamentals of plasma physics*. 2004: Springer.
16. Ohring, M., *Materials science of thin films*. 2001: Academic press.
17. Attri, P., et al. *Influence of reactive species on the modification of biomolecules generated from the soft plasma*. Scientific Reports, 2015. **5**, 1-12.
18. Lackmann, J.-W., et al., *Inactivation of microbes and macromolecules by atmospheric-pressure plasma jets*. Applied Microbiology and Biotechnology, 2014. **98**(14): p. 6205-6213.
19. Osada, Y., *Plasma polymerization and plasma treatment of polymers. Review*. Polymer Science USSR, 1988. **30**(9): p. 1922-1941.
20. Goossens, O., et al., *Application of atmospheric pressure dielectric barrier discharges in deposition, cleaning and activation*. Surface and Coatings Technology, 2001. **142**: p. 474-481.
21. Stoffels, E., et al., *Cold atmospheric plasma: charged species and their interactions with cells and tissues*. IEEE Transactions on Plasma Science, 2008. **36**(4): p. 1441-1457.
22. Hensel, K., et al., *Effects of air transient spark discharge and helium plasma jet on water, bacteria, cells, and biomolecules*. Biointerphases, 2015. **10**(2): p. 029515.
23. Haertel, B., et al., *Non-thermal atmospheric-pressure plasma can influence cell adhesion molecules on HaCaT-keratinocytes*. Experimental Dermatology, 2011. **20**(3): p. 282-284.

24. Rusu, G., et al., *Effects of Atmospheric-Pressure Plasma Treatment on the Processes Involved in Fabrics Dyeing*. Plasma Chemistry and Plasma Processing, 2016. **36**(1): p. 341-354.
25. Kogoma, M., et al., *Raising of ozone formation efficiency in a homogeneous glow discharge plasma at atmospheric pressure*. Journal of Physics D: Applied Physics, 1994. **27**(9): p. 1985.
26. Mohammadi, B., et al., *Cold atmospheric plasma discharge induced fast decontamination of a wide range of organic compounds suitable for environmental applications*. Journal of Water Process Engineering, 2016. **9**: p. 195-200.
27. Topala, I., et al., *Considerations on the use of atmospheric pressure plasma to generate complex molecular environments with relevance for molecular astrophysics*. Proceedings ISPC 22 (2016).
28. Mihaila, I., et al., *Influence of discharge geometry on extraction of positive ion populations from atmospheric pressure plasmas*. Proceedings 32nd ICPIG (2016).
29. Mihaila, I., et al., *Formation of positive ions in hydrocarbon containing dielectric barrier discharge plasmas*. Advances in Space Research.
30. Massines, F., et al., *Atmospheric pressure low temperature direct plasma technology: status and challenges for thin film deposition*. Plasma Processes and Polymers, 2012. **9**(11-12): p. 1041-1073.
31. Bazaka, K., et al., *Plasma-assisted surface modification of organic biopolymers to prevent bacterial attachment*. Acta Biomaterialia, 2011. **7**(5): p. 2015-2028.
32. Haidopoulos, M., et al., *Morphology of polystyrene films deposited by RF plasma*. Journal of Microscopy, 2007. **228**(2): p. 227-239.
33. Schutze, A., et al., *The atmospheric-pressure plasma jet: a review and comparison to other plasma sources*. IEEE Transactions on Plasma Science, 1998. **26**(6): p. 1685-1694.
34. Luo, H., et al., *Plasma polymerization of styrene with carbon dioxide under glow discharge conditions*. Applied Surface Science, 2007. **253**(12): p. 5203-5207.
35. Vizireanu, S., et al., *Plasma techniques for nanostructured carbon materials synthesis. A case study: carbon nanowall growth by low pressure expanding RF plasma*. Plasma Sources Science and Technology, 2010. **19**(3): p. 034016.
36. Morent, R., et al., *Stability study of polyacrylic acid films plasma-polymerized on polypropylene substrates at medium pressure*. Applied Surface Science, 2010. **257**(2): p. 372-380.
37. Abbas, A., et al., *Covalent attachment of trypsin on plasma polymerized allylamine*. Colloids and Surfaces B: Biointerfaces, 2009. **73**(2): p. 315-324.
38. Beck, A.J., F.R. Jones, and R.D. Short, *Plasma copolymerization as a route to the fabrication of new surfaces with controlled amounts of specific chemical functionality*. Polymer, 1996. **37**(24): p. 5537-5539.
39. Gomez, L.M., et al. *Plasma copolymerization of ethylene glycol and allylamine*. in *Macromolecular symposia*. 2009. Wiley Online Library.
40. Asandulesa, M., et al., *Chemical Investigation on Various Aromatic Compounds Polymerization in Low Pressure Helium Plasma*. Plasma Chemistry and Plasma Processing, 2014. **34**(5): p. 1219-1232.
41. Ryan, M.E., *Mechanistic studies of plasma polymerization*. 1995, Durham University: PhD Thesis.
42. d'Agostino, R., et al., *Low-Temperature Plasma Processing of Materials: Past, Present, and Future*. Plasma Processes and Polymers, 2005. **2**(1): p. 7-15.
43. Merche, D., et al., *Atmospheric plasmas for thin film deposition: A critical review*. Thin Solid Films, 2012. **520**(13): p. 4219-4236.
44. Abbas, A., et al., *Preparation and multi-characterization of plasma polymerized allylamine films*. Plasma Processes and Polymers, 2009. **6**(9): p. 593-604.

45. Chen, M., et al., *Plasma polymerization of styrene with controlled particle energy*. Journal of Polymer Science Part A: Polymer Chemistry, 1998. **36**(8): p. 1265-1270.
46. Retzko, I., et al., *Chemical analysis of plasma-polymerized films: The application of X-ray photoelectron spectroscopy (XPS), X-ray absorption spectroscopy (NEXAFS) and Fourier transform infrared spectroscopy (FTIR)*. Journal of Electron Spectroscopy and Related Phenomena, 2001. **121**(1): p. 111-129.
47. Yasuda, H.K., *Some important aspects of plasma polymerization*. Plasma Processes and Polymers, 2005. **2**(4): p. 293-304.
48. Carton, O., et al., *Improvement of the Water Stability of Plasma Polymerized Acrylic Acid/MBA Coatings Deposited by Atmospheric Pressure Air Plasma Jet*. Plasma Chemistry and Plasma Processing, 2015. **35**(5): p. 819-829.
49. Kurosawa, S., et al., *Synthesis and Characterization of Microplasma-Polymerized Styrene and Propargyl Alcohol Films*. Journal of Photopolymer Science and Technology, 2005. **18**(2): p. 273-276.
50. Aizawa, H., et al., *On-demand fabrication of microplasma-polymerized styrene films using automatic motion controller*. Journal of Photopolymer Science and Technology, 2007. **20**(2): p. 215-220.
51. Merche, D., et al., *Synthesis of polystyrene thin films by means of an atmospheric-pressure plasma torch and a dielectric barrier discharge*. IEEE Transactions on Plasma Science, 2009. **37**(6): p. 951-960.
52. Dowling, D.P., et al., *Effect of surface wettability and topography on the adhesion of osteosarcoma cells on plasma-modified polystyrene*. Journal of Biomaterials Applications, 2010. **26**: p. 327-347.
53. Bell, A.T., *The mechanism and kinetics of plasma polymerization*, in *Plasma Chemistry III*. 1980, Springer. p. 43-68.
54. Vasilev, K., et al., *Tunable antibacterial coatings that support mammalian cell growth*. Nano Letters, 2009. **10**(1): p. 202-207.
55. Förch, R., et al., *Recent and Expected Roles of Plasma-Polymerized Films for Biomedical Applications*. Chemical Vapor Deposition, 2007. **13**(6-7): p. 280-294.
56. Chinn, J.A., et al., *Enhancement of serum fibronectin adsorption and the clonal plating efficiencies of Swiss mouse 3T3 fibroblast and MM14 mouse myoblast cells on polymer substrates modified by radiofrequency plasma deposition*. Journal of Colloid and Interface Science, 1989. **127**(1): p. 67-87.
57. Meyer, U., et al., *Basic reactions of osteoblasts on structured material surfaces*. European Cell Materials, 2005. **9**: p. 39-49.
58. Anselme, K., *Osteoblast adhesion on biomaterials*. Biomaterials, 2000. **21**(7): p. 667-681.
59. Tserepi, A., et al., *Plasma Nanotextured Polymeric Surfaces for Controlling Cell Attachment and Proliferation: A Short Review*. Plasma Chemistry and Plasma Processing, 2016. **36**(1): p. 107-120.
60. Griesser, H.J., et al., *Growth of human cells on plasma polymers: putative role of amine and amide groups*. Journal of Biomaterials Science, Polymer Edition, 1994. **5**(6): p. 531-554.
61. Teare, D., et al., *Effects of serum on the kinetics of CHO attachment to ultraviolet–ozone modified polystyrene surfaces*. Journal of Colloid and Interface Science, 2001. **234**(1): p. 84-89.
62. Dunne, W.M., *Bacterial adhesion: seen any good biofilms lately?* Clinical Microbiology Reviews, 2002. **15**(2): p. 155-166.
63. Marshall, K.C., *Planktonic versus sessile life of prokaryotes*, in *The prokaryotes*. 2006, Springer. p. 3-15.
64. Renner, L.D., et al., *Physicochemical regulation of biofilm formation*. MRS Bulletin/Materials Research Society, 2011. **36**(05): p. 347-355.

65. O'Toole, G., et al. , *Biofilm formation as microbial development*. Annual Reviews in Microbiology, 2000. **54**(1): p. 49-79.
66. Malzahn, K., et al., *Antimicrobial Activity and Cyto-Compatibility of Plasma Polymerized Zinc Acetylacetonate Thin Films*. Plasma Processes and Polymers, 2013. **10**(3): p. 243-249.
67. Vasilev, K., et al., *Antibacterial surfaces for biomedical devices*. Expert Review of Medical Devices, 2009. **6**(5): p. 553-567.
68. Banerjee, I., et al. , *Antifouling coatings: recent developments in the design of surfaces that prevent fouling by proteins, bacteria, and marine organisms*. Advanced Materials, 2011. **23**(6): p. 690-718.
69. Costerton, J.W., et al. , *Bacterial biofilms: a common cause of persistent infections*. Science, 1999. **284**(5418): p. 1318-1322.
70. Høiby, N., et al., *Antibiotic resistance of bacterial biofilms*. International Journal of Antimicrobial Agents, 2010. **35**(4): p. 322-332.
71. Hall-Stoodley, L., et al. , *Bacterial biofilms: from the natural environment to infectious diseases*. Nature Reviews Microbiology, 2004. **2**(2): p. 95-108.
72. Kanematsu, H. and D.M. Barry, *Biofilm and materials science*. 2015: Springer.
73. Bazaka, K., et al., *The effect of polyterpenol thin film surfaces on bacterial viability and adhesion*. Polymers, 2011. **3**(1): p. 388-404.
74. Donlan, R.M., *Biofilms: microbial life on surfaces*. Emerging Infectious Diseases, 2002. **8**(9): p. 881-890.
75. Ertel, S.I., et al., *Endothelial cell growth on oxygen-containing films deposited by radio-frequency plasmas: the role of surface carbonyl groups*. Journal of Biomaterials Science, Polymer Edition, 1992. **3**(2): p. 163-183.
76. Tidwell, C.D., et al., *Endothelial cell growth and protein adsorption on terminally functionalized, self-assembled monolayers of alkanethiolates on gold*. Langmuir, 1997. **13**(13): p. 3404-3413.
77. Sardella, E., et al., *Homogeneous and Micro-Patterned Plasma-Deposited PEO-Like Coatings for Biomedical Surfaces*. Plasma Processes and Polymers, 2004. **1**(1): p. 63-72.
78. Rosso, F., et al., *Adhesion and proliferation of fibroblasts on RF plasma-deposited nanostructured fluorocarbon coatings: Evidence of FAK activation*. Journal of Cellular Physiology, 2006. **207**(3): p. 636-643.
79. Gristina, R., et al., *Increasing cell adhesion on plasma deposited fluorocarbon coatings by changing the surface topography*. Journal of Biomedical Materials Research Part B: Applied Biomaterials, 2009. **88**(1): p. 139-149.
80. Di Mundo, R., et al., *Cell adhesion on nanotextured slippery superhydrophobic substrates*. Langmuir, 2011. **27**(8): p. 4914-4921.
81. Dalby, M., et al., *Rapid fibroblast adhesion to 27nm high polymer demixed nano-topography*. Biomaterials, 2004. **25**(1): p. 77-83.
82. Rebl, H., et al., *Impact of plasma chemistry versus titanium surface topography on osteoblast orientation*. Acta Biomaterialia, 2012. **8**(10): p. 3840-3851.
83. Cheng, Q., et al., *Plasma surface chemical treatment of electrospun poly (L-lactide) microfibrinous scaffolds for enhanced cell adhesion, growth, and infiltration*. Tissue Engineering Part A, 2013. **19**(9-10): p. 1188-1198.
84. Zhang, P., et al., *Designing Bioinspired Anti-Biofouling Surfaces based on a Superwettability Strategy*. Small, 2016, 10.1002/sml.201503334.
85. Ivanova, E.P., et al., *Natural bactericidal surfaces: mechanical rupture of Pseudomonas aeruginosa cells by cicada wings*. Small, 2012. **8**(16): p. 2489-2494.
86. Nikiforov, A., et al., *Non-thermal plasma technology for the development of antimicrobial surfaces: a review*. Journal of Physics D: Applied Physics, 2016. **49**(20): p. 204002-204009.



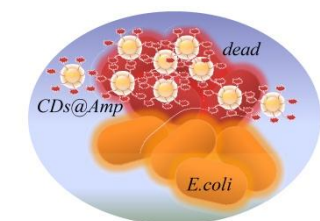
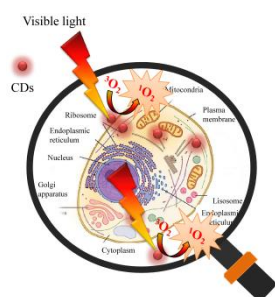
87. Wu, S., et al., *Plasma-modified biomaterials for self-antimicrobial applications*. ACS Applied Materials & Interfaces, 2011. **3**(8): p. 2851-2860.
88. Kenawy, E.-R., et al., *The chemistry and applications of antimicrobial polymers: a state-of-the-art review*. Biomacromolecules, 2007. **8**(5): p. 1359-1384.
89. Ramiasa, M., et al., *Plasma polymerised polyoxazoline thin films for biomedical applications*. Chemical Communications, 2015. **51**(20): p. 4279-4282.
90. Chan, Y.W., et al., *Plasma polymerized carvone as an antibacterial and biocompatible coating*. Materials Science and Engineering: C, 2016. **68**: p. 861-871.
91. Michl, T.D., et al., *Plasma polymerization of 1, 1, 1-trichloroethane yields a coating with robust antibacterial surface properties*. RSC Advances, 2014. **4**(52): p. 27604-27606.
92. Spange, S., et al., *Atmospheric pressure plasma CVD as a tool to functionalise wound dressings*. Journal of Materials Science: Materials in Medicine, 2015. **26**(2): p. 1-9.
93. Deng, X., et al., *Engineering of composite organosilicon thin films with embedded silver nanoparticles via atmospheric pressure plasma process for antibacterial activity*. Plasma Processes and Polymers, 2014. **11**(10): p. 921-930.
94. Deng, X., et al., *Antibacterial activity of nano-silver non-woven fabric prepared by atmospheric pressure plasma deposition*. Materials Letters, 2015. **149**: p. 95-99.
95. Kulaga, E., et al., *Effect of ageing and sterilization on plasma multilayer system*. Polymer Degradation and Stability, 2015. **116**: p. 1-13.
96. Ravve, A., *Principles of polymer chemistry*. 2013: Springer Science & Business Media.
97. Mielczarski, J., et al., *Modification of polystyrene surface in aqueous solutions*. Journal of Colloid and Interface Science, 2011. **362**(2): p. 532-539.
98. Oran, U., et al., *Surface analysis of plasma-deposited polymer films by Time of Flight Static Secondary Ion Mass Spectrometry (ToF-SSIMS) before and after exposure to ambient air*. Surface and Coatings Technology, 2005. **200**(1): p. 463-467.
99. Asandulesa, M., et al., *Chemically polymerization mechanism of aromatic compounds under atmospheric pressure plasma conditions*. Plasma Processes and Polymers, 2013. **10**(5): p. 469-480.
100. Fahmy, A., et al., *Surface and bulk structure of thin spin coated and plasma-polymerized polystyrene films*. Plasma Chemistry and Plasma Processing, 2012. **32**(4): p. 767-780.
101. Choudhury, A., et al. *Synthesis and characterization of plasma polymerized styrene films by rf discharge*. in *Journal of Physics: Conference Series*. 2010. IOP Publishing.
102. Topala, I., et al., *Hydrophobic coatings obtained in atmospheric pressure plasma*. IEEE Transactions on Plasma Science, 2009. **37**(6): p. 946-950.
103. Kim, J., et al., *The influence of CH<sub>4</sub> carrier gas in plasma polymerized styrene films*. Surface and Coatings Technology, 2004. **182**(1): p. 1-6.
104. Kinzig, B., et al., *Plasma-polymerized thin coatings from methyl-methacrylate, styrene and tetrafluoroethylene*. Surface Technology, 1981. **14**(1): p. 3-16.
105. Fahmy, A., et al., *Structure of Plasma-Deposited Copolymer Films Prepared from Acrylic Acid and Styrene: Part II Variation of the Comonomer Ratio*. Plasma Processes and Polymers, 2013. **10**(9): p. 750-760.
106. Li, Z., et al. *Styrene and methyl methacrylate copolymer synthesized by RF inductively coupled plasma*. in *Journal of physics: Conference series*. 2011. IOP Publishing.
107. Macgregor-Ramiasa, M.N., et al., *Properties and reactivity of polyoxazoline plasma polymer films*. Journal of Materials Chemistry B, 2015. **3**(30): p. 6327-6337.
108. Shao, X.-J., et al., *Comparative study on the atmospheric pressure plasma jets of helium and argon*. Applied Physics Letters, 2012. **101**(25): p. 253509.
109. McKay, K., et al., *Mass spectrometric diagnosis of an atmospheric pressure helium microplasma jet*. Journal of Physics D: Applied Physics, 2013. **46**(46): p. 464018.
110. Topala, I., et al., *Properties of the acrylic acid polymers obtained by atmospheric pressure plasma polymerization*. Nuclear Instruments and Methods in Physics Research Section B: Beam Interactions with Materials and Atoms, 2009. **267**(2): p. 442-445.

111. Gengenbach, T.R., et al., *Aging of 1, 3-diaminopropane plasma-deposited polymer films: Mechanisms and reaction pathways*. Journal of Polymer Science Part A: Polymer Chemistry, 1999. **37**(13): p. 2191-2206.
112. Boscher, N.D., et al., *Atmospheric Pressure Plasma Initiated Chemical Vapor Deposition Using Ultra-Short Square Pulse Dielectric Barrier Discharge*. Plasma Processes and Polymers, 2015. **12**(1): p. 66-74.
113. Rivas, B.L., et al., *Poly (styrene-alt-maleic acid)–metal complexes with divalent metal ions. synthesis, characterization, and physical properties*. Journal of Applied Polymer Science, 2001. **81**(6): p. 1310-1315.
114. Merche, D., et al., *Synthesis of polystyrene thin films by means of an atmospheric-pressure plasma torch and a dielectric barrier discharge*. IEEE Transactions on Plasma Science, 2009. **37**(6 PART 1): p. 951-960.
115. HaïDopoulos, M., et al., *Morphology of polystyrene films deposited by RF plasma*. Journal of Microscopy, 2007. **228**(2): p. 227-239.
116. Mielczarski, J.A., et al., *Modification of polystyrene surface in aqueous solutions*. Journal of Colloid and Interface Science, 2011. **362**(2): p. 532-539.
117. Abbas, A., et al., *Preparation and Multi-Characterization of Plasma Polymerized Allylamine Films*. Plasma Processes and Polymers, 2009. **6**(9): p. 593-604.
118. Daunton, C., et al., *Plasma parameter aspects in the fabrication of stable amine functionalized plasma polymer films*. Plasma Processes and Polymers, 2015. **12**(8): p. 817-826.
119. Lerouge, S., et al., *Nitrogen-Rich Plasma Polymer Coatings for Biomedical Applications: Stability, Mechanical Properties and Adhesion Under Dry and Wet Conditions*. Plasma Processes and Polymers, 2015. **12**(9): p. 882-895.
120. Manakhov, A., et al., *Deposition of stable amine coating onto polycaprolactone nanofibers by low pressure cyclopropylamine plasma polymerization*. Thin Solid Films, 2015. **581**: p. 7-13.
121. Manakhov, A., et al., *Optimization of cyclopropylamine plasma polymerization toward enhanced layer stability in contact with water*. Plasma Processes and Polymers, 2014. **11**(6): p. 532-544.
122. Michelmore, A., et al., *The link between mechanisms of deposition and the physico-chemical properties of plasma polymer films*. Soft Matter, 2013. **9**(26): p. 6167-6175.
123. Ruiz, J.C., et al., *Fabrication and Characterisation of Amine-Rich Organic Thin Films: Focus on Stability*. Plasma Processes and Polymers, 2010. **7**(9-10): p. 737-753.
124. Finke, B., et. al, *Structure retention and water stability of microwave plasma polymerized films from allylamine and acrylic acid*. Plasma Processes and Polymers, 2009. **6**(S1): p. S70-S74.
125. Vasilev, K., et al., *Solvent-induced porosity in ultrathin amine plasma polymer coatings*. The Journal of Physical Chemistry B, 2008. **112**(35): p. 10915-10921.
126. Rodríguez-Hernández, J., et al. *Honeycomb structured porous interfaces as templates for protein adhesion*. in *Journal of Physics: Conference Series*. 2010. IOP Publishing.
127. Jacobs, T., et al., *Plasma surface modification of biomedical polymers: influence on cell-material interaction*. Plasma Chemistry and Plasma Processing, 2012. **32**(5): p. 1039-1073.
128. Lynge, M.E., et al., *Polydopamine—a nature-inspired polymer coating for biomedical science*. Nanoscale, 2011. **3**(12): p. 4916-4928.
129. Ku, S.H., et al., *Spatial control of cell adhesion and patterning through mussel-inspired surface modification by polydopamine*. Langmuir, 2010. **26**(19): p. 15104-15108.
130. Liu, Y., et al., *Polydopamine and its derivative materials: synthesis and promising applications in energy, environmental, and biomedical fields*. Chemical Reviews, 2014. **114**(9): p. 5057-5115.

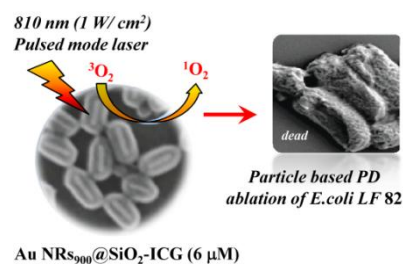
131. Lee, H., et al., *Mussel-inspired surface chemistry for multifunctional coatings*. Science, 2007. **318**(5849): p. 426-430.
132. Barnich, N., et al., *Adherent-invasive Escherichia coli and Crohn's disease*. Current opinion in gastroenterology, 2007. **23**(1): p. 16-20.
133. Glasser, A.-L., et al., *Adherent invasive Escherichia coli strains from patients with Crohn's disease survive and replicate within macrophages without inducing host cell death*. Infection and Immunity, 2001. **69**(9): p. 5529-5537.
134. Nickerson, K., et al., *Crohn's disease-associated adherent-invasive Escherichia coli adhesion is enhanced by exposure to the ubiquitous dietary polysaccharide maltodextrin*. PLoS One, 2012. **7**(12): p. e52132.
135. Ploux, L., et al., *Opposite responses of cells and bacteria to micro/nanopatterned surfaces prepared by pulsed plasma polymerization and UV-irradiation*. Langmuir, 2009. **25**(14): p. 8161-8169.
136. Xu, L.e.a., *Submicron-textured biomaterial surface reduces staphylococcal bacterial adhesion and biofilm formation*. Acta Biomaterialia, 2012. **8**(1): p. 72-81.

## ***PART II***

# ***Nanoparticles-based platforms for light-triggered anticancer and antibacterial activity, and for drug delivery***



***Enhanced antibacterial activity***



## INTRODUCTION

The increase of multidrug-resistant bacteria infections has become an important problem in modern healthcare that requires the development of new strategies for which pathogens will not be able to develop resistance. An attractive alternative to conventional antibiotics is the utilization of agents that cause physical or chemical damage to antimicrobial resistant strains under the influence of an external stimulus, such as light-responsive NPs. In recent years, photodynamic therapy (PDT) and photothermal therapy (PTT) have been established as alternative bactericidal methods to fight against infectious diseases [1-3]. PDT involves the combined use of a photosensitizer (PS), oxygen and a convenient light source to kill microorganisms. The advantage of antimicrobial PDT includes equal killing efficiency indifferent of antibiotic resistance, the repetition of therapy without cumulative toxicity and high spatial and focus control. The current applications of PDT are often limited by the PS issues, including poor water solubility, stability and selectivity, their tendency to aggregate under physiological conditions and excitation wavelength. Ideally, the absorption spectra of the PS overlap with the tissues optical window, where the penetration depth is optimal. Moreover, two-photon absorption-induced excitation of PS is another promising approach to increase light penetration. In the last years, considerable efforts have been devoted to the loading of PS onto nano-platforms in order to overcome their short-comings and to increase the singlet oxygen generation ( $^1\text{O}_2$ ). Among the different nanostructures investigated to improve the PDT efficiency, silica coated gold nanostructures are most promising candidates due to their remarkable optical properties, their surface versatility and biocompatibility. [4, 5]

In the first part, we demonstrated that near-infrared (NIR) plasmonic nanoparticles (Au nanorods), surrounded by an indocyanine green-embedded silica shell (Au NRs@SiO<sub>2</sub>-ICG) exhibit no cytotoxicity to HeLa and Caco 2 cells and show enhanced capacity to inactivate a virulent strain of *Escherichia coli* associated with Crohn's disease under 810 nm pulsed-mode laser irradiation. The results revealed that the amount of generated singlet oxygen is highly sensitive to the indocyanine green (ICG) concentration integrated to the silica shell and fine tuning of the plasmonic structures seems to increase even more the PDT efficiency. We achieved a 6 log<sub>10</sub> reduction in *E. coli* LF82 viability by using a low concentration of gold nanostructures displaying a plasmonic band at 900 nm, without any photothermal effects. It should be noted that 10<sup>6</sup> CFU/mL is a high bacterial concentration and such contamination rarely occurs. In addition, we observed a 3log<sub>10</sub> reduction of bacteria viability using Au NRs@SiO<sub>2</sub> without ICG, due to formation of reactive oxygen species (ROS) under two-photon irradiation. It is known that gold nanorods exhibit large two-photon absorption cross-sections, making them suitable for the generation of ROS. [6] We believe that this behavior is due to the physical disruption of the bacteria membrane through the impact of locally generated reactive oxygen species. [4, 5]

In summary, the particle-based photodynamic therapy combined with a pulsed laser in the NIR regions offers a new perspective for the treatment of bacterial infections, due to the increased penetration depth and high spatial resolution.

Initially, the nanoparticles (NPs) were developed to improve the pharmacokinetics of drugs, but due to their remarkable properties, the bio-medical applications of NPs increased significantly over the last years. Moreover, the NPs-based diagnostic or therapeutic products (e.g. Doxil®, Abraxane® or Feridex®) have been implemented into clinical practice. The research activity in this direction led to formation of a new field named as “*Nanomedicine*”, an interdisciplinary research area between materials science, physics, chemistry, biology and medicine.

Even though, the field of nanomedicine has experienced a huge progress in the last decades, the major challenge remains to design a single multifunctional nano-platform able to combine targeting, imaging and therapeutic functions for simultaneous detection/diagnosis and treatment of diseases, paving the avenue towards *personalized medicine*. [4, 5]

Till now, NPs have been synthesized from various building blocks (e.g. organic and inorganic materials) and synthetic routes. Iron oxide, quantum dots, carbon nanotubes, silica and gold nanoparticles are proposed for building up of NPs-based theranostics. A viable alternative might be functionalized carbon dots (CDs), due to their remarkable properties. In addition, the presence of functional groups on CDs surface allows the conjugation of various therapeutic agents (e.g. anticancer, antibacterial or antiviral agents). Further, the use of nano-sized carrier for the delivery of bioactive molecules is a promising approach, which might solve several limitations of the current drug delivery systems.

The second part of the study is focused on the synthesis, physico-chemical characterization and biological effects of carbon dots (CDs). Amino-functionalized CDs were synthesized by a simple hydrothermal treatment of citric acid and ethylenediamine. The low toxicity, excellent cell membrane permeability, high stability, solubility and fluorescence quantum yield suggest that the CDs are a promising alternative for biomedical applications. The *in vitro* results demonstrated the intrinsic theranostic application of CDs, as a non-toxic imaging probe and as a photodynamic agent, providing an effective approach to kill cancer cells. Moreover, the amino-functionalized CDs were used as a carrier for the delivery of ampicillin (Amp). The CDs@Amp conjugate integrates the fluorescence properties of CDs and the antibacterial function of ampicillin into a single unit. The *in vitro* results showed that CDs@Amp conjugate minimal inhibitory concentration was significantly reduced when compared to free ampicillin.

It has to be highlighted that only a few studies have reported the intrinsic theranostic application of CDs [7, 8] or have been focused on the development of CDs as nano-sized carriers for antibiotics delivery [9].



# CHAPTER 1. ANTIMICROBIAL PHOTODYNAMIC AND/OR PHOTOTHERMLA THERAPY

The increase of multi-drug resistant pathogens, followed by biofilm formation has become an important worldwide healthcare issue that requires the development of new antibacterial-based platforms to kill pathogens or to prevent bacteria adhesion and biofilm formation. It is estimated that approximately 60 % of nosocomial infections are determined by the multiple drug resistant bacteria (MDRB) [10]. Even third-generation antibiotics, like cephalosporins, are becoming ineffective to treat bacterial infections.

Recent advances in nanoscience and nanotechnology have contributed to the development of multifunctional nanoparticles with therapeutic, imaging and targeting properties. These composite nanoparticles have drawn considerable attention for selective labeling, detection and killing of bacteria. Therefore, an attractive alternative to conventional antibiotics is the utilization of agents that cause physical or chemical damage to antimicrobial resistant strains under the influence of an external stimulus, such as light-responsive NPs. In this context, photodynamic therapy (PDT) and photothermal therapy (PTT) are promising alternative bactericidal methods to fight against infectious diseases. In general, photo-based treatment of bacteria causes a physical disruption of the cell membrane and/or protein denaturation through oxidative reactions or local hypertermia, resulting in immediate cell lyses. Compared to Gram-positive bacteria, Gram-negative bacteria are more resistant to PDT due to their complex cell wall. [25] Thus, the additional outer membrane acts as a protective barrier, restricting the attachment PS molecules and reducing the effects of ROS species. Considerable efforts have been devoted to improve the selectivity of the PS for pathogens in order to avoid the damage of healthy cells.

## 1.1 FUNDAMENTAL AND APPLIED ASPECTS OF PHOTODYNAMIC THERAPY

Although initially the PDT efficiency was proved against micro-organisms, a great attention has been paid to the development and implementation of PDT as cancer treatment approach, as illustrated in **Figure 1.1**. In the recent years, due to remarkable results towards multidrug-resistant bacteria infections, PDT is proposed as an alternative antimicrobial therapy. Depending on the application domain, the antimicrobial PDT is known as photodynamic inactivation, lethal photosensitization, photoactivated disinfection or photodynamic antimicrobial chemotherapy.

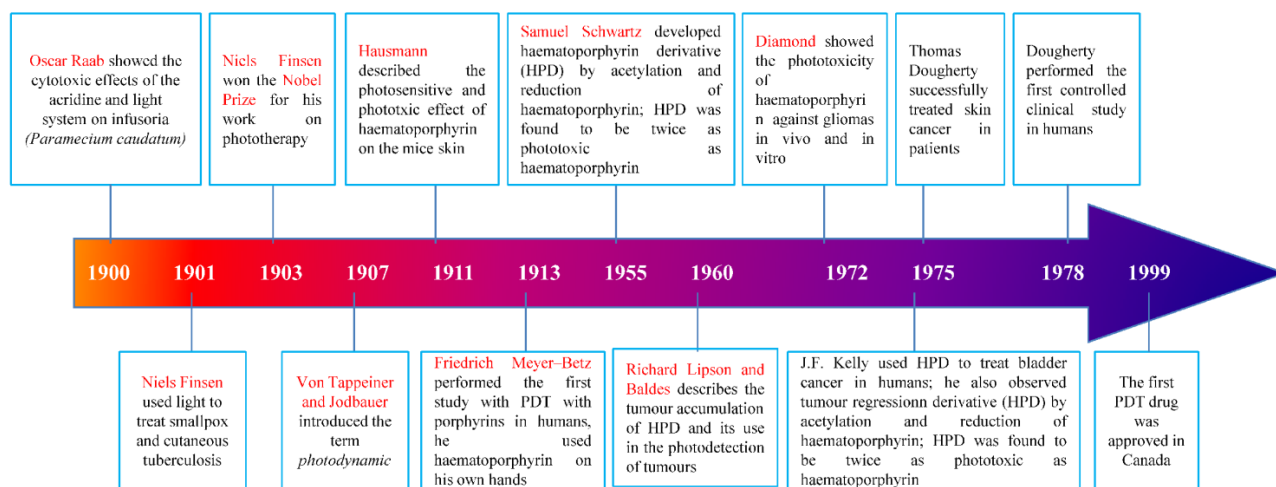


**Figure 1.1.** History of photodynamic therapy (PDT) [20].

The *in vivo* studies and clinical trials demonstrated the effectiveness of PDT to treat a wide range of infections, including skin infections (e.g. acne vulgaris [11-13], rosacea [14], erythrasma [15], cutaneous warts [16], leishmaniasis [17]), dental infections (e.g. periodontitis and endodontics) and gastric *Helicobacter Pylori* [18, 19]. For example, Ondine Biopharma (North America) is using methylene blue and 660 nm light for the treatment of periodontitis, HELBO® Photodynamic systems (Austria) and Denfotex (UK) are using toluidine blue O and 635 nm light to treat periodontitis, endodontics and/or caries.

The limitation of antimicrobial PDT is that it can be applied to treat localized infectious diseases and not systemic infections like bacteremia and sepsis. [2, 21-33]

### → Photophysics

Photodynamic therapy is based on the combined use of a photosensitizer (PS), oxygen and a convenient light source to induce cellular and tissue effects. The effects are mediated by various factors, including the physico-chemical properties and sub-cellular localization of the PS, the concentration of reactive oxygen species (ROS), the source intensity and wavelength and cell types.

Following the PS irradiation with light of specific wavelengths, usually visible or near-infrared, the PS is activated from a ground to an excited state. The ground state (known as singlet state) has two electrons with opposite spins, which after the absorption of photons one of these electrons is boosted into a high-energy orbital, keeping its spin. This is a short-lived (nanoseconds) species and it can lose its energy by emitting light (fluorescence) or through internal conversion into heat. The  $^1\text{PS}^*$  may undergo the intersystem crossing where the spin of the excited electron inverts (spin parallel) to form the relatively long-lived (microseconds) triplet excited states. The  $^3\text{PS}^*$  can relax to the ground state by emitting light (phosphorescent) or transferring energy to another molecule (e.g. to excite oxygen to its singlet state). These processes are illustrated in **Figure 1.2**. [20, 24, 33-35]

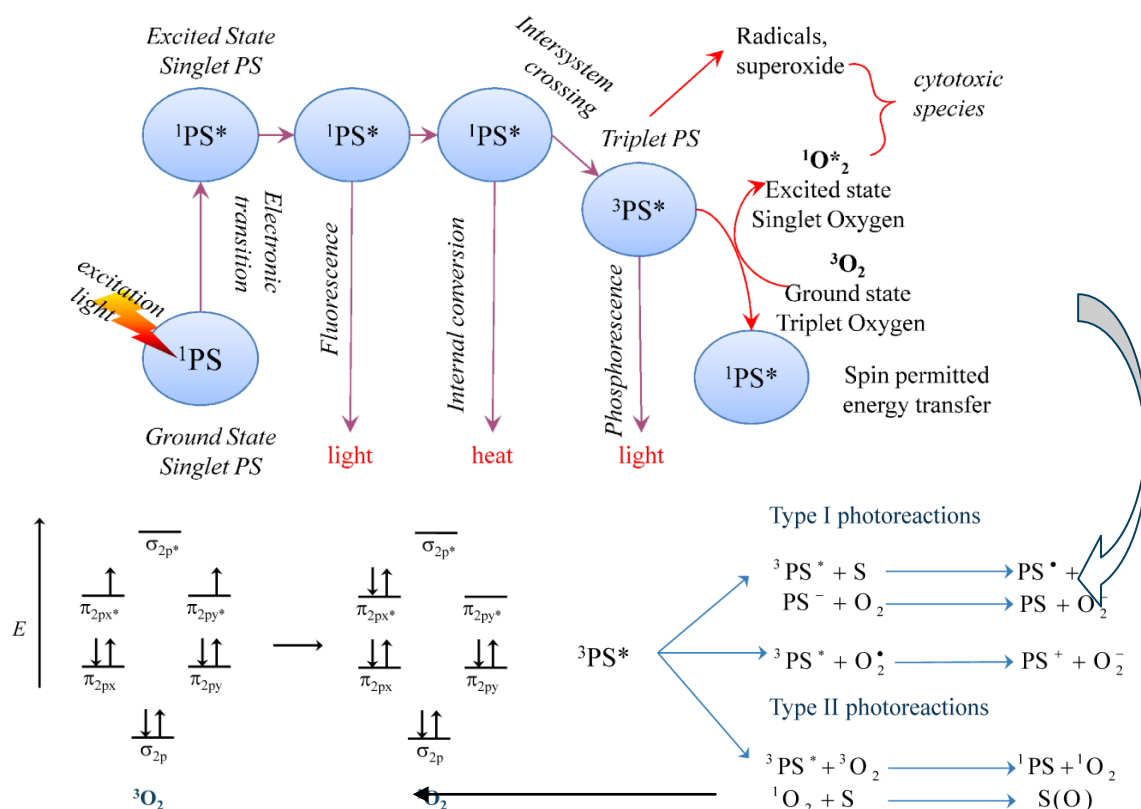


**Figure 1.2.** Photophysical and photochemical mechanisms of PDT, where  $^1\text{PS}$  is a PS in a singlet ground state,  $^3\text{PS}^*$  is a PS in a triplet excited state, S is a substrate molecule,  $\text{PS}^-$  is reduced PS,  $\text{S}^+/\text{PS}^+$  is an oxidized substrate/PS molecule, S(O) is an oxygen adduct of a substrate [33, 34].

### → *Photochemistry*

The PS triplet excited can undergo two kinds of photochemical reactions, which are known as Type I and Type II photoreactions (**Figure 1.2**).

In a Type I, the  $^3\text{PS}^*$  reacts directly with the biological substrates, such as cells membrane or biomolecules, leading to formation of radicals. Further, these radicals can react with oxygen to produce reactive oxygen species (ROS), including superoxide, hydroxyl and hydrogen peroxide radicals.

In a Type II reaction, the  $^3\text{PS}^*$  can transfer its energy to ground-state molecular oxygen ( $^3\text{O}_2$ ) to produce singlet oxygen ( $^1\text{O}_2$ ). The energy required to occurs the  $^3\text{O}_2 \rightarrow ^1\text{O}_2$  transition is 9 kJ/mol (22 kcal/mol), which corresponds to 1274 nm wavelength.

Both Type I and Type II photoreactions occur simultaneously and the ratio between these processes depends on the PS photo-chemical properties as well as the substrate and oxygen concentration. [20, 24, 33-35]

### → *Properties of singlet oxygen*

The amount of  $^1\text{O}_2$  generated by a PS is quantified by its quantum yield ( $\Phi_\Delta$ ). In general, each PS molecule can typically produce  $10^3$ - $10^5$   $^1\text{O}_2$  molecules before being degraded through photobleaching or by other processes. Singlet oxygen has a short half-life ( $< 40$  ns) and radius of the action ( $< 20$  nm) in biological systems, leading to a localized therapy. [24, 29, 34, 36]

### → *Types of photosensitizers (PSs)*

The PSs used in clinical practice are basically from three categories of porphyrins, chlorophylls and dyes. The current applications of PDT are limited by the PS issues. The ideal PS designed for biomedical applications should fulfill various properties, including low dark toxicity, selective accumulation in the interest area, water solubility, photostability and high absorption coefficient in the NIR spectral region. In addition, most of PSs produce fluorescence after light irradiation, which can be used for imaging and detection. The results revealed that the PDT reactivity is affected by “shelf-shield” (the tissue light penetration decrease due to the absorption of light by the PS molecules) and PS “photo-bleaching” (a photo-degradation of the PSs during the light exposure).[34, 35, 37, 38]

### → *Light source and wavelength*

The light source and the light delivery are two important aspects in PDT. In general, the selection of light source for PDT is imposed by PS optical properties. The light wavelength is selected to coincide with the maximum absorption wavelength of the PS. Both laser and lamps have been employed to carry out PDT treatment. Compared to lamps, laser produces highly coherent monochromatic light that can be efficiently delivered to the treatment site directly or through optical fiber. The dye lasers pumped by argon or metal vapor lasers, frequency-doubled Nd:YAG lasers, diode laser, light emitting diodes (LEDs) and femtosecond lasers have been used or investigated for PDT.

Currently approved photodynamic agents absorb in the visible spectral regions below 700 nm, limiting their application to treating surface and superficial lesions (**Figure 1.3 A**). As can be seen in **Figure 1.3 B**, the tissue optical window is in the near infrared spectral range (700-1100 nm). For this reason, there is a high interest for development of PS or PS-based nanoplatfroms absorbing in the NIR range. Naphthalocyanine (776 nm), bacteriochlorin (780 nm), indocyanine green (780 nm) and Alexa fluor (750 nm) are some photosensitizers falling into this category.

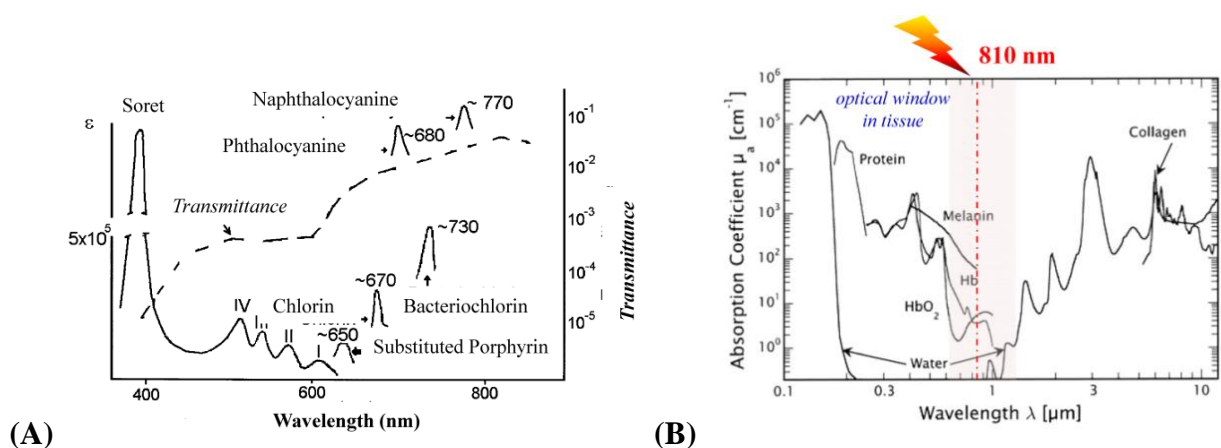


**Figure 1.3.** (A) Photosensitizer absorbance compared to tissue transmittance. (B) Absorption spectra of principal tissue chromophores in the human body [29, 36].

Two-photon absorption-induced excitation of PSs is another promising approach to increase light penetration. Femtosecond solid state laser is used for two-photon excitation. The laser emits a large number of photons during a very short pulse and the emitted photons are focused into a small volume. Compared with PS one-photon excitation that is a linear process, the PS two-photon excitation is a nonlinear process, in which two photons (NIR) are near-simultaneously absorbed ( $\tau = 10^{-16}$ s). The two photons have approximately half of the energy and double of the wavelength of the photon required for a single photon excitation (**Figure 1.4**). One photon excites the PS to a “virtual” intermediate state, while the second photon excites the PS to the excited state. For example, gold nanorods present a large two-photon absorption cross-section. [2, 3, 29, 33, 34, 38-41]

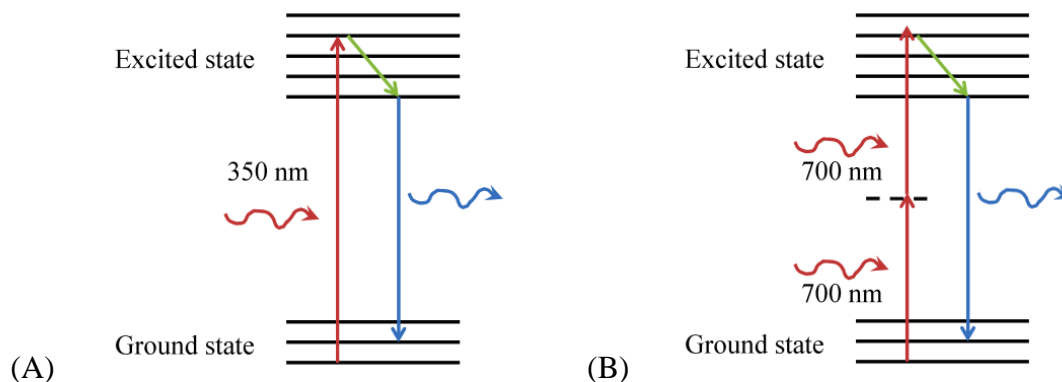


**Figure 1.4.** Simplified Jablonski diagram of (A) one and (B) two-photon absorption-induced excitation of a photosensitizer (PS) [42].

## 1.2. PARTICLE-BASED PHOTODYNAMIC AND/OR PHOTOTHERMAL TREATMENT OF BACTERIAL SUSPENSIONS

Over the last years, various published works have demonstrated the effectiveness of photodynamic and photothermal approaches based on the combination of nanostructures or PS-loaded onto nano-platforms with a convenient light source to kill micro-organisms, as can be observed in **Table 1.1**. In contrast to PDT which involves the combined use of a photosensitizer (PS), oxygen and a convenient light source to destroy pathogenic bacteria, PTT is based on the use of strong light-absorbing materials, which during laser/lamp exposure induce local hyperthermic effects. The hyperthermia induces irreversible cell damage by destroying cell membrane and denaturing proteins. [1, 43] For example, in this study [1], we demonstrated that the polyvinylpyrrolidone-coated Prussian blue nanoparticles (PVP/PB NPs) is an efficient photothermal agent able to inactivate both Gram-positive and Gram negative pathogens under 810 and 980 nm irradiation for 10 min. Moreover, a selective killing of pathogens over HeLa cells was obtained using a 980 nm CW laser and PVP/PB NPs concentration less than 50  $\mu\text{g/mL}$ . Huang *et al.* [44] demonstrated that vancomycin functionalized  $\text{Fe}_3\text{O}_4\text{@Au}$  nanoeggs are effective photothermal agents for the selective killing of pathogenic bacteria by irradiating them with NIR laser (808 nm, 250  $\text{mW cm}^{-2}$ , 3 min). Wu *et al* [46] proposed reduced graphene oxide functionalized with glutaraldehyde with embedded magnetic particles for the efficient capture and killing of both gram-positive *Staphylococcus aureus* and gram-negative *Escherichia coli* bacteria upon near-infrared (NIR) laser irradiation.

The various studies devoted to the design of nanoparticles-based platforms for light triggered antimicrobial activity, have proved that the PS  $^1\text{O}_2$  quantum yield is enhanced when the PS molecules are attached onto nano-platforms. According to Lucky *et al.* [41], the nanoparticles used in PDT can be classified into (1) carriers of PSs, (2) PSs by itself and (3) energy transducers of PS. In addition, the nanoparticles may be biodegradable (e.g. natural or synthetic polymer-based nanoparticles) and non-biodegradable (e.g. ceramic- and metal-based nanoparticles). Kuo *et al.* [24] demonstrated the eradication of methicillin-resistant *Staphylococcus aureus* (MRSA) by using toluidine blue modified gold nanorods (Au-PAA-TBO) *via* simultaneous photodynamic inactivation and hyperthermia. Khlebtsov *et al.* [26, 27] observed that the dual PD and PT properties of plasmonic nanoparticles surrounded by a hematoporphyrin-doped silica shell led to an enhanced photoinactivation of *Staphylococcus aureus* 209 P. Tomás *et al.* [28] showed that compared to free PS, the PS conjugated to gold nanoparticles displays enhanced antimicrobial efficiency. Moreover, they found a relationship between multifunctional nanoparticles concentration, irradiation time and bacteria viability. At a concentration of approximately 2 nM of SnCe6-glutathione/gold nanoparticle conjugates a 2  $\log_{10}$  reduction in the microorganisms viable count was observed. The free PS displayed a significant effect only at 50  $\mu\text{M}$  concentration. The capacity of vancomycin-conjugated multifunctional magnetic particles to target, capture and inactivate methicillin-sensitive *Staphylococcus aureus* under 510 nm irradiation was demonstrated by Choi *et al.* [25]. Strassert *et al.* [23] designed a nanoarchitecture based on zeolite L platform able to target, label and photoinactivate chloramphenicol resistant *Escherichia coli*. Turcheniuk *et al.* [21] demonstrated that gold nanorods coated with PEG-functionalized graphene oxide (rGO-PEG-AU NRs) is an effective and selective PT agent able to kill uropathogenic *E. coli* UTI 89 under 700 nm irradiation. Also, an enhanced photodynamic inactivation of the same *E. coli* strain could be achieved using plasmonic nanostructures, composed of silica coated nanorods with embedded verteporfin. Approximately 4  $\log_{10}$  reduction in the UTI 89 bacterial viable count was measured using 710 nm pulsed-laser irradiation for 30 min. In addition, the efficient photodynamic treatment of pathogenic bacteria was associated to the presence of verteporfin monomer and their good water solubility, the contribution of the plasmonic effects being minimal. [2]

**Table 1.1.** Summary of nanostructures-based photodynamic and/or photothermal treatment of bacterial suspensions.

Nanostructure	Bacteria	Conditions	Ablation efficiency	Ref.
PVP/PB NPs	<i>S. aureus</i> MRSA <i>E. coli</i> UTI89 ESBL <i>E. coli</i>	810 nm and/or 980 nm 1 W cm <sup>-2</sup> CW irradiation mode 10 min	6*log <sub>10</sub> for 50 µg/mL	Maaoui (2016) [1]
No nanostructures	<i>S. aureus</i>	809 nm	<i>S. aureus</i>	Topaloglu (2013)
ICG at different concentrations (0-150 µg mL <sup>-1</sup> )	<i>P. aeruginosa</i>	1.4 W cm <sup>-2</sup> 1-5 min	(100% at 4 µg mL <sup>-1</sup> ) <i>P. aeruginosa</i> (100% at 100-125 µg mL <sup>-1</sup> )	[47]
Au NP-tin chlorine e6	<i>S. aureus</i>	White light 10 min	2*log <sub>10</sub>	Tomas (2011) [28]
Au NRs or Au-Ag nanocages coated with hematoporphyrin-loaded silica shell	<i>S. aureus</i>	405, 625, 808 nm 70, 39, 100 mW cm <sup>-2</sup> (CW irradiation mode) 30 min	80-95 % (less at 808 nm)	Khlebtsov (2013) [26]
Vancomycin-conjugated magnetic particles modified with t-PtCP	Gram-negative Gram-positive	510 nm 6 mW cm <sup>-2</sup> 0-60 min vancomycin for targeting	6*log <sub>10</sub> in 5-60 min dependent on bacteria	Choi (2012) [25]
Zeolite L loaded with Van-FeDXP	<i>E. coli</i>	570-900 nm 3 mW cm <sup>-2</sup> 2.5 h	95 %	Strassert (2009) [23]
Van-Fe <sub>3</sub> O <sub>4</sub> @Au nanoeggs (PTT)	<i>S. pyogenes</i> <i>S. saprophyticus</i> <i>A. baumannii</i> <i>E. coli</i> O157:H7 <i>E. faecalis</i> <i>E. faecium</i> PDRAB MRSA	808 nm 250 mW m <sup>-2</sup> 3 min T <sub>f</sub> = 55 °C	< 1 %	Huang (2007) [44]
rGO-PEG-Au NRs (PTT)	<i>E. coli</i> UTI89	700 nm 4 and 8 W cm <sup>-2</sup> 10 min pulsed laser	6*log <sub>10</sub>	Turcheniuk (2015) [48]
Au NRS@SiO <sub>2</sub> -Verteporfin	<i>E. coli</i> UTI89	710 nm 1 W cm <sup>-2</sup> 20 min (CW and pulsed laser)	4*log <sub>10</sub>	Turcheniuk (2015) [2]
Au NRS@SiO <sub>2</sub> -ICG	<i>E. coli</i> UTI89	810 nm 1 W cm <sup>-2</sup> 60 min (pulsed laser)	6*log <sub>10</sub>	Jijie (2016) [3]

t-PTCP=5,5,15-bis(phenyl-10,20-bis(4-methoxycarbonylphenyl)-porphyrin] platinum; DXP = (N, N'-bis(2,6-dimethylphenyl) perylene-3,4,9,10-tetracarbondiimide)

In summary, antimicrobial photodynamic therapy involves the combined use of a photosensitizer, a convenient light source and oxygen to kill bacteria. In general, the PD activity is associated with cell membrane damage through oxidative reactions. The PDT is a complex approach that depends on various parameters that can influence treatment efficacy, including photosensitizers photo-chemical properties, light source characteristics (e.g. excitation wavelength, power density, CW and pulsed radiation) and oxygenation state of the tissues.



## BIBLIOGRAPHY

1. Maaoui, H., et al., *A 980nm driven photothermal ablation of virulent and antibiotic resistant Gram-positive and Gram-negative bacteria strains using Prussian blue nanoparticles*. Journal of Colloid and Interface Science, 2016. **480**: p. 63-68.
2. Turcheniuk, K., et al., *Highly effective photodynamic inactivation of E. coli using gold nanorods/SiO<sub>2</sub> core-shell nanostructures with embedded verteporfin*. Chemical Communications, 2015. **51**(91): p. 16365-16368.
3. Jijie, R., et al., *Particle-based photodynamic therapy based on indocyanine green modified plasmonic nanostructures for inactivation of a Crohn's disease-associated Escherichia coli strain*. Journal of Materials Chemistry B, 2016. **4**(15): p. 2598-2605.
4. Lee, D.-E., et al., *Multifunctional nanoparticles for multimodal imaging and theragnosis*. Chemical Society Reviews, 2012. **41**(7): p. 2656-2672.
5. Zhang, L., et al., *Nanoparticles in Medicine: Therapeutic Applications and Developments*. Clinical Pharmacology & Therapeutics, 2008. **83**(5): p. 761-769.
6. Zhao, T., et al., *Gold nanorods as dual photo-sensitizing and imaging agents for two-photon photodynamic therapy*. Nanoscale, 2012. **4**(24): p. 7712-7719.
7. Ge, J., et al., *Theranostics: Carbon Dots with Intrinsic Theranostic Properties for Bioimaging, Red-Light-Triggered Photodynamic/Photothermal Simultaneous Therapy In Vitro and In Vivo (Adv. Healthcare Mater. 6/2016)*. Advanced Healthcare Materials, 2016. **5**(6): p. 744-744.
8. Choi, Y., et al., *Highly biocompatible carbon nanodots for simultaneous bioimaging and targeted photodynamic therapy in vitro and in vivo*. Advanced Functional Materials, 2014. **24**(37): p. 5781-5789.
9. Krishna, A.S., et al., *Functionalized carbon dots enable simultaneous bone crack detection and drug deposition*. Journal of Materials Chemistry B, 2014. **2**(48): p. 8626-8632.
10. Ray, P.C., et al., *Nanomaterials for targeted detection and photothermal killing of bacteria*. Chemical Society Reviews, 2012. **41**(8): p. 3193-3209.
11. Hongcharu, W., et al., *Topical ALA-Photodynamic Therapy for the Treatment of Acne Vulgaris*. Journal of Investigative Dermatology, 2000. **115**(2): p. 183-192.
12. Wiegell, S., et al., *Photodynamic therapy of acne vulgaris using methyl aminolaevulinate: a blinded, randomized, controlled trial*. British Journal of Dermatology, 2006. **154**(5): p. 969-976.
13. Tuchin, V.V., et al., *A pilot study of ICG laser therapy of acne vulgaris: photodynamic and photothermolysis treatment*. Lasers in Surgery and Medicine, 2003. **33**(5): p. 296-310.
14. Bryld, L., et al., *Photodynamic therapy in a series of rosacea patients*. Journal of the European Academy of Dermatology and Venereology, 2007. **21**(9): p. 1199-1202.
15. Darras-Vercambre, S., et al., *Photodynamic action of red light for treatment of erythrasma: preliminary results*. Photodermatology, Photoimmunology & Photomedicine, 2006. **22**(3): p. 153-156.
16. Schroeter, C.A., et al., *Photodynamic Therapy: New Treatment for Therapy-Resistant Plantar Warts*. Dermatologic Surgery, 2005. **31**(1): p. 71-75.
17. Gonzalez, U., et al., *Interventions for old world cutaneous leishmaniasis (review)*. Cochrane Database Syst Rev, 2008. **4**: p. CD005067.
18. Wilder-Smith, C.H., et al., *Photoeradication of Helicobacter pylori using 5-aminolevulinic acid: Preliminary human studies*. Lasers in Surgery and Medicine, 2002. **31**(1): p. 18-22.
19. Hamblin, M.R., et al., *Helicobacter pylori accumulates photoactive porphyrins and is killed by visible light*. Antimicrobial Agents and Chemotherapy, 2005. **49**(7): p. 2822-2827.

20. Dolmans, D.E., et al., *Photodynamic therapy for cancer*. Nature Reviews Cancer, 2003. **3**(5): p. 380-387.
21. Turcheniuk, K., et al., *Plasmonic photothermal destruction of uropathogenic E. coli with reduced graphene oxide and core/shell nanocomposites of gold nanorods/reduced graphene oxide*. Journal of Materials Chemistry B, 2015. **3**(3): p. 375-386.
22. Robinson, J.T., et al., *Ultrasmall reduced graphene oxide with high near-infrared absorbance for photothermal therapy*. Journal of the American Chemical Society, 2011. **133**(17): p. 6825-6831.
23. Strassert, C.A., et al., *Photoactive Hybrid Nanomaterial for Targeting, Labeling, and Killing Antibiotic-Resistant Bacteria*. Angewandte Chemie International Edition, 2009. **48**(42): p. 7928-7931.
24. Kuo, W.-S., et al., *Antimicrobial gold nanorods with dual-modality photodynamic inactivation and hyperthermia*. Chemical Communications, 2009(32): p. 4853-4855.
25. Choi, K.-H., et al., *Photosensitizer and vancomycin-conjugated novel multifunctional magnetic particles as photoinactivation agents for selective killing of pathogenic bacteria*. Chemical Communications, 2012. **48**(38): p. 4591-4593.
26. Khlebtsov, B.N., et al., *Enhanced photoinactivation of Staphylococcus aureus with nanocomposites containing plasmonic particles and hematoporphyrin*. Journal of Biophotonics, 2013. **6**(4): p. 338-351.
27. Khlebtsov, N., et al., *Analytical and theranostic applications of gold nanoparticles and multifunctional nanocomposites*. Theranostics, 2013. **3**(3): p. 167-80.
28. Gil-Tomas, J., et al., *Lethal photosensitisation of bacteria using a tin chlorin e6-glutathione-gold nanoparticle conjugate*. Journal of Materials Chemistry, 2011. **21**(12): p. 4189-4196.
29. Chatterjee, D.K., et al., *Nanoparticles in photodynamic therapy: an emerging paradigm*. Advanced Drug Delivery Reviews, 2008. **60**(15): p. 1627-1637.
30. Hamblin, M.R., et al., *Photodynamic therapy: a new antimicrobial approach to infectious disease?* Photochemical & Photobiological Sciences, 2004. **3**(5): p. 436-450.
31. Dai, T., et al., *Photodynamic therapy for localized infections—State of the art*. Photodiagnosis and Photodynamic Therapy, 2009. **6**(3-4): p. 170-188.
32. Kharkwal, G.B., et al., *Photodynamic therapy for infections: clinical applications*. Lasers in Surgery and Medicine, 2011. **43**(7): p. 755-767.
33. Macdonald, I.J., et al., *Basic principles of photodynamic therapy*. Journal of Porphyrins and Phthalocyanines, 2001. **5**(02): p. 105-129.
34. Castano, A.P., et al., *Mechanisms in photodynamic therapy: part one—photosensitizers, photochemistry and cellular localization*. Photodiagnosis and Photodynamic Therapy, 2004. **1**(4): p. 279-293.
35. Barras, A., et al., *Hypericin-loaded lipid nanocapsules for photodynamic cancer therapy in vitro*. Nanoscale, 2013. **5**(21): p. 10562-10572.
36. DeRosa, M.C., et al., *Photosensitized singlet oxygen and its applications*. Coordination Chemistry Reviews, 2002. **233**: p. 351-371.
37. Castano, A., et al., *Mechanisms in photodynamic therapy: part one—photosensitizers, photochemistry and cellular localization*. Photodiagnosis and Photodynamic Therapy, 2004. **1**(4): p. 279-293.
38. Couleaud, P., et al., *Silica-based nanoparticles for photodynamic therapy applications*. Nanoscale, 2010. **2**(7): p. 1083-1095.
39. Brancalion, L., et al., *Laser and Non-laser Light Sources for Photodynamic Therapy*. Lasers in Medical Science, 2002. **17**(3): p. 173-186.
40. Croissant, J.G., et al., *Multifunctional Gold-Mesoporous Silica Nanocomposites for Enhanced Two-Photon Imaging and Therapy of Cancer Cells*. Frontiers in Molecular Biosciences, 2016. **3**, 10.3389/fmolb.2016.00001.

41. Lucky, S.S., K.C. Soo, and Y. Zhang, *Nanoparticles in Photodynamic Therapy*. Chemical Reviews, 2015. **115**(4): p. 1990-2042.
42. Mulligan, S.J., et al., *Two-photon fluorescence microscopy: basic principles, advantages and risks*. Modern Research and Educational Topics in Microscopy. Formatex, 2007.
43. Huang, X., et al., *Plasmonic photothermal therapy (PPTT) using gold nanoparticles*. Lasers in Medical Science, 2008. **23**(3): p. 217-228.
44. Huang, W.-C., et al., *Functional gold nanoparticles as photothermal agents for selective-killing of pathogenic bacteria*, Nanomedicine (Lond), 2007, **2**(6): p. 777-787.
45. Akhavan, O., et al., *Graphene nanomesh promises extremely efficient in vivo photothermal therapy*. Small, 2013. **9**(21): p. 3593-3601.
46. Wu, M.-C., et al., *Graphene-based photothermal agent for rapid and effective killing of bacteria*. ACS Nano, 2013. **7**(2): p. 1281-1290.
47. Topaloglu, N., M. Gulsoy, and S. Yuksel, *Antimicrobial photodynamic therapy of resistant bacterial strains by indocyanine green and 809-nm diode laser*. Photomedicine and Laser Surgery, 2013. **31**(4): p. 155-162.
48. Turcheniuk, K., et al., *Plasmonic photothermal destruction of uropathogenic E. coli with reduced graphene oxide and core/shell nanocomposites of gold nanorods/reduced graphene oxide*. Journal of Materials Chemistry B, 2015. **3**(3): p. 375-386.

## CHAPTER 2. PHOTODYNAMIC INACTIVATION OF *ESCHERICHIA COLI* USING PLASMONIC NANOSTRUCTURES LOADED WITH INDOCYANINE GREEN

In this study, we investigated the efficiency of gold nanorods (Au NRs) coated with indocyanine green (ICG)-loaded silica shell (Au NRs@SiO<sub>2</sub>-ICG) for the photodynamic ablation of a Crohn's disease-associated adherent-invasive *Escherichia coli* strain LF 82 under 810 nm pulsed-mode and CW laser irradiation (**Figure 2.1**). By using gold nanostructures displaying a plasmonic band at 900 nm, at low concentration to avoid any photothermal effects, we achieved a 6 log<sub>10</sub> reduction in *E. coli* LF82 viability. The amount of generated singlet oxygen was found to be highly sensitive to the indocyanine green (ICG) concentration integrated to the silica shell and fine tuning of the plasmonic structures seems to increase even more the PDT efficiency.

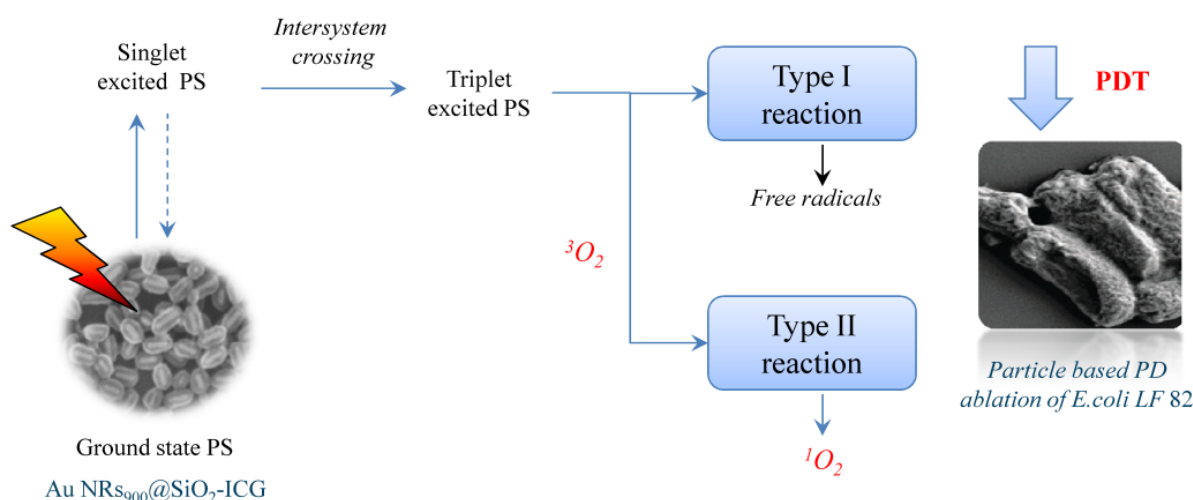


**Figure 2.1.** Particle-based photodynamic ablation of Crohn's disease-associated *E. coli* LF 82 using indocyanine green loaded plasmonic nanostructures.

### 2.1 GOLD NANO-PARTICLES: properties and applications

Gold nanospheres were first observed by Faraday and Philos in 1857. Gold nanorods were first synthesized electrochemically by Martin using oxide film templates and then by Wang using surfactant directed electrochemical growth. Later Murphy and El-Sayed optimized the surfactant-directed method for solution-phase growth, commonly used now. [1]

To date, a wide range of gold nanoparticles (GNPs) have been developed and tested in various biomedical applications, including genomics and immunoassays, bio-imaging and bio-sensing, detection and photodynamic therapy (PDT) of pathogenic micro-organisms [2, 3], detection and hyperthermia of cancer cells and tumors [4], targeted delivery of drugs [2], peptides, DNA and antigens (**Figure 2.2**). The gold and/or gold-based hybrid materials have received increased attention due to their remarkable optical and surface chemical properties. Their optical properties are highly size, shape and structure-dependent and arise from the surface plasmon resonance (SPR), a phenomenon in which free electrons collectively oscillate and scatter or absorb the incident electromagnetic wave. It is known that the plasmon resonance band of an Au nanorod can be tuned by changing its aspect ratio (length divided by width).

Considerable efforts have been devoted to synthesize GNPs that absorb light in the near infrared (NIR) region, where optical transmission through tissues and physiological fluids is optimal. In this context, gold nanorods (Au NRs) are of particular interest due to the flexibility in tuning the longitudinal band to the near-infrared region. Gold nanorods have two plasmon

absorption bands, the transverse and longitudinal plasmon band, corresponding to light absorption and scattering along the short or long particle axis. [5]

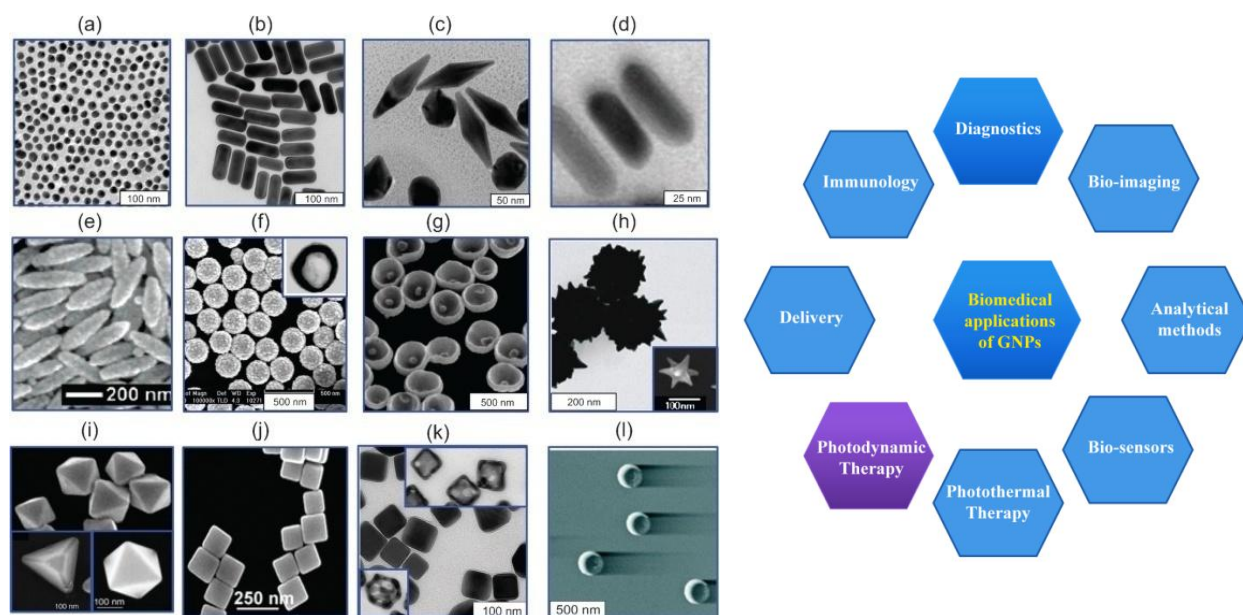


**Figure 2.2.** The various types of plasmon-resonant nanoparticles and their possible biomedical applications: (a) nanospheres (510 – 570 nm), (b) Au nanorods (650-1200 nm), (c) Au bipyramids (650 – 1100 nm), (d) Au nanorods surrounded by Ag nanoshells (550-1000 nm), (e) Au-coated  $\text{Fe}_2\text{O}_3$  nanorods (1100-1300 nm), (f)  $\text{SiO}_2/\text{Au}$  nanoshells (600-1100 nm), (g) nanobowls with bottom cores (560 -1000), (h) spiky  $\text{SiO}_2/\text{Au}$  nanoshells (600-850 nm), (i) Au tetrahedra, octahedra and cubooctahedra (550-750 nm), (j) Au nanocubes (500-700 nm), (k) Ag nanocubes and Au-Ag nanocages (450-1000), (l) Au nanocrescents (980 – 2600 nm) [6].

Compared with the available dye molecules, gold nanoparticles are photo-stable and have absorption cross-sections 5-7 orders of magnitude higher than that of dyes. [1]

Various studies proved that gold nanoparticles may be used for selective labeling and detection, monitoring the change in the optical signal after the attachment of bacteria to the nanoparticles surfaces. [7][5, 8, 9]

In recent years more and more results have proved the Au NRs efficient conversion of photon energy into heat, allowing the photothermal destruction of cancer cells, tumors and bacteria. [4, 10-12] The first study concerning the killing of *S. aureus in vitro* using a combination of pulsed laser energy and nanoparticles selectively attached to the bacterium was reported by Zharov *et al.* [13] in 2006. Wang *et al.* [14] demonstrated selective photothermal killing of *Salmonella* bacteria using bioconjugated oval-shaped gold nanoparticles.

Moreover, a large number of studies showed that the PS  $^1\text{O}_2$  quantum yield can be enhanced by attaching the PS molecules to gold NP surface, particularly when localized surface plasmon resonance bands of gold nanorods are in resonance with the PS absorption band, proving that the gold-based hybrid materials are promising nanoplatforms for loading of PS for enhanced photodynamic therapy (Table 1.1). Kuo *et al.* [15] first demonstrated the inactivation of pathogenic bacteria through combined PDT and PTT.

Therefore, Au NPs alone can be used as PT agent and loaded with PS they can serve as PD and/or PT therapeutic agents to kill cells. [1, 2, 4, 6, 16-18]



## 2.2 EXPERIMENTAL DETAILS

### 2.2.1 Chemicals

Cetyl trimethylammonium bromide (CTAB), silver nitrate ( $\text{AgNO}_3$ ), hydrogen tetrachloroaurate(III) trihydrate ( $\text{HAuCl}_4 \times 3\text{H}_2\text{O}$ ), tetraethylorthosilicate (TEOS), ascorbic acid, sodium hydroxide ( $\text{NaOH}$ ), indocyanine green (ICG), 9,10-anthracenediylbis(methylene)dimalonic acid (ABDA) and sodium borohydride ( $\text{NaBH}_4$ ) were purchased from Sigma-Aldrich and used as received.

### 2.2.2 Synthesis of gold nanorods (Au NRs)

Au NRs were synthesized according to a seed-mediated, surfactant-assisted procedure adapted from the works of El-Sayed [19] and Murphy [20] and co-workers. Seed solution was prepared by mixing  $\text{HAuCl}_4$  (10 mM, 125  $\mu\text{L}$ ) with an aqueous solution of CTAB (0.2 M, 5 mL). To this solution was added ice-cold  $\text{NaBH}_4$  (0.01 M) and the solution was stirred for 5 min. The resulting seed solution became brownish yellow, and aged for 5 min at room temperature before use.

For the growth solution, 85 or 95  $\mu\text{L}$  of the seed solution were added to 10 mM  $\text{AgNO}_3$  and 500  $\mu\text{L}$  of  $\text{HAuCl}_4$  (10 mM) and mixed with 5 mL of water and 5 mL of CTAB (0.2 mM) solution in order to synthesize Au NRs with longitudinal plasmons at 800 and 900 nm, respectively. The solution was acidified to pH 3-4 with 200  $\mu\text{L}$  of 1%  $\text{HCl}$ , then 60  $\mu\text{L}$  of 0.1 M ascorbic acid solution was added. Finally, 48  $\mu\text{L}$  of seeds was injected into the growth solution. The reaction was performed at 25 °C without stirring. The excess of CTAB surfactant was discarded from the final product by centrifugation at 10,000 rpm for 30 min and then the precipitate was re-dispersed in 10 mL of DI water to yield Au NRs at a concentration of 10 nM. The concentration was derived spectrophotometrically from the extinction coefficient determined at 800 and 900 nm longitudinal plasmons to be  $4.8 \times 10^9$  and  $6.2 \times 10^9 \text{ M}^{-1} \text{ cm}^{-1}$ , respectively.

### 2.2.3 Synthesis of Au NRs@SiO<sub>2</sub> particles

To a solution of as-prepared 10 nM Au NRs (1 mL in DI water), 187  $\mu\text{L}$  of 20 mM tetraethoxysilane (TEOS) solution in ethanol was added. The reaction was run in a 2 mL plastic Eppendorf due to a strong interaction of glassware with TEOS. The pH of the solution was adjusted to 10 by means of 10 mM  $\text{NaOH}$ . Next, vigorous stirring of horizontally placed Eppendorf (belly dancer, 300 rpm) for 24 h at 23°C was performed to properly grow the silica layer over CTAB coated Au NRs. Importantly, the concentration of CTAB prior to silica coating was carefully controlled to be precisely 1 mM. The excess of the reagents as well as simultaneously formed empty silica particles have been separated from Au NRs@SiO<sub>2</sub> by means of centrifugation (8000 rpm, 30 min). Supernatant was carefully removed and the pellet was re-dispersed in 1 mL of DI water to give 5 nM AuNRs@SiO<sub>2</sub> with a silica shell of  $20 \pm 3$  nm in thickness.

### 2.2.4 Loading of Au NRs@SiO<sub>2</sub> particles with indocyanine green (ICG)

To a solution of 5 nM Au NRs@SiO<sub>2</sub> (1 mL in DI water) was added 5  $\mu\text{L}$  or 20  $\mu\text{L}$  of ICG (100  $\mu\text{M}$  in water +10 % DMSO). The reaction mixture was stirred for 20 h at room temperature. The formed Au NRs@SiO<sub>2</sub>-ICG nanocomposite was purified by means of centrifugation (8000 rcf, 15 min) and re-dispersed in distilled water. The supernatant was used to determine the residual ICG concentration spectrophotometrically.

### 2.2.5 Characterization techniques of Au NRs@SiO<sub>2</sub> and Au NRs@SiO<sub>2</sub>-ICG particles

**UV Vis spectroscopic measurements** were carried out using a Perkin Elmer Lambda UV/Vis 950 dual-beam spectrophotometer operating at a resolution of 1 nm. The UV-Vis spectra were recorded I quartz cuvettes of path length 1 cm between 200 and 1100 nm.



**Emission fluorescence spectra** were recorded between 730 and 900 nm using a Cary Eclipse spectrometer (Agilent, France). Solutions were excited with 720 nm (excitation and emission slit: 5 nm, scan rate: 600 nm/min).

**Zeta-potential measurements** were performed using a Zeta-sizer Nano-ZS (Malvern Instruments Inc. Worcestershire, UK). Nanomaterials were diluted to 10 µg/mL and measured in Milli-Q water at pH 7.0.

**Scanning electron microscopy (SEM)** images were obtained using an electron microscope ULTRA 55 (Zeiss, France) equipped with a thermal field emission emitter and three different detectors (BSE detector with filter grid, high efficiency in-lens SE detector and Everhart-Thornley secondary electron detector). The sample was prepared by casting a concentrated aqueous solution of the material onto silicon substrate followed by drying at 100 °C for 1 h. SEM images of pathogens (covered with 5 nm platinum) were observed using a Zeiss Compact Merlin instrument and a secondary electron detector at 2 kV under high vacuum.

#### 2.2.6 Singlet oxygen ( $^1\text{O}_2$ ) detection

Singlet oxygen generation was monitored through the chemical oxidation of an aqueous solution of 9,10-anthracenediylbis (methylene)dimalonic acid (ABDA) (10 µM) in presence of ICG (6 µM), AuNRs@SiO<sub>2</sub> (200 pM) or Au NRs@SiO<sub>2</sub>-ICG (200 pM). The decrease in the ABDA absorbance at 262 nm was monitored under irradiation at 810 nm (1 W cm<sup>-2</sup>) using a continuous laser (CW, unmodelocked MIRA-900, France) or a femtosecond pulsed titanium:sapphire laser (Chameleon model, Coherent) that delivers 100 fs pulses at a repetition rate of 80 MHz. The laser beam was focused onto a cuvette (1 cm path length and 2 mm width) containing 1 mL of solution. Irradiation was stopped at several time intervals (at 1, 2, 5, 10, 20 and 30 min) and absorption spectra were recorded.

#### 2.2.7 The *in vitro* cytotoxicity study

The HeLa cell line derived from cervical carcinoma from a 31 year old female [ATCC® CCL-2™, ECACC, Sigma Aldrich, Saint-Quentin Fallavier, France] and Caco-2 cell line derived from colorectal adenocarcinoma from a 72 year old man [ATCC® HTB-37™] were cultured and maintained in Dulbecco's Modified Eagle's medium (DMEM, Gibco®) supplemented with 10 % fetal bovine serum (FBS, Gibco®) and 1 % penicillin-streptomycin (Gibco®) in a humidified incubator at 37 °C and 5 % CO<sub>2</sub>. Cells were seeded at a density of 10<sup>4</sup> cells/well in a 96-well plate and grown for 24 h before assay. The culture medium was replaced with a fresh medium containing nanoparticles. After 24 h, the old medium was aspirated and cells were washed three times with PBS. The cell viability was evaluated using Cell Counting Kit-8 (CCK-8, Sigma Aldrich) assay. Briefly, 10 µL of the CCK-8 solution were added to each well containing 100 µL of DMEM with 10% FBS and the plate was incubated for 3 h in the humidified incubator. The absorbance of each well at 450 nm was measured using a microplate reader (PHERAstar FS, BMG LABTECH GmbH, Germany). Each condition was replicated five times and the mean absorbance value of non-exposed cells was taken as 100 % cellular viability.

#### 2.2.8 Photodynamic ablation of bacteria solutions

**Bacteria growth.** A single *E. coli* colony from LB agar plate was inoculated overnight in LB (Luria-Bertani) medium at 37 °C with moderate shaking. The pre-culture was diluted 50-fold and allowed to continue for another 3 - 4 h, until the OD<sub>600 nm</sub> had reached 0.6-1.

**Bacterial assay.** In a total volume of 100 µL in 96-wells plate, bacteria (10<sup>6</sup> cfu/mL) have been mixed with the corresponding testing compounds in a sterile PBS. Both irradiated and non-irradiated controls have been created (3 wells per condition). The laser beam diameter was adjusted exactly to the square of the well to be ~ 0.3 cm<sup>2</sup>. Wells were irradiated for 30 and 60 min at 1 W cm<sup>-2</sup>. The conditions of the experiment are constructed in a way to complete the treatment within 2 h to prevent long exposure of bacteria to PBS solution.

Bacteria titer assay was used to determine the residual concentration of bacteria in wells. To perform a titer assay, 10-fold dilutions of a bacteria stock  $10^6$  cfu mL<sup>-1</sup> are prepared, and 10  $\mu$ L aliquots are dropped on the LB agar. After an incubation period of 20 h at 37 °C in a conventional thermostat, colonies were counted.

### 2.2.9 Measurements of the photothermal effect

All irradiations were performed in standard 96-well plates. The temperature changes were captured by an Infrared Camera (Thermovision A40) and treated using ThermoCam Researcher Pro 2.9 software. A femtosecond pulsed titanium:sapphire laser (Chameleon model, Coherent) that delivers 100 fs pulses at a repetition rate of 80 MHz was used for the photothermal experiments. A telescope with a magnification of 4.3 is used to roughly adapt the beam diameter to the wells' one.

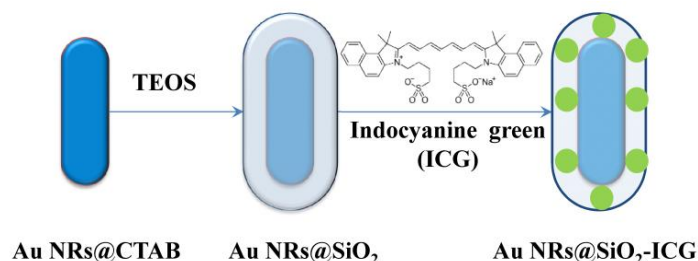
## 2.3 RESULTS AND DISCUSSION

### 2.3.1 Chemical and structural characterization of Au nanorods coated an indocyanine green-embedded silica shell

#### → Plasmonic nanostructures loaded with indocyanine green

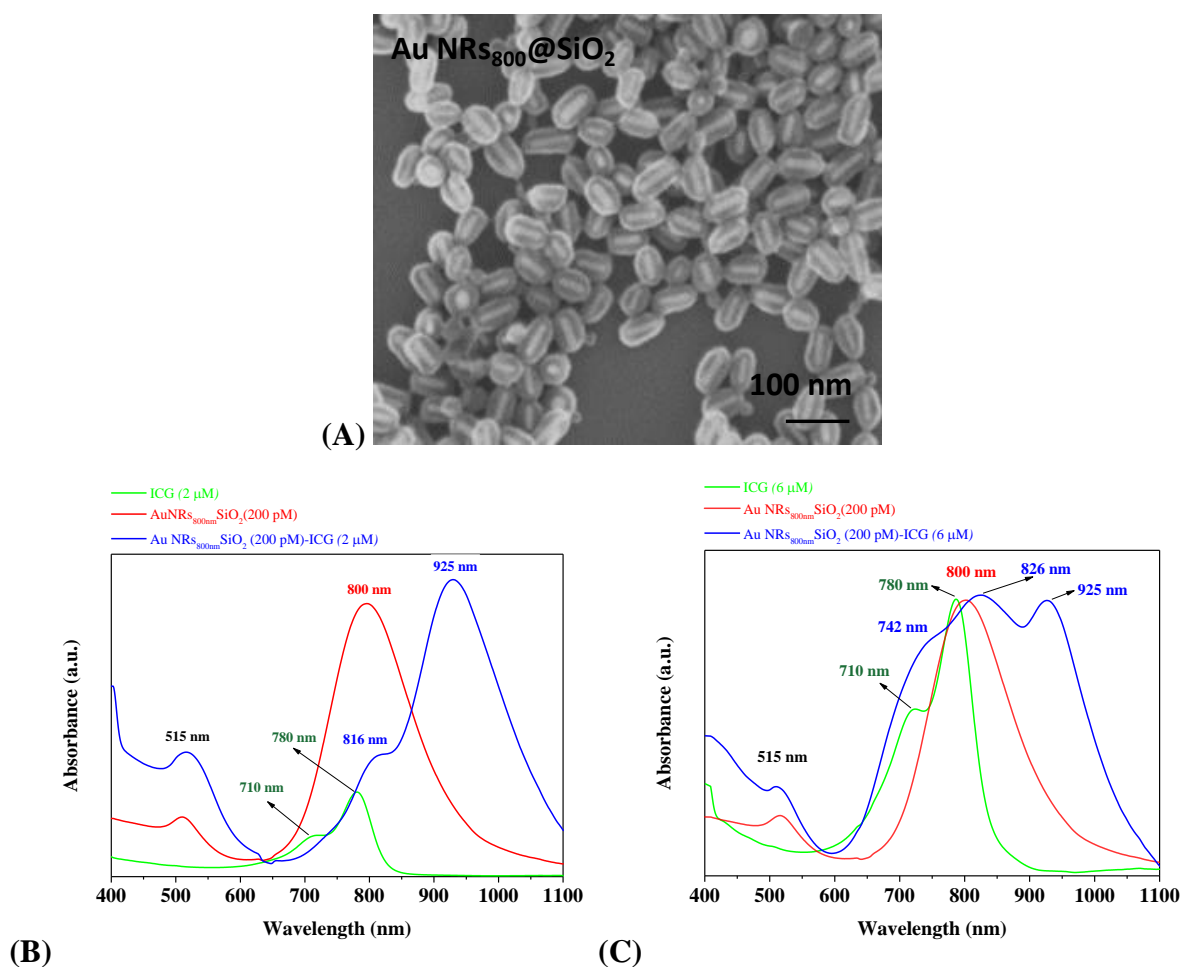
Indocyanine green (ICG) was selected in this study as a PS model, in order to develop a multifunctional biocompatible Au NRs@SiO<sub>2</sub>-ICG as an efficient photodynamic agent. ICG is a water soluble anionic PS approved by FDA (Food and Drug Administration) as imaging and diagnostic agent to observe cardiac output, hepatic function, determining burn depth and blood volume. As can be observed in **Figure 2.7**, the ICG absorbs and emits in the NIR region, being an important motivation for using it in biological applications. For example, ICG-mediated PDT and PTT is widely used to treat tumors, like pancreatic, lung, skin, colonic and breast tumors, and for treatment of acne vulgaris. Its applicability is limited by its poor aqueous and thermal stability, low quantum yield and rapid blood clearance. Therefore, the encapsulation of ICG into nano-platforms may overcome these short-comings. [21-28]

Gold nanorods coated with ICG-loaded silica shells (Au NRs@SiO<sub>2</sub>-ICG) were synthesized in three steps, as shown schematically in **Figure 2.3**. First, Au NRs were synthesized according to a seed-mediated, surfactant-assisted procedure adapted from Gorlelikov and Matsuura studies [2, 29]. The Au NRs surface was covered with a silica shell, based on the hydrolysis of tetraethoxysilane under basic conditions to solve the cytotoxicity limitation of cetyltrimethylammonium bromide (CTAB), used as surfactant during Au NRs synthesis. In addition, the synthetic conditions were adjusted to obtain Au NRs@SiO<sub>2</sub> nanostructures with a plasmonic band at around 800 or 900 nm.



**Figure 2.3.** Schematic representation of the synthesis of Au NRs@SiO<sub>2</sub>-ICG.

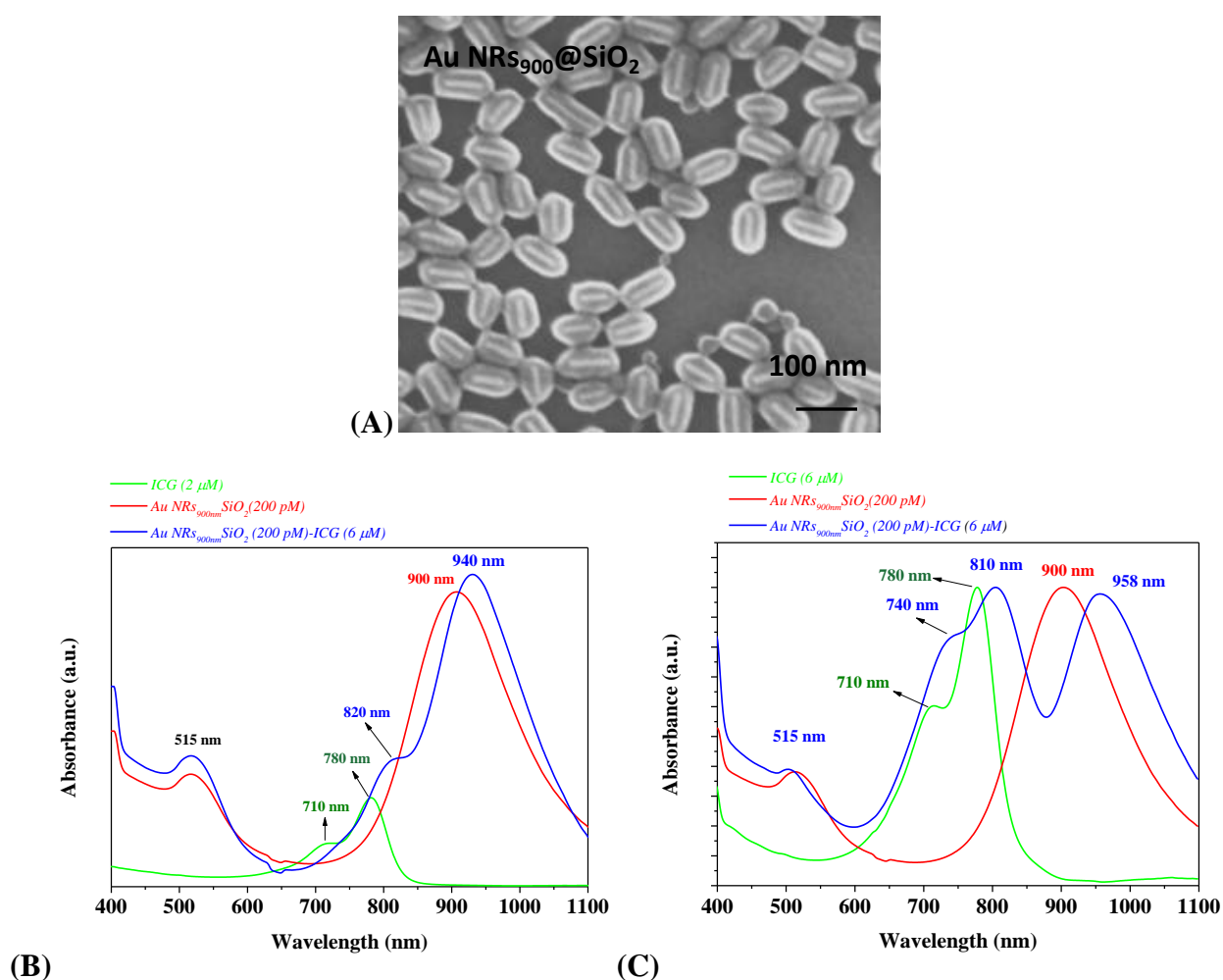
The scanning electron microscopy (SEM) image shows that in the case of Au NRs<sub>800</sub>@SiO<sub>2</sub>, the Au NR core has a mean length of  $62 \pm 20$  nm and a width of  $18 \pm 7$  nm (**Figure 2.4 A**). This corresponds to a mean aspect ratio of 3.4. The longitudinal SPR band maximum of the Au NRs coated with a 20 nm silica shell is located at  $\sim 800$  nm, with an additional transversal oscillation band at 515 nm, confirming the formation of elongated Au NRs (**Figure 2.4 B**).



**Figure 2.4.** (A) SEM image of AuNRs<sub>800</sub>@SiO<sub>2</sub> (Scale bar: 100 nm). (B, C) UV-Vis-NIR absorption spectra of ICG (2 or 6 μM), Au NRs<sub>900 nm</sub>@SiO<sub>2</sub> (200 pM) and Au NRs<sub>900 nm</sub>@SiO<sub>2</sub> (200 pM)-ICG (2 or 6 μM).

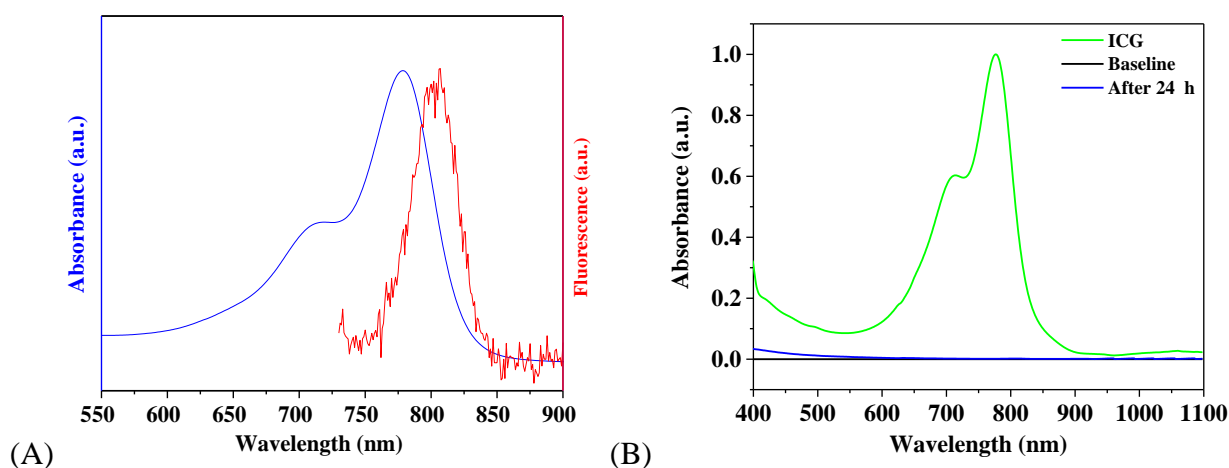
The position of the plasmon band overlaps with the strong absorption band of ICG at 780 nm and the weak absorption band at 710 nm, corresponding to the ICG monomer and oligomeric forms, respectively [15]. After loading ICG onto the silica shell, the absorption curve changes depending on the amount of ICG loaded onto the nanoparticles (**Figure 2.4 B and C**). In the case of lower ICG loading (2 μM), the plasmon band of the Au NRs was significantly shifted to the red, something already observed for methylene blue modified Au nanostructures. [30] The band at 816 nm corresponds to the red-shifted absorption band of ICG due to dye aggregation. The transversal plasmon band of Au NRs at 515 nm remained unchanged. The amount of loaded ICG was determined as described previously, [2] by measuring the ICG concentration in solution before and after loading onto Au NRs@SiO<sub>2</sub> using UV/Vis spectrometric measurements at 780 nm, where ICG showed a characteristic absorption maximum. Loading with a higher ICG concentration (6 μM) results in distinct absorption bands at 515 nm (transversal plasmon band), 742 nm (ICG), 826 nm (ICG) and 925 nm (longitudinal plasmon band) (**Figure 2.4 C**).

The loading of ICG onto the negatively charged Au NRs@SiO<sub>2</sub> (zeta potential  $\xi = -16 \pm 2$  mV) [2] is presumably based on hydrophobic effects and/or hydrogen bonds due to the negative zeta-potential of ICG ( $\xi = -24 \pm 2$  mV), resulting from charged sulfonate groups. The surface charge of the Au NRs@SiO<sub>2</sub>-ICG remained negative ( $\xi = -19 \pm 2$  mV). As was the case with verteporfin loaded nanostructures, up to 98% of ICG remained integrated on Au NRs@SiO<sub>2</sub> when the nanostructures were incubated in PBS at 37 °C for 24 h, indicating good stability of the Au NRs@SiO<sub>2</sub>-ICG nanostructures (**Figure 2.6 B**) [2].



**Figure 2.5.** (A) SEM image of AuNRs<sub>800</sub>@SiO<sub>2</sub> (Scale bar: 100 nm). (B, C) UV-Vis-NIR absorption spectra of ICG (2 or 6 μM), Au NRs<sub>900 nm</sub>@SiO<sub>2</sub> (200 pM) and Au NRs<sub>900 nm</sub>@SiO<sub>2</sub> (200 pM)-ICG (2 or 6 μM).

The SEM image of Au NRs<sub>900</sub>@SiO<sub>2</sub> nanostructures shows the Au NR core with a mean length of  $75 \pm 12$  nm and a width of  $15 \pm 2$  nm, corresponding to a mean aspect ratio of 5.0 (**Figure 2.5 A**). The longitudinal plasmon band maximum of Au NRs<sub>900</sub>@SiO<sub>2</sub> is located at  $\sim 900$  nm with the additional transversal oscillation band at 515 nm (**Figure 2.5 B**). Incorporation of ICG (2 μM) results in an absorption spectrum with a broad band at  $\sim 820$  nm and a shift of the plasmon band to 940 nm (**Figure 2.5 B**). A higher ICG loading shifts the plasmon band even further to the NIR region (958 nm) (**Figure 2.5 C**). The strong absorption between 740 and 820 nm due to ICG suggests that ICG forms aggregates upon integration into the silica shell,



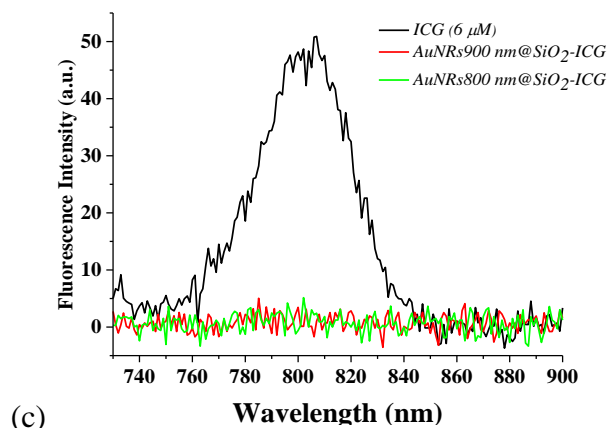


**Figure 2.6.** (A). Absorption and fluorescence emission profiles of ICG. (B) Stability of the Au NRs@SiO<sub>2</sub>-ICG nanostructures. (C) Fluorescence quenching of ICG in AuNRs@SiO<sub>2</sub> confirmed by fluorescence spectra of free ICG and AuNRs@SiO<sub>2</sub>-ICG ( $\lambda_{\text{ex}} = 720 \text{ nm}$ ).

in agreement with previous results [31]. The formation of ICG aggregates was in addition validated by the low fluorescence from Au NRs@SiO<sub>2</sub>-ICG when compared to free ICG in solution, where at low concentrations the mole fraction of dimers is negligible (**Figure 2.6**) [32].

### → Singlet Oxygen Generation

As shown recently by Li *et al.* [31] the strongly increased ICG loading on the silica shell greatly enhanced the photodynamic destruction of breast tumor cells. We were interested in evaluating the potential of the different Au NRs@SiO<sub>2</sub>-ICG nanostructures for the photodynamic destruction of pathogens. In addition, the presence of positively charged aromatic nitrogen atoms in the benzo[e]indole ring of ICG might add to the antibacterial character of the nanostructures. [33, 34]

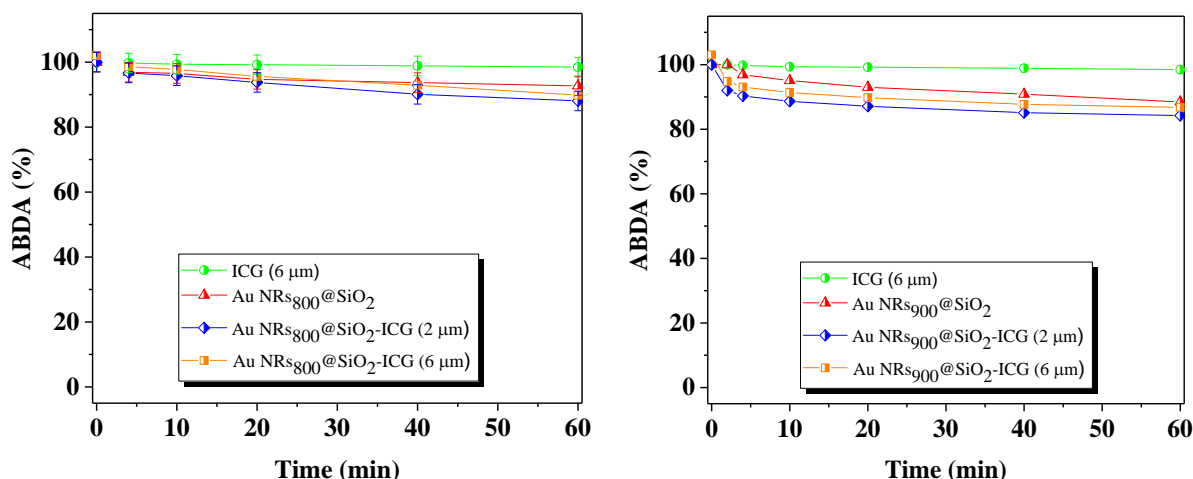


**Figure 2.7** Photo-induced degradation of ABDA (10  $\mu\text{M}$ ) under irradiation at 810 nm (laser power = 1  $\text{W cm}^{-2}$ ) using a CW laser in the presence of (A) ICG (6  $\mu\text{M}$  in water +10 % DMSO), Au NRs<sub>800</sub>@SiO<sub>2</sub> (300 pM in water), Au NRs<sub>800</sub>@SiO<sub>2</sub>-ICG (2  $\mu\text{M}$ ) and Au NRs<sub>800</sub>@SiO<sub>2</sub>-ICG (6  $\mu\text{M}$ ), and (B) ICG (6  $\mu\text{M}$  in water +10 % DMSO), Au NRs<sub>900</sub>@SiO<sub>2</sub> (300 pM in water), Au NRs<sub>900</sub>@SiO<sub>2</sub>-ICG (2  $\mu\text{M}$ ) and Au NRs<sub>900</sub>@SiO<sub>2</sub>-ICG (6  $\mu\text{M}$ ).

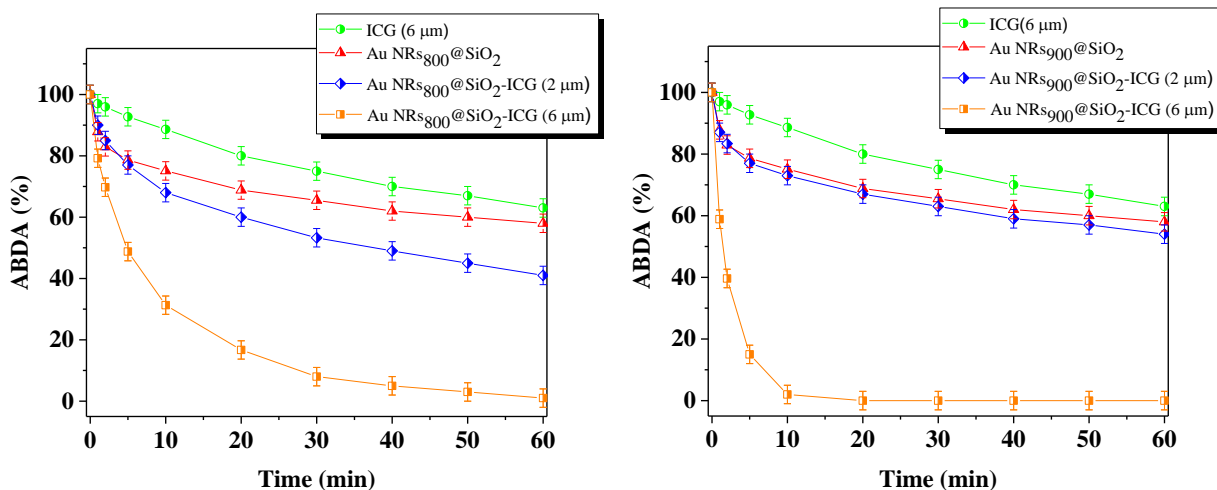


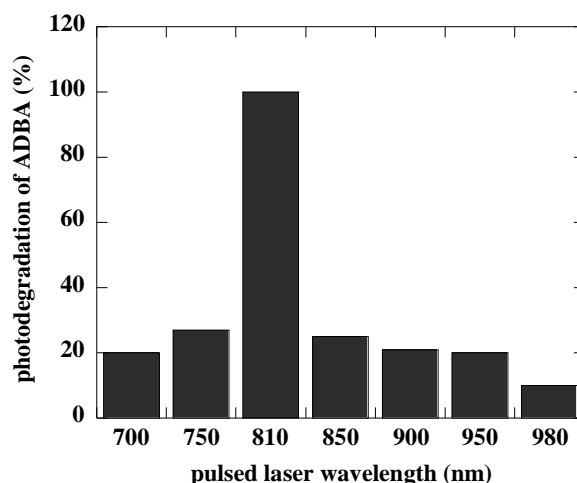
**Figure 2.8.** Photoinduced degradation of ABDA (10  $\mu\text{M}$ ) under pulsed-mode irradiation at 810 nm ( $1 \text{ W}/\text{cm}^2$ ) in the presence of ICG (6  $\mu\text{M}$ ), 200 pM Au NRs@SiO<sub>2</sub> (in water) and 200 pM Au NRs@SiO<sub>2</sub>-ICG (2 or 6  $\mu\text{M}$ ) with particles with plasmon bands at 800 nm and 900 nm.

However, efficient generation of reactive oxygen species (ROS) and in particular singlet oxygen, the most destructive species among ROS, is a pre-requisite for PDT. The singlet-oxygen generation capability was evaluated through the photochemical decomposition of 9,10-anthracenediylbis(methylene)dimalonic acid (ABDA), [2, 35] using a continuous wave (CW) or a pulsed-laser excitation. Using a continuous laser at 810 nm ( $1 \text{ W}/\text{cm}^2$ ), the degradation of ABDA and thus the formation of singlet oxygen was low (**Figure 2.7**). The use of a pulsed-mode excitation resulted in the formation of moderate to high singlet oxygen yields. **Figure 2.8** displays the decrease of the optical absorption band at 262 nm of an aqueous ABDA solution in the presence of different nanostructures as a function of irradiation time using pulsed-mode excitation, with ICG (6  $\mu\text{M}$ , water/10% DMSO) as control. The photodegradation rate of ABDA is faster in the presence of nanostructures when compared to free ICG in solution due to the enhanced formation of singlet oxygen.

The Au NR@SiO<sub>2</sub> nanostructures show in addition enhanced photodegradation of ABDA than free ICG. Indeed, two-photon excitation of Au nanostructures has been reported to generate singlet oxygen, with best efficiency when the plasmon band was tuned to the laser wavelength [35, 36]. This agrees with the enhanced photodegradation of ABDA in the presence of Au NR<sub>800</sub>@SiO<sub>2</sub> over Au NR<sub>900</sub>@SiO<sub>2</sub> at 810 nm irradiation wavelength.

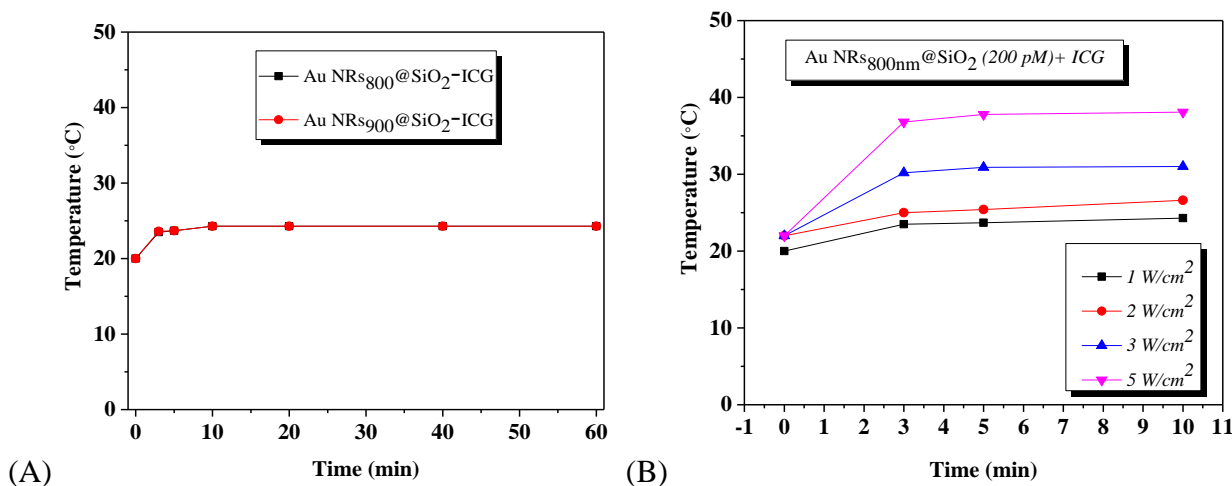
The amount of ICG loaded onto the Au NR@SiO<sub>2</sub> particles has an important effect on the singlet oxygen generation capability with Au NR@SiO<sub>2</sub> nanostructures of high ICG loading showing enhanced singlet oxygen generation (**Figure 2.8**). The overall effect was more pronounced on AuNRs<sub>900</sub>@SiO<sub>2</sub>-ICG nanostructures than on Au NRs<sub>800</sub>@SiO<sub>2</sub>-ICG. In addition, it was strongly dependent on the irradiation wavelength used (**Figure 2.9**). This indicates that no plasmonic energy transfer to ICG adsorbed on the silica shell under pulsed-laser irradiation takes place [37].





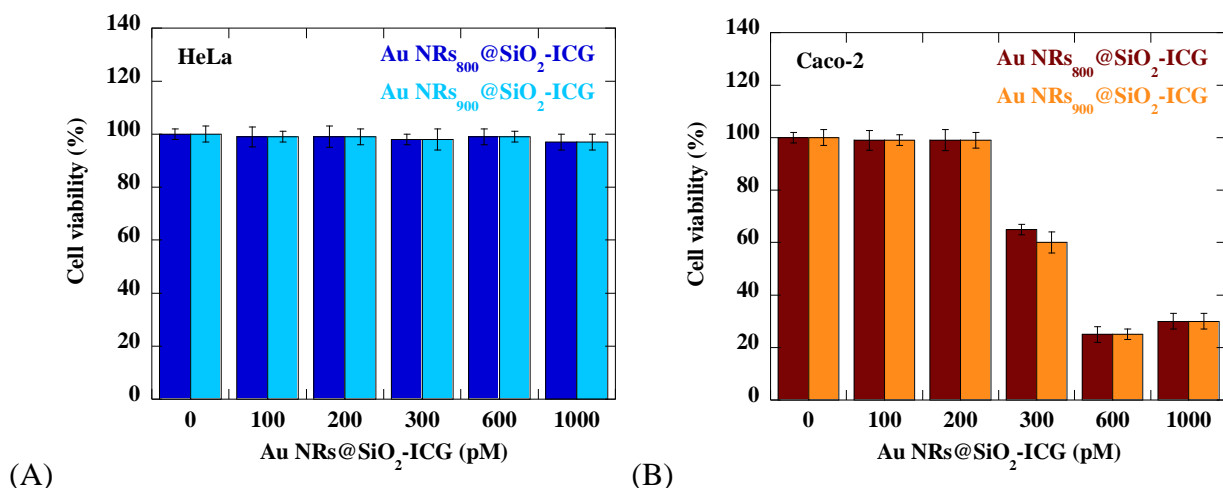
**Figure 2.9.** Photo-induced degradation of ABDA (10  $\mu$ M) using pulsed laser irradiation (1 W/cm<sup>2</sup>) at different wavelengths in the presence of 300 pM Au NRs<sub>900</sub>@SiO<sub>2</sub>-ICG (6  $\mu$ M).

To ensure that the photodegradation of ABDA occurs exclusively through a photodynamic effect and not through a synergistic photothermal effect, the temperature of the solution was in parallel monitored in the presence of Au NR<sub>800</sub>@SiO<sub>2</sub>-ICG and AuNR<sub>900</sub>@SiO<sub>2</sub>-ICG (**Figure 2. 10**). The concentration of the nanostructures (200 pM) and the laser intensity (1 W/cm<sup>2</sup>) were too low to induce any temperature increase over an irradiation period of 1 h. The degradation of ICG, which is accelerated in aqueous solutions at higher temperature, is consequently limited under our experimental conditions, resulting in moderate singlet oxygen generation from free ICG over time (**Figure 2.8**) [38]. Therefore, the loading of ICG onto nanostructures improves their chemical stability and prevents their aggregation, ensuring an efficient <sup>1</sup>O<sub>2</sub> generation, in accordance with other reports [39, 40].



**Figure 2.10.** Photothermal effect upon pulsed laser irradiation of nanostructures at 810 nm: (A) 200 pM Au NR<sub>800</sub>@SiO<sub>2</sub>-ICG (6  $\mu$ M) (black) and 200 pM Au NR<sub>900</sub>@SiO<sub>2</sub>-ICG (6  $\mu$ M) (red) at 1 W/cm<sup>2</sup>; (B) 300 pM Au NR<sub>900</sub>@SiO<sub>2</sub>-ICG (6  $\mu$ M) at 1 W/cm<sup>2</sup>, 2 W/cm<sup>2</sup> (red), 3 W/cm<sup>2</sup> and 5 W/cm<sup>2</sup>.

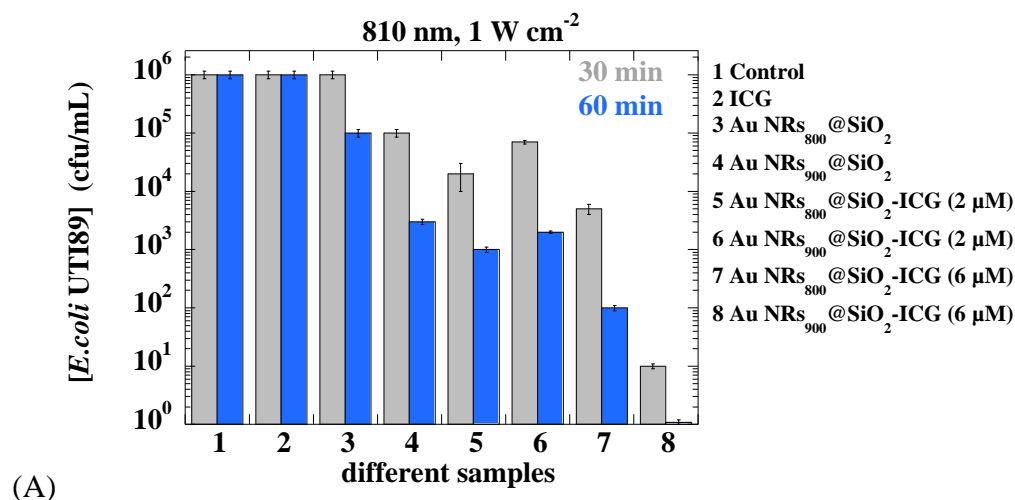
Before investigating the effect on bacterial cells, the cytotoxicity of the nanostructures was determined on HeLa (**Figure 2.11 A**) and Caco-2 epithelial (**Figure 2.11 B**) cell lines, where one might encounter *E. coli*. The nanostructures display no cytotoxicity to HeLa cells at the investigated concentration range. In the case of Caco-2 epithelial cells, the nanostructures proved to be cytotoxic at concentrations of 300 pM and above.



**Figure 2.11.** Relative cell viability of HeLa (A) and Caco-2 epithelial (B) cell lines as a function of the Au NRs@SiO<sub>2</sub>-ICG (6 μM) concentration without irradiation.

### 2.3.2 Antimicrobial photodynamic therapy

Irradiation of a suspension of *E. coli* ( $1 \times 10^6$  cfu/mL) in the presence of ICG (6 μM), Au NRs@SiO<sub>2</sub> or Au NRs@SiO<sub>2</sub>-ICG (6 μM) exhibits concentration- and nanostructures-dependent photodynamic killing effect using a pulsed-laser with 810 nm wavelength (**Figure 2.12**). ICG alone did not show any antimicrobial properties in this concentration range, in accordance with other reports using a continuous wave light source at 808 nm [41]. Au NRs@SiO<sub>2</sub> exhibited a plasmon dependent effect, with the nanostructures displaying a longitudinal plasmon band at 900 nm being more efficient for the photodynamic ablation of pathogens. This is in agreement with the higher amount of singlet oxygen produced using these nanostructures. Approximately 2.5 log<sub>10</sub> reduction in viable *E. coli* LF82 was observed after 1 h of illumination of a bacterial suspension in the presence of Au NRs<sub>900</sub>@SiO<sub>2</sub> (200 pM). Partial (5 log<sub>10</sub> decrease) and complete (6 log<sub>10</sub> decrease) pathogen ablation were observed after illumination at 810 nm for 30 and 60 min, respectively, when ICG was loaded onto the nanostructures. This result indicates considerable improvement when compared to our previous Au NRs<sub>900</sub>@SiO<sub>2</sub> nanostructures loaded with verteporfin (4 μM) (4 log<sub>10</sub> after 30 min) (**Table 1.1**) [2]. **Figure 2.12 C** displays the change in morphology of *E. coli* LF82 after 60 min irradiation in the presence of Au NRs<sub>900</sub>@SiO<sub>2</sub>-ICG (6 μM). The untreated *E. coli* cells have rod-like shape and intact surfaces, while after exposure to Au NRs<sub>900</sub>@SiO<sub>2</sub>-ICG (6 μM) irradiation, portions of the bacteria are decomposed due to the impact of locally generated reactive oxygen species.



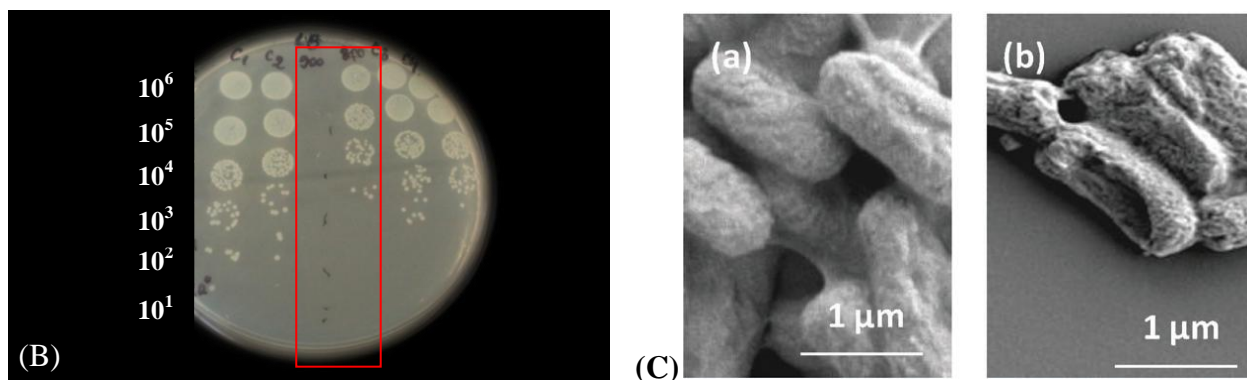


**Figure 2.12.** (A) Photodynamic efficiency of ICG (6 μM, sample 2), 200 pM Au NRs@SiO<sub>2</sub> (sample 3 and 4), 200 pM Au NRs<sub>800</sub>@SiO<sub>2</sub>-ICG (2 and 6 μM of ICG) (samples 5 and 6) and 200 pM Au NRs<sub>900</sub>@SiO<sub>2</sub>-ICG (2 and 6 μM of ICG) (samples 7 and 8) on the ablation of Gram-negative *E. coli* LF82 ( $1 \times 10^6$  CFU/mL) in solution using pulsed-laser irradiation at 810 nm ( $1 \text{ W/cm}^2$ ) for 30 and 60 min. (B) Photographs of the *E. coli* colonies incubated on the solid medium with different treatments. (C<sub>1</sub>: without irradiation, C<sub>2</sub>: with irradiation, 900: Au NRs<sub>900nm</sub>@SiO<sub>2</sub>(200 pM) – ICG(6 μM) with laser; 800: AuNRs<sub>800nm</sub>@SiO<sub>2</sub>(200 pM)-ICG (6 μM) with laser; C<sub>3</sub>: Au NRs<sub>900nm</sub>@SiO<sub>2</sub>(200 pM) – ICG(6 μM) without laser, C<sub>4</sub>: AuNRs<sub>800nm</sub>@SiO<sub>2</sub>(200 pM)-ICG (6 μM) without laser). (C) SEM images of *E. coli* LF 82 before (a) and after (b) PDT for 60 min at 810 nm ( $1 \text{ W/cm}^2$ ).

The results are consistent with a previous report on the photodynamic treatment with vancomycin-conjugated magnetic particles, where *E. faecalis* pathogens were used; laser irradiation at 510 nm resulted in comparable killing kinetics (Table 1.1) [42]. As such a short wavelength may be of limited practical utility (e.g. to kill bacteria in the blood stream), but due to strong tissue absorption the nanostructures investigated in this work might have wider range of practical applications. In addition, we found that the antibacterial particle-based photodynamic therapy efficiency is not attenuated in the presence of high protein concentrations (data not shown).

Indeed, it was postulated that PDT is more efficient if the bacteria were incubated with the photosensitizer in medium with low protein concentrations [43, 44].

## CONCLUSIONS

We have demonstrated that gold nanorods coated with an indocyanine green-loaded silica shell (Au NRs@SiO<sub>2</sub>-ICG) have good biocompatibility and are effective in completely inactivating pathogenic *E. coli* bacterial strains such as *E. coli* LF82 under pulsed-light irradiation at 810 nm ( $1 \text{ W/cm}^2$ ). Particle-based photodynamic therapy using ICG loaded Au nanostructures combined with a pulsed laser in the NIR region offers indeed a new perspective for the treatment of bacterial infections, owing to its increased penetration depth and unique spatial resolution. Using a nanoparticle concentration low enough to eliminate any additional photothermal heating effects, a  $6 \log_{10}$  reduction in the viability of the Crohn's disease-associated adherent-invasive *E. coli* strain LF82 was observed using gold nanostructures displaying a plasmonic band at 900 nm. In addition, we observed a  $3 \log_{10}$  reduction of bacteria viability using Au NRs@SiO<sub>2</sub> without ICG, due to formation of reactive oxygen species (ROS) under two-photon irradiation. It is known that gold nanorods exhibit large two-photon absorption cross-sections, making them suitable for the generation of ROS [35].

We believe that this behavior is due to the physical disruption of the bacteria membrane through the impact of locally generated reactive oxygen species.

## BIBLIOGRAPHY

1. Ray, P.C., et al., *Nanomaterials for targeted detection and photothermal killing of bacteria*. Chemical Society Reviews, 2012. **41**(8): p. 3193-3209.
2. Turcheniuk, K., et al., *Highly effective photodynamic inactivation of E. coli using gold nanorods/SiO<sub>2</sub> core-shell nanostructures with embedded verteporfin*. Chemical Communications, 2015. **51**(91): p. 16365-16368.
3. Jijie, R., et al., *Particle-based photodynamic therapy based on indocyanine green modified plasmonic nanostructures for inactivation of a Crohn's disease-associated Escherichia coli strain*. Journal of Materials Chemistry B, 2016. **4**(15): p. 2598-2605.
4. Turcheniuk, K., et al., *Plasmonic photothermal cancer therapy with gold nanorods/reduced graphene oxide core/shell nanocomposites*. RSC Advances, 2016. **6**(2): p. 1600-1610.
5. Wang, C. and J. Irudayaraj, *Gold nanorod probes for the detection of multiple pathogens*. Small, 2008. **4**(12): p. 2204-2208.
6. Dykman, L. and N. Khlebtsov, *Gold nanoparticles in biomedical applications: recent advances and perspectives*. Chemical Society Reviews, 2012. **41**(6): p. 2256-2282.
7. Singh, A.K., et al., *Gold nanorod based selective identification of Escherichia coli bacteria using two-photon Rayleigh scattering spectroscopy*. ACS Nano, 2009. **3**(7): p. 1906-1912.
8. Khan, S.A., et al., *Targeted highly sensitive detection of multi-drug resistant Salmonella DT104 using gold nanoparticles*. Chemical Communications, 2011. **47**(33): p. 9444-9446.
9. Miranda, O.R., et al., *Colorimetric bacteria sensing using a supramolecular enzyme-nanoparticle biosensor*. Journal of the American Chemical Society, 2011. **133**(25): p. 9650-9653.
10. Norman, R.S., et al., *Targeted photothermal lysis of the pathogenic bacteria, Pseudomonas aeruginosa, with gold nanorods*. Nano Letters, 2008. **8**(1): p. 302-306.
11. Mackey, M.A., et al., *The most effective gold nanorod size for plasmonic photothermal therapy: theory and in vitro experiments*. The Journal of Physical Chemistry B, 2014. **118**(5): p. 1319-1326.
12. Huang, X., et al., *Plasmonic photothermal therapy (PPTT) using gold nanoparticles*. Lasers in Medical Science, 2008. **23**(3): p. 217-228.
13. Zharov, V.P., et al., *Photothermal nanotherapeutics and nanodiagnostics for selective killing of bacteria targeted with gold nanoparticles*. Biophysical Journal, 2006. **90**(2): p. 619-627.
14. Wang, S., et al., *Rapid Colorimetric Identification and Targeted Photothermal Lysis of Salmonella Bacteria by Using Bioconjugated Oval-Shaped Gold Nanoparticles*. Chemistry—A European Journal, 2010. **16**(19): p. 5600-5606.
15. Kuo, W.-S., et al., *Antimicrobial gold nanorods with dual-modality photodynamic inactivation and hyperthermia*. Chemical Communications, 2009(32): p. 4853-4855.
16. Khlebtsov, N., et al., *Analytical and theranostic applications of gold nanoparticles and multifunctional nanocomposites*. Theranostics, 2013. **3**(3): p. 167-80.
17. Kuo, W.S., et al., *Gold nanorods in photodynamic therapy, as hyperthermia agents, and in near-infrared optical imaging*. Angewandte Chemie, 2010. **122**(15): p. 2771-2775.
18. Chu, Z., et al., *Surface plasmon enhanced drug efficacy using core-shell Au@ SiO<sub>2</sub> nanoparticle carrier*. Nanoscale, 2013. **5**(8): p. 3406-3411.
19. Nikoobakht, B. and M.A. El-Sayed, *Preparation and growth mechanism of gold nanorods (NRs) using seed-mediated growth method*. Chemistry of Materials, 2003. **15**(10): p. 1957-1962.
20. Gou, L. and C.J. Murphy, *Fine-tuning the shape of gold nanorods*. Chemistry of Materials, 2005. **17**(14): p. 3668-3672.

21. Topaloglu, N., et al., *Antimicrobial photodynamic therapy of resistant bacterial strains by indocyanine green and 809-nm diode laser*. Photomedicine and Laser Surgery, 2013. **31**(4): p. 155-162.
22. Namihisa, T., *Indocyanine green test and its development*. Tokai Journal of Experimental and Clinical Medicine, 1982. **7**(4): p. 419-423.
23. Fickweiler, S., et al., *Indocyanine green: intracellular uptake and phototherapeutic effects in vitro*. Journal of Photochemistry and Photobiology B: Biology, 1997. **38**(2): p. 178-183.
24. Abels, C., et al., *Indocyanine green (ICG) and laser irradiation induce photooxidation*. Archives of Dermatological Research, 2000. **292**(8): p. 404-411.
25. Bäumlér, W., et al., *Photo-oxidative killing of human colonic cancer cells using indocyanine green and infrared light*. British Journal of Cancer, 1999. **80**(3-4): p. 360.
26. Tseng, W.W., et al., *Infrared laser activation of indocyanine green inhibits growth in human pancreatic cancer*. Pancreas, 2003. **27**(3): p. e42-e45.
27. Crescenzi, E., et al., *Photodynamic therapy with indocyanine green complements and enhances low-dose cisplatin cytotoxicity in MCF-7 breast cancer cells*. Molecular Cancer Therapeutics, 2004. **3**(5): p. 537-544.
28. Omar, G.S., M. Wilson, and S.P. Nair, *Lethal photosensitization of wound-associated microbes using indocyanine green and near-infrared light*. BMC Microbiology, 2008. **8**(1): p. 111.
29. Gorelikov, I. and N. Matsuura, *Single-step coating of mesoporous silica on cetyltrimethyl ammonium bromide-capped nanoparticles*. Nano Letters, 2008. **8**(1): p. 369-373.
30. Seo, S.-H., et al., *NIR-light-induced surface-enhanced Raman scattering for detection and photothermal/photodynamic therapy of cancer cells using methylene blue-embedded gold nanorod@SiO<sub>2</sub> nanocomposites*. Biomaterials, 2014. **35**(10): p. 3309-3318.
31. Li, Y., et al., *Localized Electric Field of Plasmonic Nanoplatfrom Enhanced Photodynamic Tumor Therapy*. ACS Nano, 2014. **8**(11): p. 11529-11542.
32. Kirchherr, A.-K., A. Briel, and K. Mäder, *Stabilization of indocyanine green by encapsulation within micellar systems*. Molecular pharmaceutics, 2009. **6**(2): p. 480-491.
33. Maisch, T., et al., *Fast and effective photodynamic inactivation of multiresistant bacteria by cationic riboflavin derivatives*. PloS one, 2014. **9**(12): p. e111792.
34. Hamblin, M.R., et al., *Photodynamic therapy: a new antimicrobial approach to infectious disease?* Photochemical & Photobiological Sciences, 2004. **3**(5): p. 436-450.
35. Zhao, T., et al., *Gold nanorods as dual photo-sensitizing and imaging agents for two-photon photodynamic therapy*. Nanoscale, 2012. **4**(24): p. 7712-7719.
36. Zhao, T., et al., *Gold nanorod enhanced two-photon excitation fluorescence of photosensitizers for two-photon imaging and photodynamic therapy*. ACS Applied Materials & Interfaces, 2014. **6**(4): p. 2700-2708.
37. Chen, N.-T., et al., *Enhanced plasmonic resonance energy transfer in mesoporous silica-encased gold nanorod for two-photon-activated photodynamic therapy*. Theranostics, 2014. **4**(8): p. 798-807.
38. Saxena, V., M. Sadoqi, and J. Shao, *Degradation kinetics of indocyanine green in aqueous solution*. Journal of Pharmaceutical Sciences, 2003. **92**(10): p. 2090-2097.
39. Sharker, S.M., et al., *pH triggered in vivo photothermal therapy and fluorescence nanoplatfrom of cancer based on responsive polymer-indocyanine green integrated reduced graphene oxide*. Biomaterials, 2015. **61**: p. 229-238.
40. Kuo, W.-S., et al., *Gold nanomaterials conjugated with indocyanine green for dual-modality photodynamic and photothermal therapy*. Biomaterials, 2012. **33**(11): p. 3270-3278.
41. Topaloglu, N., M. Gulsoy, and S. Yuksel, *Antimicrobial photodynamic therapy of resistant bacterial strains by indocyanine green and 809-nm diode laser*. Photomedicine and Laser Surgery, 2013. **31**(4): p. 155-162.

42. Choi, K.-H., et al., *Photosensitizer and vancomycin-conjugated novel multifunctional magnetic particles as photoinactivation agents for selective killing of pathogenic bacteria*. Chemical Communications, 2012. **48**(38): p. 4591-4593.
43. Nitzan, Y., A. Balzam-Sudakevitz, and H. Ashkenazi, *Eradication of Acinetobacter baumannii by photosensitized agents in vitro*. Journal of Photochemistry and Photobiology B: Biology, 1998. **42**(3): p. 211-218.
44. Decraene, V., J. Pratten, and M. Wilson, *Assessment of the activity of a novel light-activated antimicrobial coating in a clinical environment*. Infection Control & Hospital Epidemiology, 2008. **29**(12): p. 1181-1184.



## CHAPTER 3. THERAPEUTIC AND BIOIMAGING PLATFORMS BASED ON CARBON DOTS

*In this study, fluorescent carbon dots (CDs) were synthesized by a simple hydrothermal treatment of citric acid and ethylenediamine in a Teflon autoclave reactor. The detailed characterization of as-prepared CDs shows the signatures of nitrogen and oxygen functional groups, responsible for their strong fluorescence intensity and high aqueous dispersibility. We demonstrated that the CDs can be used as a non-toxic imaging probe and as a photosensitizer. Their photodynamic activity was studied on human cervical carcinoma (HeLa) cells under visible light exposure. Moreover, the presence of amino functionalities on their external surface allows the conjugation of therapeutic molecules. We used CDs as a carrier for the delivery of ampicillin. The antibacterial activity of CDs@Amp conjugate was tested towards Escherichia coli (E. coli).*

### 3.1 CARBON DOTS: synthesis, properties and applications

#### 3.1.1 Introduction

In the last years, carbon nanomaterials have attracted considerable interest in a wide range of fields, including nanoelectronics, energy conversion and storage, catalysis and biomedicine due to their unique physical and chemical properties. According to their bonding configurations, nano-carbons can be classified into  $sp^2$  and  $sp^3$ -carbon nanomaterials. In general,  $sp^2$ -carbon nanomaterials include zero-dimensional (0D) fullerene and carbon dots (CDs), one-dimensional (1D) carbon nanotubes (CNTs), two-dimensional (2D) graphene and  $sp^3$ -carbon nanomaterials include three-dimensional (3D) diamond (**Figure 3.1**) [1, 2]. The 1996 and 2010 Nobel Prizes in Chemistry and respectively Physics have been awarded for the discovery of fullerenes and graphene.

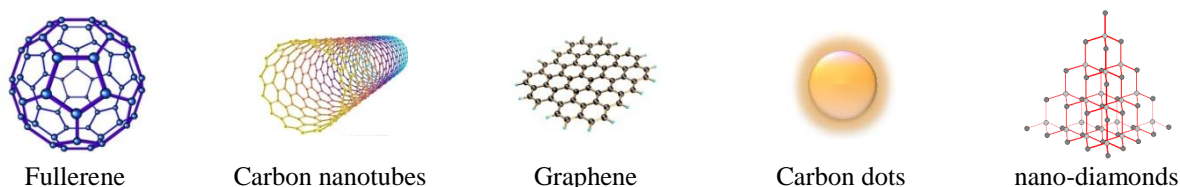


**Figure 3.1** Different structures of carbon nanomaterials [1].

Among these various forms of carbon nanomaterials, carbon dots attract more and more interest due to their attractive properties, including low cost, eco-friendliness, high quantum yield with tunable excitation and emission wavelength, low toxicity and excellent cell membrane permeability, high chemical and photo-stability, versatile surface chemistry, and high solubility in water-based solutions. Moreover, these properties make the fluorescent carbon dots useful in a wide range of applications such as in bio-sensing, bio-imaging, as nanocarriers for drug delivery, as visible light active photo-catalysts or other bio-medical related applications.

Carbon dots (CDs) are small nanoparticles (less than 10 nm in size) with relatively simple particle surface functionalization [3-7]. CDs were first observed as fluorescent impurities in dispersion of nanotubes synthesized by an arc discharge in 2004 [8]. Till now, various starting materials and synthetic routes to synthesize CDs have been developed. These can be prepared by either *top-down* (e.g., arc discharge [8, 9], laser ablation [10, 11], electrochemical oxidation of graphite target [12, 13] and ultrasonic synthesis) or *bottom-up approaches* (hydrothermal treatment and microwave-assisted pyrolysis [14-16]). Among them *hydrothermal synthesis route* is mostly used, because it is a simple and efficient way to prepare CDs [3, 8, 17-21]. Recent

studies have demonstrated that biocompatible multifunctional CDs may be prepared by using biological precursors, such as soybean milk [22], pomelo peel [23], strawberry and orange juice [24, 25], milk [26], hair fibers [27], grass [28] histidine [15] or chitosan [29].

### 3.1.2 Nitrogen-doped carbon dots

The CDs surface functional groups such as hydroxyl (-OH), carboxyl (-COOH) or amino (-NH<sub>2</sub>) allows the conjugation of active therapeutic molecules (e.g. targeting biomolecules, drugs or genes) and to prepare platforms for specific applications. Also, their chemical structure enables the integration of molecules into the sp<sup>2</sup> carbon network [30, 31]. The major challenge remains to design a single nano-platform able to combine therapeutic, imaging and targeting functions in order to treat cancer or different types of infectious diseases.

Many studies have demonstrated that biocompatible CDs decorated with multiple functional groups, with high fluorescence quantum yields and good water solubility could be synthesized directly using the suitable starting materials (e.g. nitrogen [32-34], sulphur [35, 36] - containing precursors), without surface passivating agents (e.g. amine-terminated compounds) (**Table 3.1**). Recently, nitrogen-doped CDs have attracted great attention among researchers because of their remarkable photo-physical and chemical properties. Fluorescent nitrogen-doped carbon dots were used as fluorescent probes for cell imaging [26, 32, 37-40], for detection of Fe<sup>3+</sup>, Hg<sup>2+</sup> [24, 41, 42] and Cu<sup>2+</sup> [28], as electrocatalysts for oxygen reduction [22], photo-degradation of methyl orange under visible light [43] and as printing ink [44].

**Table 3.1** Literature review – nitrogen-doped carbon dots.

Synthesis	Precursor	% N	QY %	Application	Ref.
Maillard reaction/microwave	glucose (C <sub>6</sub> H <sub>12</sub> O <sub>6</sub> ) + amino acids	-	69.1		Wei (2014) [37]
	ethylenediamine tetraacetic acid (C <sub>10</sub> H <sub>16</sub> N <sub>2</sub> O <sub>8</sub> )	6.33	78		Hui (2014) [38]
	folic acid (C <sub>19</sub> H <sub>19</sub> N <sub>7</sub> O <sub>6</sub> )	10.45	23		Wang (2014) [32]
	lactose (C <sub>12</sub> H <sub>22</sub> O <sub>11</sub> ) and Tris (C <sub>4</sub> H <sub>11</sub> NO <sub>3</sub> )	5.04	12.5	as imaging probes	Zhang (2013)[39]
	citric acid (C <sub>6</sub> H <sub>8</sub> O <sub>7</sub> ) and L-cysteine	4.85	73		Dong (2013) [40]
	polyvinyl pyrrolidone (C <sub>6</sub> H <sub>9</sub> NO) <sub>n</sub> and 4,7,10-trioxa-1,13-tridecanediamine		19.6		Hui (2014) [38]
hydrothermal treatment	milk	-	12		Wang (2014) [26]
	glutamic acid (C <sub>5</sub> H <sub>9</sub> NO <sub>4</sub> )	-	28	detection of amoxicillin	Niu (2014) [33]
	citric acid (C <sub>6</sub> H <sub>8</sub> O <sub>7</sub> ) and polyene polyamine	N/O = 0.68	21	as nano-carriers for drug delivery	Zheng (2014) [45]
	glycolic acid (C <sub>2</sub> H <sub>4</sub> O <sub>3</sub> ) + urea (CH <sub>4</sub> N <sub>2</sub> O)	5.4	12.9	emission can be tuned <i>via</i> varying the content of –COOH groups from carbon source	Wang (2015) [46]
	malic acid (C <sub>4</sub> H <sub>6</sub> O <sub>5</sub> ) + urea (CH <sub>4</sub> N <sub>2</sub> O)	6.9	32.4		
	citric acid (C <sub>6</sub> H <sub>8</sub> O <sub>7</sub> ) + urea (CH <sub>4</sub> N <sub>2</sub> O)	9.5	54.9		

strawberry juice	6.88	6.3	as fluorescent probe for detection of $\text{Fe}^{3+}$ and/or $\text{Hg}^{2+}$	Huang (2013) [24]
cocoon silk	11.36	38		Li (2013) [41]
$\alpha$ -lipoic acid ( $\text{C}_8\text{H}_{14}\text{O}_2\text{S}_2$ )	-	54.4		Ding (2014) [42]
grass	4.23	6.2	as fluorescent probe for detection of $\text{Cu}^{2+}$	Liu (2012) [28]
ammonium citrate	5.35	13.5	-	Yang (2014) [34]
soy milk	10.39	2.6	as electrocatalysts for oxygen reduction	Zhu (2012) [22]
citric acid ( $\text{C}_6\text{H}_8\text{O}_7$ ) and ethylenediamine ( $\text{C}_2\text{H}_8\text{N}_2$ )	10.63-16.25	3.8 – 80.6	as printing ink and fluorescent probe for detection of $\text{Fe}^{3+}$	Zhu (2013) [44]
glucose ( $\text{C}_6\text{H}_{12}\text{O}_6$ ) and ammonium hydroxide ( $\text{NH}_4\text{OH}$ )	7.45	6.65	photo-degradation of methyl orange under visible light	Ma (2012) [43]

### 3.1.3 Biological applications of carbon dots

#### ❖ Bio-imaging

It is a significant interest in the development of fluorescent nanomaterials as contrast agents for *in vivo* optical imaging and sensing. Fluorescent CDs compared with conventional organic dyes and semiconductor quantum dots, are bright, chemically inert, biocompatible and stable against photobleaching, being a promising alternative for imaging applications [47].

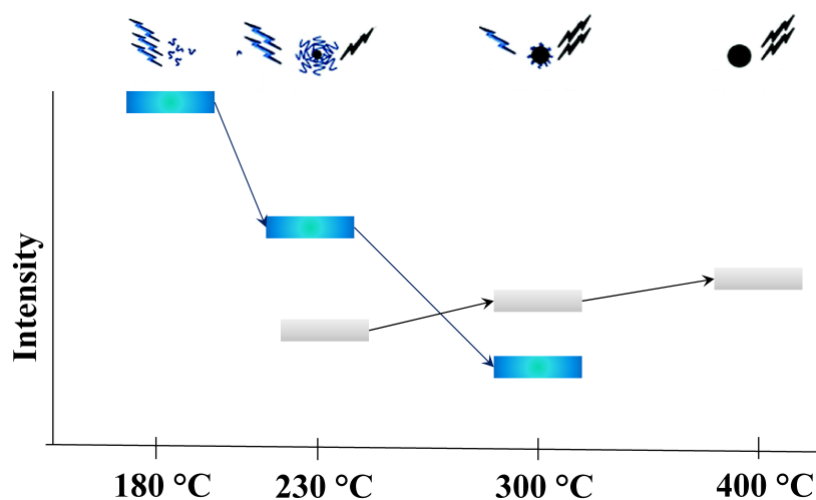


**Figure 3.2** Schematic representation of the CDs formation mechanism and emission characteristics [48].

However, the exact mechanism of CDs photoluminescence is still elusive. Generally, the photoluminescence properties are associated with confinement effect, stabilizing surface trap or the radiative recombination of excitations, depending on both the carbogenic cores and surface functional groups (molecular fluorophores) [37, 46, 48-52].

Several authors reported that the emission mechanism of carbon dots depends on the precursor chemical structure and preparation conditions. For example, Krysmann *et al.* [48] observed that the CDs photoluminescence behavior strongly depends on the synthesis conditions (such as temperature). They performed a systematic investigation of the CDs formation mechanism and emission characteristics by following the pyrolysis of citric acid and ethanolamine at different temperatures. As shown in **Figure 3.2**, the results indicate that initially the PL spectrum is mostly due to amide-containing fluorophores (blue groups) and during the pyrolysis the organic fluorophores are consumed for the buildup of the carbogenic core (black group). This observation is similar to that reported by Shi *et al.* [36], describing the CDs synthesis through three stages: decomposition, polymerization and carbonization. Bhunia *et al.* [53] showed that the existence of a correlation between the particle size and defect sites, and the emission. Moreover, the presence of oxygen, nitrogen and phosphorous, and their relative ratios in the carbon matrix dictate the quantum yield. A similar result was found by Liu *et al.* [28].

According to previous studies, by doping CDs, it is possible to modulate the photoluminescence properties. It should be noted that most of the research papers have been devoted to nitrogen-doped carbon dots and only a few studies focused on other dopants. For example, sulphur-doped fluorescent CDs were synthesized for the first time by Chandra *et al.* [35]. On the other hand, Hu *et al.* [36] demonstrated that the co-existence of O/N radicals in CDs structures results in strong photoluminescence, while CDs containing O and Cl radicals show high photo-catalytic activity. Ding *et al.* [42] performed a comparative study between sulfur-doped carbon dots (S-CDs) and nitrogen, sulfur co-doped carbon dots (N,S-CDs). The results proved that N,S-CDs exhibit much stronger blue-emission than S-CDs with a QY of 54.4 %, similar to that reported previously by Dong *et al.* [40].

#### → Cellular imaging

There has been a considerable amount of research carried out on the cellular uptake of various carbon dots and their fluorescence brightness in the cellular environment. For example, Wang *et al.* [54] incubated silica-loaded CDs with the human gastric carcinoma cells (BGC823) for 24 h and observed that the hybrid nanoparticles easily penetrated into the cell, but not into the nucleus. Qiao *et al.* [49] showed that CDs with TTDDA (4,7,10-trioxa-1,13-tridecanediamine) surface-passivation is able to label both the cell membrane and the cytoplasm of COS-7 cells, after an incubation of 24 h with the nanoparticles. Liu *et al.* [16] incubated 100 µg/mL TTDDA-passivated CDs for 24 h with HepG-2 cells and then observed the nanoparticles' emission (blue, green and red) under various excitation wavelengths (405 nm, 488 nm and 543 nm) using a laser scanning confocal microscope. The results proved that the CDs have been internalized into the cells through endocytosis. Several studies have shown that CDs labeled both the cell membrane and the cytoplasm without reaching the nucleus in a significant way [29, 32, 39, 55] (**Figure 3.3**). Jana *et al.* [52] observed that after 6 h of incubation with L929 fibroblast, the CDs have selectivity over living cells. This selectivity is due to the quenching of CDs fluorescence; at acidic pH, the CDs lose the fluorescence and in general dead cells have a pH of 4-5.

In addition, Liu *et al.* [56] used polyethylenimine (PEI) functionalized CDs for gene delivery and bioimaging. The CDs-PEI internalized into cells display tunable fluorescence emission under varying excitation wavelengths and could mediate gene transfection in COS-7 and HepG2 cells with comparable or higher efficiency and lower cytotoxicity compared with pristine PEI25k. The cationic polymer layer has the ability to mediate plasmid DNA transfection.

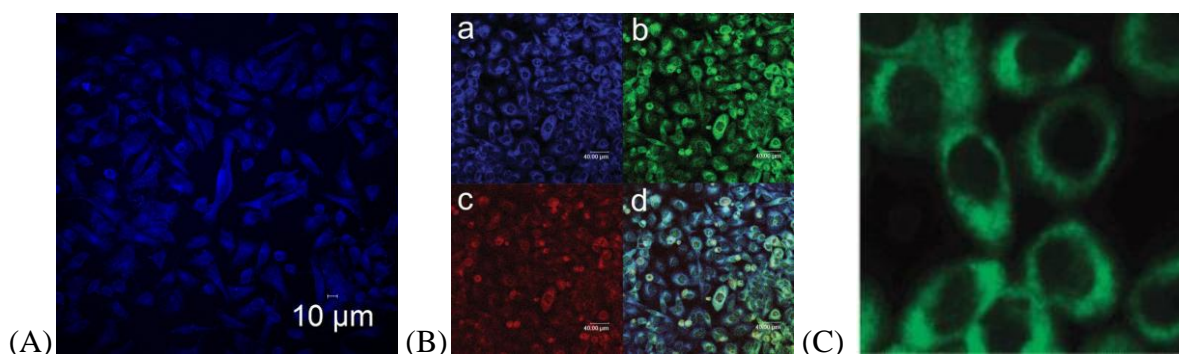


**Figure 3.3** Laser scanning confocal microscopy images of (A) HeLa cells after 1 h of incubation with CDs ( $\lambda_{\text{ex}} = 405$  nm,  $\lambda_{\text{em}} = 500$  nm), (B) CDs labeled HepG-2 cells (a:  $\lambda_{\text{ex}} = 405$  nm, b:  $\lambda_{\text{ex}} = 488$  nm, c:  $\lambda_{\text{ex}} = 543$  nm and d: overlay) and (C) of MCF-7 cells with internalized CDs (Two photon excitation, 800 nm). [16, 55, 57]

#### → Optical imaging in vivo

The carbon dots have been used successfully for *in vivo* imaging in mice models [6, 30, 47, 57, 58]. Li *et al.* [57] evaluated the *in vivo* and *in vitro* CDs optical imaging performance. They observed a diffuse distribution within the cells (**Figure 3.3**) and the nanoparticles were entrapped in lysosomes/endosome compartment located near the cell nucleus and in mitochondria, endoplasmic reticulum and Golgi body. On the other hand, the results show that the intravenously injected CDs are observed in all organs, like heart, liver, spleen, lung kidney, intestine and brain at 6 h, 16 h and 24 h post-injection. The detection of CDs in brain suggests that the nanoparticles are able to cross the blood-brain barrier. Also, Yang *et al.* [47] reported CDs as a contrast agent for optical imaging. Goh *et al.* [59] proposed CDs and hyaluronic acid-CDs conjugate as promising bioimaging agents.

The limitation is that the majority of fluorescence imaging studies were conducted under UV or visible excitation, the biological tissues in this optical window showing a very shallow penetration depth. Ideal condition is to carry out *in vivo* imaging in the near-infrared (NIR) region, that coincides with the tissue transparency window. Tao *et al.* [60] explored the CDs for fluorescence imaging in mice by using varied excitation wavelengths from 455 nm to 704 nm. A CDs aqueous solution was subcutaneously injected in the mice, followed by fluorescence imaging. As can be seen in **Figure 3.4**, the best fluorescence contrast was obtained at 595 nm excitation. Similar to [57], the CDs are observed in the organs and a gradual clearance of CDs from the mouse body was observed through both renal and fetal excretions. Yang *et al.* [47] reported that the intravenously injected CDs are primarily excreted *via* urine.

Cao *et al.* [55] reported that CDs are excellent fluorescent agents for optical cell imaging using both one (argon ion excitation at 458 nm) and two photon excitation (femtosecond pulsed laser excitation at 800 nm). In order to demonstrate the potential of aminopolymer-functionalized CDs for cell imaging, the nanoparticles were incubated with MCF-7 cells for 2 h. The results prove that CDs were able to label both the cell membrane and the cytoplasm without reaching the nucleus.

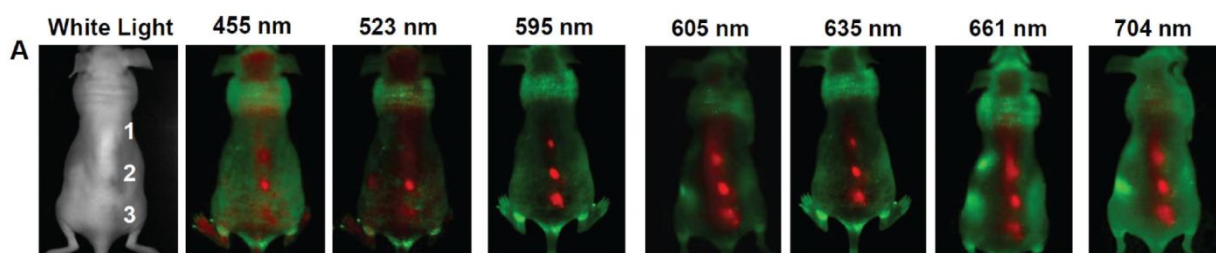


**Figure 3.4** *In vivo* fluorescence images of a CDs-M-injected mouse, under various excitation wavelengths [60].



→ *Optical labeling of Escherichia coli (E. coli) cells*

Sun *et al.* [11] have reported that PEG<sub>1500</sub>N-passivated CDs can be used as fluorescent markers for imaging of bacteria cells (**Figure 3.5**). In addition, Nandi and co-workers [4] have proposed amphiphilic CDs as a platform for bacteria detection and imaging. They observed that the amphiphilic CDs exhibited different affinities to bacterial cell surfaces, the CDs fluorescence intensity and maximum emission wavelength depending on the bacterial strains. To investigate cell labeling and interactions, they incubated the carbon nanoparticles with four bacterial species, including *E. coli*, *P. aeruginosa*, *S. typhimurium* (Gram-negative) and *B. cereus* (Gram positive).

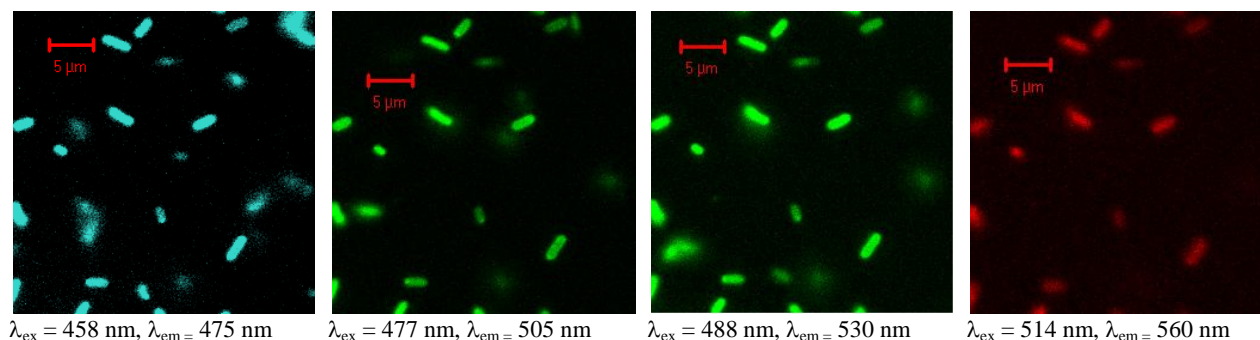


**Figure 3.5** Confocal microscopy images of *E. coli* ATCC 25922 cells labeled with CDs [11].

The CDs showed encouraging cell-imaging application *in vivo* and *in vitro*.

❖ **Biosensing.** CDs conjugated with different biomolecules have drawn considerable attention for selective labeling and detection of Gram-positive and Gram-negative bacteria, as seen in **Table 3.2**. However, the exact mechanism of specific labeling is not yet known and needs to be explored. The major challenge remains to design a simple, selective and sensitive approach for detection of trace bacteria.

**Table 3.2** Platforms based on carbon dots for bactericidal applications.

Samples	Synthesis of CDs	Conjugation	Tested against	Results	Ref.
amikacin modified CDs	5 mg amikacin + 30 mg di-ammonium hydrogen citrate, 10 mL, 4 h, 180 °C	-	for labeling and detecting <i>E. coli</i>	linear range between $3.9 \times 10^5$ – $7.6 \times 10^2$ CFU/mL	Chandra (2016) [61]
mannose-functionalized CQDs	0.1 g ammonium citrate and 0.005 g mannose, 10 mL, 2 h, 180 °C	-		limit of detection of 450 CFU/mL	Weng (2015) [3]
CDs modified with vancomycin	3 g citric acid and 3 g urea, 10 mL, 750 W microwave	EDC/NHS	for detecting <i>S. aureus</i>	linear range between $3.18 \times 10^5$ - $1.59 \times 10^8$ CFU/mL	Zhong (2015) [14]
amphiphilic CDS	6-oacylated fatty acid ester of D-glucose, 2.5 h, 125°C	-	for bacterial detection and imaging	-	Nandi (2015) [4]

CDs	1 g of casein, 50 mL, 12 h, 200 °C	for selectively label <i>E. coli</i> and exclude <i>S. aureus</i>	-	Bhushan (2016) [17]
-----	------------------------------------	---	---	---------------------

#### ❖ As antibacterial agent

Dou *et al.* [62] proved that the quaternary linear and branched PEI (polyethyleneimine) passivated carbon dots exhibit promising antibacterial activity against both gram negative (*Escherichia coli*) and gram positive (*Staphylococcus aureus*) bacteria. The antimicrobial ability of the quaternized CDs was evaluated by the Broth minimum inhibitory concentration (MIC). As can be observed in **Table 3.3**, the quaternary linear PEI passivated CDs showed better efficiency. They assumed that the antibacterial property of the quaternized CDs is due to the ability of CDs to adsorb onto the cytoplasmic membrane, causing its disruption.

**Table 3.3.** MICs test of the CDs on *E. coli* and *S. aureus* [62].

Samples	MIC (µg/mL)	
	Gram-positive bacteria	Gram-negative bacteria
quaternary CD <sub>branched</sub>	32	64
quaternary CD <sub>linear</sub>	16	16

#### ❖ Photodynamic therapy

Huang *et al.* [30] designed and prepared multifunctional chlorine e6-conjugated C-dots (C-dots-Ce6) as the light-triggered theranostics for simultaneous enhanced-PFD and PDT by FRET mechanism. Covalent binding of Ce6 to the PEG-coated C-dots (C-dots-NH<sub>2</sub>) was performed using a modified EDC-NHS reaction.

Meziani *et al.* [7] demonstrated the bactericidal function of 2,2' - (ethylenedioxy)bis(ethylamine) (EDA) CDs under visible illumination. The antibacterial properties of photoexcited EDA-CDs with light exposure against *E. coli* K12 cells was evaluated by cell growth measurements based on the optical density at 600 nm (OD<sub>600nm</sub>) and by plating method to determine the viable cell number. They concluded that the redox species and emissive excited states may be responsible for the observed bactericidal functions.

Choi *et al.* [31] designed biocompatible, fluorescent, folic acid (FA)-functionalized CDs as a carrier for the PS zinc phthalocyanine to achieve simultaneous biological imaging and targeted photodynamic therapy.

#### ❖ Photodynamic and photothermal therapy

Ge *et al.* [63] prepared CDs with intrinsic theranostic properties by using polythiophene benzoic acid as precursor. The CDs exhibit dual photodynamic and photothermal effects under 635 nm laser irradiation with a singlet oxygen generation efficiency of 27 % and high photothermal conversion efficiency of 36.2 %. They proposed also a <sup>1</sup>O<sub>2</sub> generation mechanism. The bimodal OPDT/PTT efficacy and cytotoxicity were tested *in vitro* against B16-F0 skin cancer cells and *in vivo* using nude mice and HeLa tumor-bearing nude mice as animal model. Their results proved that CDs can be applied as an imaging probe and as an efficient photodynamic/hyperthermia agent.

#### ❖ As a drug delivery system

Gogoi *et al.* [64] investigated carbon dot (CD) and calcium alginate-carbon (CA-CDs) dot beads as pH dependent sustained drug delivery vehicles for tetracycline and tetracycline associated with β-cyclodextrin. Compared with CD, the CA-CDs exhibit a higher loading rate and a better drug release profile, the maximum release being obtained for pH 1.

### Carbon dots-based platforms for anticancer applications

Li *et al.* [50] coupled CDs with human transferrin *via* carbodiimide chemistry in order to target HeLa cells. Compared with the non-conjugated, the bioconjugated CDs were able to penetrate cancer cell membrane.

#### ❖ As a drug delivery system

Lai *et al.* [51] employed CDs@mSiO<sub>2</sub>-PEG nanocomposites as a delivery system for anti-cancer drug doxorubicin (DOX). They observed that DOX loaded on the nanocomposites exhibited higher toxicity to HeLa cells in contrast with free DOX. Moreover, as shown in **Figure 3.6**, the DOX release occurred inside the cells, being accumulated in the nucleus. Therefore, the CDs@mSiO<sub>2</sub>-PEG nanocomposites are suitable for cell imaging and drug release. Whereas, Wang *et al.* [5] proposed hollow carbon dots (HCDs) as a delivery system for the delivery of DOX. The DOX was directly mixed with nanoparticles in solution, where the drug was physisorbed through  $\pi$ - $\pi$  stacking (due to the benzene rings in its chemical structure), hydrophobic and van der Waals interactions. The main advantage of the HCDs as a drug delivery vehicle are: (i) the rapid uptake by cells, (ii) pH-controlled release of DOX and (iii) the DOX activity is maintained.

Zheng *et al.* [45] integrated the therapeutic and bioimaging capabilities into one single agent by means of the condensation reaction between the amino groups on the CDs's surface and the carboxyl group of oxaliplatin (anticancer agent). The *in vivo* results demonstrated that CDs-Oxa possess good biocompatibility, bioimaging function and anticancer effect and the *in vivo* results proved that the distribution of the drug can be followed by monitoring the complex fluorescence intensity.

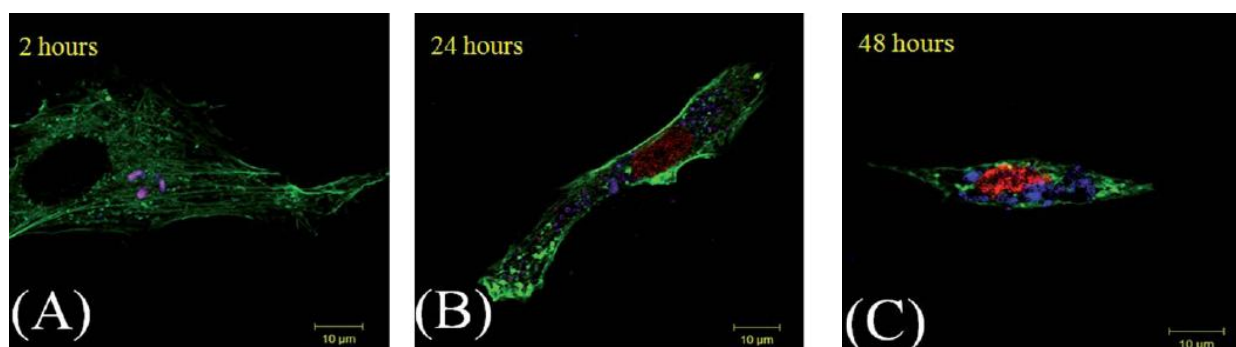


**Figure 3.6** The confocal images of HeLa cells treated with 100  $\mu\text{g/mL}$  DOX@CDs@mSiO<sub>2</sub>-PEG at different time intervals (CDs- blue, DOX- red) [51].

## 3.2 EXPERIMENTAL DETAILS

### 3.2.1 Chemicals

Citric acid, ethylenediamine, 9,10-anthracenediylbis(methylene)dimalonic acid (ABDA), ampicillin, N-(3-dimethylaminopropyl)-N'-ethylcarbodiimide hydrochloride (EDC), N-hydroxysuccinimide (NHS), acetic acid, sodium acetate, ninhydrin, potassium cyanide (KCN), pyridine, phenol, quinine sulfate, Hoechst 33342, and paraformaldehyde were purchased from Sigma-Aldrich and used as received.

### 3.2.2 Synthesis of carbon dots (CDs)

Functionalized CDs were synthesized following a method similar to that reported by Zhu *et al.* [44]. In brief, citric acid (2.1014 g) and ethylenediamine (670  $\mu$ L) were dissolved in Milli-Q water (20 mL). Then the mixture was transferred into a Teflon-lined autoclave (125 mL acid digestion vessel no. 4748, Parr, France) and heated at 250 °C for 5 h. The resulting product was cooled to room temperature and dialyzed against Milli-Q water using a cellulose ester dialysis membrane for 3 days (SpectraPor®, pore size 500 -1000 kDa) in order to remove unreacted small molecules. To estimate the exact mass concentration of CDs solution, we used a Sartorius microbalance (TG 209 F3 Tarsus, Netzsch). The production yield was about 60 % and the stock solution was stored at 4 °C.

### 3.2.3 Conjugation of ampicillin onto CDs (CDs@Amp)

Ampicillin was dissolved in PBS at a concentration of 1 mg/mL. The carboxyl group of ampicillin was activated with an equimolar of EDC and NHS for 30 min. CDs dissolved in PBS at a concentration of 1 mg/mL and the ampicillin solution were mixed at a volume ratio of 2/1 at room temperature overnight. After that, CDs@Amp conjugate solution was dialyzed (SpectraPor®, pore size 500 -1000 kDa) against Milli-Q water for 3 days to remove unattached ampicillin and kept at 4 °C until use.

### 3.2.4 Characterization techniques of CDs and CDs@Amp conjugate

**UV-Vis spectroscopic measurements** were carried out using a Perkin Elmer Lambda UV/Vis 950 dual-beam spectrophotometer operating at a resolution of 1 nm. The UV-Vis spectra were recorded in quartz cuvettes of path length 1 cm between 200 and 1100 nm.

**Emission fluorescence spectra** were recorded between 220 and 800 nm using a Cary Eclipse spectrometer (Agilent, France). Solutions were excited from 200 to 420 nm in a 20 nm increment excitation (excitation and emission slit: 5 nm, scan rate: 600 nm/min).

**Fourier transform infrared (FTIR) spectra** were recorded using a ThermoScientific FTIR instrument (Nicolet 8700) at a resolution of 4  $\text{cm}^{-1}$ . Dried CDs (around 1 mg) was mixed with KBr powder (200 mg) in an agar mortar. The mixture was pressed into a pellet under 10 tons of load for 2-4 min, and the spectrum was recorded immediately. A total of 16 accumulative scans were collected. The signal from a pure KBr pellet was subtracted as a background.

**Raman spectroscopy measurements** were performed with a Horiba Jobin Yvon LabRam HR MicroRaman system with a 473 nm laser diode excitation source. Visible light was focused by a 100 $\times$  objective. The scattered light was collected by a monochromator (18000 mm focal length) and detected by a CCD.

**Zeta-potential measurements** were performed using a Zeta-sizer Nano-ZS (Malvern Instruments Inc. Worcestershire, UK). CDs were diluted to 10  $\mu\text{g/mL}$  and measured in Milli-Q water at pH 7.0.

**Thermogravimetric analysis (TGA)** was carried out using a TG 209 F3 Tarsus Netzsch in the temperature range of 30 to 980 °C under nitrogen flow with a heating rate of 10 °C/min.

**Atomic force microscopy (AFM)** measurements (NT-MDT Solver Pro-M type apparatus) were carried out in ambient air, in the tapping (non-contact) mode, with commercial standard silicon-nitride tip with a radius of approximately 10 nm (NT-MDT NGS01/Au). The

samples were prepared by dropping an aqueous CDs suspension on silicon surfaces and dried at 37 °C.

#### → Quantum yields measurements

Quinine sulfate (0.1 M H<sub>2</sub>SO<sub>4</sub> as a solvent; QY = 0.54) was chosen as reference. The quantum yield of CDs (in PBS) was determined by slope method [44] by comparing the integrated photoluminescence intensity and absorbance of each sample with that of reference. The quantum yield was calculated using the following equation:

$$\phi_x = \phi_{st} (K_x/K_{st}) (\eta_x/\eta_{st})^2$$

where  $\phi$  is the quantum yield,  $K$  is the slope determined by the curves and  $\eta$  is the refractive index of the solvent. The subscript “st” refers to the standard with the known quantum yield and “x” for the sample. In order to minimize re-absorption effects, absorption in the 10 mm fluorescence cuvette was kept below 0.10 at the excitation wavelength (360 nm). For these aqueous solutions,  $\eta_x/\eta_{st}=1$ . Series of concentrations of both the reference and samples were measured to obtain the slopes of the curves.

#### → Quenching of fluorescence of CDs in solution

Different concentrations of ampicillin were mixed with CDs, and after 12 h, the samples fluorescence spectra were recorded at 350 nm excitation wavelength.

#### → Quantification of amino groups by a modified Kaiser test

The primary amino groups were quantified using a modified photometric assay based on the Kaiser test reported by [65]. Briefly, the amino functionalized CDs powder (0.25 – 1 mg/mL) was dissolved in 1 mL Milli-Q water. To this suspension was added 1 mL of the buffer solution (1) and then sonicated for 15 min. After that, 1 mL of KCN solution (2) and 1 mL of phenol solution (3) were added and the suspension was heated at 120 °C for 10 min; 1 mL of ninhydrin solution (4) was added and heated for another 10 min. After the solution was cooled to room temperature 5 mL of ethanol was added (5).

1. *Buffer solution:* 36g sodium acetate was dissolved in 6.9 mL of acetic acid and filled with Milli-Q water until a volume of 100 mL.
2. *KCN solution:* 2 mL of 0.03 M KCN solution were diluted to a volume of 100 mL with pyridine.
3. *Phenol solution:* 80 g phenol were dissolved in 20 mL of ethanol.
4. *5 % ninhydrin solution:* 5 g of ninhydrin were dissolved in 100 mL of ethanol.
5. *60 % ethanol solution.*

#### → Singlet oxygen (<sup>1</sup>O<sub>2</sub>) detection

Singlet oxygen generation was measured through the chemical oxidation of an aqueous solution of 9,10-anthracenediylbis(methylene)dimalonic acid (ABDA) (10 μM) in presence of CDs under visible light irradiation. The decrease in the ABDA absorbance at 262 nm was monitored at several time intervals. The light emitted by a visible lamp (Spot Light Source, 420 nm – 700 nm, L9566-03, Hamamatsu, Japan) was focused onto a quartz cuvette (1 cm path length and 2 mm width) containing 1 mL of the solution.

### 3.2.5 The *in vitro* cytotoxicity study and cellular uptake

**Cytotoxicity Assay.** The HeLa cell line derived from cervical carcinoma from a 31 year old female [ATCC® CCL-2™, ECACC, Sigma Aldrich, Saint-Quentin Fallavier, France] and Caco-2 cell line derived from colorectal adenocarcinoma from a 72 year old man [ATCC® HTB-37™] were cultured and maintained in Dulbecco’s Modified Eagle’s medium (DMEM, Gibco®)



supplemented with 10 % fetal bovine serum (FBS, Gibco®) and 1 % penicillin-streptomycin (Gibco®) in a humidified incubator at 37 °C and 5 % CO<sub>2</sub>. Cells were seeded at a density of 10<sup>4</sup> cells/well in a 96-well plate and grown for 24 h before assay. The culture medium was replaced with a fresh medium that contains the CDs. The final concentrations of CDs were 12.5, 25, 50, 100 and 200 µg/mL. After 24 h, the old medium was aspirated and cells were washed three times with PBS. The cell viability was evaluated using Uptibblue (Interchim) method. Briefly, 10 µL of the Uptibblue solution were added to each well containing 100 µL of DMEM with 10% FBS and the plate was incubated for 4 h in the humidified incubator. The fluorescence of each well at 570 nm was measured using a microplate reader (PHERAstar FS, BMG LABTECH GmbH, Germany). Each condition was replicated five times and the mean absorbance value of non-exposed cells was taken as 100 % cellular viability.

**Cell imaging.** HeLa cells were seeded in a 24-well plate with sterile coverslips on the bottom at a density of  $2 \times 10^5$  cells/well and grown for 24 h before assay. The CDs and CDs@Amp solutions were diluted to a final concentration of 100 µg/mL by DMEM without serum. After incubation for 24 h, the HeLa cell monolayer was washed three times with PBS, fixed on a slide with 4 % paraformaldehyde at room temperature for 15 min and then stained with 0.2 µg/mL DAPI in PBS at room temperature in the dark for 5 min. After gentle washing with PBS for 3 times, the coverslips were mounted on glass slides and observed using a Nikon A1-R (Nikon Instruments, tempe, AZ) laser confocal microscope.

### 3.2.6 Evaluation of the photodynamic properties

HeLa cells were seeded at a density of 10<sup>4</sup> cells/well in a 96-well plate and grown for 24 h before assay. The culture medium was replaced with a fresh medium containing CDs at different concentrations. After 4 h incubation, the cells were irradiated using a visible light (420 – 700 nm, 0.31 W) for 10 or 20 min. Light positive controls and dark controls (with and without CDs) were incubated. After 24 h, cell viability was evaluated using Uptibblue (Interchim) method, where the fluorescence at 570 nm is measured using a microplate reader, as above.

In **Figure 3.7** are schematically illustrated the protocol followed to study CDs cytotoxicity, cellular uptake and their photodynamic activity under visible light irradiation.

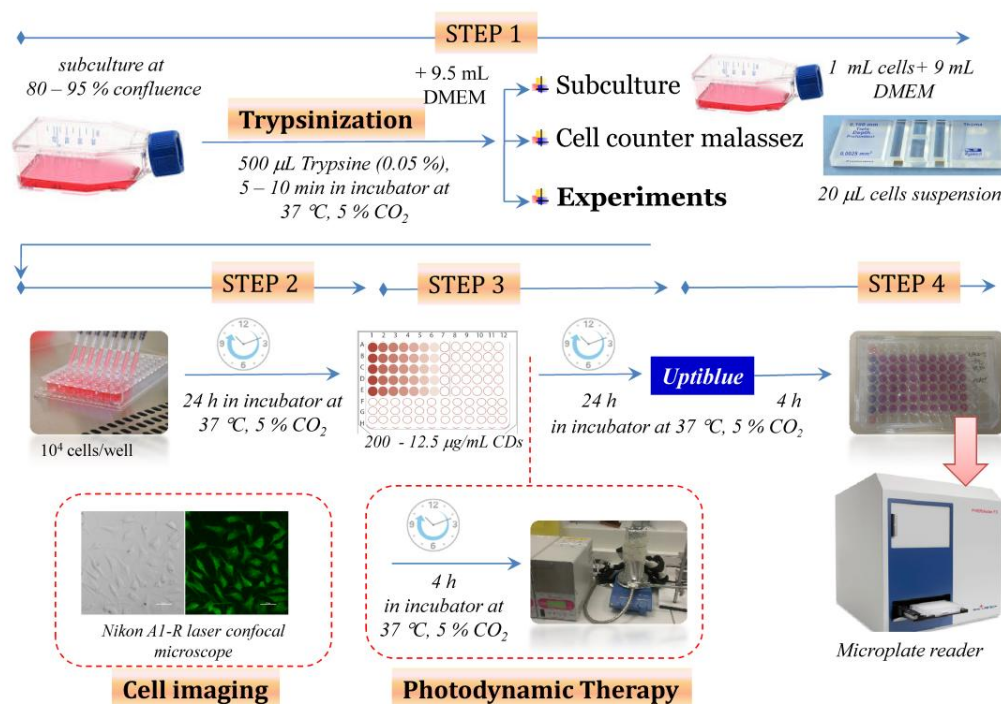


**Figure 3.7.** Schematic illustration of the different steps involved in the eukaryotic cells studies.

### 3.2.7 Antibacterial activity of CDs@Amp conjugate

**Bacteria growth.** A single *E. coli* colony from LB agar plate was inoculated overnight in LB (Luria-Bertani) medium at 37 °C with moderate shaking. The pre-culture was diluted 50-fold and allowed to continue for another 3 - 4 h, until the OD<sub>600 nm</sub> had reached 0.6-1.

**Bacterial assay.** Antibacterial activity was evaluated using two bacterial strains *E. coli* K12 – MG 1655 and *E. coli* C43. The cells were incubated in LB medium with 10, 25, 50, 100 and 200 µg/mL ampicillin (Amp), ampicillin mixed with CDs, and CDs@Amp conjugate at 37 °C for 8 h. The minimal inhibitory concentration (MIC) of ampicillin and CDs@Amp was calculated for both strains.

Growth rates and bacterial concentrations were determined by measuring optical density at 600 nm. Also, bacteria titer assay was used to evaluate the MIC and to determine the residual concentration of bacteria in wells. To perform a titer assay, 10-fold dilutions of a bacteria stock  $10^6$  cfu mL<sup>-1</sup> are prepared, and 10 µL aliquots are dropped on the LB agar. After an incubation period of 20 h at 37 °C in a conventional thermostat, colonies were counted. All the experiments were performed in triplicate.

In **Figure 3.8** is schematically illustrated the protocol followed to study the antibacterial activity of CDs@Amp conjugate towards *E. coli* cells.

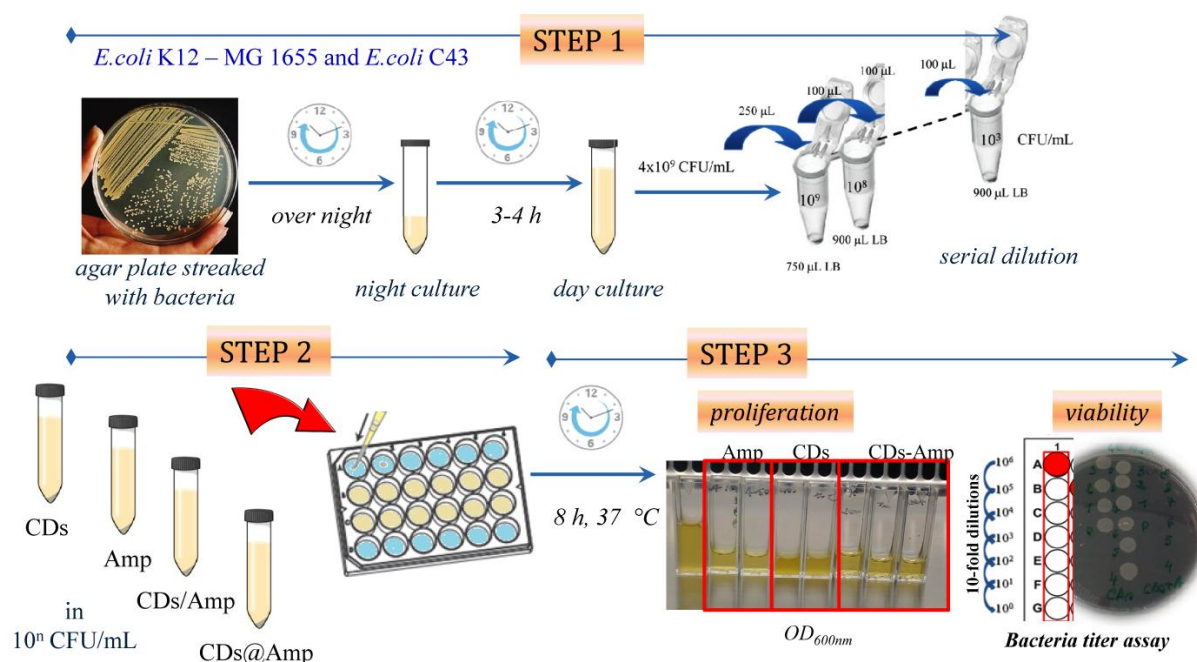


**Figure 3.8.** Schematic illustration of the different steps involved in the prokaryotic cells studies.

### 3.3 RESULTS AND DISCUSSION

#### 3.3.1 Chemical and structural characterization of fluorescent amino-functionalized carbon dots

The strategy employed for the synthesis of functionalized CDs is illustrated in **Figure 3.9** and it is based on the hydrothermal approach using citric acid as a carbon source and ethylenediamine as a surface passivation reagent.



**Figure 3.9.** Schematic illustration of the amino-functionalized CDs synthesis.

UV-Vis absorption and fluorescence studies were carried out to explore the optical properties of the resulting CDs. The UV-Vis spectrum of as-synthesized CDs is shown in **Figure 3.10 B**. The CDs absorption spectrum exhibits three bands at 237, 342 and 450 nm. According to the literature [33, 46, 66, 67], the shoulder peak at 237 nm, known as aromatic core section, corresponds to a  $\pi \rightarrow \pi^*$  transition of aromatic C=C bond, while the peak at 342 nm (known as surface section) is due to  $n \rightarrow \pi^*$  transition of the C=O bond and the band at 450 nm may originate from the amino functionalized surface of the CDs. The radiative relaxation of the  $n \rightarrow \pi^*$  excitation leads to fluorescence [67].

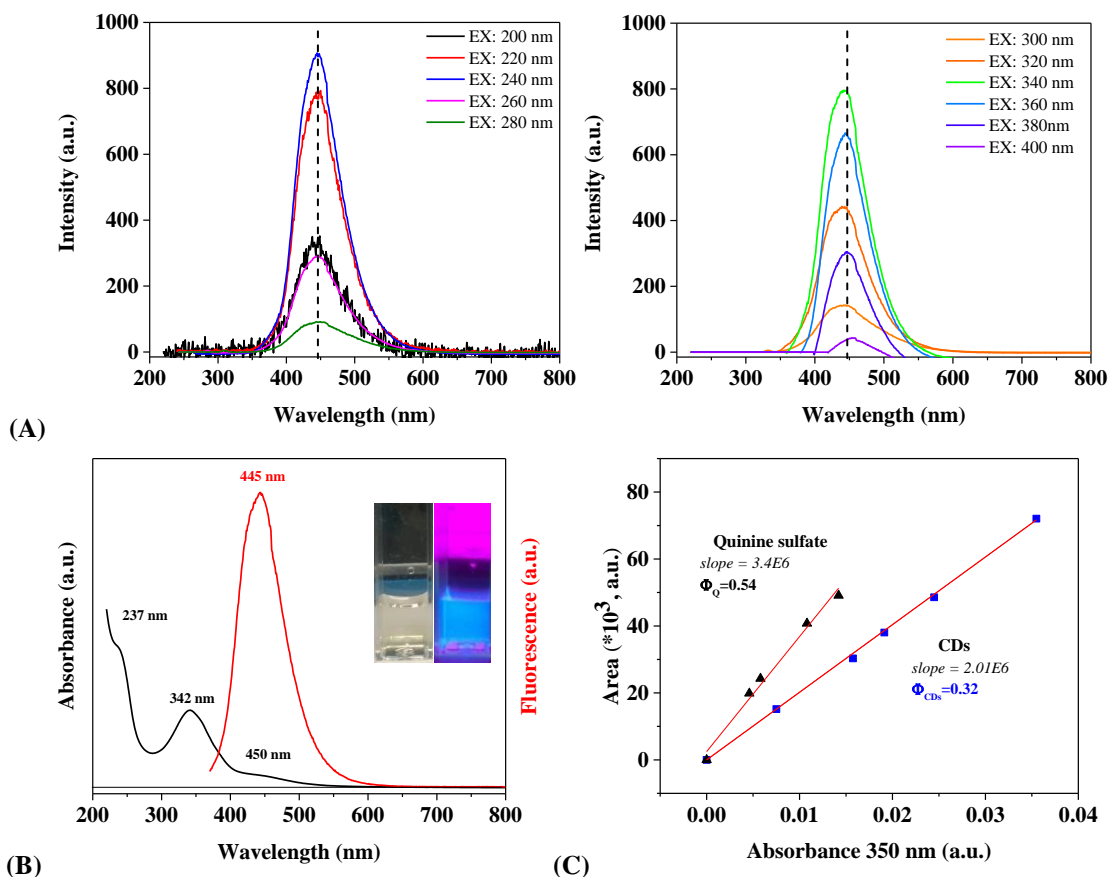


**Figure 3.10** (A) Fluorescence spectra of functionalized CDs (2.5 µg/mL) at different  $\lambda_{\text{ex}}$  from 200 to 420 nm with a 20 nm increment. (B) UV-Vis absorption (black) and fluorescence spectra (red,  $\lambda_{\text{ex}} = 350$  nm) of the CDs in aqueous solution. Insets are digital photos of the CDs alone (50 µg/mL) under sunlight and UV light irradiation ( $\lambda_{\text{ex}} = 350$  nm). (C) Plots of integrated fluorescence spectra against absorbance of quinine sulfate and CDs in PBS.

The CDs solution is yellowish under sunlight and exhibits strong blue fluorescence under UV-light (Figure 3.10 B). The fluorescence spectra exhibit an excitation ( $\lambda_{\text{ex}}$ ) independent emission ( $\lambda_{\text{em}}$ ) behavior (**Figure 3.10 A**), in agreement with [34]. The excitation-independent emission behavior may originate from the CDs uniform size and from the homogeneous distribution of emissive sites [34]. The maximum fluorescence intensity was at 445 nm under 240 nm and 340 nm excitation, similar with previous reports [3, 14] with a full width at half maximum (FWHM) of  $\sim 76$  nm. The fluorescence quantum yield (QY) of functionalized CDs was estimated to be 32 %, which is higher than that of other nitrogen-doped CDs reported before, as shown in Table 3.1 [45]. The fluorescence signal may be attributed to various functional groups, especially to nitrogen-containing functional groups, which are remarkable auxochromes and to the poly-aromatic  $\text{sp}^2$  carbon nanostructures in the CDs [68]. It is accepted that the CDs surface state play an important role in the fluorescence properties [10, 30, 60]. In addition, the CDs remain stable in aqueous solutions for at least two months at 4 °C without visible precipitation or a decrease in absorbance/fluorescence intensity (data not shown). For biomedical applications, the stability under physiological conditions is very important.

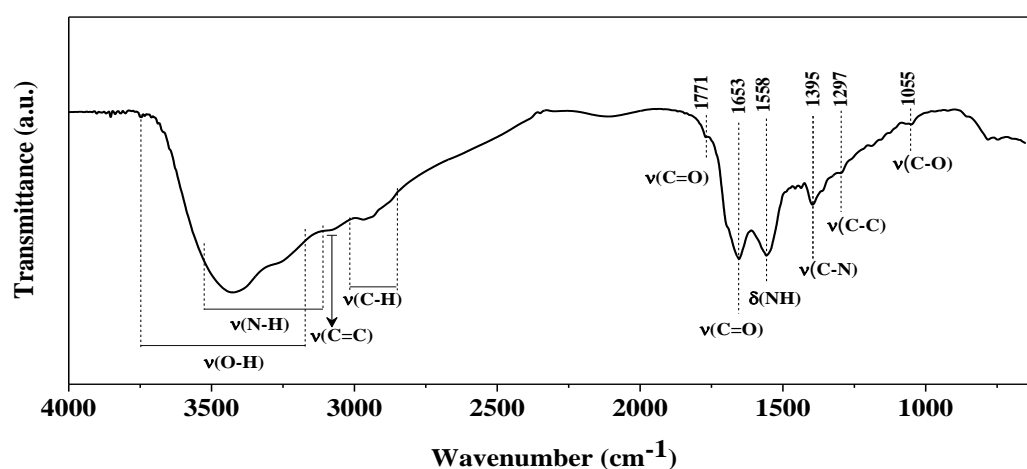


**Figure 3.11** FTIR spectrum of as-prepared CDs.

The FTIR and XPS measurements were carried out in order to get more information about the chemical composition of as-prepared CDs. In the FTIR spectrum (**Figure 3.11**), we can identify the characteristic absorption bands corresponding to stretching vibrations of O-H ( $3428 \text{ cm}^{-1}$ ), C=C-H ( $3080 \text{ cm}^{-1}$ ), C-H ( $2964 \text{ cm}^{-1}$ ), C=O ( $1771 \text{ cm}^{-1}$  and  $1653 \text{ cm}^{-1}$ ), C-C ( $1297 \text{ cm}^{-1}$ ) and C-O ( $1055 \text{ cm}^{-1}$ ). Moreover, the existence of amino-containing functional groups is confirmed by the stretching vibration and deformation bands of  $\nu_{\text{C-N}}$ ,  $\nu_{\text{C=N}}$  and  $\nu_{\text{N-H}}/\delta_{\text{N-H}}$  centered at  $3250$ ,  $1640$ ,  $1558$  and  $1395 \text{ cm}^{-1}$ , respectively. The presence of carbonyl, hydroxyl and amino groups makes CDs water soluble and expands their application field through conjugation of therapeutic agents.

**Table 3.4.** Detailed assignment of relevant features in the CDs IR spectra.

Wavenumber ( $\text{cm}^{-1}$ )	Type of vibration	Ref.
3428	O-H stretch	[15, 17, 32, 36, 61]
3250	NH stretch	[15, 17, 36, 61]
3080	C=C-H stretch	[41]
2966, 2854	C-H antisym. and sym. stretch	[17, 26, 34, 53]
1705	C=O stretch	[15, 17, 43, 56, 61]
1640	C=N stretch	[42]
1608	C=C stretch	[31]

1558	NH <sub>2</sub> deformation	[45, 53, 56]
1395	C-N stretch	[15, 17, 34, 36, 56, 61]
1297	C-C stretch	[17]
1055	C-O stretch	[15, 17, 36, 53]

As illustrated in **Figure 3.12**, the XPS survey spectrum of as-prepared CDs exhibits three peaks at 532.1, 399.1 and 285.1 eV, revealing the presence of oxygen, nitrogen and carbon. The atom ratio of C:O:N is 1:0.36:0.21. It should be noted that the nitrogen content (13.3 %) is higher compared with other nitrogen-doped CDs reported before (**Table 3.1**). We deconvoluted the high resolution spectrum of C<sub>1s</sub> into three main peaks, which are attributed to C-C, C=C (284.5 eV) and oxygen/nitrogen bonded carbon at 285.5 and 288 eV, respectively (Figure 3.12. B). The high-resolution XPS spectrum of N<sub>1s</sub> (Figure 3.12. C) displays three peaks at 398.6, 399.7 and 401.1 eV, which correspond to C-N-C, C-NH and N-C<sub>3</sub>, respectively [42, 69-71]. Moreover, the presence of C=O (531.8 eV) and C-O (533.8 eV) bonds proves that the surface of CDs was rich in oxygen containing groups (**Figure 3.12 D**).

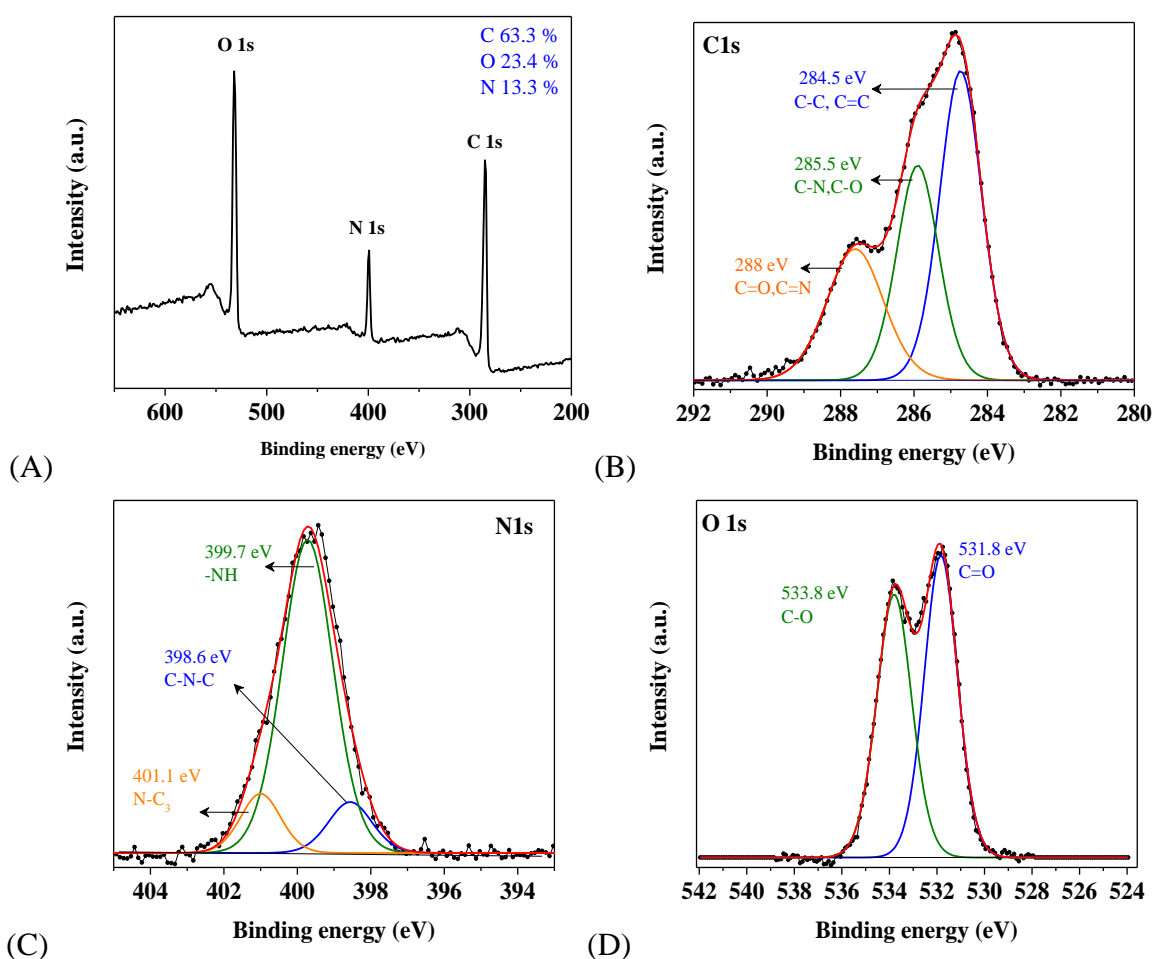


**Figure 3. 12.** XPS survey spectrum of as-prepared CDs (A), and high resolution XPS spectra of the C<sub>1s</sub> (B), N<sub>1s</sub> (C) and O<sub>1s</sub> (D).

The Kaiser test [72] is a sensitive and useful method for quantification of primary amino groups, involving the formation of Ruhemann's Blue by the reaction of ninhydrin with the primary amino groups. **Figure 3.13** shows the absorption spectra of amino functionalized carbon dots solutions after reaction with ninhydrin and the calibration curve obtained by plotting the absorbance at 570 nm for the CDs concentration ( $R^2 = 0.9967$ ). Benzylamine ( $C_6H_5CH_2NH_2$ )



was used as reference sample. According to the modified Kaiser test, the surface loading is about 0.7 mmol/g.

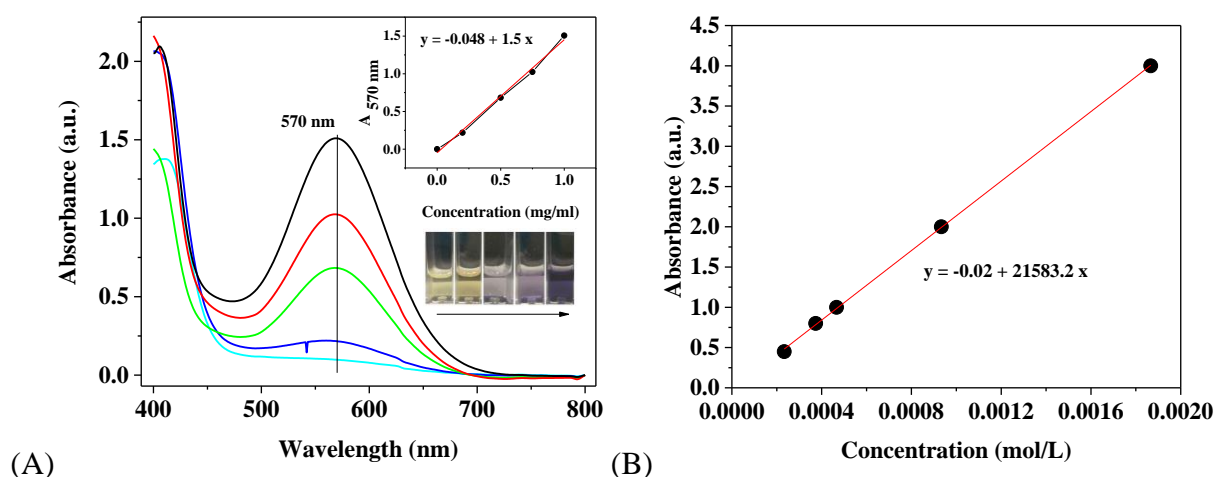


**Figure 3.13.** Quantification of primary amino groups by a modified photometric assay based on the Kaiser test reported in [65]. (A) Absorption spectra of amino-functionalized CDs solutions after reaction with ninhydrin and the calibration curve obtained by plotting the absorbance at 570 nm for different CDs concentrations. (B) The corresponding calibration curve with benzylamine.

The presence of various functional groups on the surface of the CDs not only gives a negative charge ( $\xi$ -potential =  $-14 \pm 2$  mV), but also enhances their solubility and stability (Figure 3.14).

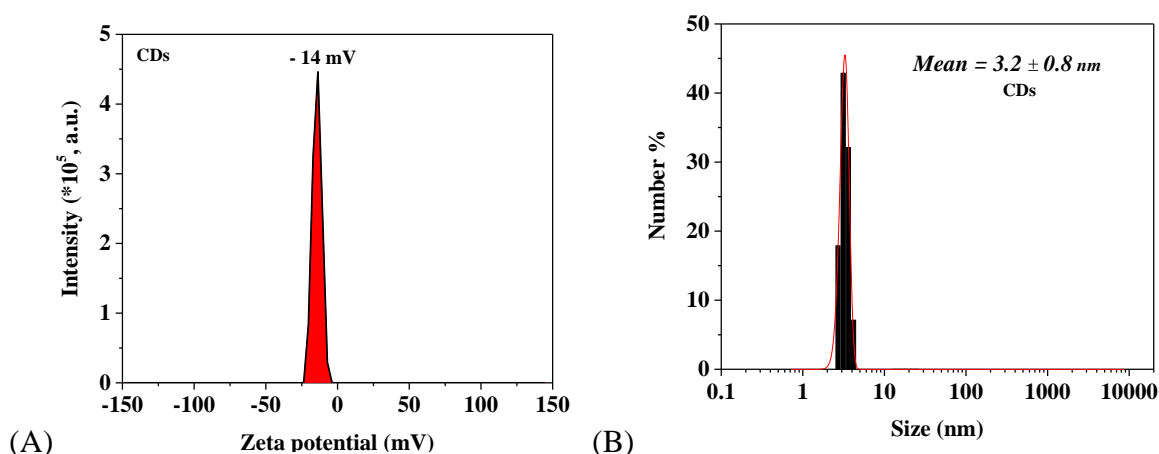


**Figure 3.14.** (A) Zeta potential plot of CDs recorded in water. (B) Particle size distribution graph of CDs in Milli-Q water as revealed by Dynamic Light Scattering.

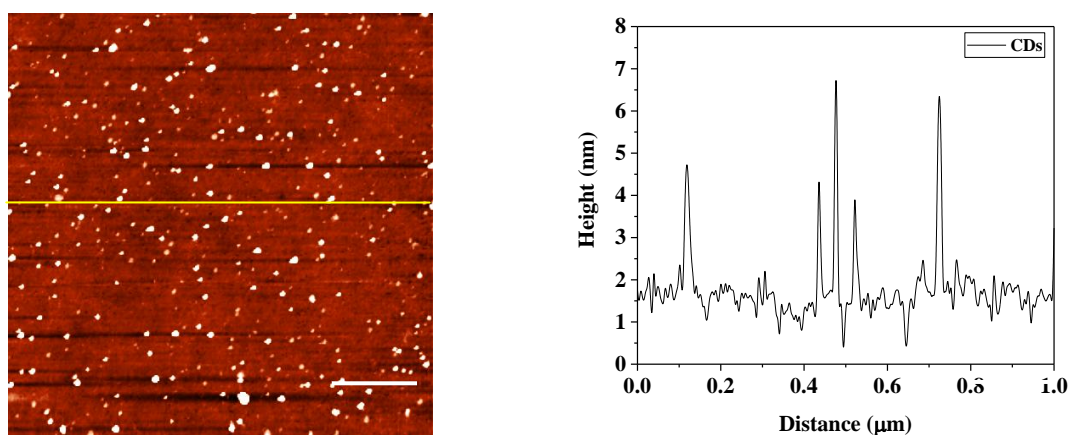


**Figure 3.15.** AFM topography image of CDs on silicon substrate, with the height profile along the line in the image.

The size and the topography of as-prepared CDs were characterized by AFM measurements. AFM images revealed the presence of spherical nanoparticles with an average height of  $6 \pm 2$  nm, which agrees with DLS results (**Figure 3.15**). According to DLS measurements the aqueous solution has an average hydrodynamic diameter of  $3.2 \pm 0.8$  nm, as seen in **Figure 3.14B**.

The Raman spectrum of as-prepared CDs displays contributions from both the G band at  $1570\text{ cm}^{-1}$  related to the in-plane vibration of  $\text{sp}^2$  carbon and the D band at  $1350\text{ cm}^{-1}$ , related to the presence of  $\text{sp}^3$  defects, as shown in **Figure 3.16**. The intensity ratio of the D and G band ( $I_D/I_G$ ) is a measure of the defects in CDs and is around 0.85. In addition, a broad peak centered at around  $2920\text{ cm}^{-1}$  corresponding to the 2D component of graphitic structures is observed [42, 73, 74].

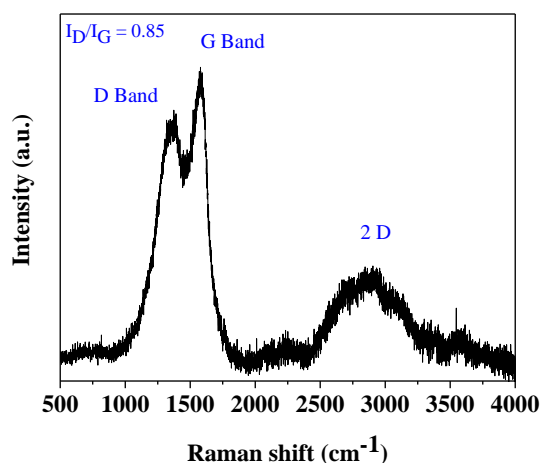


**Figure 3.16.** Raman spectrum of CDs shows contributions of both  $\text{sp}^2$  (G-band  $1590\text{ cm}^{-1}$ ) and  $\text{sp}^3$  carbons (D-band at  $1320\text{ cm}^{-1}$ ).

### 3.3.2 Carbon dots for visible-light-triggered photodynamic therapy

Photodynamic therapy (PDT) is a clinically approved cancer treatment approach, which utilizes a photosensitizer (PS), oxygen and a suitable light to kill cancer cells. The cell death, as response to PDT, is induced either by apoptosis or necrosis and depends on various factors, including concentration, physico-chemical properties and sub-cellular location of the PS, oxygen concentration, light wavelength and intensity, as well as cell type properties. Compared with conventional cancer therapies (such as surgery, chemotherapy and radiotherapy), PDT is non-invasive with high localized cytotoxicity and little collateral damage. The reactive oxygen species (ROS) affecting only the biological structures located in their close proximity. For example, the action radius of single oxygen has been estimated to be approximately 20 nm and the half life time in biological systems  $\sim 40$  ns, respectively. The current applications of PDT are often limited by the PS drawbacks, including poor water solubility, stability and selectivity, their tendency to aggregate under physiological conditions and excitation wavelength. In the last years, considerable efforts have been devoted to the development of new PDT drugs and of nano-sized carriers for the delivery of PS in order to overcome their short-comings [9, 63, 75-77]. Four types of interactions between nanoparticles and PS molecules have been reported: (i) PS embedded in hybrid nanoparticle networks, (ii) PS bound to the surface of nanoparticles, (iii) PS alongside nanoparticles and (iv) nanoparticles as the PS [78].

There are many motivations and reasons of using nanomaterials in biomedical applications, such as small size, biocompatibility, high reactivity and large surface area to mass ratio. For example, due to their size, nanomaterials are able to accumulate in pathological areas *via* the enhanced permeability and retention (EPR) effect.

An ideal PS should exhibit the following properties: low level of toxicity in absence of light exposure, absorb light in the range of 700 – 1000 nm, a high penetration depth, high absorption bands in order to minimize the PS dose needed to achieve the desired effect, water solubility, PS selective accumulation in tumor tissue for targeted therapeutic efficiency [79, 80].

It has to be highlighted that a very few studies has been focused on the intrinsic theranostic application of CDs, for simultaneous imaging and photodynamic/thermal therapy [31, 63].

As can be seen in **Figure 3.17 A**, no significant changes in cell viability were observed upon incubation of cells with various CDs concentrations ranging from 12.5 to 200  $\mu\text{g/mL}$ . It was found that more than 90% cells survive even at a CDs concentration of 200  $\mu\text{g/mL}$  for 24 h, demonstrating that CDs are suitable for biomedical applications. In addition, the confocal images (**Figure 3.17 B**) confirmed that the CDs have been internalized into the cells (possible through endocytosis), in accordance with previous studies [16, 29, 32, 39, 49, 54, 55]. The CDs labeled both the cell membrane and the cytoplasm, but also are able to penetrate the nucleus and stain the cells uniformly. In these experiments, Hoechst 33342 was used to stain the nucleus.

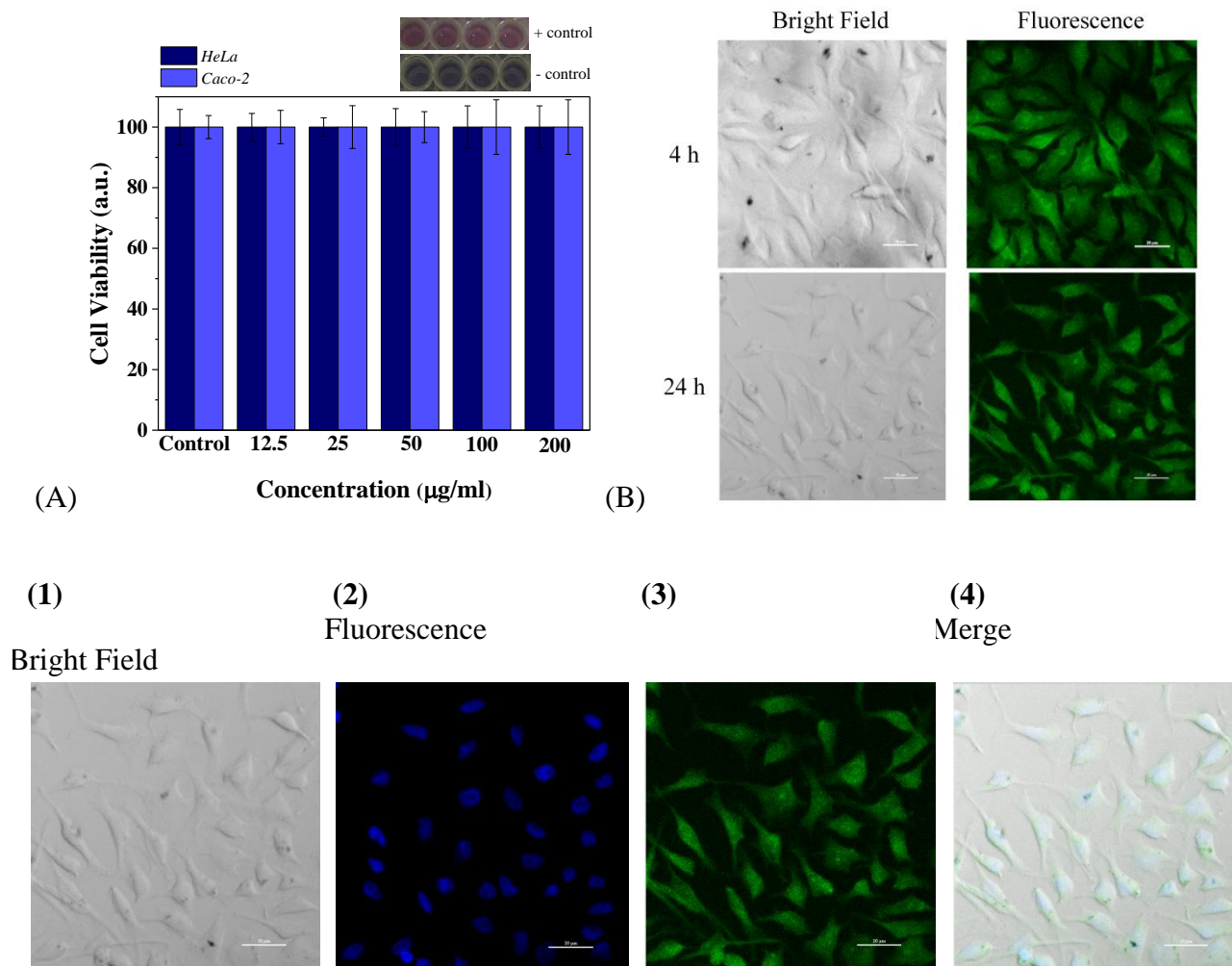


**Figure 3.17.** (A) Relative viabilities of human cervical carcinoma (HeLa) and human epithelial colorectal adenocarcinoma (Caco-2) cells after being incubated with CDs at varied concentrations for 24 h (normalized to the untreated control). The error bars represent standard deviation of five independent experiments. (B) Confocal images of HeLa cells: (1) brightfield, (2) showing the uptake of DAPI ( $\lambda_{\text{ex}} = 405 \text{ nm}$  and  $\lambda_{\text{em}} = 450 \text{ nm}$ , nuclei staining), (3) of CDs ( $\lambda_{\text{ex}} = 488 \text{ nm}$  and  $\lambda_{\text{em}} = 525 \text{ nm}$ ), (4) overlay image of 2 and 3 (Scale bar 10  $\mu\text{m}$ , cells were incubated with 100  $\mu\text{g/mL}$  CDs for 4/24 h).

The generation of singlet oxygen ( $^1\text{O}_2$ ) was measured by the use of ABDA as a selective scavenger under visible light irradiation. As shown in **Figure 3.18 A and B**, the amount of singlet oxygen increased with illumination time and with raising of the visible lamp intensity. Moreover, during the light exposure, we did not observe a significant decrease of CDs absorbance, demonstrating that CDs are stable against photo-bleaching.

The sub-cellular localization of CDs predicted the available photodynamic effects. The photodynamic activity of CDs on HeLa cells showed a decrease of the cell viability to 46 % at 100  $\mu\text{g/mL}$  and 9.4 % at 200  $\mu\text{g/mL}$ , after 10 min of irradiation (**Figure 3.19**).

The major limitation of CDs is that they absorb light in the visible region. It is known that the therapeutic window where tissue have maximum transparency to light, ideal for optical imaging and phototherapy, is between 700-900 nm. Therefore, carbon dots could be used for the simultaneous imaging and photodynamic therapy of skin cancer and tumors located near the skin.

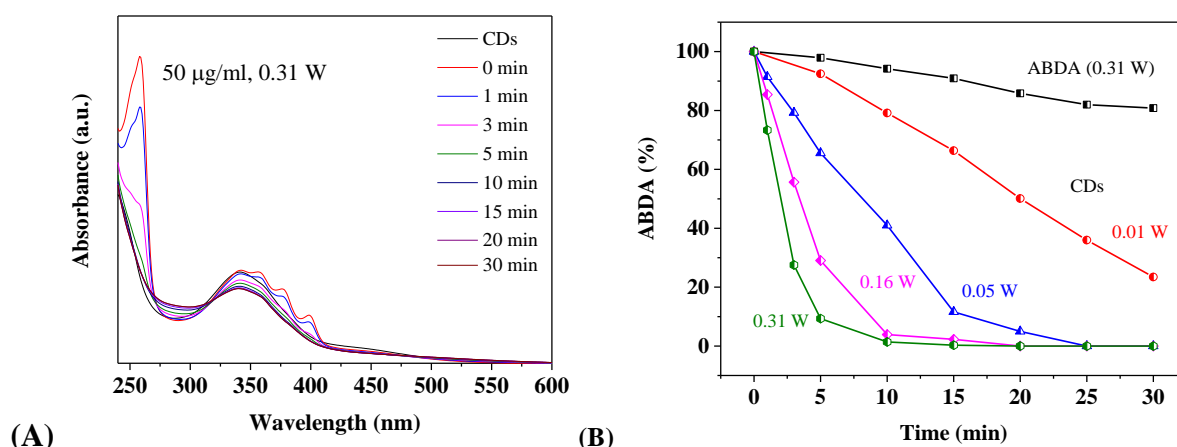


**Figure 3.18.** (A) Photodegradation of ABDA (10  $\mu\text{M}$ ) under visible light irradiation in the presence of CDs (50  $\mu\text{g/mL}$ ) under 0.31 W. (B) Decay curve of ABDA absorption at 260 nm as a function of irradiation time in the presence of CDs (50  $\mu\text{g/mL}$ ) for different powers.

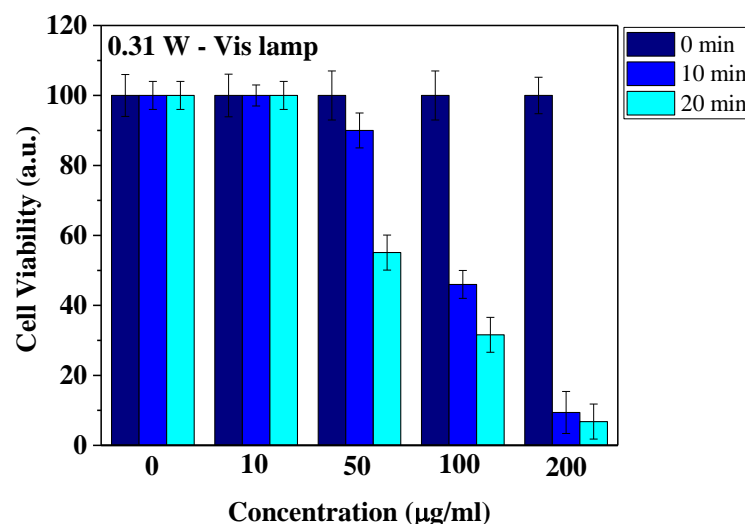


**Figure 3.19.** Relative viability of HeLa cells incubated with various concentrations of CDs upon irradiation at 0.31 W for 10 min or 20 min.

In summary, the *in vitro* results demonstrated the intrinsic theranostic application of CDs, as non-toxic imaging probe and as photodynamic agent, providing an effective approach to kill cancer cells.

### 3.3.3 Enhanced antibacterial activity of ampicillin conjugated fluorescence carbon dots

The increase of multidrug-resistant bacteria infections represents an important biomedical problem that requires the development of new antibacterial-based platforms for which pathogens will not be able to develop resistance (**Figure 3.20 B**). The use of antimicrobial nanoparticles or nanosized carriers for the delivery of therapeutic agents is a promising approach which might solve several limitations of the conventional drug delivery systems, including poor distribution in the body fluid, nonspecific interactions, poor stability against various physico-chemical agents, and drug resistance due to repetitive administration. In some situations, even the aggressive antibiotic treatment is not able to eradicate the infection due to the ability of bacteria to form biofilms.

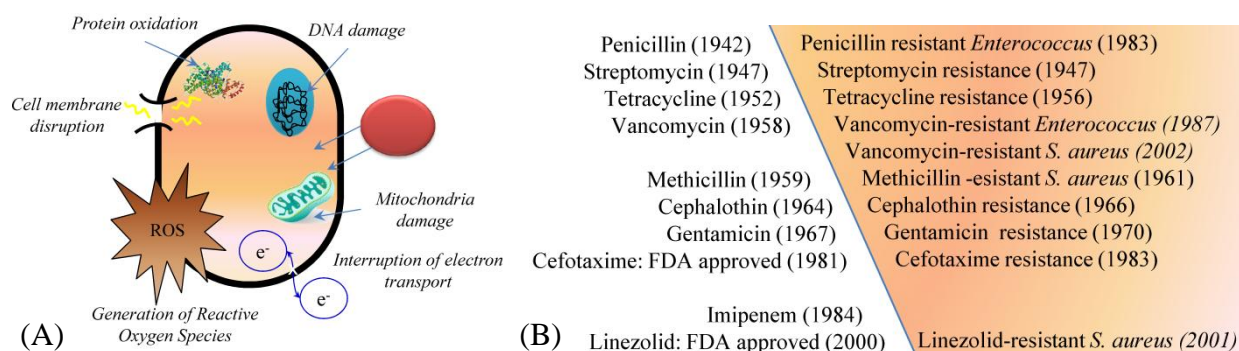


**Figure 3.20.** (A) The main mechanisms involved in the activity of antibacterial agents. (B) Evolution of antimicrobial agents and emergence of drug resistant bacteria. The form was inspired from the sketch in [81, 82].

In recent years, numerous studies have proved the antimicrobial activity of nanoparticles and nanosized platforms for efficient antibiotics delivery, to treat infectious diseases, *in vitro* as well as *in vivo* on animal models. In general, the antibacterial NPs consist of metal and metal oxides, carbon-based nanomaterials, and naturally occurring compounds (e.g. aminoglycosides). The activity of antibacterial agents is highly strain specific and may be related to several mechanisms, including the interruption of energy transduction, disruption of cell envelope, inhibition of enzyme activity and DNA synthesis or with the production of secondary products such as reactive oxygen species (**Figure 3.20 A**). Compared with Gram positive, Gram negative cell walls are more complex, consisting of an inner cytoplasmic membrane and an outer membrane that are separated by the peptidoglycan-containing periplasm. The outer membrane acts as a physical and functional barrier between the cell and its environment, providing resistance to external factors. In addition, in the outer membrane are present different biological molecules, such as lipopolysaccharides, which increase the negative charge of cell membrane and are essential for maintaining the structural integrity and the shape of the bacteria. In summary, the activity of antibacterial agents depends on both their physico-chemical properties and type of bacteria [81, 82].

Several reports exist on the attachment of antibiotics to nanoparticles (**Table 3.4**). These studies demonstrated that the resulting conjugates exhibit enhanced bactericidal activity and higher stability compared to free antibiotic drug and the antibiotic strategy employed is particularly important.

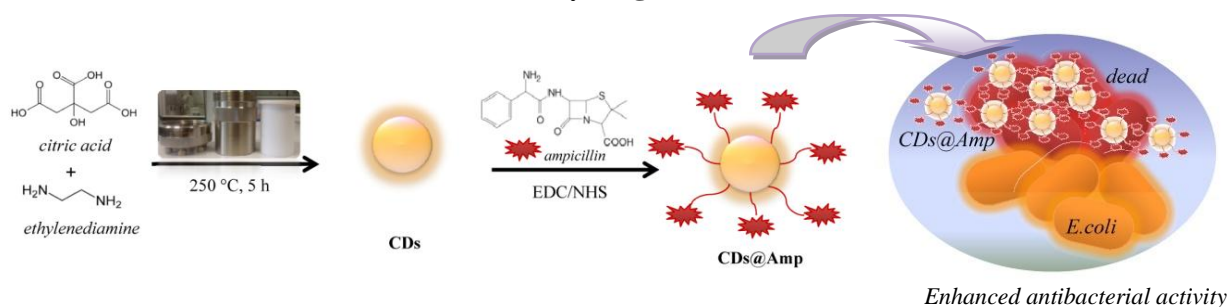
Among the different nanoparticles, a viable alternative may be the CDs as antimicrobial agents [7] or as carriers for the delivery of antimicrobial drugs due their low toxicity, high cell membrane permeability, high stability and solubility. At the moment, there are a very few studies on using of fluorescent CDs as nanosized carriers for antibiotics delivery [83, 84] or of others drugs [5, 45, 51].



**Table 3.4** Summary of nanoparticle-antibiotic conjugates for bactericidal applications.

Carrier	Antibiotic	Tested against	MIC (µg/mL)		Ref.
			Free	Sample	
C-dots	ciprofoxacin		inhibition zone (mm)		Thakur (2014) [84]
		<i>B. subtilis</i>	2.5	3.1	
		<i>S. aureus</i>	2.7	2.5	
		<i>E. coli</i>	2.6	2.5	
		<i>P. aeruginosa</i>	3.1	3.3	
		<i>E.coli</i>		1.5	Krishna (2014) [83]
MWNT	amphotericin	<i>C. parapsilosis</i>	20	1.6	Wu (2005) [85]
		<i>C. albicans</i>	>80	6.4	
		<i>C. neoformans</i>	5	0.8	
SWNT		<i>C. parapsilosis</i>	20	1.6	
		<i>C. albicans</i>	>80	13.8	
		<i>C. neoformans</i>	5	0.8	
AuNPs	ampicillin	<i>E. coli K-12 (R)</i>	-	1	Brown (2012) [86]
		<i>E. coli K-12 S</i>		1	
		<i>E. coli O157:H7 (S)</i>		1	
		<i>E. coli O91:H21 (S)</i>		2	
		<i>V. cholera (S)</i>		2	
		<i>P. aeruginosa (R)</i>		4	
		<i>E. aerogenes (R)</i>		4	
		<i>S. aureus (MRSA) (R)</i>		4	
AgNPs		<i>E. coli K-12 (R)</i>	-	1	
		<i>E. coli K-12 S</i>		1	
		<i>E. coli O157:H7 (S)</i>		1	
		<i>E. coli O91:H21 (S)</i>		1	
		<i>V. cholera (S)</i>		2	
		<i>P. aeruginosa (R)</i>		2	
		<i>E. aerogenes (R)</i>		4	
		<i>S. aureus (MRSA) (R)</i>		4	
Au NPs	ampicillin	<i>E. coli DH5α</i>	50	45	Saha <i>et al.</i> (2007) [87]
		<i>M. luteus</i>	0.52	0.45	
		<i>S. aureus</i>	0.45	0.37	
streptomycin	<i>E. coli DH5α</i>	14	7		
	<i>M. luteus</i>	22	17		
	<i>S. aureus</i>	9	5.8		
kanamycin		<i>E. coli DH5α</i>	30	12	
		<i>M. luteus</i>	22	17	
		<i>S. aureus</i>	32.5	23	

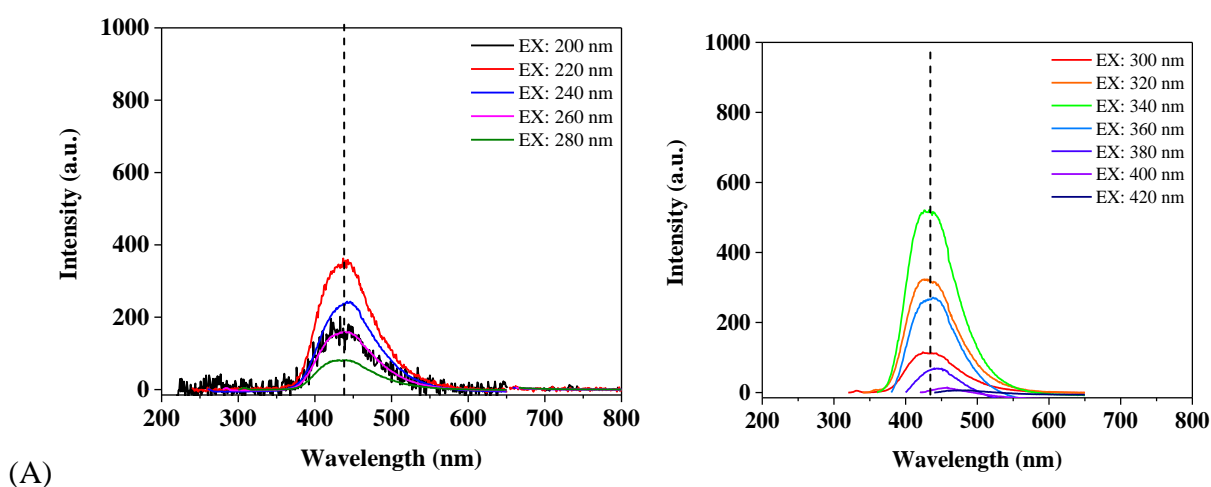
In this context, we used CDs as a carrier for the delivery of ampicillin and the antibacterial activity of CDs@Amp conjugate was tested against *Escherichia coli*. The carboxyl group of ampicillin is able to conjugate with amino groups on the CDs surface by means of the condensation reaction *via* EDC/NHS chemistry (**Figure 3.21**).



**Figure 3.21.** Schematic illustration of the synthesis of CDs and conjugation with ampicillin using EDC/NHS chemistry.

Ampicillin (Amp), part of the aminopenicillin family, was chosen in this study as a model drug due to its antibacterial activity. It is an antibiotic used to treat various bacterial infections, including respiratory tract infections, urinary tract infections, meningitis, salmonella infections and endocarditis. The ampicillin was a first-line agent used for the treatment of infections caused by *Enterococci*. It can be found in both oral and intravenous formulations. It is active against many Gram-negative and Gram-positive bacteria. Its spectrum of activity is enhanced by co-administration of *sulbactam*, a drug that inhibits lactamase, an enzyme produced by bacteria to inactivate ampicillin and related antibiotics. The action mode is related with cell wall synthesis, inactivating transpeptidases on the inner surface of the bacteria cell membrane. Various studies proved that ampicillin stability in solution is function of pH and temperature ([Sigma Aldrich](#)).

The increase of absorption in the UV region, associated with ampicillin absorption band and the decrease of fluorescence quantum yield from 32 % to 19 % suggests the conjugation of ampicillin to CDs surface (**Figure 3.22 A-C**). It should be noted that, the simple mixture of CDs with ampicillin did not have any impact on their PL properties; moreover, the emitted fluorescence can be used to monitor the distribution of the antibiotic moiety. The results confirmed the presence of same absorption and fluorescence bands for CDs@Amp conjugate as those of as-prepared CDs.



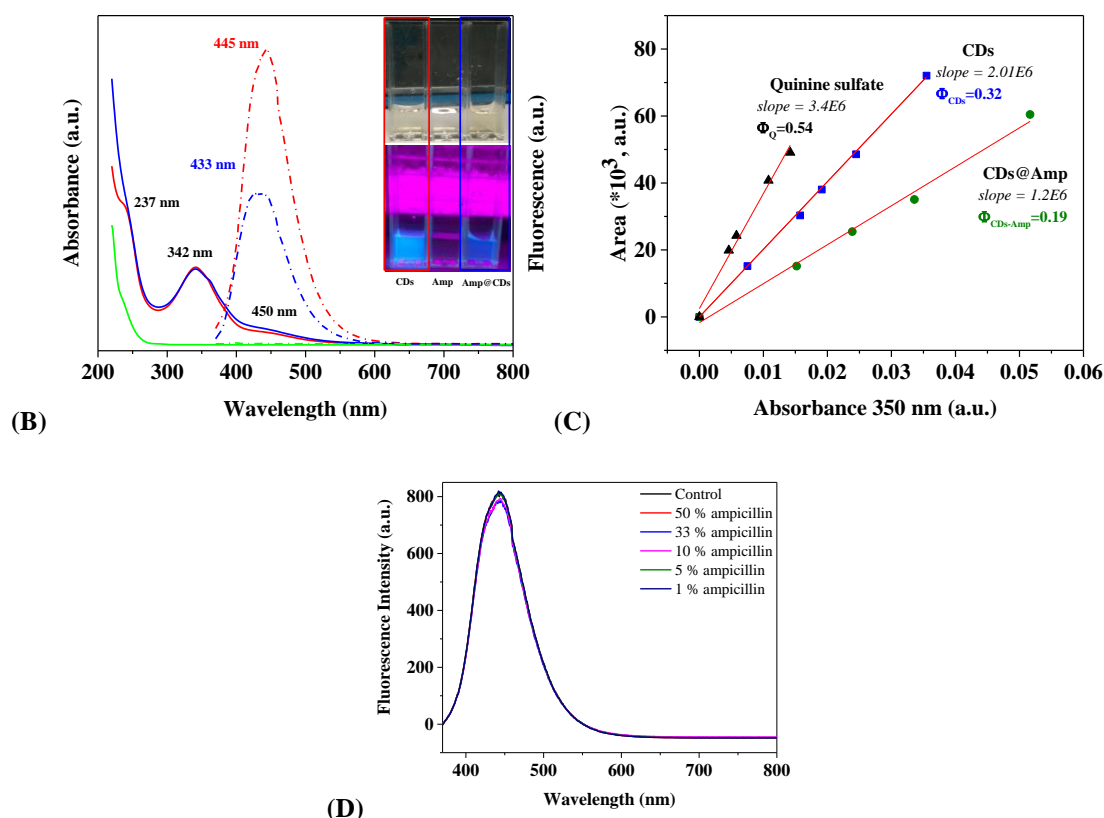


**Figure 3.23.** (A) Fluorescence spectra of CDs@Amp conjugate for different  $\lambda_{ex}$  from 200 to 420 nm with a 20 nm increment. (B) UV-Vis absorption (solid lines) and fluorescence spectra (dashed lines,  $\lambda_{ex} = 350$  nm) of the CDs (red), Ampicillin (green) and CDs@Amp conjugate (blue) aqueous solution. Insets are digital photos of the CDs alone under sunlight and UV light irradiation (350 nm). (C) Plots of integrated fluorescence spectra against absorbance of quinine sulfate, CDs and CDs@Amp conjugate in PBS. (D) Quenching of PL properties of the CDs / ampicillin mixture.

The absorption band associated with C=O at  $1771\text{ cm}^{-1}$  reflects the loading of ampicillin onto CDs (**Figure 3.24**). It is difficult to confirm the conjugation of antibiotic molecules onto CDs using FTIR technique, due to the presence of amide bonds (–CO–NH–) in the ampicillin chemical structure.

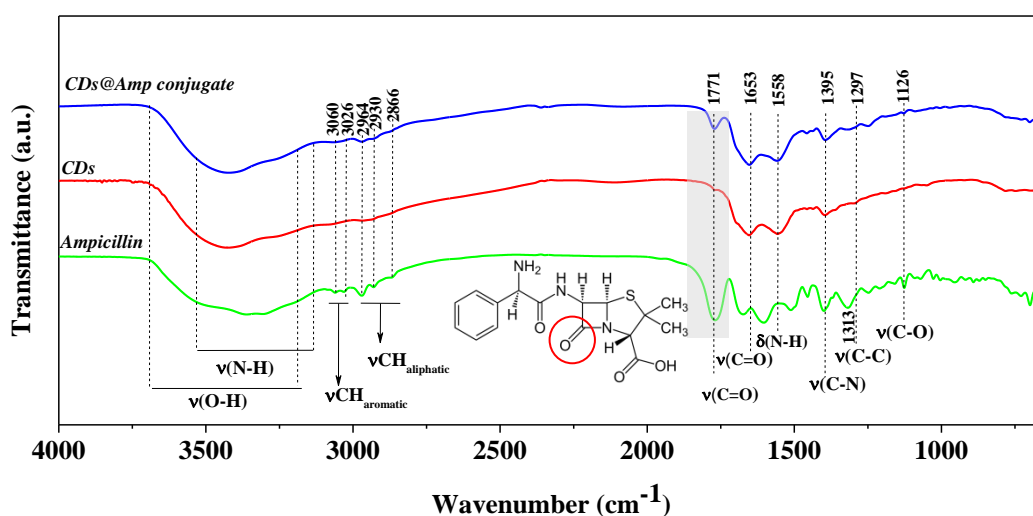


**Figure 3.24.** FTIR spectra of (a) ampicillin, (b) CDs and (c) CDs@Amp conjugate.

In order to confirm the linkage of ampicillin to CDs, thermogravimetric analysis (TGA) was performed for CDs and CDs@Amp conjugate. According to the TGA measurements, the immobilization ratio of ampicillin was calculated to be 14 %. A similar result was reported by

Krishana *et al.* [83], the amount of ciprofloxacin conjugated onto 1 mg conjugate was quantified as 96  $\mu\text{g}$  ( $\sim 10\%$ ). As can be seen in the **Figure 3.25**, CDs@Amp conjugate decomposes at a faster rate compared to as-prepared CDs and the maximum weight loss is between 150 and 450  $^{\circ}\text{C}$ , indicating the conjugation of ampicillin to CDs surface, thus higher energy is required to decompose/desorb the antibiotic from the surface.

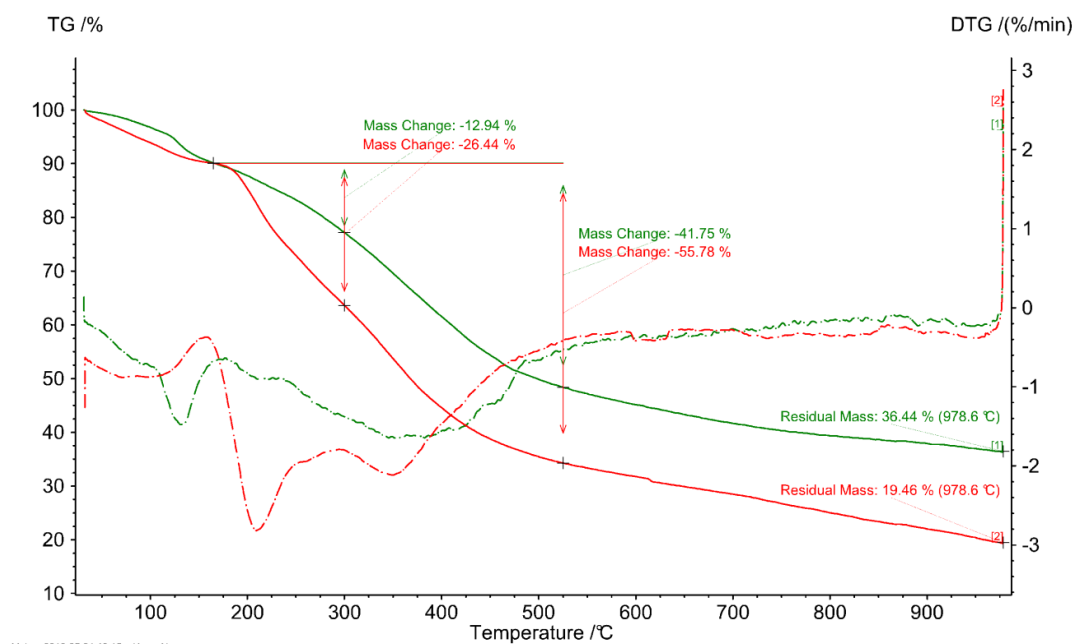


**Figure 3.25.** Thermogravimetric analysis curve of CDs and Amp@CDs conjugate.

As can be seen in **Figure 3.14 - 3.15 and 3.26 – 3.27**, after conjugation with ampicillin the average size of CDs@Amp conjugate is much larger than that of as-prepared CDs, which is probably because of the formation of aggregated structures, similar to those reported in [83]. The decrease of fluorescence intensity can be attributed to the formation of aggregates. The surface charge of the CDs@Amp conjugate remained negative ( $\xi$ -potential =  $-8 \pm 2$  mV).

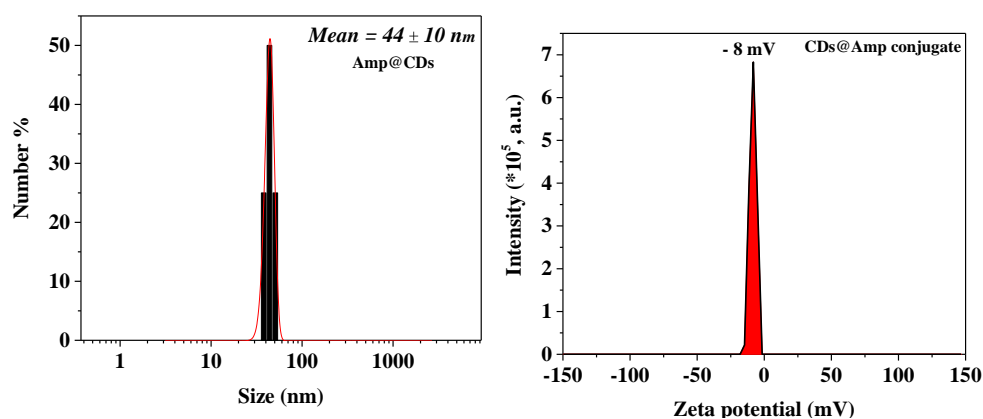


**Figure 3.26.** (A) Particle size distribution graph of CDs and Amp@CDs conjugate in Milli-Q water as revealed by Dynamic Light Scattering. (B) Zeta potential plot of CDs and Amp@CDs conjugate recorded in water.

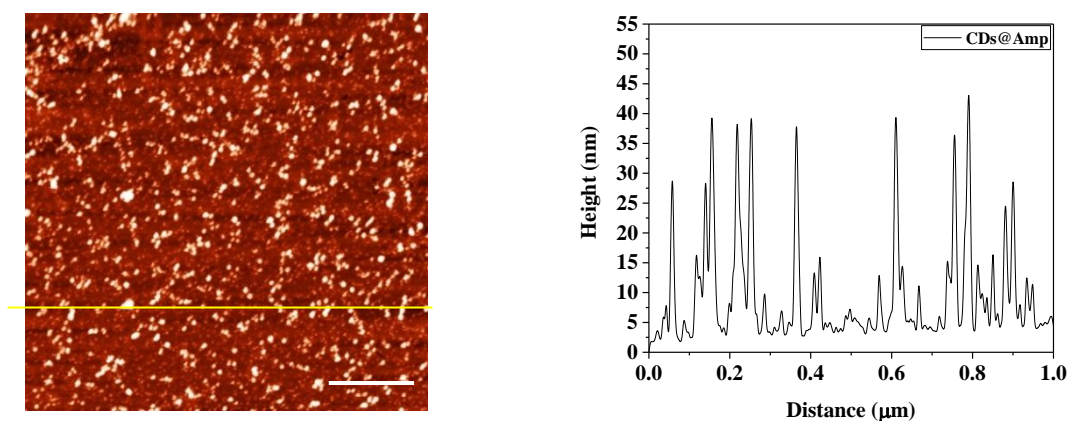


**Figure 3.27.** AFM topography images of CDs and CDs@Amp on silicon substrate, with the height profile along the line in the image.

Cytotoxicity studies showed that CDs@Amp exhibit low cell growth inhibition for both cell lines, human cervical carcinoma (HeLa) and human epithelial colorectal adenocarcinoma (Caco-2) cells up to 200  $\mu\text{g/mL}$ . The confocal images confirmed the internalization of CDs@Amp in the cells, in agreement with [85]. In addition, Wei *et al.* [85] showed that the conjugation of amphotericin B to carbon nanotubes (CNTs) reduced the toxic effects of the antibiotic on mammalian cells due to the excellent cell membrane permeability of CNTs.

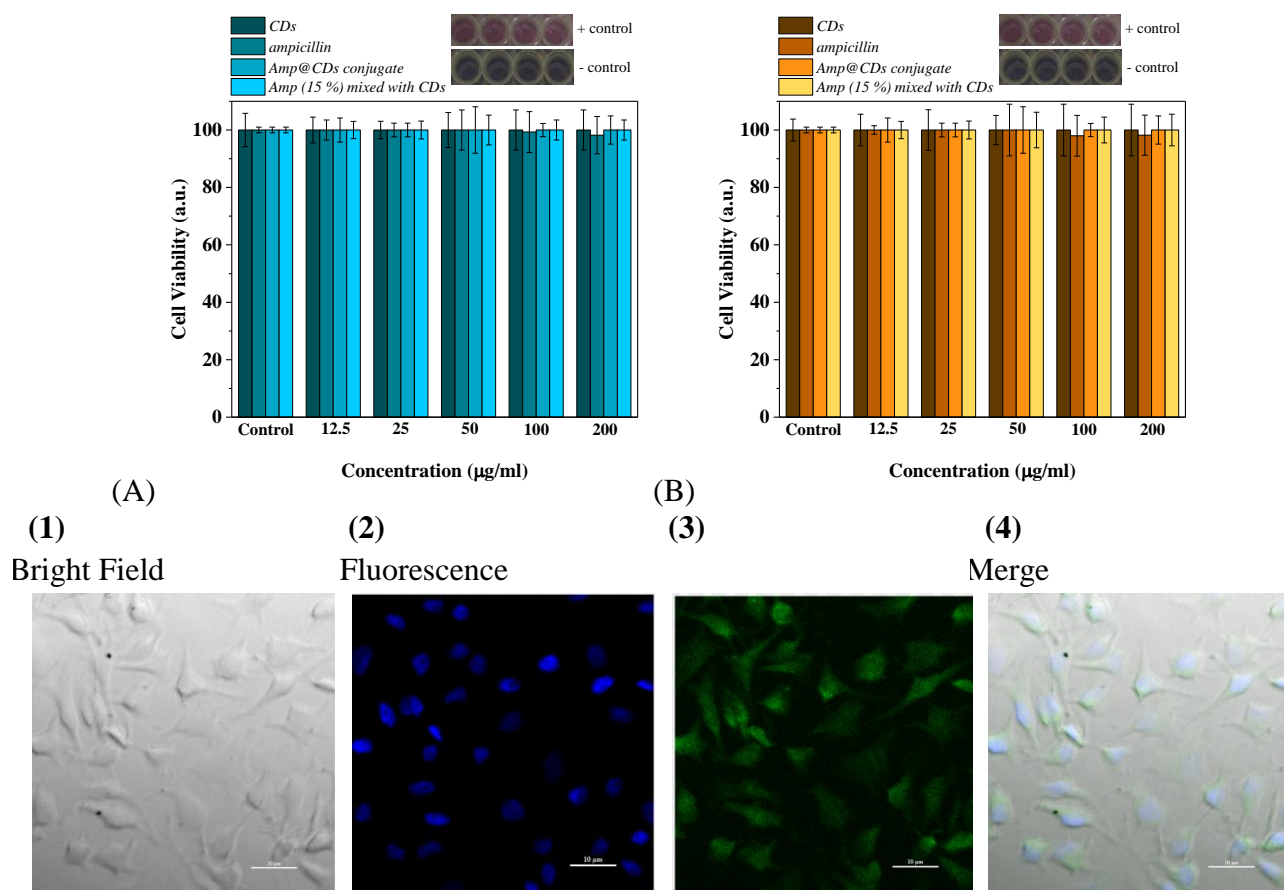


**Figure 3.28.** Relative cell viabilities of (A) human cervical carcinoma (HeLa) and (B) human epithelial colorectal adenocarcinoma (Caco-2) cells after being incubated with CDs, ampicillin, CDs@Amp conjugate and Amp (15 %) mixed with CDs at varied concentrations for 24 h (normalized to the untreated control). The error bars represent standard deviation of five independent experiments. (C) Confocal images of HeLa cells: (1) brightfield, (2) showing the uptake of DAPI ( $\lambda_{\text{ex}} = 405 \text{ nm}$  and  $\lambda_{\text{em}} = 450 \text{ nm}$ , nuclei staining) (3) of CDs ( $\lambda_{\text{ex}} = 488 \text{ nm}$  and  $\lambda_{\text{em}} = 525 \text{ nm}$ ) (4) overlay image of 2 and 3 (Scale bar 10  $\mu\text{m}$ , cells were incubated with 100  $\mu\text{g/mL}$  CDs@Amp for 24 h).



In this study, the antibacterial activity of ampicillin and CDs@Amp conjugate was evaluated using two bacterial strains *E. coli* K12 – MG 1655 and *E. coli* C43 by cell growth measurements based on the optical density at 600 nm (OD<sub>600nm</sub>) (Figure 3.29 A) and by plating method to quantify the viable cell number (Figure 3.29 B). The minimum inhibitory concentration values were determined after 8 h of incubation with different doses of free ampicillin and of CDs@Amp conjugate.

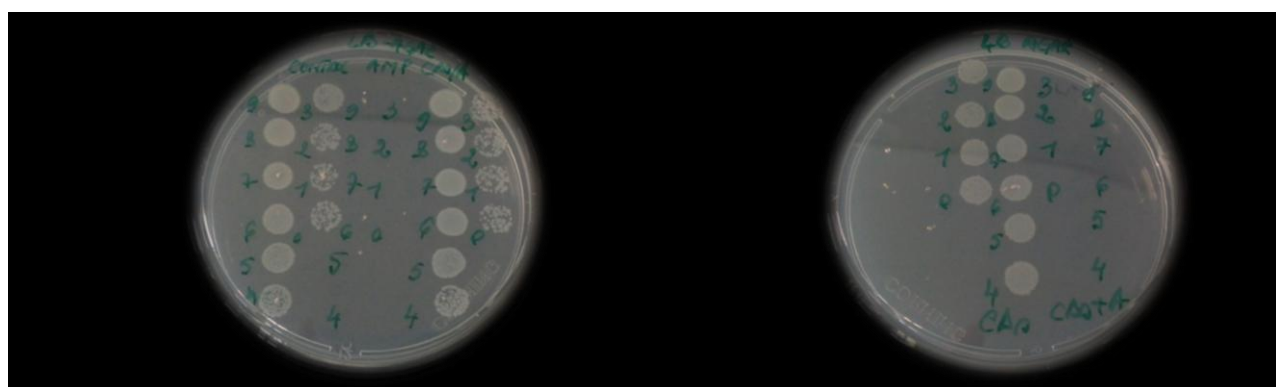
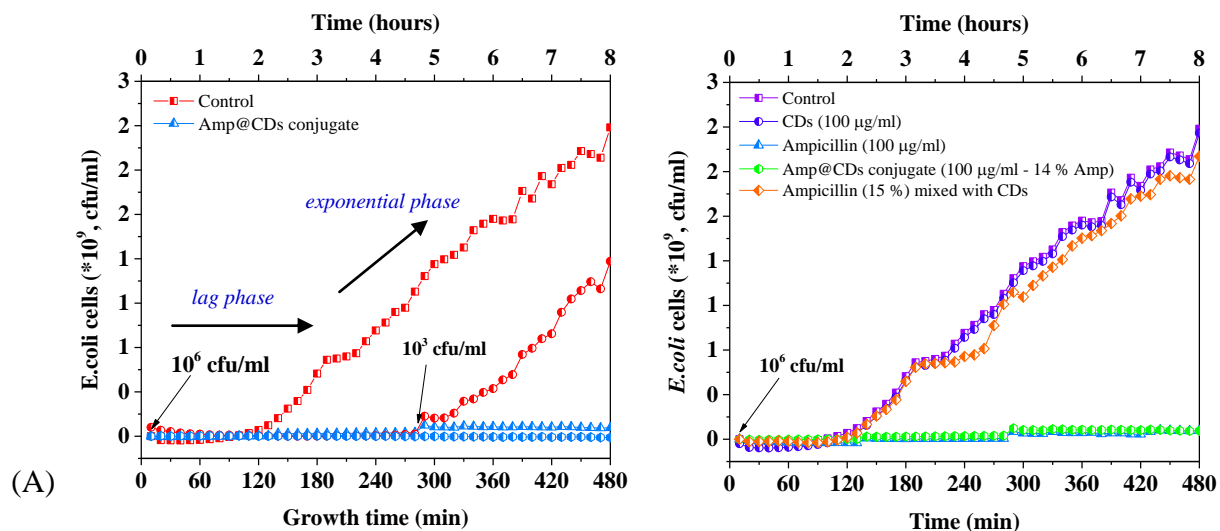


**Figure 3.29.** Bacteria dynamic growth curves in LB medium with samples and comparison of antibacterial activity of Amp@CDs conjugate with respective ampicillin mixed with CDs against *E. coli* K12 – MG 1655 by drop culture titer assay.

As seen in the Table 3.5, the covalent attachment of ampicillin to the carbon dots improved the efficacy of the antibiotic; the MIC of CDs@Amp conjugate for both strains were significantly reduced when compared to ampicillin, in agreement with other results (Table 3.4).

**Table 3.5.** Minimum concentration of ampicillin required to inhibit the growth of *E. coli* K12 and C43 cells.

Name of bacteria strain	Minimal inhibitory concentration (µg/mL)		% change in MIC
	Free ampicillin	Amp@CDs conjugate	
<i>E.coli</i> K 12	25	14	- 44 %
<i>E.coli</i> C 43	5	2	- 60 %

## CONCLUSIONS

Amine-rich and fluorescent carbon dots were synthesized by a simple hydrothermal treatment of citric acid and ethylenediamine in a Teflon autoclave reactor.

The detailed characterization of as-prepared CDs shows the signatures of nitrogen and oxygen functional groups responsible for their high aqueous dispersibility and stability. The CDs fluorescence spectra showed an excitation independent emission behavior with maximum fluorescence intensity at 445 nm at 340 nm excitation wavelength. The presence of primary amino groups on the surface of CDs was confirmed by a modified Kaiser test. According to the modified Kaiser test, the surface loading was about 0.7 mmol/g.

Cytotoxicity studies proved that as-prepared CDs exhibit low cell growth inhibition for both human cervical carcinoma (HeLa) and human epithelial colorectal denocarcinoma (Caco-2) cells up to 200 µg/mL. The confocal images showed that the CDs have been internalized into the cells, without any significant effect on cell morphology.

The low toxicity, the excellent cell membrane permeability, the high stability, solubility and fluorescence quantum yield suggest that the CDs may represent a promising alternative for biomedical applications.

The *in vitro* results demonstrated the intrinsic theranostic application of CDs, as a toxic imaging probe and as a photodynamic agent. The photodynamic activity of CDs on human cervical carcinoma (HeLa) cells led to a decrease of the cell viability to 46 % at 100 µg/mL and 9.4 % at 200 µg/mL, after 10 min of irradiation (420 – 700 nm, 0.31 W).

The presence of amino groups on the CDs surface allowed the conjugation of ampicillin to CDs surface. According to the TGA measurements the immobilization ratio of ampicillin was calculated to be 14 %. Compared with as-prepared CDs, the conjugate form displayed a decreased fluorescence quantum yield from 32 % to 19 %.

The *in vitro* results proved that CDs@Amp conjugate is more effective compared to free ampicillin towards both *E. coli* K12 – MG 1655 and *E. coli* C43 strains.

In summary, the CDs@Amp conjugate integrates the fluorescence properties of amino-functionalized CDs and the antibacterial function of ampicillin into a single unit.

## BIBLIOGRAPHY

1. Liu, Z., et al., *Nano-carbons as theranostics*. *Theranostics*, 2012. **2**(3): p. 235-237.
2. Skaltsas, T., et al., *All-Carbon Nanosized Hybrid Materials: Fluorescent Carbon Dots Conjugated to Multiwalled Carbon Nanotubes*. *The Journal of Physical Chemistry C*, 2016. **120**(16): p. 8550-8558.
3. Weng, C.-I., et al., *One-step synthesis of biofunctional carbon quantum dots for bacterial labeling*. *Biosensors and Bioelectronics*, 2015. **68**: p. 1-6.
4. Nandi, S., et al., *Bacterial detection with amphiphilic carbon dots*. *Analyst*, 2015. **140**(12): p. 4232-4237.
5. Wang, Q., et al., *Hollow luminescent carbon dots for drug delivery*. *Carbon*, 2013. **59**: p. 192-199.
6. Cao, L., et al., *Competitive performance of carbon "quantum" dots in optical bioimaging*. *Theranostics*, 2012. **2**(3): p. 295-301.
7. Meziani, M.J., et al., *Visible-Light-Activated Bactericidal Functions of Carbon "Quantum" Dots*. *ACS Applied Materials & Interfaces*, 2016. **8**(17): p. 10761-10766.
8. Xu, X., et al., *Electrophoretic analysis and purification of fluorescent single-walled carbon nanotube fragments*. *Journal of the American Chemical Society*, 2004. **126**(40): p. 12736-12737.
9. Juzenas, P., et al., *Photoactivatable carbon nanodots for cancer therapy*. *Applied Physics Letters*, 2013. **103**(6): p. 063701.
10. Hu, S.-L., et al., *One-step synthesis of fluorescent carbon nanoparticles by laser irradiation*. *Journal of Materials Chemistry*, 2009. **19**(4): p. 484-488.
11. Sun, Y.-P., et al., *Quantum-sized carbon dots for bright and colorful photoluminescence*. *Journal of the American Chemical Society*, 2006. **128**(24): p. 7756-7757.
12. Lu, J., et al., *One-pot synthesis of fluorescent carbon nanoribbons, nanoparticles, and graphene by the exfoliation of graphite in ionic liquids*. *ACS nano*, 2009. **3**(8): p. 2367-2375.
13. Zheng, L., et al., *Electrochemiluminescence of water-soluble carbon nanocrystals released electrochemically from graphite*. *Journal of the American Chemical Society*, 2009. **131**(13): p. 4564-4565.
14. Zhong, D., et al., *Employing carbon dots modified with vancomycin for assaying Gram-positive bacteria like Staphylococcus aureus*. *Biosensors and Bioelectronics*, 2015. **74**: p. 546-553.
15. Huang, H., et al., *Histidine-derived nontoxic nitrogen-doped carbon dots for sensing and bioimaging applications*. *Langmuir*, 2014. **30**(45): p. 13542-13548.
16. Liu, C., et al., *One-step synthesis of surface passivated carbon nanodots by microwave assisted pyrolysis for enhanced multicolor photoluminescence and bioimaging*. *Journal of Materials Chemistry*, 2011. **21**(35): p. 13163-13167.
17. Bhushan, B., et al., *Multifunctional carbon dots as efficient fluorescent nanotags for tracking cells through successive generations*. *Journal of Materials Chemistry B*, 2016. **4**(28): p. 4862-4871.
18. Zhu, H., et al., *Microwave synthesis of fluorescent carbon nanoparticles with electrochemiluminescence properties*. *Chemical Communications*, 2009(34): p. 5118-5120.
19. Karthik, S., et al., *Photoresponsive quinoline tethered fluorescent carbon dots for regulated anticancer drug delivery*. *Chemical Communications*, 2013. **49**(89): p. 10471-10473.
20. Pandey, S., et al., *Cysteamine hydrochloride protected carbon dots as a vehicle for the efficient release of the anti-schizophrenic drug haloperidol*. *RSC Advances*, 2013. **3**(48): p. 26290-26296.

21. Pandey, S., et al., *Carbon dots functionalized gold nanorod mediated delivery of doxorubicin: tri-functional nano-worms for drug delivery, photothermal therapy and bioimaging*. Journal of Materials Chemistry B, 2013. **1**(38): p. 4972-4982.
22. Zhu, C., et al., *Bifunctional fluorescent carbon nanodots: green synthesis via soy milk and application as metal-free electrocatalysts for oxygen reduction*. Chemical Communications, 2012. **48**(75): p. 9367-9369.
23. Lu, W., et al., *Economical, green synthesis of fluorescent carbon nanoparticles and their use as probes for sensitive and selective detection of mercury (II) ions*. Analytical Chemistry, 2012. **84**(12): p. 5351-5357.
24. Huang, H., et al., *One-pot green synthesis of nitrogen-doped carbon nanoparticles as fluorescent probes for mercury ions*. RSC Advances, 2013. **3**(44): p. 21691-21696.
25. Sahu, S., et al., *Simple one-step synthesis of highly luminescent carbon dots from orange juice: application as excellent bio-imaging agents*. Chemical Communications, 2012. **48**(70): p. 8835-8837.
26. Wang, L. and H.S. Zhou, *Green synthesis of luminescent nitrogen-doped carbon dots from milk and its imaging application*. Analytical Chemistry, 2014. **86**(18): p. 8902-8905.
27. Sun, D., et al., *Hair fiber as a precursor for synthesizing of sulfur- and nitrogen-co-doped carbon dots with tunable luminescence properties*. Carbon, 2013. **64**: p. 424-434.
28. Liu, S., et al., *Hydrothermal Treatment of Grass: A Low-Cost, Green Route to Nitrogen-Doped, Carbon-Rich, Photoluminescent Polymer Nanodots as an Effective Fluorescent Sensing Platform for Label-Free Detection of Cu (II) Ions*. Advanced Materials, 2012. **24**(15): p. 2037-2041.
29. Yang, Y., et al., *One-step synthesis of amino-functionalized fluorescent carbon nanoparticles by hydrothermal carbonization of chitosan*. Chemical Communications, 2012. **48**(3): p. 380-382.
30. Huang, P., et al., *Light-triggered theranostics based on photosensitizer-conjugated carbon dots for simultaneous enhanced-fluorescence imaging and photodynamic therapy*. Advanced Materials, 2012. **24**(37): p. 5104-5110.
31. Choi, Y., et al., *Highly biocompatible carbon nanodots for simultaneous bioimaging and targeted photodynamic therapy in vitro and in vivo*. Advanced Functional Materials, 2014. **24**(37): p. 5781-5789.
32. Wang, L., et al., *Aqueous phase synthesis of highly luminescent, nitrogen-doped carbon dots and their application as bioimaging agents*. Langmuir, 2014. **30**(47): p. 14270-14275.
33. Niu, J., et al., *Synthesis and drug detection performance of nitrogen-doped carbon dots*. Journal of Luminescence, 2014. **149**: p. 159-162.
34. Yang, Z., et al., *Nitrogen-doped, carbon-rich, highly photoluminescent carbon dots from ammonium citrate*. Nanoscale, 2014. **6**(3): p. 1890-1895.
35. Chandra, S., et al., *Luminescent S-doped carbon dots: an emergent architecture for multimodal applications*. Journal of Materials Chemistry B, 2013. **1**(18): p. 2375-2382.
36. Shi, Q.-Q., et al., *High-yield and high-solubility nitrogen-doped carbon dots: formation, fluorescence mechanism and imaging application*. RSC Advances, 2014. **4**(4): p. 1563-1566.
37. Wei, W., et al., *Non-enzymatic-browning-reaction: a versatile route for production of nitrogen-doped carbon dots with tunable multicolor luminescent display*. Scientific Reports, 2014. **4**: p. 3564.
38. Hui, D., et al., *Nitrogen-doped carbon dots derived from polyvinyl pyrrolidone and their multicolor cell imaging*. Nanotechnology, 2014. **25**(20): p. 205604.
39. Zhang, Y.-Y., et al., *A new hydrothermal refluxing route to strong fluorescent carbon dots and its application as fluorescent imaging agent*. Talanta, 2013. **117**: p. 196-202.

40. Dong, Y., et al., *Carbon-Based Dots Co-doped with Nitrogen and Sulfur for High Quantum Yield and Excitation-Independent Emission*. Angewandte Chemie International Edition, 2013. **52**(30): p. 7800-7804.
41. Li, W., et al., *Simple and Green Synthesis of Nitrogen-Doped Photoluminescent Carbonaceous Nanospheres for Bioimaging*. Angewandte Chemie International Edition, 2013. **52**(31): p. 8151-8155.
42. Ding, H., et al., *Nitrogen and sulfur co-doped carbon dots with strong blue luminescence*. Nanoscale, 2014. **6**(22): p. 13817-13823.
43. Ma, Z., et al., *One-step ultrasonic synthesis of fluorescent N-doped carbon dots from glucose and their visible-light sensitive photocatalytic ability*. New Journal of Chemistry, 2012. **36**(4): p. 861-864.
44. Zhu, S., et al., *Highly photoluminescent carbon dots for multicolor patterning, sensors, and bioimaging*. Angewandte Chemie International Edition, 2013. **52**(14): p. 3953-3957.
45. Zheng, M., et al., *Integrating oxaliplatin with highly luminescent carbon dots: an unprecedented theranostic agent for personalized medicine*. Advanced Materials, 2014. **26**(21): p. 3554-3560.
46. Wang, H., et al., *Fluorescently tuned nitrogen-doped carbon dots from carbon source with different content of carboxyl groups*. APL Materials, 2015. **3**(8): p. 086102.
47. Yang, S.-T., et al., *Carbon dots for optical imaging in vivo*. Journal of the American Chemical Society, 2009. **131**(32): p. 11308-11309.
48. Krysmann, M.J., et al., *Formation mechanism of carbogenic nanoparticles with dual photoluminescence emission*. Journal of the American Chemical Society, 2011. **134**(2): p. 747-750.
49. Qiao, Z.-A., et al., *Commercially activated carbon as the source for producing multicolor photoluminescent carbon dots by chemical oxidation*. Chemical Communications, 2010. **46**(46): p. 8812-8814.
50. Li, Q., et al., *Photoluminescent carbon dots as biocompatible nanoprobe for targeting cancer cells in vitro*. The Journal of Physical Chemistry C, 2010. **114**(28): p. 12062-12068.
51. Lai, C.-W., et al., *Facile synthesis of highly emissive carbon dots from pyrolysis of glycerol; gram scale production of carbon dots/mSiO<sub>2</sub> for cell imaging and drug release*. Journal of Materials Chemistry, 2012. **22**(29): p. 14403-14409.
52. Jana, J., et al., *One pot synthesis of intriguing fluorescent carbon dots for sensing and live cell imaging*. Talanta, 2016. **150**: p. 253-264.
53. Bhunia, S.K., et al., *Carbon nanoparticle-based fluorescent bioimaging probes*. Scientific Reports, 2013. **3**: p. 10.1038/srep01473.
54. Wang, F., et al., *Highly luminescent organosilane-functionalized carbon dots*. Advanced Functional Materials, 2011. **21**(6): p. 1027-1031.
55. Cao, L., et al., *Carbon dots for multiphoton bioimaging*. Journal of the American Chemical Society, 2007. **129**(37): p. 11318-11319.
56. Liu, C., et al., *Nano-carrier for gene delivery and bioimaging based on carbon dots with PEI-passivation enhanced fluorescence*. Biomaterials, 2012. **33**(13): p. 3604-3613.
57. Li, N., et al., *Biodistribution study of carbogenic dots in cells and in vivo for optical imaging*. Journal of Nanoparticle Research, 2012. **14**(10): p. 1-9.
58. Ahmad, Z., et al., *Alginate nanoparticles as antituberculosis drug carriers: formulation development, pharmacokinetics and therapeutic potential*. Indian Journal of Chest Diseases and Allied Sciences, 2006. **48**(3): p. 171.
59. Goh, E.J., et al., *Bioimaging of hyaluronic acid derivatives using nanosized carbon dots*. Biomacromolecules, 2012. **13**(8): p. 2554-2561.
60. Tao, H., et al., *In vivo NIR fluorescence imaging, biodistribution, and toxicology of photoluminescent carbon dots produced from carbon nanotubes and graphite*. Small, 2012. **8**(2): p. 281-290.



61. Chandra, S., et al., *One-step synthesis of amikacin modified fluorescent carbon dots for the detection of Gram-negative bacteria like Escherichia coli*. RSC Advances, 2016. **6**(76): p. 72471-72478.
62. Dou, Q., et al., *Multi-functional fluorescent carbon dots with antibacterial and gene delivery properties*. RSC Advances, 2015. **5**(58): p. 46817-46822.
63. Ge, J., et al., *Theranostics: Carbon Dots with Intrinsic Theranostic Properties for Bioimaging, Red-Light-Triggered Photodynamic/Photothermal Simultaneous Therapy In Vitro and In Vivo* (Adv. Healthcare Mater. 6/2016). Advanced Healthcare Materials, 2016. **5**(6): p. 744-744.
64. Gogoi, N., et al., *Novel carbon dot coated alginate beads with superior stability, swelling and pH responsive drug delivery*. Journal of Materials Chemistry B, 2014. **2**(26): p. 4089-4099.
65. Jarre, G., et al., *Synthesis of nanodiamond derivatives carrying amino functions and quantification by a modified Kaiser test*. Beilstein Journal of Organic Chemistry, 2014. **10**(1): p. 2729-2737.
66. Zhang, X., et al., *Color-switchable electroluminescence of carbon dot light-emitting diodes*. ACS Nano, 2013. **7**(12): p. 11234-11241.
67. Shi, L., et al., *Carbon dots with high fluorescence quantum yield: the fluorescence originates from organic fluorophores*. Nanoscale, 2016. **8**(30): p. 14374-14378.
68. Thiry, D., et al., *Plasma diagnostics for the low-pressure plasma polymerization process: A critical review*. Thin Solid Films, 2016. **606**: p. 19-44.
69. Permatasari, F.A., et al., *Role of C–N Configurations in the Photoluminescence of Graphene Quantum Dots Synthesized by a Hydrothermal Route*. Scientific Reports, 2016. **6**: p. 10.1038/srep21042.
70. Du, X., et al., *Fabrication of graphene oxide decorated with nitrogen-doped graphene quantum dots and its enhanced electrochemiluminescence for ultrasensitive detection of pentachlorophenol*. Analyst, 2015. **140**(4): p. 1253-1259.
71. Xu, Y., et al., *Nitrogen-Doped Carbon Dots: A Facile and General Preparation Method, Photoluminescence Investigation, and Imaging Applications*. Chemistry—A European Journal, 2013. **19**(7): p. 2276-2283.
72. Kaiser, E., et al., *Color test for detection of free terminal amino groups in the solid-phase synthesis of peptides*. Analytical Biochemistry, 1970. **34**(2): p. 595-598.
73. Barras, A., et al., *High Efficiency of Functional Carbon Nanodots as Entry Inhibitors of Herpes Simplex Virus Type 1*. ACS Applied Materials & Interfaces, 2016. **8**(14): p. 9004-9013.
74. Mewada, A., et al., *Swarming carbon dots for folic acid mediated delivery of doxorubicin and biological imaging*. Journal of Materials Chemistry B, 2014. **2**(6): p. 698-705.
75. Robertson, C., et al., *Photodynamic therapy (PDT): a short review on cellular mechanisms and cancer research applications for PDT*. Journal of Photochemistry and Photobiology B: Biology, 2009. **96**(1): p. 1-8.
76. Castano, A.P., et al., *Mechanisms in photodynamic therapy: part one—photosensitizers, photochemistry and cellular localization*. Photodiagnosis and Photodynamic Therapy, 2004. **1**(4): p. 279-293.
77. Jijie, R., et al., *Particle-based photodynamic therapy based on indocyanine green modified plasmonic nanostructures for inactivation of a Crohn's disease-associated Escherichia coli strain*. Journal of Materials Chemistry B, 2016. **4**(15): p. 2598-2605.
78. Paszko, E., et al., *Nanodrug applications in photodynamic therapy*. Photodiagnosis and Photodynamic Therapy, 2011. **8**(1): p. 14-29.
79. Castano, A., et al., *Mechanisms in photodynamic therapy: part one—photosensitizers, photochemistry and cellular localization*. Photodiagnosis and photodynamic therapy, 2004. **1**(4): p. 279-293.

80. Barras, A., et al., *Hypericin-loaded lipid nanocapsules for photodynamic cancer therapy in vitro*. *Nanoscale*, 2013. **5**(21): p. 10562-10572.
81. Huh, A.J. and Y.J. Kwon, "Nanoantibiotics": *A new paradigm for treating infectious diseases using nanomaterials in the antibiotics resistant era*. *Journal of Controlled Release*, 2011. **156**(2): p. 128-145.
82. Hajipour, M.J., et al., *Antibacterial properties of nanoparticles*. *Trends in Biotechnology*, 2012. **30**(10): p. 499-511.
83. Krishna, A.S., et al., *Functionalized carbon dots enable simultaneous bone crack detection and drug deposition*. *Journal of Materials Chemistry B*, 2014. **2**(48): p. 8626-8632.
84. Thakur, M., et al., *Antibiotic conjugated fluorescent carbon dots as a theranostic agent for controlled drug release, bioimaging, and enhanced antimicrobial activity*. *Journal of Drug Delivery*, 2014. **2014**.
85. Wu, W., et al., *Targeted delivery of amphotericin B to cells by using functionalized carbon nanotubes*. *Angewandte Chemie International Edition*, 2005. **44**(39): p. 6358-6362.
86. Brown, A.N., et al., *Nanoparticles functionalized with ampicillin destroy multiple-antibiotic-resistant isolates of *Pseudomonas aeruginosa* and *Enterobacter aerogenes* and methicillin-resistant *Staphylococcus aureus**. *Applied and Environmental Microbiology*, 2012. **78**(8): p. 2768-2774.
87. Saha, B., et al., *In Vitro Structural and Functional Evaluation of Gold Nanoparticles Conjugated Antibiotics*. *Nanoscale Research Letters*, 2007. **2**(12): p. 614-622.

## List of abbreviations and acronyms

**0D** - zero-dimensional  
**1D** - one-dimensional  
**3D** – three-dimensional  
**A. baumannii** - *Acinetobacter baumannii*,  
**ABDA** - 9,10-anthracenediylbis(methylene)dimalonic acid  
**AAPD** - aerosol-assisted plasma deposition  
**AA** – acrylic acid  
**AFM** – atomic force microscopy  
**APPs** – atmospheric pressure plasmas  
**APP DBD** – atmospheric pressure plasma dielectric barrier discharge  
**APTMS** – (3-aminopropyl)trimethoxysilane  
**BAECs** – bovine aorta endothelial cells  
**BSMCs** - bovine smooth muscle cells  
**C. albicans** - *Candida albicans*  
**CCK-8** – Cell counting kit - 8  
**CDs**- carbon dots  
**CDs@Amp** – carbon dots conjugated ampicillin  
**CNTs** - carbon nanotubes  
**C. parapsilosis** – *Candida parapsilosis*  
**C. albicans** - *Candida albicans*  
**C. neoformans** – *Cryptococcus neoformans*  
**CTAB** - Cetyl trimethylammonium bromide  
**DOX** – doxorubicin  
**DAPI** - 4',6'-diamidino-2-phenylindole  
**DC** – direct current  
**DMEM** - Dulbecco's Modified Eagle's Medium  
**E. coli** – *Escherichia coli*  
**E. aerogenes** - *Enterobacter aerogenes*  
**ESBL** – extended spectrum  $\beta$ -lactamase (*ESBL*)  
**EDC** - N-(3-Dimethylaminopropyl)-N'-ethylcarbodiimide hydrochloride  
**FBS** - fetal bovine serum  
**FCS** - fetal-calf serum  
**FTIR** – Fourier transform infrared spectroscopy  
**HDF** – primary human dermal fibroblasts  
**ICG** - Indocyanine Green  
**K. pneumonia** – *Klebsiella pneumonia*  
**LB** - Luria-Bertani  
**MIC** - minimum inhibitory concentration  
**MWNT-AMB** – multiwalled carbon nanotubes conjugated amphotericin  
**MRSA** - methicillin-resistant *S. aureus*  
**NPs** –nanoparticles  
**NHS** - N-Hydroxysuccinimide  
**OD** - optical density  
**OXA** - oxaliplatin  
**PEO** – polyethyleneoxide  
**ppAAc** – poly-acrylic acid plasma-polymerized films  
**PLLA** – poly (l-lactide)

**PTFE** – poly(tetrafluoroethylene)  
**pPAAc** - plasma polymerized polyallylamine coatings  
**PLLA** – poly(L-lactic acid)  
**pPS** – plasma polymerized styrene films  
**PI** - propidium iodide  
**PEI** - polyethylenimine  
**PDT** – photodynamic therapy  
**PS** – photosensitizer  
***P. aeruginosa*** - *Pseudomonas aeruginosa*  
**PDRAB** - *pan-drug-resistant A. baumannii*  
**PVP/PB NPs** – poly(vinylpyrrolidone)-coated Prussian blue nanoparticles  
**rGO-PEG-Au NRs** – Au nanorods modified with PEG-functionalized reduced graphene oxide  
**QY** – quantum yield  
***S. aureus*** – *Staphylococcus aureus*  
**SEM** – scanning electron microscopy  
**TMDSO** – tetramethyldisiloxane  
**TH-S** - thioflavin S  
**SLM** – standard liter per minute  
***S. aureus*** - *Staphylococcus aureus*  
***S. pyogenes*** - *Staphylococcus pyogenes*,  
***S. saprophyticus*** – *Staphylococcus saprophyticus*  
***S. aureus*** – *Staphylococcus aureus*  
**SWNT –AMP** – single carbon nanotubes conjugated amphotericin  
**TTDDA** - 4,7,10-trioxa-1,13-tridecanediamine  
***V. cholerae* THR7000** - *Vibrio cholerae* THR7000  
**VRE1-** *vancomycin-resistant Enterococcus faecalis*  
**VRE4** - *vancomycin-resistant Enterococcus faecium*.  
**WCA** - water contact angle  
**XPS**- X-ray photoelectron spectroscopy

## SCIENTIFIC ACTIVITY

### LIST OF PUBLICATIONS

#### 1. ISI papers published during the PhD period

1. Volodymyr Turcheniuk, Viktoria Raks, Rahaf Issa, Ian R. Cooper, Peter J. Cragg, **Roxana Jijie**, Nicoleta Dumitrascu, Lyuba I. Mikhalovska, Alexandre Barras, Vladimir Zaitsev, Rabah Boukherroub, Sabine Szunerits, *Antimicrobial activity of menthol modified nanodiamond particles*, *Diamond & Related Materials* 57(2015)2-8.  
**AIS: 0.482**, IF: 2.125, Cited by 2 publications  
Most Downloaded Diamond and Related Materials Articles (August 2015)
2. K. Hensel, K. Kučerová, B. Tarabová, M. Janda, Z. Machala, K. Sano, C. T. Mihai, M. Ciorpac, L. D. Gorgan, **R. Jijie**, V. Pohoata and I. Topala, *The effects of air transient spark discharge and helium plasma jet on water, bacteria, cells and biomolecules*, *Biointerphases* 10(2)(2015) 029515.  
**AIS: 0.665**, IF: 2.105, Cited by 3 publications  
Most Read Biointerphases Author (June 2015)
3. **Roxana Jijie**, Tetiana Dumych, Li Chengnang, Julie Bouckaert, Kostiantyn Turcheniuk, Charles-Henri Hage, Laurent Heliot, Benoit Cudennec, Nicoleta Dumitrascu, Rabah Boukherroub and Sabine Szunerits, *Particle-based photodynamic therapy based on Indocyanine green modified plasmonic nanostructures for inactivation of Crohn's disease-associated Escherichia coli*, *Journal of Materials Chemistry B*, 2016, **4**, 2598-2605.  
**AIS: 0.971**, IF: 4.872, Cited by 1 publication
4. Maaoui Houcem, **Roxana Jijie**, GuoHui Pan, Djamel Drider, Delphine Caly, Julie Bouckaert, Nicoleta Dumitrascu, Radouane Chtourou, Sabine Szuneritz, Rabah Boukherroub, *A 980 nm driven photothermal ablation of virulent and antibiotic resistant Gram-positive and Gram-negative bacteria strains using Prussian blue nanoparticles*, *Journal of Colloid and Interface Science*, 480 (2016) 63-68.  
**AIS: 0.805**, IF: 3.782
5. Ilarion Mihaila, Valentin Pohoata, Roxana Jijie, Andrei Vasile Nastuta, Ioana Alexandra Rusu, Ionut Topala, *Formation of positive ions in hydrocarbon containing dielectric barrier discharge plasma*, *Advances in Space Research* (2016) in press.  
**AIS: 0.462**, IF: 1.409

**AIS: 3.385**



*Publications not directly related to this thesis:*

1. **Roxana Jijie**, Valentin Pohoata and Ionut Topala, *Thermal behavior of bovine serum albumin after exposure to barrier discharge helium plasma jet*, Applied Physics Letters, **101** (2012) 144103.  
**AIS: 1.045**, IF: 3.142, Cited by 4 publications
2. **Roxana Jijie**, Cristina Luca, Valentin Pohoata and Ionut Topala, *Effects of Atmospheric Pressure Plasma Jet on Pepsin Structure and Function*, IEEE Transactions On Plasma Science, **40 (11)** (2012) 2980-2985.  
**AIS: 0.270**, IF: 0.958, Cited by 1 publication

**AIS: 4.7**

**2. Scientific articles published in extenso in international journal without impact factor**

1. Delia Ciubotaru, **Roxana Jijie**, Valentin Pohoata, Ilarion Mihaila, Andrei Vasile Nastuta, Marius Dobromir, Ionut Topala, *Spectroscopic studies of gas phase and deposited films in He/H<sub>2</sub>/CnH<sub>2n+2</sub> atmospheric pressure plasmas*, 23<sup>rd</sup> Europhysics Conference on Atomic and Molecular Physics of Ionized Gases (2016).
2. **Roxana Jijie**, Tedora Teslaru, Marius Dobromir, Valentin Pohoata, Ionut Topala, Rabah Boukherroub, Nicoleta Dumitrascu, *Copolymerization and Water Stability of Atmospheric Pressure Plasma Polymerized Films from Allylamine and Styrene*, ISPC 22 – 22<sup>nd</sup> International Symposium on Plasma Chemistry (2015).
3. Ionut Topala, **Roxana Jijie**, Andrei Nastuta, Ioana Rusus, Ilarion Mihaila and Valentin Pohoata, *Considerations on the use of atmospheric pressure plasma to generate complex molecular environments with relevance for molecular astrophysics*, ISPC 22 – 22<sup>nd</sup> International Symposium on Plasma Chemistry (2015).
4. **Roxana Jijie**, Tedora Teslaru, Marius Dobromir, Valentin Pohoata, Ionut Topala, Alexandre Barras, Rabah Boukherroub, Nicoleta Dumitrascu, *Influence of carrier gas on the behavior of plasma polymerized polystyrene films in aqueous media*, Proceedings of the XXXII International Conference on Phenomena in Ionized Gases - ICPIG (2015).
5. Teodora Teslaru, **Roxana Jijie**, Marius Dobromir, Valentin Pohoata, Ionut Topala, V. Antoci, C.-I. Ciobanu, Nicoleta Dumitrascu, *On the polymerization reactions of thiophene monomers under atmospheric plasma conditions*, Proceedings of the XXXII International Conference on Phenomena in Ionized Gases - ICPIG (2015).
6. **Roxana Jijie**, Lavinia Curecheriu, George Rusu, Valentin Pohoata, Ionut Topala, Rabah Boukherroub, Nicoleta Dumitrascu, *Copolymerization of ethylene glycol with styrene: synthesis, characterization and stability in biological media*, JNRDM, 26-28 May 2014, Lille, France.

### 3. International conference

#### □ 2013- 2016

1. K Hensel, M. Janda, K. Tarabova, B. Tarabova, Z. Machala, **R. Jijie**, C. T. Mihai, L. Gorgan, I. Topala, *Inactivation of bacteria and cells by DC transient spark discharge*, 5<sup>th</sup> International Conference on Plasma Medicine (ICPM5), 18 -23 May 2014, Nara, Japan (poster: 19–P03-13)
2. **Roxana Jijie**, Lavinia Curecheriu, George Rusu, Valentin Pohoata, Ionut Topala, Rabah Boukherroub, Nicoleta Dumitrascu, *Copolymerization of ethylene glycol with styrene: synthesis, characterization and stability in biological media*, JNRDM, 26-28 May 2014, Lille, France (poster)
3. **Roxana Jijie**, Lavinia Curecheriu, George Rusu, Marius Dobromir, Valentin Pohoata, Ionut Topala, Rabah Boukherroub, Nicoleta Dumitrascu, *Deposition and characterization of plasma (co)polymerized films at the interface with biological medium*, High-Tech Plasma Processes, 22-27 June 2014, Toulouse, France (poster: PS1-19)
4. **Roxana Jijie**, Valentin Pohoată, Ionuț Topală, Nicoleta Dumitrașcu, *Study of plasma polymerization process using atyrene and ethylene glycol vapors*, 13<sup>th</sup> International Conference on Global Research and Education (inter-Academia), 10-12 September 2014, Riga, Latvia (*short oral presentation of special poster session for young researchers*, iAY 22)
5. **R. Jijie**, V. Turcheniuk, T. Filipiak, J. Bouckaert, M. Dobromir, A. Barras, S. Szunerits, R. Boukherroub, *Surface Plasmon Resonance: a useful technique for studying bacteria ashesion on menthol-functionalized surfaces*, 10<sup>th</sup> International Conference On Physics Of Advanced Materials (ICPAM-10), 22-28 September 2014, Iasi, Romania (poster: P-9).
6. K. Hensel, K. Tarabova, K. Sano, B. Tarabova, M. Janda, Z. Machala, **R. Jijie**, C. T. Mihai, L. Gorgan, V. Pohoata, I. Topala, *DC Transient Spark Discharge in Water effects on cells, DNA, proteins and enzymes*, 20<sup>th</sup> Symposium on Application of Plasma Processes, SAPP XX & COST TD1208 Workshop on Application of Gaseous Plasma with Liquids, 17-22 January 2015, Tatranska Lomnica, Slovakia (poster: P-35)
7. Teodora Teslaru, **Roxana Jijie**, Ionut Topala, Marius Dobromir, Valentin Pohoata, Nicoleta Dumitrascu, *Stability of Polymers obtained in plasma reactors at atmospheric pressure*, European Winter Conference on Plasma Spectroscopy (EWCPS), 22-26 February 2015, Munster, Germany (poster: FU2-PO08)
8. Ilarion Mihaila, **Roxana Jijie**, Valentin Pohoata, Andrei Vasile Nastuta, Ioana Alexandra Rusu, Ionut Topala, *Mass spectrometry diagnosis of hydrocarbon containing plasmas with relevance for molecular astrophysics of hot cores*, COST

Action Our Astrochemical History CM1401, 25 – 29 May 2015, Prague, Czech Republic (poster – P16).

9. **Roxana Jijie**, Tedora Teslaru, Marius Dobromir, Valentin Pohoata, Ionut Topala, Rabah Boukherroub, Nicoleta Dumitrascu, *Copolymerization and Water Stability of Atmospheric Pressure Plasma Polymerized Films from Allylamine and Styrene*, ISPC 22 – 22<sup>nd</sup> International Symposium on Plasma Chemistry, 5 – 10 July 2015, Antwerp, Belgium (poster – P-III-6-23).
10. **Ionut Topala**, **Roxana Jijie**, Andrei Vasile Nastuta, Ioana Alexandra Rusu, Ilarion Mihaila and Valentin Pohoata, *Considerations on the use of atmospheric pressure plasma to generate complex molecular environments with relevance for molecular astrophysics*, ISPC 22 – 22<sup>nd</sup> International Symposium on Plasma Chemistry, 5 – 10 July 2015, Antwerp, Belgium (poster – P-I-2-68).
11. **Roxana Jijie**, Tedora Teslaru, Marius Dobromir, Valentin Pohoata, Ionut Topala, Alexandre Barras, Rabah Boukherroub, Nicoleta Dumitrascu, *Influence of carrier gas on the behavior of plasma polymerized polystyrene films in aqueous media*, International Conference on Phenomena in Ionized Gases – XXXII ICPIG, 26- - 31 July 2015, Iasi, Romania (poster – P4.58 )
12. **Teodora Teslaru**, **Roxana Jijie**, Marius Dobromir, Valentin Pohoata, Ionut Topala, V. Antoci, C.-I. Ciobanu, Nicoleta Dumitrascu, *On the polymerization reactions of thiophene monomers under atmospheric plasma conditions*, International Conference on Phenomena in Ionized Gases – XXXII ICPIG, 26- - 31 July 2015, Iasi, Romania (poster – P3.39)
13. **Ilarion Mihaila**, Valentin Pohoata, **Roxana Jijie**, Andrei Vasile Nastuta, Ioana Alexandra Rusu, Ionut Topala, *Influence of discharge geometry on extraction of positive ion populations from atmospheric pressure plasmas*, International Conference on Phenomena in Ionized Gases – XXXII ICPIG, 26- -31 July 2015, Iasi, Romania (poster – P2.18)
14. **I. Topala**, K. Hensel, K. Kucerovala, B. Tarabova, M. Janda, Z. Machala, C. T. Mihai, L. D. Gorgan, **R. Jijie**, M. Ciorpac and V. Pohoata, *Cell exposure to atmospheric pressure plasmas: modification of cell cycle and molecular structure*, International Conference on Phenomena in Ionized Gases – XXXII ICPIG, 26- - 31 July 2015, Iasi, Romania (invited presentation)
15. **Z. Machala**, K. Hensel, K. Kučerová, B. Tarabová, M. Janda, C.T. Mihai, L. Gorgan, **R. Jijie**, I. Topala, *Air transient spark discharge vs. helium plasma jet: The effects on bacteria, cells, and biomolecules*, Bioplasmas & Plasmas with Liquids - Joint Conference of COST TD1208 ‘Electrical discharges with liquids for future applications’, Bertinoro (Italy), September 13-17, p. USB (2015)
16. **K. Kučerová**, M. Janda, Z. Machala, K. Hensel, **R. Jijie**, C.T. Mihai, L. Gorgan, I. Topala, *Chemical and Biological Effects of Air DC Transient Spark Discharge*

*in Water Electrode System*, 6th Central European Symposium on Plasma Chemistry CESPC, Bressanone (Italy), September 6-10, p. USB (2015).

17. Kostiantyn Turcheniuk, **Roxana Jijie**, Julie Boukaert, Nicoleta Dumitrascu, Rabah Boukherroub, Sabine Szunerits, *Plasmonic nanostructures for the inactivate of bacteria strains*, 2016 E-MRS Spring Meeting, Materials – Established and emerging nanocolloids/ from synthesis and characetrization to applications II (invited presentation J.1.5)
18. **Roxana Jijie**, Tetiana Dumych, Kostiantyn Turcheniuk, Charles-Henri Hage, Laurent Helio, Nicoleta Dumitrascu, Julie Boukaert, Rabah Boukherroub, Sabine Szunerits, *Photodynamic inactivation of pathogenic bacteria by plasmonic nanostructures embedded with indocyanine green*, 2016 E-MRS Spring Meeting, Biomaterials – Multifunctional nanostructures for diagnostic and therapeutic of diseases (poster R.9.54)
19. Houcem Maaoui, Roxana Jijie, Radouane Chtourou, Sabine Szunerits and Rabah Boukherroub, *980-nm driven photothermal ablation of virulent and antibiotic resistant Gram- positive and Gram-negative bacteria strains*, 2016 E-MRS Spring Meeting, Biomaterials –Smart biointerfaces for functional biomaterials (oral presentation Q.10.2)
20. Delia Ciubotaru, **Roxana Jijie**, Valentin Pohoata, Ilarion Mihaila, Andrei Vasile Nastuta, Marius Dobromir, Ionut Topala, *Spectroscopic studies of gas phase and deposited films in He/H<sub>2</sub>/C<sub>n</sub>H<sub>2n+2</sub> atmospheric pressure plasmas*, 2016, 23<sup>rd</sup> Europhysics Conference on Atomic and Molecular Physics of Ionized Gases, July 12-16, 2016, Bratislava, Slovakia (poster P03-08-01).
21. Ionut Topala, Cristina Gerber, Dennis Hein, Andrei Nastuta, **Roxana Jijie**, Valentin Pohoata, Ilarion Mihaila, Cosmin Mihai , Lucian Gorgan, *Atmospheric pressure plasma jets for life science*, 23<sup>rd</sup> Europhysics Conference on Atomic and Molecular Physics of Ionized Gases, July 12-16, 2016, Bratislava, Slovakia (invited presentation TL4).
22. **Roxana Jijie**, Teodora Teslaru, Valentin Pohoata, Marius Dobromir, Julie Bouckaert, Sabine Szunerits, Rabah Boukherroub, Nicoleta Dumitrascu, *Antibiofouling properties of plasma polymerized styrene film*, 11<sup>th</sup> International Conference On Physics Of Advanced Materials (ICPAM-11), 8-14 September 2016, Cluj-Napoca, Romania (oral presentation).
23. **Roxana Jijie**, Delia Ciubotaru, Valentin Pohoata, Ilarion Mihaila, Andrei Vasile Nastuta, Marius Dobromir, Ionut Topala, *Characterization of carbonaceous deposits as interstellar dust analogs produced in hydrocarbon containing plasmas at atmospheric pressure*, 11<sup>th</sup> International Conference On Physics Of Advanced Materials (ICPAM-11), 8-14 September 2016, Cluj-Napoca, Romania (poster).

#### **4. Specializations and short research visits:**

- 1. Mars – June 2016, August - November 2015, February - May 2014**, three PhD mobilities at Institut d'Electronique, de Microélectronique et de Nanotechnologie (IEMN, UMR 8520), Université Lille 1 Sciences et Technologies, France
- 2. 2 February – 2 June 2015**, ERASMUS + Study Mobility at Institut d'Electronique, de Microélectronique et de Nanotechnologie (IEMN, UMR 8520), Université Lille 1 Sciences et Technologies, France
- 3. 24– 28 November 2014**, visiting researcher at the National Institute of Research - Development of Biological Sciences, Bucharest , Romania
- 4. 15 - 21 November 2013** visiting researcher at the University of Cyprus, Department of Electrical and Computer Engineering – The bilateral project Romania – Cyprus, titled Development, Diagnostics and Modelling of Cold Plasma Jets at Atmospheric Pressure for Direct Treatment of Living Tissues (MEDPLASMA) 2012 -2013

#### **5. Member contracts**

- 1. RESEARCHERS' NIGHT in ROMANIA 2013: Science. The great escape (2013)**, Funding agency: European Commission under FP7, grant no. 609771 (RNR 2013)
- 2. Development, diagnostic and modelling of cold plasma jets at atmospheric pressure for direct treatment of living tissues (2011-2013)**, Funding agency: UEFISCDI, Romania-Cyprus Bilateral cooperation
- 3. Effects of atmospheric pressure cold discharge plasmas to bacteria and cell cultures (2013-2014)**, Funding agency: UEFISCDI, Romania-Slovakia Bilateral cooperation
- 4. Assistant researcher in the project Synthesis of transient complex molecular systems in laboratory plasmas as with relevance for molecular astrophysics of hot cores (2013-2016)**, Funding agency: Romanian Space Agency, under the programme Space Technology and Advanced Research, grant no. 96/11.12.2013 (under implementation)